
**NIFS-PROC-93**

# Physics and Application of Plasmas Based on Pulsed Power Technology, Jan. 10 - 11, 2013

(Ed.) K. Takasugi

Aug. 26, 2013

**Physics and Application of Plasmas Based on Pulsed Power Technology**
**Jan. 10 – 11, 2013**

**(Ed.) K. Takasugi**

# Physics and Application of Plasmas Based on Pulsed Power Technology

Edited by Keiichi Takasugi

January 10 – 11, 2013
National Institute for Fusion Science
Toki, Gifu, Japan

## ABSTRACT

The papers presented at the symposium on "Physics and Application of Plasmas Based on Pulsed Power Technology" held on January 10 – 11, 2013 at National Institute of Fusion Science are collected. The papers in this proceedings reflect the current status and progress in the experimental and theoretical researches on physics and application of plasmas produced by pulsed power technology.

## Keywords

high energy density plasma, pulsed power technology, high power particle beam, z-pinch, plasma focus, soft x-ray, EUV lithography, water window, x-ray laser, medical application

# Preface

The symposium entitled "Physics and Application of Plasmas Based on Pulsed Power Technology" was organized as a part of the General Collaborative Research of National Institute for Fusion Science (NIFS) and held on January 10 – 11, 2013 at NIFS, Toki.

In the symposium 27 papers were presented in two days, of which 21 papers are reported in this proceeding. The total number of participants was 44 including students and researchers from universities and a company.

As the field of high energy density plasma has a multidisciplinary nature, the extensive discussion of related subjects is difficult in conventional scientific meeting. The objective of the symposium is to provide a forum to discuss technical developments, applications, increased understandings, new trends and the future prospects in the field of high energy density plasmas, as well as the issues of pulsed power technology. It is my great pleasure if the symposium could provide some kind of opportunity for all of the attended people, especially for young scientists.

I would like to express my sincere thanks to all of the participants, the authors and the staff of NIFS.

Keiichi Takasugi
Institute of Quantum Science
Nihon University

# Contents

# List of Participants

| | |
|---|---|
| Ando, T. | Nihon University |
| Gu, Y.J. | Utsunomiya University |
| Hasegawa, J. | Tokyo Institute of Technology |
| Hashimoto, Y. | Kobe City College of Technology |
| Hayashi, R. | Nagaoka University of Technology |
| Higashiguchi, T. | Utsunomiya University |
| Horioka, K. | Tokyo Institute of Technology |
| Hotta, E. | Tokyo Institute of Technology |
| Ikeda, S. | Tokyo Institute of Technology |
| Imada, G. | Niigata Institute of Technology |
| Imasaka, K. | Kyushu Sangyo University |
| Inagaki, R. | Nagaoka University of Technology |
| Isono, F. | Tokyo Institute of Technology |
| Ito, H. | Toyama University |
| Jiang, W. | Nagaoka University of Technology |
| Kamada, K. | Kanazawa University |
| Kakuhari, R. | Niigata Institute of Technology |
| Kawamura, T. | Tokyo Institute of Technology |
| Kikuchi, T. | Nagaoka University of Technology |
| Kitajima, K. | Toyama University |
| Kondo, K. | Tokyo Institute of Technology |
| Matsuda, R. | Nagaoka University of Technology |
| Miyamori, H. | Niigata Institute of Technology |
| Miyata, Y. | Toyama University |
| Miyazaki, T. | Nihon University |
| Munamoto, N. | Tokyo Institute of Technology |
| Murata, T. | Niigata Institute of Technology |
| Nagashima, T. | Utsunomiya University |
| Nishio, M. | Nihon University |
| Nobe, K. | Tokyo Institute of Technology |
| Noguchi, K. | Utsunomiya University |
| Ogasawara, K. | Nagaoka University of Technology |
| Ogawa, T. | Kanazawa University |
| Onda, M. | Nagaoka University of Technology |
| Oya, R. | Gunma University |
| Ozaki, T. | National Institute for Fusion Science |
| Park, Y. | Kanazawa University |
| Sakai, Y. | Tokyo Institute of Technology |
| Soga, Y. | Kanazawa University |

| | |
|---|---|
| Sugai, T. | Nagaoka University of Technology |
| Takasugi, K. | Nihon University |
| Tazima, T. | National Institute for Fusion Science |
| Tokuchi, A. | Pulsed Power Japan Laboratory Ltd. |
| Yamada, S. | Niigata Institute of Technology |

# Numerical Analysis for Evaluation of Thermal and Optical Properties in Warm Dense Matter Generated by Pulsed Power Discharge

Takashi Kikuchi, Hirotaka Saito, Yasutoshi Miki, Ryota Hayashi, Takuya Takahashi, Toru Sasaki, Tsukasa Aso, Nob. Harada

*Nagaoka University of Technology*

**ABSTRACT**

Both numerical and experimental approaches are applied to evaluation for warm dense matter. To clear thermal and optical properties of warm dense matter, the numerical simulation of time-dependent one-dimensional thermal diffusion with radiative transfer is carried out in a compact pulsed power discharge device. The numerical model is described to include multi-group approximation for the radiation energy density distribution. Using the numerical model, the radiation energy density depended on the frequency is indicated with the experimental condition.

**Keywords**

Numerical Simulation, Pulsed Power Discharge, Warm Dense Matter, Thermal Diffusion, Radiation Energy Density, Absorption Coefficient, Multi-Group Approximation

## 1 Introduction

Property data of warm dense matter (WDM), which is in a transition regime from a solid to plasma, are important to control implosion dynamics in a fuel pellet of inertial confinement fusion (ICF) [1]. Because, to irradiate an energy driver such as intense lasers, high power X-ray, and high-current heavy ion beams, the material phase of the fuel pellet changes from solid to plasma conditions.

Since the WDM regime is in an extreme high pressure situation, it is difficult to create stationary the condition with a measurable setup. Consequently, the properties in the WDM regime are unclear.

Pulsed power discharge devices were used to generate the extreme state of matter from a solid to plasma [2–4]. For the generation of WDM with a well-defined condition, the apparatus with isochoric heating using a sapphire hollow capillary as a rigid body wall was proposed by using a table-top pulsed-power device [5]. In the experimental apparatus, the emission from the heated sample was observable due to the transparent sapphire capillary.

In our previous studies [6–8], we numerically investigate to generate the WDM by using pulsed power discharge devices to obtain the properties of the WDM. In this study, the numerical model with the thermodynamics and the radiation energy density is developed to obtain the thermal and optical properties of the WDM.

## 2 Numerical Modeling

In this study, we solve simultaneously the thermal diffusion and radiative transfer, and the details of the numerical model used in this paper were explained in Ref. [7]. Time-dependent one-dimensional thermal diffusion equation with cylindrical symmetry configuration is numerically solved to simulate the WDM generation in the compact

pulsed power discharge experiment [5].

In the experimental setup [5], we can assume to calculate the phenomena in the foam/plasma ignoring the hydrodynamics, because the fluid dynamics of the sample plasma is limited by the capillary. For this reason, we only calculate the thermodynamics in the foam/plasma without the fluid dynamics of plasma. In the apparatus, a foamed copper is used as a sample, and is surrounded with a hollow sapphire capillary. The computational box used in this paper is adjusted in the experimental setup [6–8]. The inner region ($0 < r <$ 2.5 mm) is the foamed copper as a sample, and the outer region (2.5 mm $< r <$ 4 mm) is the sapphire as a rigid capillary. The capillary length $L_{\rm cap}$ is 10 mm.

The density of the foamed copper surrounded in the hollow capillary is 0.1 times the solid density (8920 kg/m$^3$). The mass density of the sapphire is 3970 kg/m$^3$ as the solid. Since the sample is a foamed material, we assumed that the skin effect can be ignored. As a result, the discharge current distribution is assumed as uniform in the copper region.

The initial temperature is set as 300 K by a room temperature in the whole computational region. The conventional thermal property data of copper in solid, liquid, and gas phases are given by Refs. [9–12]. In the sapphire region, the material parameters for numerical simulation are 42 W/m-K for the thermal conductivity and 750 J/kg-K for the specific heat, as room temperature values.

The radiative transfer equation is solved by the diffusion approximation [13]. Although, the WDM regime is expected to be quite thick optically, the radiation generated in the interior of the WDM region is not able to pass through the WDM region. For this reason, the diffusion equation for the radiation energy density $E^g$ is modified by

$$\frac{\partial E^g}{\partial t} = (4\pi\, B^g - c\, E^g)\, \kappa_{\rm P}^g, \tag{1}$$

along the radius $r$ in the cylindrical coordinate with a multi-group approximation in the frequency domain group $g$ [14]. Here, $E^g$ is the radiation energy density at $g$ th group,

$$E^g = \frac{\int_{\nu_g}^{\nu_{g+1}} E_\nu\, d\nu}{\int_{\nu_g}^{\nu_{g+1}} d\nu}, \tag{2}$$

and

$$\kappa_{\rm P}{}^g = \frac{\int_{\nu_g}^{\nu_{g+1}} \kappa_\nu\, B_\nu\, d\nu}{\int_{\nu_g}^{\nu_{g+1}} B_\nu\, d\nu}, \tag{3}$$

is the Planck absorption coefficient at $g$ th group [15], $k_{\rm B}$ is the Boltzmann constant, and the blackbody intensity is

$$B^g = \frac{\int_{\nu_g}^{\nu_{g+1}} B_\nu\, d\nu}{\int_{\nu_g}^{\nu_{g+1}} d\nu}. \tag{4}$$

According to the measuring instrument in the experimental setup [16], the frequency domain is divided and grouped as the following Table 1.

Table 1: Relation between group number and frequency domain for multi-group approximation of radiation energy density. Here, the wavelength $\lambda$ of radiation is defined by the speed of light $c$ / the frequency $\nu$.

| Group $g$ | Wavelength $\lambda$ |
|---|---|
| 1 | $>$ 800 nm |
| 2 | 800 $\sim$ 680 nm |
| 3 | 680 $\sim$ 520 nm |
| 4 | 520 $\sim$ 370 nm |
| 5 | 370 $\sim$ 340 nm |
| 6 | $<$ 340 nm |

The $\kappa_\nu$ [1/cm] is the frequency $\nu$ dependent absorption coefficient [17],

$$\kappa_\nu = 7.13 \times 10^{-16} \frac{n_{\rm i}(Z^*+1)^2 \exp\{-(\xi-\chi)\}}{T^2\chi^3}, \tag{5}$$

where $n_{\rm i}$ is the ionic density [1/cm$^3$], $Z^*$ is the mean ionization degree (0.5 is assumed from the previous experimental result [5]), $\chi = h\nu/T$, and $\xi = I_0/T$. $h$ is the Planck constant, $I_0$ is the mean ionization potential (7.73 eV for Cu), and $T$ is the temperature with unit [eV] in this equation.

The radiative transfer with the flux limited diffusion approximation [18] is calculated by [7]

$$\frac{\partial E^g}{\partial t} = -\frac{c}{r}\frac{\partial E^g}{\partial r}, \tag{6}$$

in the sapphire region.

The input power history is given by the corresponding experimental data [5, 16].

# 3 Calculation Result

The numerical simulation confirmed that the sample was achieved to be the temperature generating WDM [6, 7], and the result could be compared

with the experimental result [5]. The result indicated that the temperature at the interface between the copper foam and the sapphire capillary was diffused, and the temperature around the edge of copper region is reduced due to the difference of the heat capacities [7,8]. The numerical result with one-group approximation for the radiation transfer was compared with the experimental result [16].

Figure 1 shows the radiation energy density distributions as a function of time at each frequency group given by the numerical simulation of time-dependent phenomena in the copper foam and the sapphire capillary regions. The radiation energy density distribution at each frequency group corresponds to the temperature distribution [7].

Figure 2 shows the numerically obtained radiation energy density observed at edge of capillary ($r = 4$ mm) as a function of time at each frequency group. The previous experiment indicated that the sample temperature achieved to be around 5000 K [5]. From Wien displacement law [19], the wavelength of the maximum blackbody emission, which is given by $\lambda_W = 2.5 \times 10^{-7}/(T[\mathrm{eV}])$, is estimated at 580 nm for 5000 K. In this calculation, the wavelength of 580 nm is included in the domain at $g = 3$, and the calculation result in Fig. 2 is confirmed with the experimental result.

When the emission intensity measurement with the multi-channel spectroscopy system [16] is completed, the radiative transfer calculation can be confirmed with the experimental results, and the calculation result will support the experimental results through the radiation distribution.

# 4 Conclusion

In this study, it was considered that both the numerical and experimental approaches were applied to evaluation for WDM. To clear the thermal and optical properties of WDM, the numerical simulation of time-dependent one-dimensional thermal diffusion with radiative transfer was carried out in the compact pulsed-power discharge device. The numerical model was described to include the multi-group approximation for the radiation energy density. Using the numerical model, the radiation energy density depended on the frequency was shown with the experimental condition.

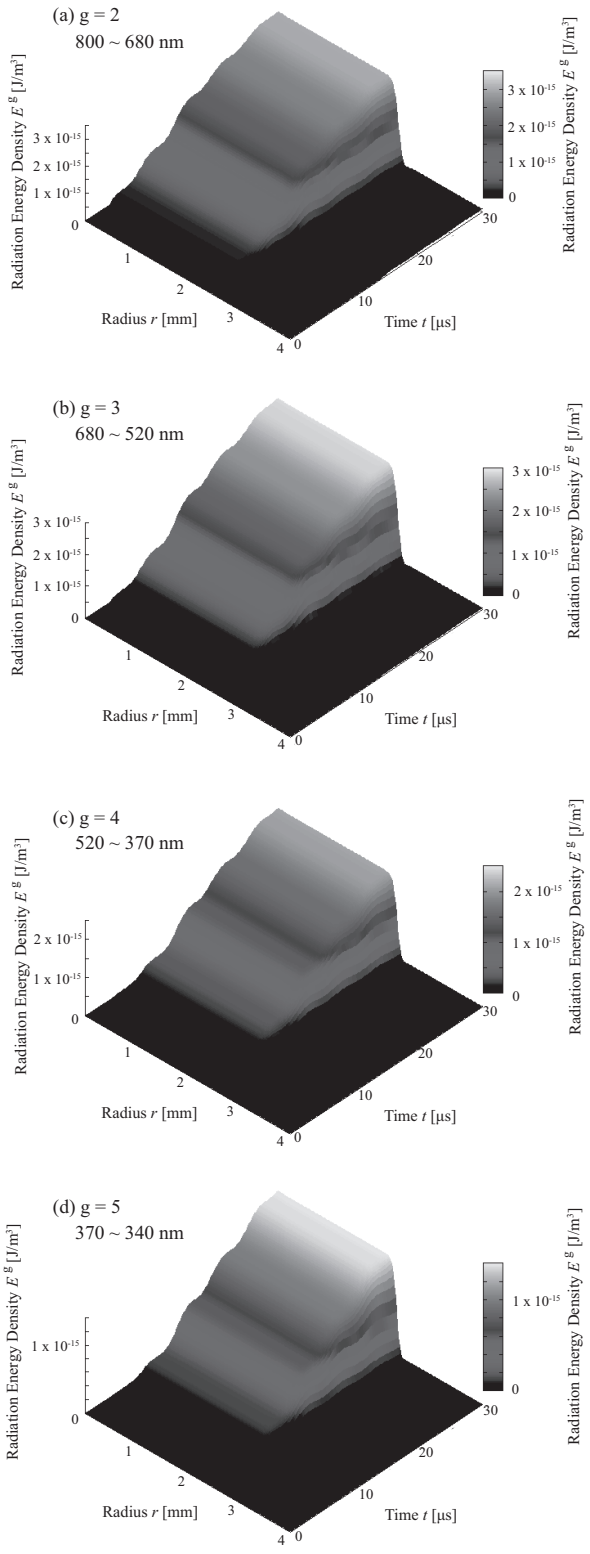


Figure 1: Radiation energy density distributions as a function of time at each frequency domain grouped, (a) for $g = 2$, (b) for $g = 3$, (c) for $g = 4$, and (d) for $g = 5$, respectively.

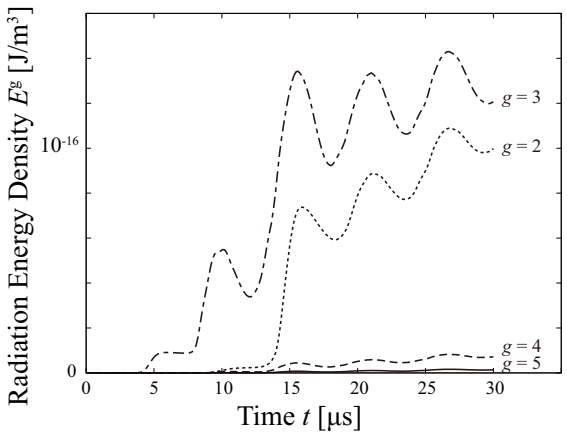


Figure 2: Radiation energy density observed at edge of capillary ($r = 4$ mm) as a function of time at each frequency grouped. The dotted line indicates the radiation energy density for $g = 2$, the dashed-dotted curve indicates the radiation energy density for $g = 3$, the dashed line shows the radiation energy density for $g = 4$, and the solid curve shows the radiation energy density for $g = 5$, respectively.

For the evaluation of the optical and thermal properties in the WDM regime, the numerical model developed will be applied in the various experimental conditions, and the calculation results will be confirmed with the experimental results in our near future work.

# Acknowledgment

This work was supported from the Grant-in-Aid for Scientific Research from the Ministry of Education, Science, Sports, Culture and Technology, Japan, and by Program for High Reliable Materials Design and Manufacturing in Nagaoka University of Technology.

# References

[1] S. ATZENI and J. MEYER-TER-VEHN, *The Physics of Inertial Fusion: Beam Plasma Interaction, Hydrodynamics, Hot Dense Matter* (Oxford Univ., N.Y., 2004).

[2] A.W. DESILVA and J.D. KATSOUROS, *Phys. Rev.* **E 57**, 5945 (1998).

[3] T. SASAKI, M. NAKAJIMA, T. KAWAMURA, and K. HORIOKA, *Phys. Plasmas*, **17**, 084501 (2010).

[4] T. SASAKI, T. SUZUKI, Y. AMANO, Y. MIKI, T. KIKUCHI, Nob. HARADA, and K. HORIOKA, *IOP Conf. Series: Material Science and Engineering*, **21**, 012016 (2011).

[5] Y. AMANO, Y. MIKI, T. SASAKI, T. KIKUCHI, and Nob. HARADA, *Rev. Sci. Instrum.*, **83**, 085107, 2012.

[6] T. KIKUCHI, T. SASAKI, Nob. HARADA, W. JIANG, and A. TOKUCHI, "Numerical Analysis for Low-Temperature and Dense Plasma Generation using Pulsed Power Discharge Devices", *Plasma 2011*, Kanazawa, Nov. 22-25, (2011) 23P162-R.

[7] T. KIKUCHI, H. SAITO, R. HAYASHI, T. SASAKI, and Nob. HARADA, "Numerical Analysis and Experimental Evaluation for Low-Temperature and Dense Plasma Generation using Pulsed Power Discharge Device", to be published in *NIFS -PROC*.

[8] T. KIKUCHI, Y. MIKI, H. SAITO, R. HAYASHI, T. TAKAHASHI, T. SASAKI, T. ASO, and Nob. HARADA, *Proceedings of 4th Euro-Asian Pulsed Power Conference and 19th International Conference on High-Power Particle Beams (EAPPC2012 / BEAMS2012)*, September 30 - October 4, 2012, Karlsruhe, Germany, P2C-3, Paper_320.

[9] C.Y. HO, R.W. POWELL, and P.E. LILEY, "Thermal Conductivity of the Elements", *JPCRD*, **1(2)**, pp.279-422 (1972).

[10] C.Y. HO, R.W. POWELL, and P.E. LILEY, "Thermal Conductivity of the Elements: A Comprehensive Review", *JPCRD*, **3(Suppl. 1)**, pp.1-796 (1974).

[11] NIST Standard Reference Database Number 69, http://webbook.nist.gov/chemistry/

[12] M.W. CHASE, NIST-JANAF Thermochemical Tables, Fourth Edition, *J. Phys. Chem. Ref. Data*, Monograph 9 (1998).

[13] J.I. CASTOR, *Radiation Hydrodynamics* (Cambridge University Press, 2007).

[14] S. ATZENI and J. MEYER-TER-VEHN, *The Physics of Inertial Fusion: Beam Plasma Interaction, Hydrodynamics, Hot Dense Matter* (Oxford Univ., N.Y., 2004) Chap. 7.3.

[15] L. DRSKA and M. SINOR, *Computer Phys. Communications*, **997**, pp.1-12 (1996).

[16] H. SAITO, Y. MIKI, T. TAKAHASHI, T. SASAKI, T. KIKUCHI, T. ASO, and Nob. HARADA, "Study on Optical Properties for Warm Dense Matter Generated by Pulsed-Power Discharge Device", *11th APCPST (Asia Pacific Conference on Plasma Science and Technology) and 25th SPSM (Symposium on Plasma Science for Materials)*, Kyoto, October 2-5, 1-P67, 2012.

[17] A. MANCIC, J. ROBICHE, P. ANTICI, P. AUDEBERT, C. BLANCARD, P. COMBIS,

F. DORCHIES, G. FAUSSURIER, S. FOURMAUX, M. HARMAND, R. KODAMA, L. LANCIA, S. MAZEVET, M. NAKATSUTSUMI, O. PEYRUSSE, V. RECOULES, P. RENAUDIN, R. SHEPHERD, and J. FUCHS, *High Energy Density Phys.*, **6**, pp.21-28 (2010).

[18] C.D. LEVERMORE and G.C. POMRANING, *Astrophysical Journal*, **248**, pp.321-334 (1981).

[19] J.D. HUBA, *NRL Plasma Formulary* (Naval Research Labratory, 2011).

# Production of dissociated hydrogen gas by electro-magetically driven shock

*Kotaro Kondo*, Takao Moriyama, Jun Hasegawa,*
*Kazuhiko Horioka, Yoshiyuki Oguri (Tokyo Institute of Technology)*

Evaluation of ion stopping power which has a dependence on target temperature and density is an essential issue for heavy-ion-driven high energy density experiment. We focus on experimentally unknown dissociated hydrogen atoms as target for stopping power measurement. The precise measurement of shock wave velocity is required because the dissociated gas is produced by electro-magnetically driven shock. For beam-dissociated hydrogen gas interaction experiment, shock velocity measurement using laser refraction is proposed.

(Pulsed power, Electro-magnetically driven shock, Dissociated hydrogen, Ion stopping power)

## 1. Introduction

The Evaluation of ion stopping power which depends target temperature and density is important for heavy ion fusion target design and heavy-ion-driven high energy density physics experiment. Stopping power is defined as the average energy loss of the particle per unit path length in the target. The stopping power in solid matter was studied in ion implantation or radiology[(1) (2)]. The stopping power for low energy beam depends on the electronic state. For example, the stopping power in high temperature and low density plasma is larger than that in room temperature gas because free electrons in plasma are carriers of energy transfer between ion beam and target. The stopping power in warm dense matter is lower due to electron degeneracy[(3)]. However, the effects of dissociation of the target molecules up to ionization in stopping cross section have not been experimentally investigated. We are interested in dissociation effect on the stopping power of hydrogen target.

Electro-magnetically driven shock wave was proposed for production of well-defined dissociated target, which is desirable for the stopping power measurement. The method generated quasi-steady and one-dimensional strong shock wave[(4)]. The discharge plasma with piston velocity $u_p$ drives shock wave with shock velocity $u_s$ to dissociate the target gas as shown in Fig. 1. The shock wave method has an advantage because Rankine-Hugoniot relations[(5)] with shock wave velocity can give the shocked condition.

For beam-dissociated hydrogen interaction experiment, the previous experiment showed that the duration of the shocked region between the shock front and the discharge plasma is desired to be in the order of microseconds. A long shock tube could generate the dissociated hydrogen target with long duration time because Fig. 1 shows that compression region length $L$ increases with the propagation length of the shock wave. We have the new shock tube with long propagation section.

The previous experiment[(6)] showed 25 km/s shock velocity in initial pressure of 1000 Pa is required for pure dissociated hydrogen gas without ionization. We need precise shock velocity measurement because the shocked condition is sensitive to the velocity. The laser refraction, which needs only simple and compact devices, is proposed as the method of velocity measurement. In this paper, we showed the measurement results of the electro-magnetically driven shock velocity.

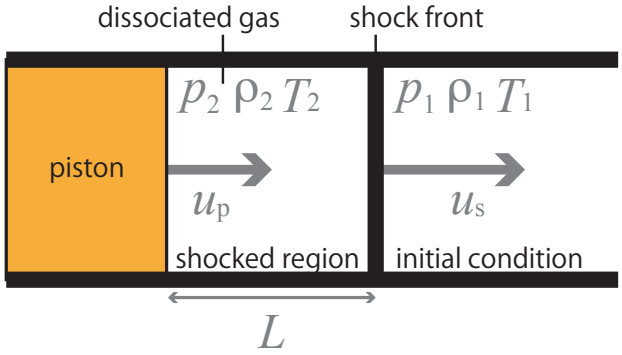


Fig. 1. It shows the region in front of the shock as subscript 1 with the subscript 2 defining the region behind the shock. $p$ , $\rho$, $T$ mean pressure, mass density, and temperature, respectively.

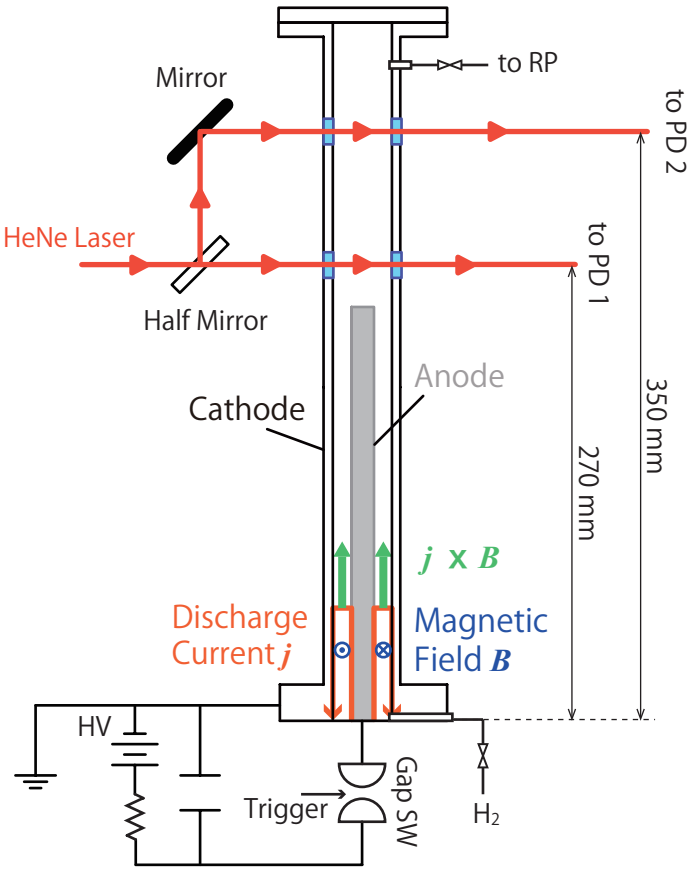


Fig. 2. This experimental setup consists of eletro-magnetically driven shock tube, equivalent circuit, and HeNe laser with optical devices for shock measurement.

## 2. Experimental setup and procedure

### ⟨2・1⟩ Renewed shock tube

Fig. 2 shows this experimental setup of electro-magnetically driven shock tube and the equivalent circuit with He-Ne Laser system for velocity measurement. Hydrogen gas with pressure from 300 to 1000 Pa was filled in the renewed shock tube. The electrodes were connected with a gap switch and capacitors with 3.5 μF. The charging voltage was from 16 to 18 kV. In order to produce the dissociated hydrogen with long duration, the center electrode with 12 mm outer diameter is 180 mm longer than before. The inner diameter of cathode is 30 mm. The discharge plasma is generated between the electrodes after the trigger signal into the gap switch. The discharge current sheet, which was accelerated by the magnetic pressure, produces a shock wave. The dissociated hydrogen target can be formed between the shock front and the discharge plasma when we have the proper shock velocity.

### ⟨2・2⟩ Velocity measurement using laser refraction

Shock velocity is sensitive to produce pure dissociated hydrogen target. In order to measure the velocity, we propose a laser refraction method as shown in Fig. 2. He-Ne laser (NEC, Inc., GLG5740, Max output: 50 mW), which is divided by a half mirror, passed through the optical windows on the axis of the shock tube. When shock wave reaches to the window, the density gradient at the shock front causes the laser refraction. At this moment, the photodiode (Hamamatsu, Inc., S5972) behind the shock tube detected the change of the laser signal and the arrival time of shock wave. The two divided lasers were alined with two photodiodes (PD1 and PD2). PD1 and PD2 were placed 270 mm and 350 mm from the bottom of the central electrode, respectively. From the two photodiode signals, the averaged velocity was estimated.

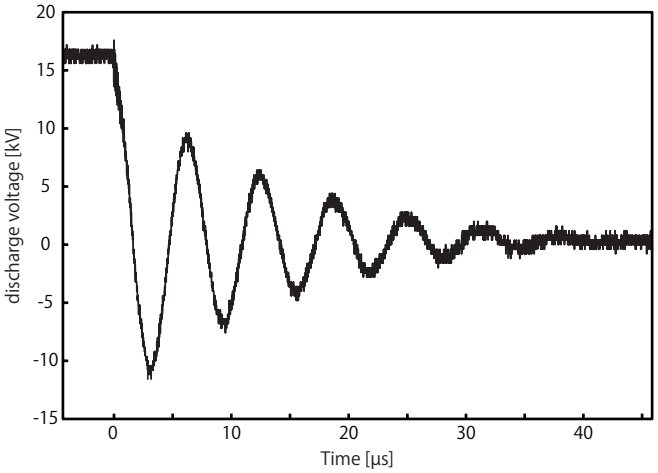


Fig. 3. It shows discharge voltage signal for charging voltage of 16 kV. That is a damped sine wave with period of 6.5 μs.

〈2・3〉 Experimental procedure

A delay pulser (Stanford Research System, Inc., DG535) with amplifiers controls the main discharge to supply the trigger signal to the gap switch. The discharge pulse shape was obtained by high voltage probe (Tektronix, Inc., P6015A) as shown in Fig. 3. In this experiment, dependence of initial hydrogen gas pressure and charging voltage is investigated. For dependence of initial pressure, we have initial pressure of 360 Pa, 700 Pa, and 1000 Pa with 16 kV charging voltage. For dependence of charging voltage, we have charging voltage of 16 kV, 17 kV, and 18 kV with 1000 Pa initial pressure. In order to investigate the reproducibility, three measurements were performed each experiment.

## 3. Experimental setup and procedure

〈3・1〉 Photodiode signal

Output signals from photodiodes are shown in Fig. 4. The vertical axis stands for time after the discharge. The discharge voltage was 16 kV and initial hydrogen gas pressure was 1000 Pa in Fig. 4. The signal baselines of PD1 and PD2 shifted to 8 mV and 10 mV, respectively because CW laser was used. Noise signals of two photodiodes were observed until 5 μs due to the discharge. As shown in Fig. 4, we observed signal changes at 19.9 μs and at 32.2 μs for PD1 and PD2, respectively.

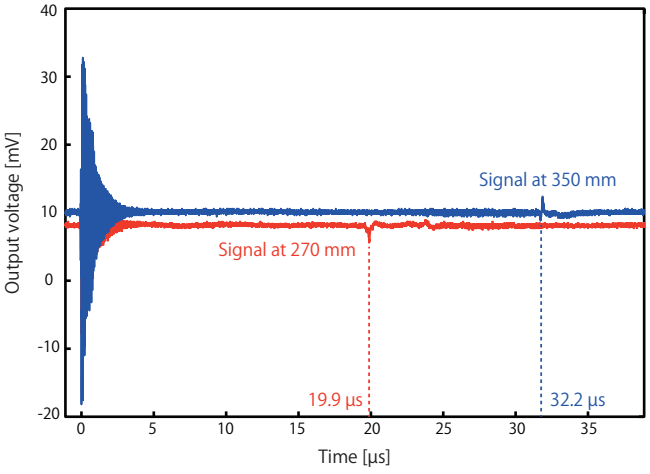


Fig. 4. Output signals from 2 photodiodes (PD1 and PD2).

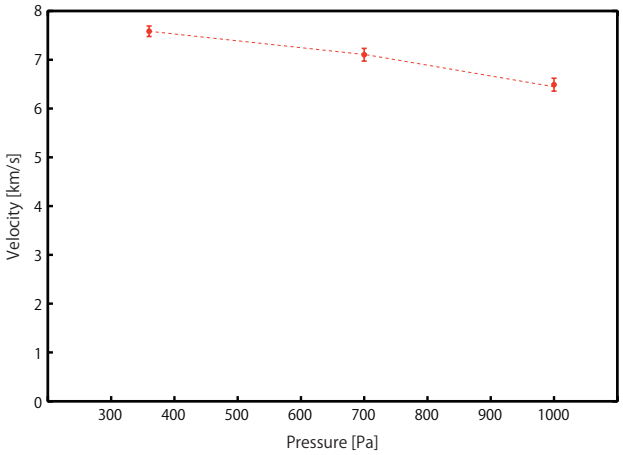


Fig. 5. Average shock wave velocity VS initial pressure (360 Pa, 700 Pa, and 1000 Pa). Dot means the average value for three measurements and error bar shows standard deviation. Each average point are connected by the dash line.

〈3・2〉 Initial gas pressure dependence

Average shock wave velocity for the initial hydrogen gas pressure is shown in Fig. 5. These results show that the higher velocity was observed for the lower initial pressure. The qualitative behavior could be correct because the the discharge voltage was fixed to 16 kV for these measurements. Fig. 5 shows reproducibility in this experiment.

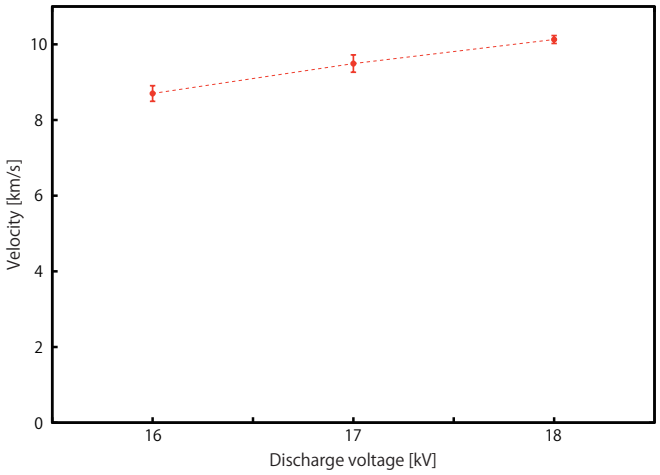


Fig. 6. Average wave velocity VS charging voltage (16 kV, 17 kV, and 18 kV). Dot means the average value for three measurements and error bar shows standard deviation. Each average point are connected by the dash line.

〈3・3〉 Discharge voltage dependence

Fig. 6 shows average shock wave velocity for the charging voltage. These results show that the higher shock wave velocity was observed for the high charging voltage. The qualitative behavior could be also correct. Reproducibility in this experiment is shown in Fig. 6.

## 4. Summary

We measured the average shock wave velocity by laser refraction. The velocity measurement by this method can be reliable because the qualitative behavior of the results can be correct from the initial gas pressure and discharge voltage dependence. On the other hand, the shock wave velocity is not enough to dissociate hydrogen gas. The more input energy is required for pure dissociated hydrogen gas target with large volume using the renewed long shock tube.

## References


(1) D. I. Thwaites:“Current status of physical state effects on stopping power”, Nucl. Instrum. Methods Phys. Res. B 12, No.1, pp. 84-89 (1985).

(2) P. Bauer, F. Kastner, A. Arnau, A. Salin, P.D. Fainstein, V.H. Ponce and P.M. Echenique:“Phase effect in the energy loss of H projectiles in Zn targets: Experimental evidence and theoretical explanation”, Phys. Rev. Lett., 69, No.7, pp.1137-1139 (1992).

(3) P.T. Leon, S. Eliezer, J.M. Martinez-Val, M.Piera:“Fusion burning waves in degenerate plasmas”, Phys. Lett. A 289, No.3, pp. 135-140 (2001).

(4) K. Kondo, M. Nakajima, T. Kawamura and K. Horioka: “Compact pulse power device for generation of one-dimensional strong shock waves”, Rev. Sci. Instrum. 77, No.3, pp. 036104-1-3(2006).

(5) H.W. Liepmann and A. Roshko:“Elements of gasdynamics”, Dover Publications, New York (1993).

(6) J. Hasegawa, H. Ikagawa, S. Nishinomiya, T. Watahiki and Y. Oguri: “Beam-plasma interaction experiments using electromagnetically driven shock wave”, Nucl. Instrum. Methods Phys. Res. A 606, No.1-2, pp.205-211 (2009).

# Control of Ion Beam Generation in Intense Short Pulse Laser Target Interaction

T. Nagashima[1], T. Izumiyama[1], D. Barada[1], S. Kawata[1], W. M. Wang[2]
Y. Y. Ma[3], Q. Kong[4], Y. J. Gu[1, 4]

[1]*Graduate School of Engineering, Utsunomiya University*

[2]*Institute of Physics Chinese Academy of Sciences, China*

[3]*National University of Defense Technology, China*

[4]*Institute of Modern Physics, Fudan University, China*

## ABSTRACT

In intense laser plasma interaction, several issues still remain to be solved for future laser particle acceleration. In this paper we focus on a control of generation of high-energy ions. In this study, near-critical density plasmas are employed and are illuminated by high intensity short laser pulses; we have successfully generated high-energy ions, and also controlled ion energy and the ion energy spectrum by multiple-stages acceleration. We performed particle-in-cell simulations in this paper. The first near-critical plasma target is illuminated by a laser pulse, and the ions accelerated are transferred to the next target. The next identical target is also illuminated by another identical laser pulse, and the ion beam introduced is further accelerated and controlled. In this study four stages are employed, and finally a few hundreds of MeV of protons are realized. A quasi-monoenergetic energy spectrum is also obtained.

## Keywords

Laser ion acceleration, target plasma, post acceleration, multistage acceleration

## 1. Introduction

Particle accelerators have played important roles in various fields, such as basic particle physics, cancer therapy, industrial applications, inertial confinement fusion, etc. Existing accelerator has a limitation of the acceleration gradient, and its size and cost are huge.

On the other hand, intense short-pulse lasers are now available. Based on the new laser technology, new acceleration mechanisms have been proposed using the laser pulse, as alternatives of the conventional accelerator. However, there are also issues in the laser particle acceleration method. In the laser particle acceleration, the issues includes a lack of controllability for particle beam quality and for its lower energy efficiency. These issues should be addressed toward a realistic laser particle accelerator. In this study we focus a laser proton beam generation.

In the laser ion acceleration, first target electrons are kicked by the incoming intense laser pulse, and form an electron cloud at the target surfaces. The target substrate becomes positively charged, and a strong electric field is created at the target surfaces. At the target rear surface, if an ion source is located, the ions are accelerated. This ion acceleration

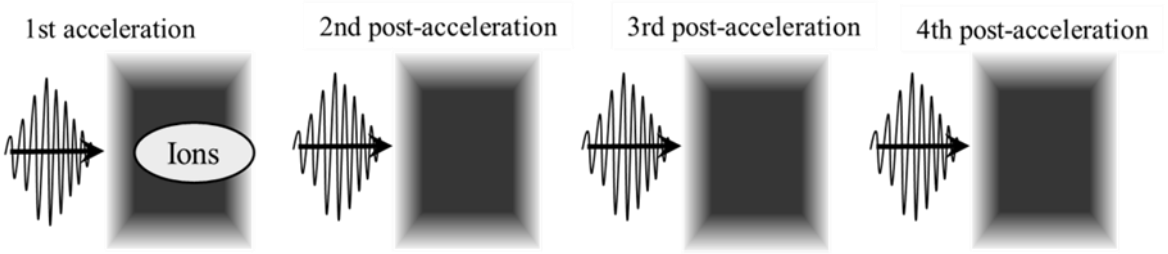


Fig. 1 Simulation model for multi-stage ion acceleration

mechanism is called as the TNSA (Target Normal Sheath Acceleration). When the target is a gas target, a laser would penetrate the gas plasma target with a lower speed than the speed of light *c* in vacuum. When the intense laser illuminate the gas plasma target, electrons are also accelerated and propagate in the plasma. Then the strong electron current is generated, and then a strong magnetic field is generated. At the increase phase of the strong magnetic field, an inductively generated longitudinal field is created. The inductive electric field propagates with a lower speed than *c*, depending on the plasma density. When the inductive electric field speed is close to the ion beam propagation speed in the plasma, the ion beam is continuously accelerated.

In this study, we perform 2.5-dimensional PIC (Particle-In-Cell) [1] simulations to improve the ion beam quality and to control the ion energy spectrum. Our simulation results demonstrate that the multi-stage ion acceleration provides a remarkable increase in the proton energy and also provides a control method of the proton energy spectrum.

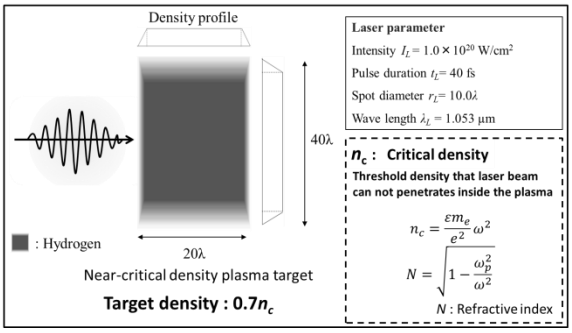


Fig. 2 Simulation target model

## 2. Generation of High Energy Ions Using Plasma

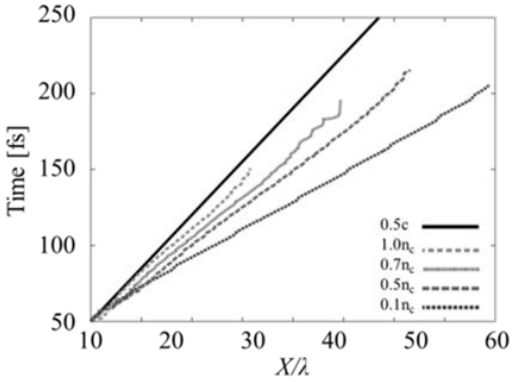


Fig. 3 Laser speed in plasma target

Figure 1 represents a simulation model for the multi-stage laser ion acceleration. The laser intensity is $1.0\times10^{20}$W/cm$^2$, the pulse length is 40fs, the spot size is $10\lambda$, and the wavelength is $\lambda = 1.053\,\mu$m. We use a plasma target In Fig. 2 the simulation model is shown. The density of the plasma target is set to be $0.7n_c$, and the target has a linear density gradient in $0.2\lambda$ in all the directions. Here $n_c$ shows the critical density, at which the plasma frequency is equal to the laser frequency. In this paper we employ the 4 stages for the laser proton acceleration. The huge simulation is divided into 4 simulations. Each simulation box has one target, and in each simulation box one laser illuminates the plasma target (see Fig. 2). At the 1st ion source stage, the accelerated protons reaches to the right boundary and are transferred to the next simulation. This simulation procedure is repeated.

Figure 3 shows laser speeds in various plasma densities. When the target density is $1.0n_c$, the speed of light becomes $0.501c$ in the plasma. When the

target density is $0.7n_c$, the speed of light becomes $0.624c$. At the 4th stage, our results show that the proton speed becomes $0.5c$～$0.6c$, which is generally required for cancer treatment. When the plasma density is about $0.7n_c$, the laser speed coincides with the proton speed, so that protons are continuously accelerated well. Therefore, we employ the target density of $0.7n_c$ in the simulations.

Figure 4 shows the results of the simulations for the 4 stages. The first stage is the ion source, and the other three stages are the post accelerations. We employ the same target and the same laser in all stages.

In the ion source, the maximum electric field is 16.7MV/μm at the target rear side. The electric field is the TNSA field. The energy conversion efficiency is 2.12% from the laser to the protons. The high-energy protons more than 20MeV are loaded into the 2nd post-acceleration. In the 2nd post-acceleration stage, 17.4% of the beam protons loaded have reached more than 60MeV. The energy conversion efficiency of the ion beam from the laser is 0.566%. The protons accelerated more than 60MeV in the 2nd post-acceleration are introduced to the 3nd post-acceleration. In the 3rd stage, 7.58% of the beam protons introduced have reached more than 120MeV. The energy conversion efficiency of the ion beam from the laser was $4.67\times10^{-2}$%. The protons more than 120MeV in the 3nd post-acceleration are introduced to the 4th post-acceleration. In the 4th stage, 5.87% of the beam protons loaded reached

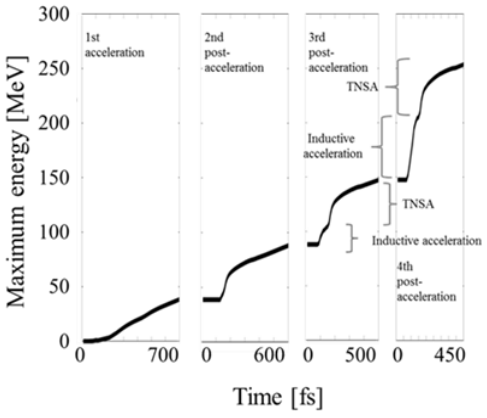


Fig. 4 Maximum ion energy history

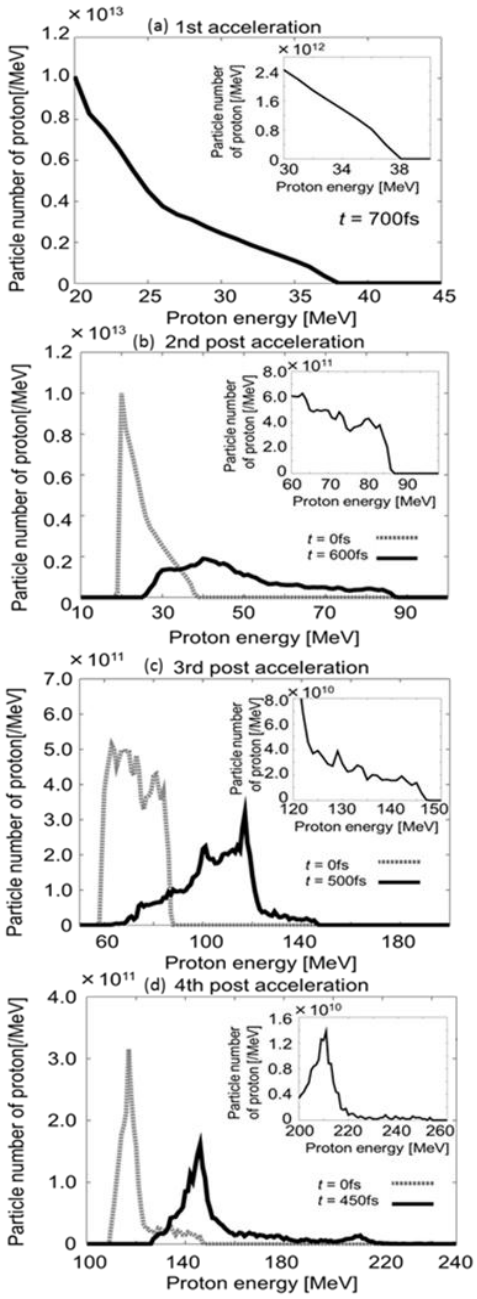


Fig. 5 Proton kinetic energy spectra. (a) 1st acceleration at 700fs, (b) 2nd post-acceleration at 0fs and 600fs, (c) 3rd post-acceleration at 0fs and 500fs, and (d) 4th post-acceleration at 0fs and 450fs

more than 200MeV. The energy conversion efficiency of the ion beam from the laser was $1.46\times10^{-2}$ %.

In Fig. 4 the maximum energy history is presented in each stage of the 1st~4th accelerations. The

maximum energy of protons reaches 254MeV in the 4th post-acceleration.

In the 1st ion source stage and the 2nd post-acceleration stage, TNSA works mainly for the proton acceleration. In the 3rd and 4th post-acceleration, the inductive acceleration works first for the continuous proton acceleration inside the plasma target and then TNSA contributes to the further proton acceleration at the target rear surface. In the 3rd and 4th stages the speed of the induced electric field was almost identical to the ion beam speed. The velocity of ion beam is about 0.566c ~ 0.653*c*, the group velocity of the induced electric field within the plasma target is 0.548c in 4th post-acceleration.

In Figs. 5 (a)-(d) we shows the proton kinetic energy spectra in each acceleration stage. The inset figures at the upper right in each figure shows the high energy part. The actual total number of the protons more than 200MeV is about $1.39 \times 10^{11}$ particles/cm. The spectrum peak of the high-energy proton group is located at about 210MeV.

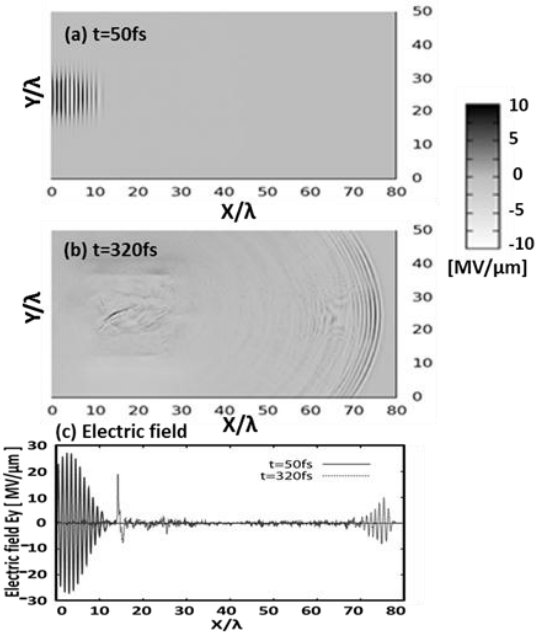


Fig. 6 Spatial distributions of the laser electric field *Ey*. (a)t=50fs, (b)t=320fs. And (c)The magnitude of the electric field *Ey* for *x* region

## 3. Effect of Target Debris on Multi-Stage Acceleration

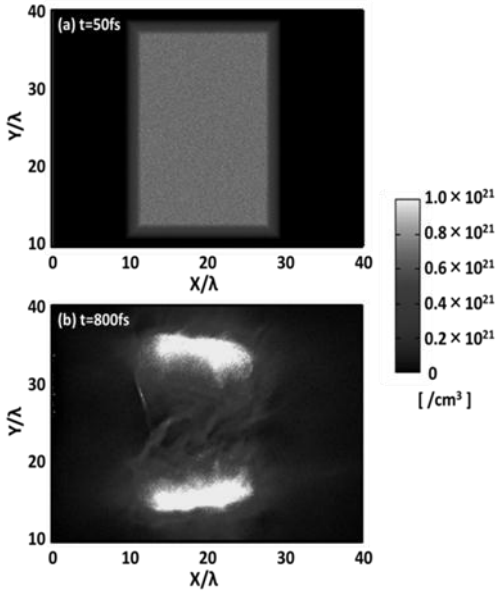


Fig. 7 Electron density of the plasma target, after the laser passed through the target

In this chapter, we investigate the afterglow effect of the first laser pulse on the second target and the effect of the first-target debris on the second laser pulse propagation and also the second target. The simulation parameters used here are the same as in Chapter 2.

First, we examine the afterglow laser field after passing through the first target. Figures 6 show the spatial distributions of the laser electric field *Ey* at 50fs (solid line) and at 320fs (dashed line). The electric field of the first transmitted laser becomes weak so that the second target is not significantly influenced.

Figures 7 show the electron density of the first plasma target, after the first laser passed through the target. Figures 7 show that the electron density around the central axis decreases well.

When the second incoming laser passes through the first target debris toward the 2nd post-acceleration, we find that the debris effect is minor. Figure 8 presents the history of the average electron density along the center axis of the target.

We also examined how much the second laser

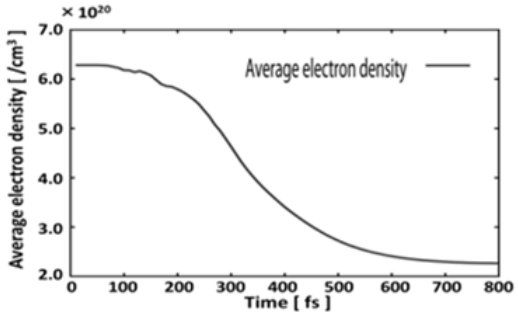


Fig. 8 Time variation of the average electron density in （$20\lambda < y < 30\lambda$, $9.5\lambda < x < 29.5\lambda$）

electric field decreases, when the second laser illuminates the second target through the first target debris. Figure 9 shows the laser electric field. The second laser does not feel any significant effect by the first target debris, except the diffraction effect.

## 4. Conclusions

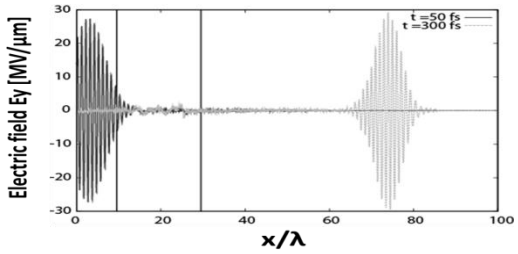


Fig. 9 Laser electric field *E*y in *x* region at 50fs and 300fs

In this study, we focused on the intense laser proton acceleration using a near-critical gas plasma target, in which the inductive acceleration field moves with a speed less than *c*. The slower speed of the inductive acceleration field contributed to the continuous proton acceleration inside the plasma target. The TNSA also contributes to the ion acceleration in this study at the target rear surface.

In this particular study, we have focused on the improvement of the peak energy of the ion beam and also on the mono-energetic spectrum control. Our present study results demonstrated that the multi-stage acceleration realizes the high-energy of protons more than 200MeV or more and provides a tool to produce a mono-energetic proton beam. The proton energy of 200-250MeV could be used for the cancer therapy.

The laser-based multiple ion acceleration provides a new tool to control the ion energy and the ion energy spectrum. The idea of the multi-stage acceleration in the controllable manner may open a new direction of the laser particle acceleration scheme.

## Acknowledgements

This study is party supported by MEXT, JSPS, CORE (Center for Optical Research and Education, Utsunomiya Univ.), ASHULA project (JSPS Asia Core to Core Program: Asian Core Program for High Energy Density Science Using Intense Laser Photons) / ILE Osaka University.

## References

[1] B. F. LASINSKI, et al., “Particle-in-cell simulations of ultra intense laser pulses propagating through overdense plasma for fast-ignitor and radiography applications”, *Phys. Plasmas*, **6**, 2041 (1999)

[2] I. VELCHEV, et al., “Laser-induced Coulomb mirror effect: Applications for proton acceleration”, *Phys. Plasmas*, **14**, 033106 (2007)

[3] T. NAKAMURA, et al., “High-Energy Ions from Near-Critical Density Plasmas via Magnetic Vortex Acceleration”, *Phys. Rev. Lett.*, **105**, 135002 (2010)

[4] M. ROTH, et al., “Fast Ignition by Intense Laser-Accelerated Proton Beams”, *Phys. Rev. Lett.*, **86**, 436 (2001).

[5] M. NAKATSUTSUMI, et al., “Fast focusing of short-pulse lasers by innovative plasma optics toward extreme intensity”, *Opt. Lett.*, **35**, No. 13 (2010)

[6] A. P. ROBINSON, et al ., “Effect of Target Composition on Proton Energy Spectra in Ultraintense Laser-Solid Interactions”, *Phys.*

*Rev. Lett.*, **96,** 035005 (2006)

[7] J. PSIKAL, et al., "Ion acceleration by femtosecond laser pulses in small multispecies targets", *Phys. Plasmas*, **15**, 053102 (2008)

[8] E. FOURKAL, et al., "Coulomb explosion effect and the maximum energy of protons accelerated by high-power lasers", *Phys. Rev. E.*, **71**, 036412 (2005)

[9] F. LINDAU, et al., "Laser-Accelerated Protons with Energy-Dependent Beam Direction", *Phys. Rev. Lett.*, **95**, 175002 (2005)

[10] M. NAKAMURA, et al., "Robustness of a Tailored Hole Target in Laser-Produced Collimated Proton Beam Generation", *J. Appl. Phys.*, **101**, 113305 (2007)

[11] T. NAKAMURA, et al., "High-Energy Ions from Near-Critical Density Plasma via Magnetic Vortex Acceleration", *Phys. Rev. Lett.*, **105**, 135002 (2010).

[12] Y. J. GU, et al., "Steady plasma channel formation and particle acceleration in an interaction of an ultraintense laser with near-critical density plasma", *Phys. Plasmas*, **18**, 030704 (2011).

[13] L. WILLINGALE, et al., "Collimated Multi-MeV Ion Beams from High-Intensity Laser Interactions with Underdense Plasma", *Phys. Rev. Lett.*, **96**, 245002 (2006).

[14] S. V. BULANOV, et al., "Ion Acceleration in a Dipole Vortex in a Laser Plasma Corona", *Plasma Phys. Rep.*, **31**, 5, pp.369-381 (2005).

# Particle Acceleration in Near Critical Density Plasma

Y. J. Gu [1,2], Q. Kong[1], S. Kawata[2], T. Izumiyama[2], and T. Nagashima[2]
[1]*Applied Ion Beam Physics Laboratory, Key Laboratory of the Ministry of Education, Institute of Modern Physics, Fudan University, Shanghai 200433, People's Republic of China*
[2]*Department of Advanced Interdisciplinary Sciences, Utsunomiya University, Yohtoh 7-1-2, Utsunomiya 321-8585, Japan*

## Abstract

Charged particle acceleration schemes driven by ultra intense laser and near critical density plasma interactions are presented. They include electron acceleration in a plasma channel, ion acceleration by the Coulomb explosion and high energy electron beam driven ion acceleration. It is found that under the near critical density plasma both ions and electrons are accelerated with a high acceleration gradient. The electron beam containing a large charge quantity is accelerated well with 23GeV/cm. The collimated ion bunch reaches 1GeV. The investigations and discussions are based on 2.5D PIC (particle-in-cell) simulations.

## Keywords

laser-plasma interaction, particle acceleration, near-critical density plasma

## 1. Introduction

The rapid developments of laser technology make petawatt pulses applicable nowadays.[1,2] Such the ultra-intense pulse interacting with plasma to accelerate charged particles is one of the interesting topics in physics. When the intense laser pulse propagates through the plasma, it induces a wakefield to trap a part of electrons and accelerate them to a high energy. This is the so-called laser-wakefield-acceleration (LWFA) regime[3], which realizes a high acceleration gradient than that of conventional accelerators. The accelerated electron beam with a low emittance, small energy spread and large charge has been observed in experiments and simulations in recent years.[4] Generally, a relatively low density plasma, for example $n_0$~$10^{-2}$-$10^{-3}n_c$, is used to study the electron acceleration. Here, $n_0$ and $n_c$ are the plasma initial and the critical densities, respectively. At the same time, an over-dense plasma with $n_0$~$10n_c$ is used to investigate the ion acceleration by laser-foil target interactions. High-energy ion beams are useful in many aspects such as cancer therapy[5], fusion ignition[6], particle physics[7], injection into conventional accelerators[8] and so on. Several regimes of ion acceleration have been proposed including target normal sheath acceleration (TNSA),[9] shock wave acceleration,[10] radiation pressure,[11] laser break-out afterburner (BOA)[12] and Coulomb explosion[13]. Besides above, many other theoretical and experimental reports are

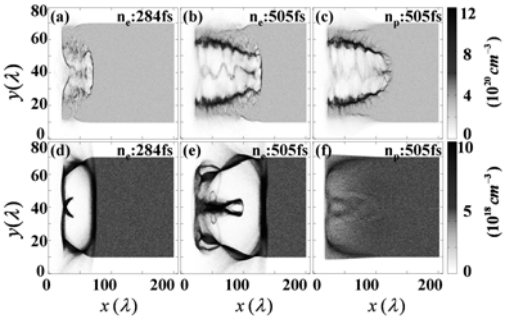


**Fig.1** The comparison between the near-critical density case (CASE-A) and the lower density case (CASE-B). The electron density profiles at $t$=284fs and $t$=505fs are presented in (a) and (b) for CASE-A, while (d) and (e) for CASE-B, respectively. (c) and (f) depict the corresponding proton density distribution at $t$=505fs.

focusing on laser-plasma interaction induced charged-particle acceleration[14]. Usually, near critical density plasma is thought to be inappropriate to the particle acceleration. However, nowadays laser systems can produce ultra-short pulses with intensities above $10^{21}$W/cm$^2$, with such a condition, many non-linear effects appear and some of these phenomena differ greatly from those of lower intensity lasers. In this paper, we present some of our researches on ultra intense laser interacting with near critical density plasmas. Through the scheme, remarkable electron acceleration and ion acceleration are realized[15].

## 2. Electron Acceleration in Plasma Channel

When ultra-intense laser pulses interact with a near critical density plasma, the phenomenon is quite different from the "bubble regime" under lower density plasma cases. In Fig. 1, two typical simulations for near critical density plasma $0.3n_c$ (Case-A) and lower density plasma $0.005n_c$ (Case-B) are presented to give the illustrations. Both simulations have the same laser parameters: a Gaussian laser pulse, which is linearly polarized in y direction with intensity $I\lambda^2 = 1.23\times10^{22} W/cm^2\cdot\mu m^2$ and radius $W_0$=10$\lambda$, incident from left in $x$ direction and focused at the left plasma boundary at $x$=20$\lambda$, here $\lambda$=1.053μm is the pulse wavelength. The pulse amplitude rises as $a = a_0 \exp[-(\frac{t-\tau}{0.5\tau})^2]$, where $a_0$=$eE_0$/($m_e\omega c$) is the normalized amplitude and the pulse duration $\tau$=35fs. Instead of forming a closed electron bubble in Case-B (see Fig. 1 (e)), there exists a plasma channel in Case-A (see Fig. 1 (b)). Inside the channel, both the electron and proton density are much lower than the initial density $n_0$. A charge-balanced particle shell is surrounding the channel and forms a high density boundary. It is found that the laser pulse propagating through such the plasma channel is well confined. The radius of laser should be $W(z) = W_0\sqrt{1+(z/z_R)^2} = 12.6\lambda$ after propagating 245$\lambda$, where $z_R$=$\pi W_0^2/\lambda$ is the Rayleigh length. However the radius in Case-A is less than 10$\lambda$ as shown in Fig. 1. According to the relativistic self-focusing condition $P > P_c \approx 17(\omega_0/\omega_p)^2(GW)$, the laser power threshold is inversely proportional to the plasma density. The self-focusing phenomenon is apparent in the

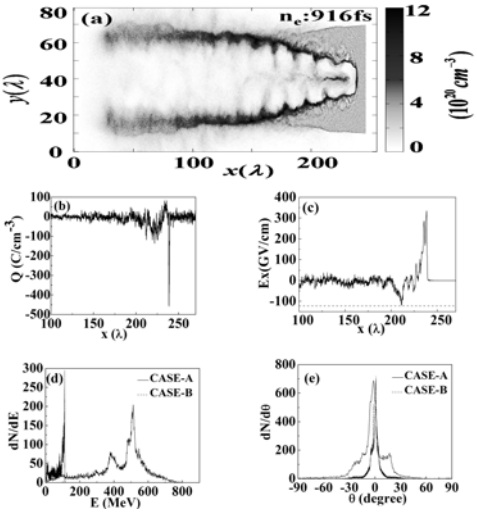


**Fig. 2** Electron acceleration by the charge-separated field. (a) The density distribution of electron in Case-A at $t$=916fs. (b) and (c) show the charge density and longitudinal electric field along y=40λ. The dashed line in (c) depicts the minimum value of $E_x$. (d) and (e) present the energy spectrum and the angular distribution of the accelerated electron bunch, respectively. The solid line in (d) and (e) represents the value of Case-A, while the dashed line represents the quality of the accelerated electron beam at the same simulation time in Case-B.

near-critical density plasma in short distance about 100$\lambda$, since the higher plasma density and the ultra-intense laser lead it more easily to appear. The mechanism of this laser self-focusing effect is understood as the following: Because the transverse and longitudinal ponderomotive forces are nearly the same magnitude due to the ratio of $c\tau/W_0\approx1$, the background electrons are scattered in both transverse and longitudinal direction. Therefore it forms a dense electron wall, surrounding the laser pulse transversely, which confines the laser against the diffraction effect. Without the

diffraction, the laser maintains its intensity in the distance longer than the Rayleigh length, and the phenomenon do benefit to the electron acceleration by increasing the interaction length.

Figure 2 (a) depicts the electron density distribution at 916fs in Case-A. There is a high density electron shell driven by the longitudinal ponderomotive force, and it forms a negative charge region in front of the channel. There is a positive charge region behind the electron shell as shown in Fig. 2 (b). Such the charge distribution induces a longitudinal electric field which accelerates electrons violently. Since the initial density is near critical, the charge separated field is also intense with the maximum value about 122 GV/cm (see in Fig. 2 (c)). We present the energy and angular spectrum of the accelerated electron beam at 916*fs* in Figs. 2 (d) and (e) (black solid lines for Case-A and red dashed lines for Case-B), respectively. Within about 220 wavelengths, the peak energy of the electron beam in Case-A reaches about 512 *MeV*, *i.e.,* the effective accelerated gradient is about 23 GeV/cm. The peak energy in the lower density case (Case-B) is about 150*MeV*. The total charge of the accelerated electrons in Case-A is about 3nC/μm, while it is about 0.57nC/μm in Case-B. The accelerated beam in Case-A also shows good qualities with the energy spread $\Delta E / E \approx 0.062$, the angular divergence $\theta_{div} = \sqrt{\sum_{i=1}^{N} (\Delta\theta_i)^2 / N} \approx 0.158$ and the transverse emittance 0.52*mm·mrad* (which contains about 1.52nC/μm from 450MeV to 580MeV).

## 3. Ion Acceleration by Coulomb Explosion

In this section, we describe the ion acceleration on the rear side of the plasma channel by the Coulomb explosion effect. Since the electrons inside the channel have been expelled away by the laser pulse, the unneutralized ions begin expand under the Coulomb pressure. Some ions move transversely to form the channel shell, while some move forward to generate a shock wave, that excites the persistent Coulomb explosion. A part of ions move backwards and form a recoiled ion beam. Figures 3 (a) and (b) display the electron and ion density distributions at 3636 fs, respectively. An

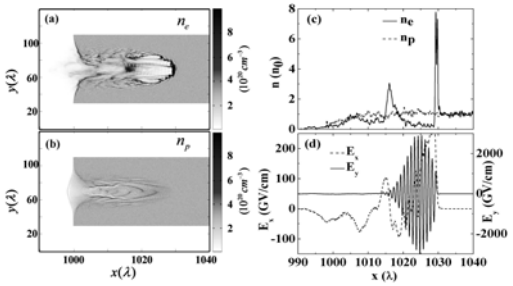


**Fig. 3** (a) Electron and (b) proton density distributions at 3636fs. (c) Electron density on the central axis ($y$=70λ) (solid line) and the corresponding proton density (dashed line). (d) Longitudinal (dashed line) and transverse (solid line) electric field on the central axis.

electron cavity has been formed by the ultra-intense pulse and a significant amount of protons expand in the backward direction. The corresponding density profiles on the central axis, *i.e.* $y$=70λ, are plotted in Fig. 3 (c), while the transverse and longitudinal electric fields are shown in Fig. 3 (d). The electron density peak in front of the laser pulse (at about $x$=1030λ) indicates the electrons directly driven by the ponderomotive force. The second peak at about $x$=1017$\lambda$ represents the electrons trapped and accelerated by the wakefield. Near the left plasma boundary, *i.e.* $x$=1000$\lambda$, the negative longitudinal electric field formed by the unbalanced charge distribution (several tens of GV/cm) accelerates the ions backwards violently. The number of the backward ejected protons are increasing with time evolution. This suggests that the Coulomb explosion continuously occurs with the pulse propagation inside the plasma, and such the mechanism has the potential to acquire large charge quantities. In Figs. 4 (a) and (b), we plot the time evolution of the recoiled proton beams' energy and angular spectra. The maximum and peak energy both increase with

time. At 3852 fs, that is, about 350 fs after the beginning of the Coulomb explosion, the peak energy and the maximum energy are 23.3 MeV and 63.9 MeV, respectively. After about 4000 fs, the peak energy increases to 45.4 MeV while the maximum energy increases to 191.3 MeV. The

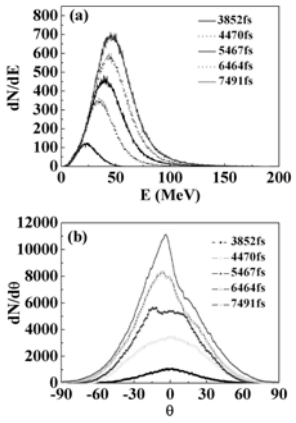


**Fig. 4** The (a) energy and (b) angular spectra of the backwards accelerated ion bunch at $t$ = 3852, 4470, 5467, 6464, and 7491fs.

angular spectrum indicates that the beam is also reasonably collimated. The energy spread, the angular divergence, and the transverse emittance of the ejected ion beam at 7491 fs are $\Delta E / E \approx 0.81$ , $\theta_{div} = \sqrt{(\sum_{i=1}^{N} (\Delta\theta_i)^2)/N} \approx 0.47$ and $4/N\sqrt{\sum_{i=1}^{N}(y_i - \langle y\rangle)^2} \times \sqrt{\sum_{i=1}^{N}(\theta_i - \langle\theta\rangle)^2} \approx 71.1\, mm\, mrad$ , respectively.

As we pointed out in the previous section, the laser pulse is effectively confined, when the plasma density is near critical and the intensity in the pulse center still rises after propagating over the depletion length. This suggests that the effective propagation length, *i.e.* the distance for the ion Coulomb explosion, is much longer than the depletion length. Therefore, even with the underdense plasma, the total quantity of acquired charge is fairly large, which can be estimated using the cylindrical model. At any moment $t$, the ions which can be backward-scattered, satisfy the condition: $v_{ion}(t - x/v_g) = x$, where $x$ is the initial position of the ions, and $v_{\rm ion}$ and $v_{\rm g}$ are the average velocity of the ions and the pulse group velocity, respectively. The whole charge quantity at time t is $Q(t) = n_0 W_0 x$ . We define $\zeta = \frac{v_{ion}}{v_{ion} + v_g}$ , so that $x = \zeta v_g t$ and $Q(t) = n_0 W_0 v_g \zeta t$ . Since the ion velocity increases from 0 to 0.3$c$ during the acceleration process, it is reasonable to estimate the average velocity as

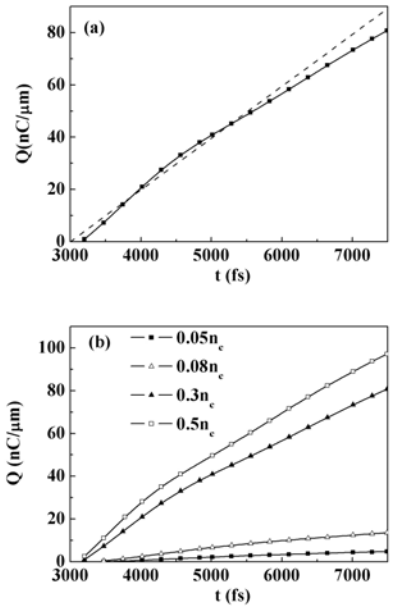


**Fig. 5** (a) Time evolution of the acquired charge quantity with time evolution in the simulation (dotted line) and the corresponding results according to the theoretical estimate (dashed line). (b) Time evolution of the total acquired charge quantity with different initial plasma densities.

$v_{ion} = 0.15c$ . In Fig. 5 (a) we present the acquired charge quantity as predicted by the above theoretical analysis (dashed line), compared to corresponding results from our simulations (black line/ square symbols). The small deviation between the two curves at the later time is caused by electron attraction effects, and ions' escaping from the bottom and top simulation boundaries. The total charge acquired in the simulation is about 80.74nC/μm, which is much larger than the current reported charge quantities acquired from other regimes. Bulanov

*et al*[16] undertook a study for a system with similar parameters and obtained ~1 GeV proton energy for acceleration in the forward direction. However, the charge quantity they acquired was only at a level of hundreds of pC, which is much less than the amount seen in our regime. Figure 5 (b) shows how the acquired charge quantity with the different initial plasma densities varies with time. The acquired charge is also approximately proportional to the initial plasma density.

## 4. LWFA Electron Beam driven Ion Acceleration

In this section, we focus on the proton acceleration driven by the charged-separated field, which is induced by the energetic laser wakefield accelerated (LWFA) electrons. From Fig. 6, one can see clearly about the proton beam generation. Before the LWFA electrons ejected out of the plasma, a small sheath field had appeared near the rear boundary of plasma (see Fig. 6 (a)), which is formed by the laser direct accelerated electrons. After the LWFA electrons ejected, as shown in Fig. 6 (b), the sheath field quickly increases and expands, the maximum amplitude reaches hundreds GV/cm, which is strong enough to drive protons. At this stage (Fig.6 (a)-(b)), the protons near the rear boundary started to move by the longitudinal field. The accelerated electrons at that time drift with a relativistic velocity $v \approx c$ relative to the background protons. The large gap between the velocity of protons and electrons is susceptible to induce the Buneman instability[17] and then efficiently accelerate ions. It should be noted that the most of the high energy protons come from the rear boundary of the plasma, rather than that of the proton bunch inside of plasma channel in Figs. 6 (a) and (b).

Different from the TNSA or BOA scheme in an overdense plasma, the leading electron bunch in this scheme is accelerated by the laser wakefield. We compare the electron beam quality in our simulation with that of a typical BOA results with the same laser parameters. The initial plasma density is $n_0=15n_c$ ($2.6\times10^{22}$cm$^{-3}$) and plasma thickness is 0.8μm in the BOA case. We plot the energy and angular spectrum in Figs.

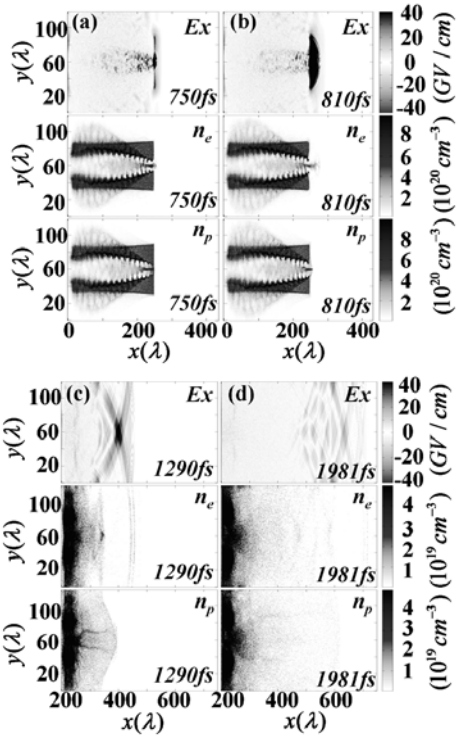


**Fig. 6** The longitudinal electric field ($E_x$), the electron density distribution ($n_e$) and the proton density distribution ($n_p$) at $t$=750fs, $t$=810fs, $t$=*1290*fs and $t$=1981fs are plotted in (a), (b), (c) and (d), respectively.

7 (a) and (b), where the solid line represents the near-critical density case at 720fs, while the dashed line depicts the quality of the hot electrons, which penetrate through the target in the BOA case. One can find that the electron beam from the BOA case is generated by the direct laser acceleration process, the energy spectrum is almost the Maxwellian distribution with the highest energy about 250 MeV, and the angular distribution has two peaks around the cylindrical axis. On the other hand, the electron beam in the near-critical density case is quasi-monoenergetic with a peak energy about 300 MeV and the maximum energy becomes 800 MeV. The angular spectrum shows that this electron beam is also well collimated.

Figure 7 (c) depicts the longitudinal electrical

field along $x$=250λ, *i.e.* the right boundary of the plasma, at 750 fs. It suggests that the largest field is about 180 GV/cm and the strong region is tightly localized near the center. It is consistent with the spatial distribution of electron beam. Since the initial density of the plasma is the near critical, the charge separated field reaches hundreds GV/cm. Affected by such a strong field, the protons located near the center of right boundary are violently accelerated into the high energy in a short time and short distance. At the same time, the tightly focused size of the longitudinal field insures the accelerated proton beam to be well collimated. Near the right boundary of the target, a bunch of proton followed behind the electron beam is generated as shown in Fig. 6 (c).

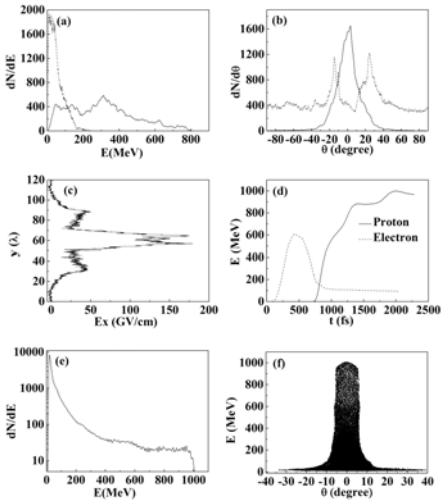


**Fig. 7** (a) and (b) show the comparison between the energy spectrum and angular spectrum of overdense BOA case (dashed line) and the case of Fig.1 (solid line) respectively. (c) The longitudinal electric field along x=250λ at 750fs. The maximum energy of proton (solid line) and the energy of a typical leading electron (dashed line) with time evolution are presented in (d). (e) and (f) depicted the beam quality of the accelerated proton bunch at 2011fs. (e) The energy spectrum. (f) The energy angular related distribution.

The time evolution of the energy of a typical leading electron (dashed line) and the maximum energy of proton beam (solid line) are presented in Fig. 7 (d). The electron energy increases steadily before 500 fs and quickly decreases from 600 MeV to 100 MeV. After 750 fs, the decrease in the electron energy becomes slow and steady to about 100 MeV. On the other hand, the energy of protons increases violently since 750 fs and reaches 1 GeV at about 2000 fs. It is found the maximum energy of protons decreases slightly after 2011 fs, and at that time the leading electrons are ejected out of the simulation box at that time. But it is believed that the proton bunch is still accelerated by the electron beam, if the simulation area is larger enough. The protons begin to be accelerated around 750 fs, when the LWFA electrons are ejected out of the plasma; it means that the accelerated protons mainly come from the rear plasma boundary, as mentioned above. It is different from the magnetic vortex acceleration, by which the protons were accelerated inside of the plasma channel.

We present the energy spectrum and angular distribution of the proton bunch at 2011 fs, *i.e.* the last acceleration moment in our simulation in Figs. 7 (e) and (f). After the acceleration length about 400$\lambda$, the maximum energy of the proton bunch reaches 1 GeV; the effective acceleration gradient is about 32 GeV/cm. The scaling law of the TNSA acceleration mechanism suggests that with the laser intensity about $10^{22}$W/cm$^2$ the energy of proton beam reaches hundreds of MeV. Since then, this scheme is much effective than that of TNSA. The total charge of the protons whose energy is larger than 50 MeV is about 4.05nC/μm. The total energy of the laser pulse in the simulation is about 37.3J/μm, then the energy transfer efficiency between the laser pulse and these high energy protons (E>50 MeV) is about 1.57%. If all the protons are taken into consideration, the energy laser-proton conversion efficiency is about 5.62%. From the energy angular related distribution, one can find that these high energy protons are well collimated between the angle $-10^\circ < \theta < 10^\circ$. The angular divergence of the proton bunch is

$\theta_{div} = \sqrt{\sum_{i=1}^{N} (\Delta\theta_i)^2 / N} \approx 0.144$ and the transverse emittance 7.706*mm·mrad*.

## 5. Conclusions

In summary, ultra intense laser pulse interacting with near critical density plasma has been investigated. A laser self-focusing phenomenon and a steady plasma channel formation were found. The electrons captured by the laser wakefield inside the channel are accelerated by the large gradient. There exists both ion acceleration at the rear side by the Coulomb explosion and at the front side driven by the LWFA electron beam. This work is useful to laser-plasma charged particle acceleration scheme.

## Acknowledgements

This work was partly supported by NSFC (No. 11175048), Shanghai Nature Science Foundation (No. 11ZR1402700), and Shanghai Scientific research innovation key projects No. 12ZZ011. Supports by China Scholarship Council, Shanghai Leading Academic Discipline Project B107, JSPS, MEXT, and CORE of Utsunomiya University are also acknowledged.

## References

[1] Mourou G. Barty C, Perry M: Physics Today, **51**, 22 (1998)
[2] Perry D., Mourou G: Science. **264**, 917 (1994)
[3] Sprangle P, Esarey E, Ting A, and Joyce G, Appl. Phys. Lett. **53**, 2146 (1988)
[4] Mangles S. P. D. *et al*., Nature **431**, 535-538 (2004); Geddes C. G. R. *et al.*, Nature **431**, 538-541 (2004); Faure J. *et al.*, Nature **431**, 541-544 (2004).
[5] Tajima T, J. Jpn. Soc. Therapy Rad. Oncol., **9**, 83 (1998); Bulanov S V, Khoroshkov V S, Plasma Phys. Rep., **28**, 453 (2002).
[6] Roth M. *et al*., Phys. Rev. Lett., **86**, 436 (2001); Bychenkov V Yu *et al*., Plasma Phys. Rep., **27**, 1017 (2001); Macchi A. *et al*., Nucl. Fusion, **43**, 362 (2003); Honrubia J J. *et al*., Phys. Plasmas, **16**, 102701 (2009).
[7] Esarey E, Schroeder C B and Leemans W P, Rev. Mod. Phys., **81**, 1229 (2009).
[8] Krushelnick K. *et al*., IEEETrans. Plasma Sci., **28**, 1184 (2000).
[9] Wilks S. C. et al., Phys. Plasmas, **8**, 542 (2001).
[10] Ohsawa Y., Phys. Fluids, **28**, 2130 (1985); Silva L. O. *et al*., Phys. Rev. Lett., **92**, 015002 (2004).
[11] Esirkepov T., *et al*., Phys. Rev. Lett., **92**, 175003 (2004); Pegoraro F. and Bulanov S. V., Phys. Rev. Lett., **99**, 065002 (2007).
[12] Yin L. *et al*., Laser Part. Beams, **24**, 291 (2006); Yin L. *et al.*, Phys. Plasmas, **14**, 056706 (2007).
[13] Last I. *et al.*, J. Chem. Phys., **107**, 6685 (1997); Bulanov S.V. *et al.*, Phys. Lett. A, **299**, 240 (2002).
[14] Leemans W. P. *et al*., Nature **439**, 445 (2006); Malka V. *et al*., Science **298**, 1596 (2002).
[15] Gu Y. J. *et al.*, Phys. Plasmas, **18**, 030704 (2011) ; Gu Y. J. *et al.*, Euro. Phys. Lett., **95**, 35001 (2011) ; Gu Y. J. *et al*., Phys. Plasmas, **19**, 092308 (2012).
[16] Bulanov S. *et al*., Phys. Plasmas **17**, 043105 (2010).
[17] Buneman O., Phys. Rev., **115**, 503 (1959).

# Study on long time operation of inertial electrostatic confinement fusion (IECF) device

Keita Nobe *, Kazuki Nanjo, Hiroki Imaji , Wantapon Ngamdee,
Masato Watanabe, Eiki Hotta

*Tokyo Institute of Technology, Department of Energy Sciences*

## ABSTRACT

Inertial Electrostatic Confinement Fusion (IECF) device is a compact fusion proton/neutron source with an extremely simple configuration, high controllability, and hence high safety. We notice that neutrons have really high biological effectiveness and aim to use the IECF device as an irradiation facility for a biological application. One of problems in using an IECF device is variation in neutron production rate observed in long time operation. We found that time dependency of NPR fluctuation is dependent on input power. The experiment shows NPR fluctuation stops after 20 minutes of operation in case of input power of 1200 W.

## Keywords

Inertial Electrostatic Confinement Fusion, Neutron source, Biological application, Long time operation

## 1. Introduction

Inertial Electrostatic Confinement Fusion (IECF) is a scheme to confine ions electrostatically between two concentric electrodes. Fig.1 shows the idea of IECF briefly. In the case of D-D fusion, deuterons are accelerated to the center of the cathode and collide with each other causing nuclear fusion.

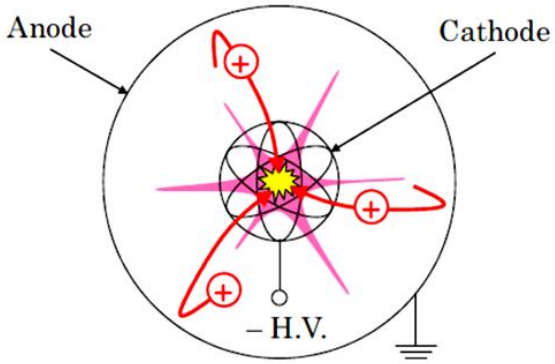


Fig. 1 Principle of Inertial Electrostatic Confinement Fusion (IECF) device

Fig.2 shows ion trajectories and converged ions in the center of a cathode grid of cylindrical IECF device which we are using currently.

Today, neutrons are used in wide range of applications such as material analysis, non-destructive inspection and cancer therapy. These applications are conducted in huge facilities and they cost much money and waiting time. Hence there is a great demand for realizing small and low-cost neutron sources. IECF research has a potential to expand applications of neutrons. However, Neutron Production Rate (NPR) obtained so far in IECF devices is too low to be practically used for the applications described above.

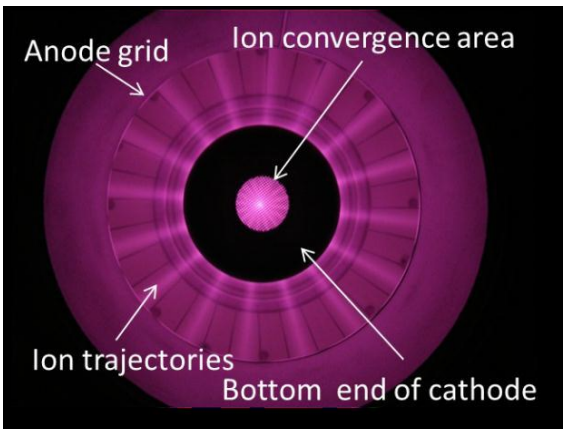


Fig. 2 Picture of a plasma discharge in a cylindrical IECF device

In this research, a new application of IECF devices and its feasibility was studied. Biology is one of potential applications because neutrons have high biological effect. To perform biological experiments using an IECF device, a few hours of operation, which is quite a long time compared with usual experiments, is probably required. Therefore, there is a possibility of NPR fluctuations caused by various factors. Actually, when we operated the device for several tens of minutes, NPR variation of about 10% was observed in DC operation. In this report, the time dependence of NPR in long time DC and pulsed operation will be presented.

## 2. Biological applications of neutrons

One eminent characteristic of a neutron is a relatively high biological effect. This means that damage caused by neutrons is greater than other ionizing radiation at the same absorbed dose. Main factor which determines a biological effect of radiation is Linear Energy Transfer (LET) and a neutron has high LET.

There are several characteristics of the disorder caused by high LET radiation. First, the disorder can be rarely recovered with its own restoration mechanism. In addition, enhancement of radiation effect by the protective agent, sensitizer or oxygen is less likely to occur [4]. Therefore, for the application of neutrons in the biological field even a neutron source with low NPR has a possibility to become useful. There are several biological applications of radiation such as radiation breeding and sterile insect technique. First, we will discuss features of IECF and then go on to explain these biological applications.

### 2.1 Characteristics of the IECF device

IECF features compared to sealed radiation source are: NPR can be controlled; NPR does not decrease with time. The major difference between an accelerator type neutron source and the IECF device is the construction and maintenance cost, facility size and neutron output. The IECF device is inexpensive and small but NPR is not high enough.

### 2.2 Radiation breeding

There are several good points in radiation breeding. First, it enables a creation of new traits which plants do not have inherently [5]. Moreover, plants which have difficulty in breeding can be improved.

Currently, cobalt 60 gamma ray source is used since it is relatively safe and excellent in availability. Advantage of the IECF device compared to the cobalt 60 source is that neutrons have specific mutation spectrum and higher biological effect [6]. Moreover, the mutation rate increased by the addition of boric acid to irradiation target has been reported [6]. This is believed to be due to the influence of α-ray generated by neutron capture reaction of boron 10 which is the isotope of boron 11. The research of radiation breeding using neutrons is mainly carried out by using nuclear fission reactors. The development of inexpensive neutron source will hence greatly encourage the use of neutrons for breeding.

### 2.3 Sterile insect technique

When mass rearing pests are released after sterilization, insect mating frequency among wild pests will drop. Then the eggs given birth by infertility male do not hatch. Hence the number of wild insects of the next generation will be reduced. The pests will be eradicated by continuing release of sterile insects in this way. This kind of pest eradication method is called sterile insect technique (SIT).

The eradication of melon fly in Okinawa, Japan achieved by this method has been reported. Though the number of studies on the preparation of sterile insects by neutron irradiation is small, it is known that neutrons have higher biological effect than gamma rays [7].

## 3. Experimental Setup

### 3.1 Characteristics of cylindrical IECF device

Fig.3 shows a schematic of the cylindrical IECF device. The vacuum vessel is made of stainless steel, which has a diameter of 393 mm and a height of 340

mm. An anode grid (with a diameter of 200 mm and a height of 320 mm) which is composed of 32 stainless steel plates with a width of 5 mm and a thickness of 1 mm, is set inside the vessel. Moreover, a cathode grid is set in the center of the chamber. Its diameter is 40 mm and the height is 380 mm. Both of electrodes are isolated from the ground so that the voltage can be applied independently. A CVCC DC power supply used has electric capacity of 60 mA and -100 kV. A pulse generator can generate a pulse of 100 kV with a peak current of 10 A at 10-200 pps. The pulse width can be adjusted in the range of 10-500 μs. The anode grid is connected to another CVCC DC power supply capable of 20 mA and -60 kV. Deuterium gas is introduced through a mass flow controller and the pressure is controlled in the range of 0.1-10 Pa.

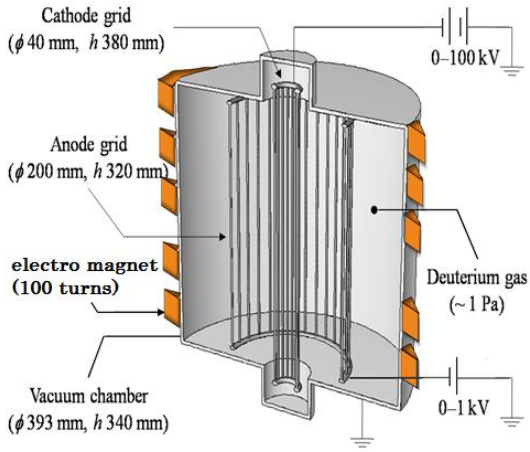


Fig. 3 Schematic of a cylindrical IECF device

### 3.2 Measurement of NPR

Fusion oriented neutrons which have energy of 2.45 MeV are counted with a $^{3}$He proportional counter covered with a polyethylene moderator. We derived NPR on the assumption that neutrons are generated from the radiation source on the central axis of a linear system and emitted isotropically.

### 3.3 Typical pulsed discharge waveforms

Fig.4 shows the typical voltage and current waveforms of pulsed discharge. First, current with a narrow peak for charging the coaxial cable between the power supply and the cathode flows. The cathode voltage rises to the charging voltage in a few μs

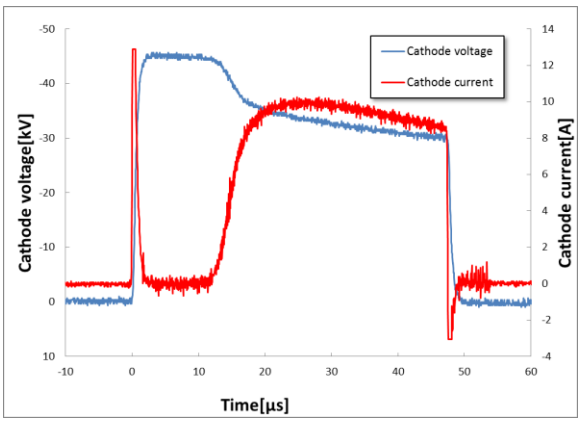


Fig. 4 Typical pulsed discharge waveforms

followed by the peaked current. Then, after a time delay of 1 to several 10s μs, cathode current begins to rise. When the current begins to flow, the cathode voltage drops by a few kV due to the series resistance of 1 kΩ for a switch protection against overcurrent.

Pulse width is defined as the full width at half maximum of the pulsed current. The term “pulsed current ($I_{pulse}$)” is defined as the maximum value of the cathode current after charging. Also, the charging voltage of the cathode ($V_{charge}$) is defined as the maximum value of the cathode voltage. The pulsed voltage is derived from the following equation. $V_{pulse} = V_{\_charge} - I_{\_pulse} \times 1$ kΩ, where 1 kΩ is the current-limiting resistor.

## 4. Time variation of NPR in DC operation

The fact that NPR varies with time in DC operation has been confirmed. Fig.4-5 shows the evolution of NPR, in which NPR is found to have a peak at around 5-10 minutes under the conditions other than the current of 30 mA. The position of the NPR peak is shifted to the right with increasing current. At 40 mA, NPR becomes almost constant after around 15 minutes. However, NPR still decreases after 15 minutes at 50 mA. It suggests that higher current causes continuous NPR drop. Therefore, it can be concluded the greater current leads to the larger variation of NPR.

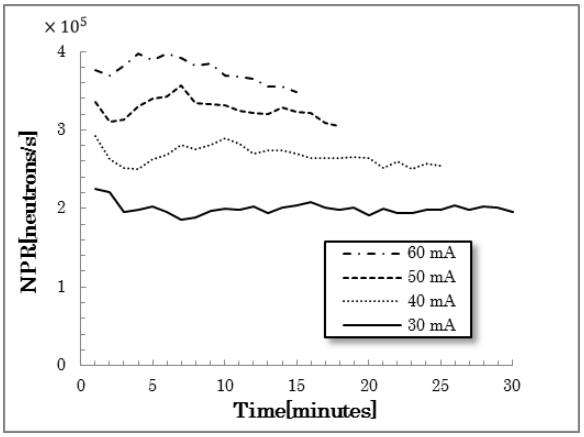


Fig.5 Time evolution of NPR at pulsed current of 5 A, pulse voltage of 37 kV and pulsed width of 28 μs

## 5. Time variation of NPR in pulsed operation

### 5.1 Characteristics of basic IECF setup

As found in DC operation, time variation of NPR was also observed in pulsed operation. Repetition rate of pulsed operation is 120 pps in any experiment. Time dependency of NPR shown in Fig.6 is similar to that in the case of 20 kV, 60 mA DC operation described in Fig.5. In these two experiments the input power is almost the same as 1200 W. It implies that NPR fluctuation is dependent on input power. Fig.7 shows NPR fluctuation in long time (~1 hour) operation. It suggests that NPR fluctuation stops after 20 minutes.

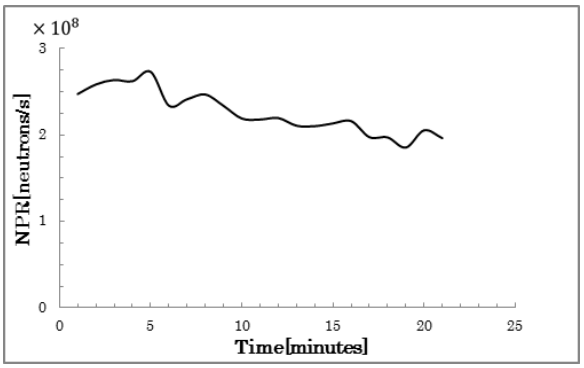


Fig. 6 Time variation of NPR at pulsed current of 10 A, pulse voltage of 30 kV and pulse width of 33 μs

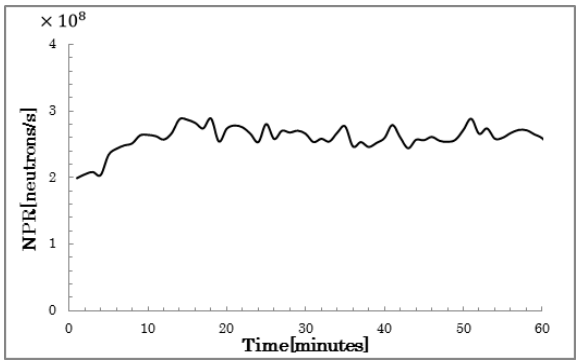


Fig. 7 Time variation of NPR at pulsed current of 5 A, pulse voltage of 37 kV and pulse width of 28 μs

### 5.2 Discussion

A possible reason for the phenomenon described in the sections 4 and 5 may be a change in nuclear fusion reaction rate between deuterium, which is embedded in the chamber wall or the cathode, and fast deuterium. Fusion reaction of this type is; so called “embedded fusion”.

The temperature of the cathode becomes higher when the operation time becomes longer, which leads to the change in surface density of deuterium absorbed on the cathode and wall. It leads to a variation in embedded nuclear fusion reaction rate. It is difficult to cool the cathode for structural reasons. However, the wall can be cooled by water circulation system. Measuring the time variation of NPR in a cooled device is significant since there is a chance to prevent NPR fluctuation by cooling.

## 6. Summary and future plan

The goal of this research is the biological application of IECF device which is a small and inexpensive neutron source. Neutrons have higher biological effect than gamma ray which is conventionally used in biological field.

In this paper, we studied the fluctuation phenomenon of neutron output of the IECF device observed in long time (~1 hour) operation. Cause of NPR variation is presumably the change in embedded fusion reaction rate due to the temperature rise of the gas, the vacuum chamber and the cathode. NPR variation can be avoided by performing the pre-conditioning interim operation since the variation

occurs in a few tens of minutes after the start of IECF device operation. We also believed to prevent this as well by introducing the cooling system. As a future plan, we will measure the time variation of NPR in IECF device with cooling system preparing for long time operation. Organisms used as irradiation target is planned for cereals such as barley and rice since they are easy to obtain and grow fast.

## References


[1]G. H. MILEY et al., "Inertial-Electrostatic Confinement Neutron/Proton Source", *Proc. 3rd Int. Conf. on Dense Z-pinches*, AIP Press, pp.675–688 (1994).

[2]K. YAMAUCHI et al., "Neutron Production Characteristics and Emission Properties of Spherically Convergent Beam Fusion", *Fusion Technol.*, **39**, 3, pp.1182–1187 (2001).

[3]H. BRUNNER "Radiation Induced Mutations for Plant Selection", *Appl. Radiat. Isot*, Vol. 46, No. 6/7, pp. 589-594(1995)

[4] ATOMICA (09-02-02-15)

[5]http://www.irb.affrc.go.jp/

[6]http://www.rada.or.jp/database/home4/normal/ht-docs/member/synopsis/020179.html

[7]http://ci.nii.ac.jp/naid/110001093935

[8]V. CONGER et al., "Effects of Fission Neutron, beta and gamma radiation on seedling growth of dormant and germinating seeds of barley" *Radiation Botany*, Vol. 13, pp. 173 to 180 (1973)

# Characteristics of The Magnetic Wall Reflection Model on Ion Acceleration in Gas-Puff Z Pinch

M. Nishio and K. Takasugi *

*College of Science and Technology, Nihon University, Tokyo 101-8308, Japan*
** Institute of Quantum Science, Nihon University, Tokyo 101-8308, Japan*

**ABSTRACT**

The magnetic wall reflection model was examined with the numerical simulation of the trajectory calculation of particles. This model is for the ions accelerated by some current-independent mechanism. The trajectory calculation showed angle dependency of highest velocities of accelerated particles. This characteristics is of the magnetic wall reflection model, not of the other current-independent acceleration mechanism. Thomson parabola measurements of accelerated ions produced in the gas-puff z-pinch experiments were carried out for the verification of the angle dependency.

**Keywords**

z pinch, gas-puff, ion acceleration, trajectory calculation

## 1. Introduction

Accelerated ions having energy in the order of MeV have been observed in many studies of high current experiments, particularly in the plasma foci [1, 2] and z pinches [3, 4]. Ion accelerations independent of the electric current direction in gas-puff z-pinch plasma were measured [5]. However, the mechanism of the current-independent ion acceleration is still under discussion [6–9]. Candidate models except for the current-directional electric field model should be discussed. The mechanical reflection model proposed by Gureev (1980) [6] is considered to be the most reasonable model. In the short time of pinch phenomena, the strong acceleration of particles may needs multiple head-on collisions with imploding wall like the first-order shockwave Fermi acceleration in astrophysics. In the collisional z-pinch plasma, particles in the hollow area of radially imploding annular cylinder can always obtain the gains of kinetic energy by the multiple head-on collisions. Energy distributions of particles indicates power-law condition in general statistical acceleration (even in the first order Fermi process), and maximum energies exist because that some realistic velocity of shockwave discovered in astrophysics may control the limitation of accelerated ions. While, the accelerations in this study may be limited by another process, because the configuration of reflection surface is different from that in the astrophysical condition. Multiple reflection process in the self-contracting plasma have to be discussed. Because the mechanical acceleration proposed by Gureev (1980) has not take the various experimental conditions into account (only ideal elastic collisions between ions and a rigid wall), the reflection processes with the various magnetic wall is discussed in this study.

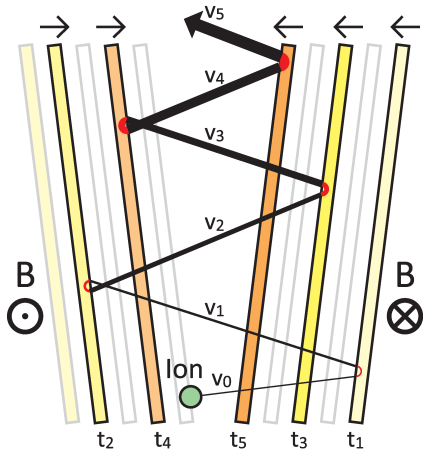


Fig. 1: Schematic diagram of multiple collisions in the magnetic wall reflection model

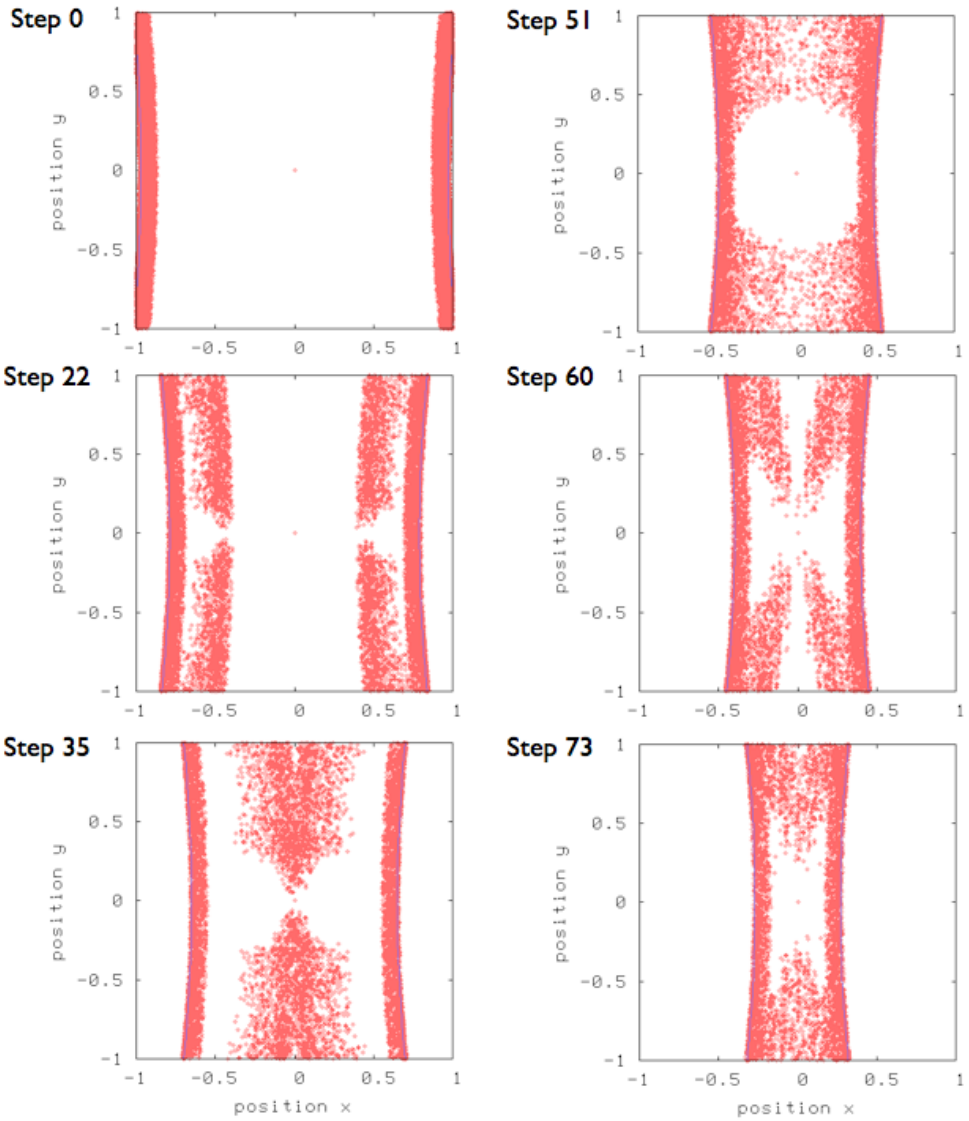


Fig. 2: Typical spatial changes of traveling particles between the rigid wall.

## 2. Numerical Calculation

Numerical simulation of the trajectory calculation was carried out for the understanding of the magnetic wall reflection model. Equation of motion of particles were solved with the Euler method. In real, ionized particles can interact intricately with the current sheet of the plasma. For simple, the imploding current sheet is assumed to be a rigid wall. Particles collide with the rigid wall completely elastically. The rigid wall contracts toward the discharge axis. Particles can be reflected by the collision with the wall, and they obtain twice the velocity of the wall. Interactions among particles are ignored. In the magnetic wall reflection model, the final ion velocity can change depending on the angle of the wall. This tendency should be shown in the numerical calculation. After that, it should be verified by the discharge experiments.

In $x-y$ cordinates, particles having a velocity $v = (v_x, v_y)$ are distributed inside the cylindrical wall contracting toward the discharge axis ($y$ axis). It is assumed that whole particles have same velocity, but velocity components are all different. For calculation, present coordinate is transformed rotationally to the coordinate with reference to the rigid wall surface. The angle between the rigid surface and the $x$ axis (horizontal axis) is defined as $\theta$. The $\theta$ is the function of the position $(x, y)$. The velocity components parallel and perpendicular to the rigid wall surface are defined as $v_{//}$ and $v_{\perp}$, respectively. The $v_{//}$ and $v_{\perp}$ are calculated by following equation. Schematic diagram of multiple collisions in the magnetic wall reflection

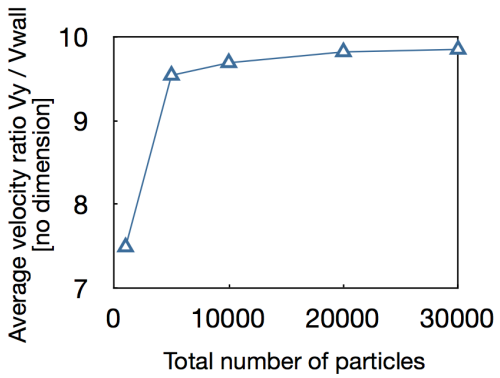


Fig. 3: Dependency of total number of particles against the highest velocities to the $y$ direction

model is shown in Fig. 1.

$$\begin{pmatrix} v_{//} \\ v_{\perp} \end{pmatrix} = \begin{pmatrix} \cos\theta & \sin\theta \\ -\sin\theta & \cos\theta \end{pmatrix} \begin{pmatrix} v_x \\ v_y \end{pmatrix} \quad (1)$$

Assumed that the velocity component of a particle perpendicular to the rigid wall surface before a collision is $v'_{\perp}$, twice the velocity component of the rigid wall perpendicular to its surface ($V_{\mathrm{wall}}$)is added to $v'_{\perp}$. The wall velocity $+V_{\mathrm{wall}}$ remain unchanged between before and after the collision. Reflection coefficient in this situation can be assumed to be 1(elastic collision).

$$\frac{V_{\mathrm{wall}} - v_{\perp}}{V_{\mathrm{wall}} - (-v'_{\perp})} = -1 \quad (2)$$

$$v_{\perp} = v'_{\perp} + 2V_{\mathrm{wall}} \quad (3)$$

After the rotational coordinate transformation to the coordinate with reference to the $x-y$ axises, $v_x$ and $v_y$.

$$\begin{pmatrix} v_x \\ v_y \end{pmatrix} = \begin{pmatrix} -\sin\theta & \cos\theta \\ \cos\theta & \sin\theta \end{pmatrix} \begin{pmatrix} v_{\perp} \\ v_{//} \end{pmatrix} \quad (4)$$

As the rigid wall contracts toward the discharge axis, particles gain the velocity increment by the multiple collisions with the contracting rigid wall every collision. As shown in the above equations, particle velocities are the function of the rigid wall angle $\theta$. The $\theta$ is defined as the angle between $x$ axis and the rigid wall surface. As the surface of the rigid wall close to the $y$ axis, the angle $\theta$ increases. However, experimental stuff are defined as angles between y axis and themselves according to the custom. Assumed that the angle is defined as $\phi$, the criteria $\phi = (\pi/2) - \theta$ is satisfied. According to Gureev (1980), the current sheet was simulated by a quadratic curve in this calculation. In this calculation, the equation like $x = (1/a) \cdot y^2$ was used as the basic shape of the wall, where $a$ is the slope of the equation. The relation between the angle $\theta$ and the slope $a$ is defined as $\theta = \arctan a$. The slope $a$ was set between $1 \sim 5$. Larger $a$ means that larger $\theta$ and smaller $\phi$.

## 3. Calculation Results

Results of the calculation are shown as follows. Figure 2 shows a typical spatial changes of traveling particles between the rigid wall. Parameters of the calculation were shown; slope $a$ 4.5, initial velocity of the wall 0.01, initial velocity of particles 0.01, the total number of particles $3\times10^4$, total time step 100. Red points are all particles. Curved blue lines show the cylindrical rigid wall.

Figure 3 shows the dependency of total number of particles against the highest velocity to the $y$ direction under the condition of slope $a$ 4.5, initial velocity of the wall 0.01, initial velocity of particles 0.01. Total number of $3\times10^4$ particles are considered to be enough for the correctness of this calculation.

Figure 4 shows an temporal change of highest velocity of whole particles to the $y$ direction. At the time step 100, the rigid wall reaches $y$ axis (discharge axis). The light blue line shows the initial velocity (0.01). The cross point between cobalt-color line and the horizontal axis is the timing of end of the contraction. As particles travel between the wall, they obtained velocity increments step by step. From the start to step 80, particles have almost constant velocities. After around 80 steps, velocities rise drastically. Final velocities reached about 0.12 which is twelve times larger than the initial velocity.

Figure 5 shows an temporal change of total collision numbers for each particle. After almost 70 steps, total collision number increased gradually. Once the total number reached to eight at about 90 steps, they were constant till the end of the calculation.

Figure 6 shows the slope dependency of the highest velocity to the $y$ direction. This slope means the slope of the quadratic curves having the shape like $x = (1/a) \cdot y^2$. Larger slope $a$ means that larger angle $\theta$ between the rigid

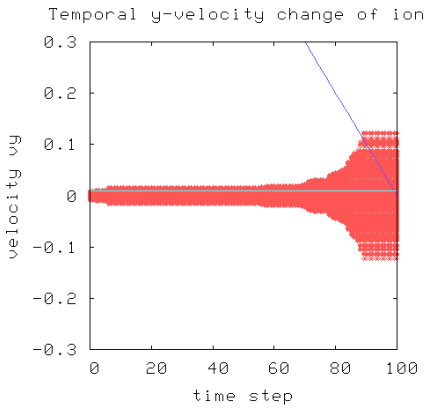


Fig. 4: Temporal change of highest velocity of whole particles to the $y$ direction.

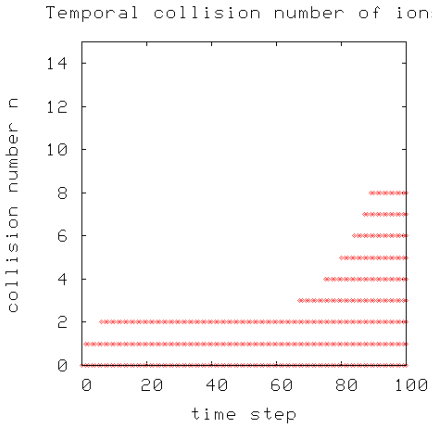


Fig. 5: Temporal change of total collision numbers for each particle.

wall and $x$ axis. As shown in Fig. 6, highest velocities of particles to the $y$ direction were maximized at the slope of 4.5. In smaller and larger than the slope 4.5, $y$-directional velocities of particles decreased. Compared with slope 1 and 4.5, the velocities increased 60%. Accordingly, the magnetic wall reflection model derived the clear angle dependency of velocity of accelerated particles in this calculation. This tendency should be verified by using z-pinch plasmas produced by the experimental method.

## 4. Experimental Results

According to a numerical simulation with the magnetic wall reflection model, the highest kinetic energies of accelerated ions are likely to be the function of the angle of the plasma current sheet. If ion energies have the dependency of the current-sheet angle in the experiments, that could lead the correctness of the magnetic

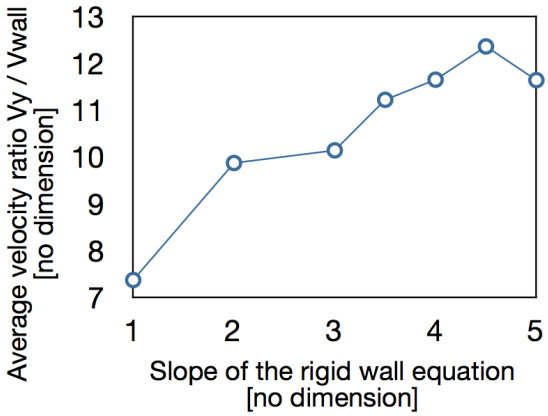


Fig. 6: Slope dependency of the highest velocity to the $y$ direction.

wall reflection model. Angles of the current sheet can be changed by the gas-puff nozzles and cathode apertures.

The gas-puff z-pinch experiments were carried out with the SHOTGUN-III device in the Nihon University [10]. The Thomson parabola analyzer [11] was used for measuring ion energies and species. Discharge gas was Ar (5 atm). Three types of gas nozzles (10, 20 and 30 degrees) and three types of cathode apertures (35, 40 and 45 degrees) were used. As the angle of gas nozzles decreased, the highest kinetic energies of accelerated ions increased. The tendency is consistent with the magnetic wall reflection model. While, as the angle of cathode apertures decreased, the energies decreased. This is inconsistent with the model. Although the decrease of the current sheet angle was expected by the decrease of cathode aperture, at the same time, it may have caused the decrease of the distance capable of the ion accelerations along the discharge axis.

## 5. Conclusion

Trajectory calculation of particles showed angle-dependency of the rigid wall in this study. This angle-dependency is the characteristics of the magnetic wall reflection model. This fact could indicates that current-independent ion acceleration in the divergent gas-puff z-pinch experiments is attributed to the magnetic wall reflection model. Experimental results also showed the validity of the model. Consequently, the validity of the magnetic wall reflection model

could be certified by this study.

## References


[1] A. Moser *et al.*, J. Appl. Phys. **53**, 2959 (1982).

[2] H. Heo and D. K. Park. Physica Scripta **65**, 350 (2002).

[3] X. M. Guo and C. M. Luo, J. Phys. D Appl. Phys. **29**, 388 (1996).

[4] C. Luo *et al.*, IEEE Trans. Nucl. Sci. **28**, 1599 (2000).

[5] M. Nishio et al., Plasma Fus. Res. **6**, 1201009 (2011).

[6] K. G. Gureev, Sov. Phys. Tech. Phys., **25**, 192 (1980).

[7] V. V. Vikhrev and V. D. Korolev, Plasma Phys. Report, Vol. 33, No. 5, 356-380, (2007).

[8] T. Haruki *et al.*, Phys. Plasmas, Vol. 13, 082106, (2006).

[9] S. P. Gary, and H. W. Bloomberg, Appl. Phys. Lett., Vol. 23, No. 2, 112-113, (1973).

[10] K. Takasugi and E. Kiuchi, Plasma Fusion Res. Rapid Commun. **2**, 036 (2007).

[11] M. J. Rhee, Rev. Sci. Instru. **55**, 1229 (1984).

# Development of Pulsed X-Ray Source Based on Vacuum-Arc for the Measurement of Fine Particles in Gas-Puff Z Pinch

Takanori Miyazaki[1], Mineyuki Nishio[1] and Keiichi Takasugi[2]

[1] *College of Science and Technology, Nihon University, Tokyo 101-8308, Japan*
[2] *Institute of Quantum Science, Nihon University, Tokyo 101-8303, Japan*

## ABSTRACT

Metallic fine particles have been observed in gas-puff z pinch with Sn electrodes. We planned the spatial distribution measurement by x-ray shadowgraphy of direct exposure method, in order to understand the scattering process of metallic fine particles. We developed a pulsed x-ray source with FWHM of 60 ns, for the time resolved spatial measurement. The exploratory experiment using a Sn wires with the diameter of 150 μm was successful.

## Keywords

gas-puff z pinch, fine particle, pulsed x-ray source, x-ray shadowgraphy

## 1. Introduction

Behavior of fine particles in plasma has attracted attention in many fields, such as the generation of dust in magnetically confined fusion device [1], strongly coupled plasma [2], and the dust plasma in space [3]. In the field of development of light source for semiconductor lithography, fine particles occur together with high-temperature and high-density plasma. The removal mechanism have been devised, because the particles might corrupt the condensing optical system [4].

The gas-puff z-pinch is one of the method of generating high-temperature and high-density plasma. Plasma and Sn particles of 1~100 μm occur in gas-puff z pinch with Sn electrodes [5,6]. The metallic fine particles take a cloud like structure and are located in the surroundings of the hot spot of z-pinch plasma [7]. Cloud-like spatial structure is Kα emission from metallic particles. The emission is excited by the electron beam generated in the maximum pinch time [8].

We focused on the generation process of metallic fine particles, and the development of spatial distribution of them in this research. X-ray shadowgraph of time resolved photography was planned. We developed the pulsed x-ray source for x-ray shadowgraph measurement.

This paper describes the performances of the x-ray source and the result of the exploratory experiment with Sn wire.

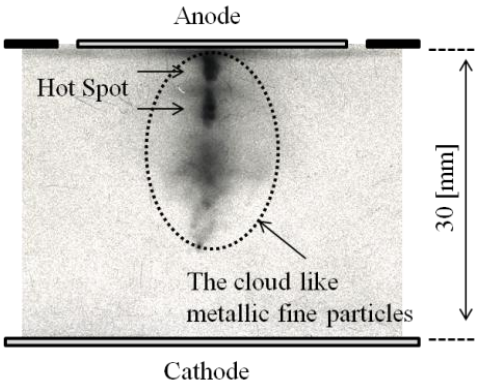


Fig. 1 The cloud-like structure and hot spots in the x-ray pinhole photograph.

## 2. Measurement of fine particles

### 2.1 X-ray shadowgraphy

The key map of direct exposure x-ray shadowgraph measurement is shown in Fig 2. X-ray is applied to the z-pinch plasma and negatives are developed on

the x-ray film. The filter which shields the Bremsstrahlung radiation from z-pinch plasma and transmits only the light from x-ray source is inserted.

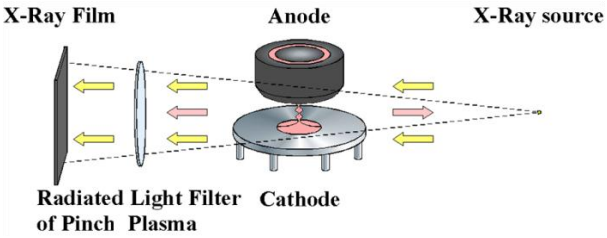


Fig. 2 Schematics of x-ray shadowgraphy.

At the same time, the x-ray for the shadowgraph should be in the spectral range which can be absorbed in the particles. Figure 3 shows the transmission rate of incident photon on the Sn foil. Photon with the energy between 1 and 30 keV is suitable for the observation of Sn particles with the size between 1 and 100 μm.

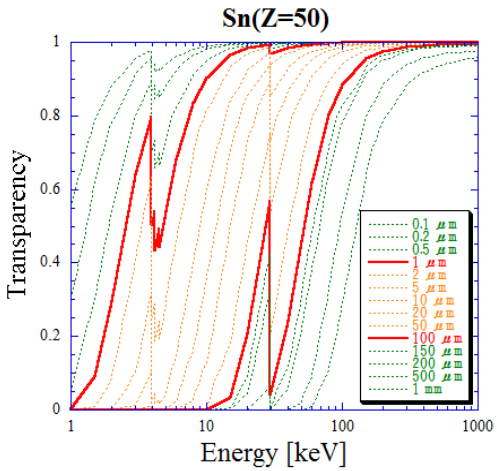


Fig. 3 Transmission rate of incident photon on the Sn foil.

Our gas-puff z pinch is an electric discharge with half period of 10 μs. Referring to the time scale of discharge the pulse width of x-ray source must be much shorter than 10 μs. We developed a pulsed x-ray source based on vacuum-arc to fill these performance requests.

### 2.2 X-ray source based on vacuum-arc

Metal vapor has a role of discharge current carrier in the vacuum-arc. Electric discharge starts when enough fast electrons reach at the high-voltage electrode from the other grounded electrode. Before the forming of main discharge path between inter-electrodes, some fast electrons collide with the metallic electrode surface. At the timing of the collision of the fast electrons, the Bremsstrahlung radiations are emitted.

It is possible to obtain both inner shell radiation and Bremsstrahlung radiation by applying appropriate voltage between the electrodes. We have noted that the x-ray radiation occurs on a very short time, and it can be applicable as a pulsed x-ray source.

## 3. Experimental Setup

### 3.1 The pulsed x-ray source

The vacuum-arc device is comprised of a vacuum chamber, spark electrodes and a pulsed power supply as shown in Fig. 4. The electrodes are a brass needle (Φ4 × 70 mm) and a copper target electrode (0.5 mm thick × 20 mm in width, angle of inclination is 45 degree). The distance between the electrodes is 1 mm. The base pressure is $8.93 \times 10^{-5}$ Pa.

We used a 3-stage Marx generator for the power supply (Fig. 5). The capacitance and the charging voltage of each capacitor are 0.04 μF and 20 - 30 kV. The discharge is started by a trigatron gap switch. The filling gas of the switch is $N_2$ at $2.0 \times 10^5$ Pa, and the trigger pulse voltage is 7.0 kV. A Rogowski coil and a capacitive voltage divider are used for the measurement of discharge characteristics.

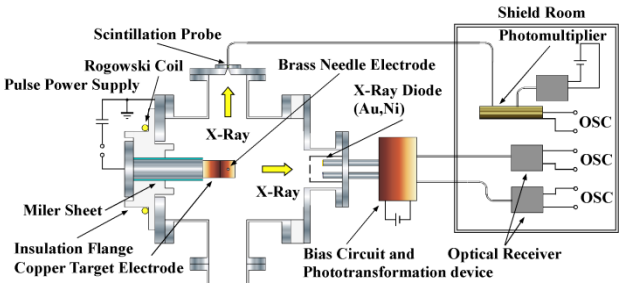


Fig. 4 The pulsed x-ray source device based on vacuum-arc and the measurement system of x-ray.

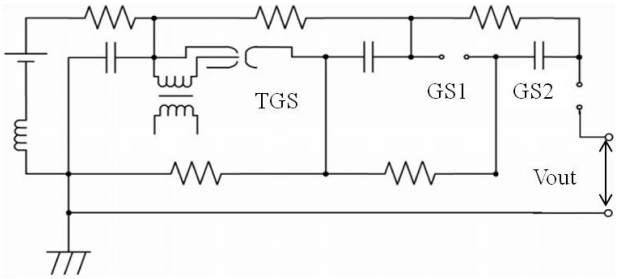


Fig. 5 Marx generator for the vacuum-arc discharge.

### 3.2 Measurement of x-ray

A scintillation probe and XRDs (X-Ray Diode) were used for temporal measurement of x-ray radiation. The scintillation probe consists of a plastic scintillator of 3 mm in diameter, a photomultiplier, and a high-voltage power supply. The sensitive energy range of photon is about 10 - 100 keV. XRD consists of a photo cathode of Au or Ni, and the bias voltage of 320 V is applied to it. The sensitive energy ranges of photon are about 0.01 - 10 keV (Au) and about 0.01 - 1 keV (Ni). The signals were recorded on the oscilloscope. The waveforms of discharge current and x-rays were displayed simultaneously.

X-ray radiation spectrum was measured by a convex crystal spectroscope. A sheet of mica crystal was used in the spectroscope and Kodak Biomax MS film was used for recording the spectrum.

## 4. X-ray radiation in vacuum-arc

### 4.1 Pulse width of x-ray

X-ray pulse of 60 ns was measured from x-ray source developed this time. Figure 6 shows discharge current and x-ray signals. Pulse width of x-ray is defined as the full width at half maximum of the scintillation-probe waveform. High energy x-ray was measured just before the current begins to flow. The pulse width of the x-ray was 60 ns. Moreover, low energy x-ray was measured while the current flows.

Probably, the x-ray of low energy is not suitable for shadowgraph measurement. It is because the energy region resembles the radiation from z-pinch plasma. At the time of x-ray shadowgraph measurement, the x-ray of low energy is rejected by using a filter.

Accordingly, this electric discharge can be used as a x-ray source for 60 ns. It is shown that this result has 1/80 of time resolution to the half priod of the discharge current in the gas-puff z pinch.

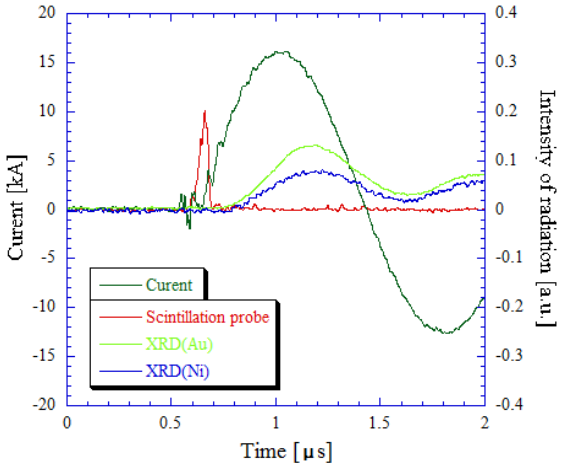


Fig. 6 Current and x-ray waveforms in a typical vacuum-arc (generator voltage 90kV).

### 4.2 The spectrum and energy of x-rays

The spectroscopic measurement result by the convex crystal spectroscope is shown in Fig. 8. A continuous emission and a characteristic emission at about 1.5Å were observed. The continuous emission is considered to be Bremsstrahlung radiation generated by high energy electrons. The characteristic line is considered to be Kα radiation of 1.542Å originating from the copper electrode.

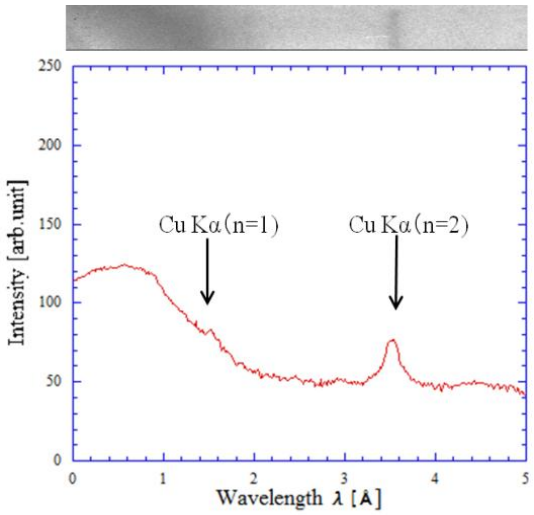


Fig. 7 Details of the spectrum of the x-ray source (generator voltage 90kV, 100 shots).

Moreover, a characteristic line is also observed at about 3.5Å. This is a secondary diffraction of Bragg reflection of the crystal.

### 4.3 Size of the x-ray source

X-ray source needs to be small in order to have good spatial resolution in the x-ray shadowgraphy. Then, the size of the light source was measured using the x-ray pinhole camera. The image of the x-ray source is shown in Fig. 8.

The sizes of the light source were about 2.2 mm in the machine direction and about 3.0 mm in the cross direction. Since a shadow of the needle electrode was observed, it is thought that the x-ray is emitted from the copper target.

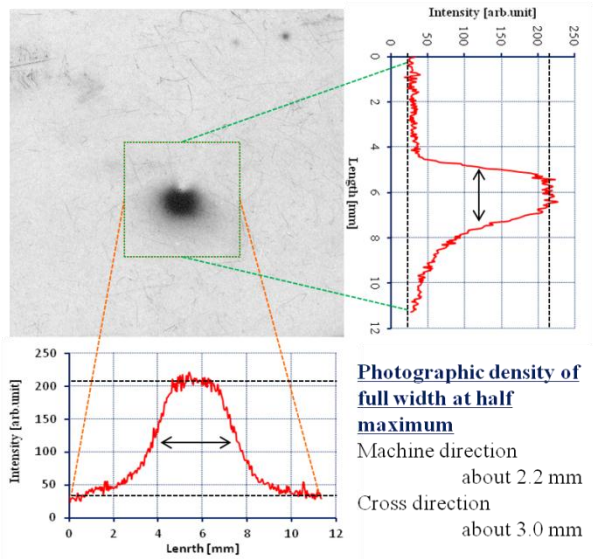


Fig. 8 The image of x-ray source measured by x-ray pinhole camera. The sizes were evaluated using full width at half maximum of the photographic density.

## 5. The x-ray shadowgraph using the x-ray source

In the preceding section the details of the characteristics of the x-ray source were discussed. As a simulation of metallic fine particles Sn wires are used for the x-ray shadowgraphy.

Sn wires with a diameter of 150 μm were stretched between the electrodes. Figure 9 shows the visible view and the x-ray shadowgraph of the wires. Although the shadowgraphy took 5 shots of discharge, it was successful in taking the image of Sn wires. The generator voltage was 20 kV.

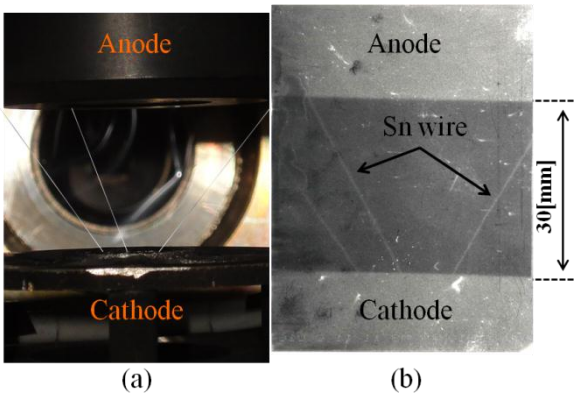


Fig. 9 (a) Visible view and (b) x-ray shadowgraph of the electrodes and Sn wires with the diameter of 150 μm.

## 6. Discussions

From the observations in Fig. 6 and Fig. 7, it was found that the pulse width of the Bremsstrahlung radiation was 60 ns. Moreover, the low energy x-ray which is detected by XRD after the start of the current is not used for x-ray shadowgraphy. Application of discharge current causes consumption of the electrodes in the vacuum-arc discharge. Although Cu target electrode was used this time, it is better to change the electrode metal to have better heat resistance.

From the observation in Fig. 8 it was found that the x-ray radiation source spread on the target electrode. This shows that the electrons emitted from the needle electrode spread and collide with the target electrode. This weakening of the electric field intensity between the electrodes needs to be considered. It is thought that the weakening of the electric field intensity causes reduction of the field emission current from the needle electrode, which is connected with the shortage of x-ray intensity. Also in order to obtain the increase of the x-ray intensity, and the point light source, electrode structure needs to be improved.

## 7. Conclusions

The purpose of this research was to measure the scattering process of metallic fine particles. X-ray

shadowgraphy was adopted as the measurement technique of metallic fine particles, and the x-ray source for the measurement was developed. Quality assessment of the x-ray source was reported.

About the time resolution, pulsed x-ray source of 60 ns was realized. The pulse width was 1/80 to that of the discharge current of 10 μs. The x-ray source was applied for taking the image of Sn wires with a diameter of 150 μm. On the other hand, for performing shadowgraph measurement by one shot, the intensity of x-rays was insufficient. Moreover, the size of the x-ray source was also large. The structure of electrodes needs to be changed for the improvement of point x-ray source.

## References


[1] N. Ohno and N. Asakura, "Dust Production and Transport in Fusion Plasma Experiment Devices", J. Plasma Fusion Res. **87**, 153 (2011).

[2] Y. Hayashi, "Crystalization and Transition of Strongly Coupled Dusty Plasma", J. Plasma Fusion Res. **73**, 1230 (1997).

[3] T. Yokota, "Simulation Experiment on Space Fine Particle Plasmas", J. Plasma Fusion Res. **82**, 92 (2006).

[4] I.H. Song, K.Iwata, Y.Homma, S.R. Mohanty, M.Watanabe, T. Kawasaki, A. Okino, K. Yasuoka, K. Horioka and E. Hotta, "Development of gas jet type Z-pinch EUV light source for lithography", 2005 IEEE. 1049 (2005).

[5] Keiichi Takasugi, Fuminari Kobayashi, "EUV Radiation Characteristics of Ar Gas-puff Z-pinch Plasma with Axial Magnetic Field" Proc. 15th Beam Conf. 7019 (2005).

[6] Akiko Maeda, Mineyuki Nishio and Keiichi Takasugi, "Production and Dispersal of Tin Fine Particles in a Gas-Puff Z-Pinch Experiment", NIFS-PROC-87, 26 (2010).

[7] E.O.Baronova, K. Takasugi, V.V. Vikhrev and T. Miyamoto, "X-Ray Spectra of Argon and Iron Ions in a Gas-puff Z-Pinch", Proc. 13th Beam Conf. 784 (2001).

[8] Keiichi Takasugi, Satoru Narisawa and Hisashi Akiyama, "Spatial Structure of Emission of a Gas-puff Z-Pinch Plasma", AIP Conf Proc. **651**, 131 (2002).

# Hot Electron Spectra in plain, cone and integrated targets for FIREX-I using Electron Spectrometer

T. Ozaki,

*National Institute for Fusion Science, 322-6, Oroshi, Toki, Gifu 509-5292, Japan*

Traditional fast ignition scheme is that a compressed core created by the imploding laser is auxiliary heated and ignited by the hot electron (produced by the short pulse laser guided through the cone). Here, the most suitable target for fast ignition can be searched by comparison of the spectra between varied targets using the electron spectrometer.

## 1. Introduction

Fast ignition (FI) [1-3] has been performed as follows;

An imploded core with a density of several hundred times of solid density is created by an imploding laser. The imploding core is auxiliary heated and ignited by a hot electron. The hot electron is produced by the interaction between a chirped ultra-short pulse laser and the pre-formed plasma created by the pre-pulse of the heating laser at the tip of a guiding cone. According to the simulation, the maximum coupling efficiency between the core and the hot electron can be expected at the typical hot electron energy of 2 MeV or less[4]. Usually if a scale length (1/e-hold length) of the plasma density is long, the effective electron temperature $T_{eff}$ (=slope of the electron spectrum) is high and the coupling efficiency is reduced because the electron passes through the core with small energy deposition. The low energy electron, which is suitable for FI, is reduced because most of the laser energy spends for the creation of the super energetic electron. In many cases, $T_{eff}$ becomes high because the scale length of the pre-formed plasma is longer than the expected value due to low laser contrast (main pulse/ pre-pulse ratio). Therefore it is one of the most important issues for FI that $T_{eff}$ keeps low with high laser to electron conversion efficiency.

Here escaped hot electron spectra can be observed at the 1 m from the target by using an electron spectrometer (ESM)[5] based on a permanent magnet and an imaging plate. Only the tail component of the hot electron can be observed because the escaped electron is affected by a target potential.

In this paper, the difference of $T_{eff}$ in varied targets, which are measured by ESM are shown. The deposition mechanism of the hot electron in different targets is described. The most suitable target for FI is searched from $T_{eff}$, the electron flux and neutron yield.

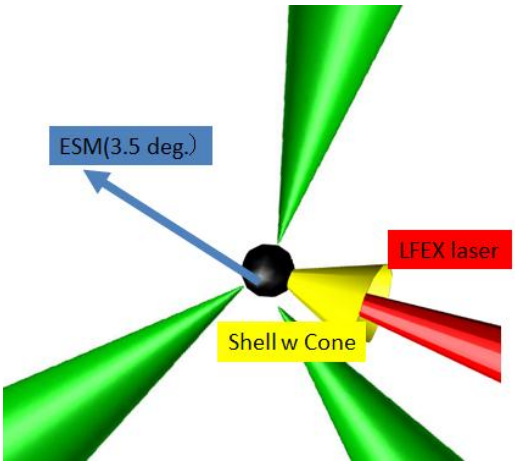


Fig. 1. Experimental setup

Shell with cone is imploded by the green laser. Imploded core is auxiliary heated by the hot electron created by the interaction between

## 2. Experimental Setup

The experimental setup is shown in Fig. 1. Gekko XII (GXII, 9-12 beams, 250J/beam, 0.53μmϕ, 2ω)[6] is used for implosion of the deuterated polystyrene shell (500 μmϕ, 7 μm thickness) with the cone. The LFEX laser (two beams, 1.053 μm)[7] energy is from 500 J to 1.6 kJ. The pulse width is 1.5 ps in the experiments. The energy of 82% is focused at the focal spot size (50%) of 40-100 μmϕ.

Table I. Targets in FI01.

| |
|---|
| Plate |
| Aluminum, Copper(Cu), Gold(Au) |
| Cone |
| Gold cone |
| DLC w/wo Au-coat |
| Fundamental experiments (with imploding plasma) |
| Au-cone + semi-sphere CD shell + Ta/Cu-1mm$^t$ |
| W-cone + semi-sphere CD shell + Ta/Cu-1mm$^t$ |
| Open hole Au-cone + semi-sphere CD shell + Ta/Cu-1mm$^t$ |
| DLC-cone + semi-sphere CD shell + Ta/Cu-1mm$^t$ |
| Integrated experiments |
| Au-cone + Imploded core |
| DLC-cone + Imploded core |
| Open hole Au-cone + Imploded core |
| Open hole DLC-cone + Imploded core |
| $B_{ext}$ application |
| Open hole-shell + $B_{ext}$ + Imploded core |
| DLC-cone + $B_{ext}$ + Imploded core |

We used three different type targets of plain, cone and integrated cone-shell listed in Table I. The time history and the spatial information of the imploded core and the cone (outer and inner) can be observed by MIXS[8]. The behavior of the cone inner can be seen by using DLC (diamond-like-carbon)-cone[9] which is optically thin. The γn-neutron can be reduced in DLC-cone. DD-neutron is monitored by MANDALA[10] with strong γn-neutron shield.

The calibrated ESM is installed on the GXII target chamber I at 3.5 degrees (port number 53) against the laser forward direction where it is almost at the rear side of the target but slightly oblique.

## 3. Comparison of the spectra between varied targets

At the beginning, the LFEX laser irradiates plain targets for measuring the spot size and tuning diagnostics. We can compare the difference of pre-formed plasma creation mechanism in varied materials. $T_{eff}$ defined from the slope of the electron spectrum is strongly depended on the scale length of the pre-formed plasma, which is mainly produced by the pre-pulse and/or the pedestal of the LFEX laser. According to Phukov scaling[11] obtained by simulation, the relation between $T_{eff}$ and the scale length is as follows;

$$T_{eff} \sim (\alpha/3.546)(I/I_{18})^{(1/2)} * (2.465\, L^{(1/4)} - 2.223), \quad (1)$$

where $\alpha$, $I$, $I_{18}$ and $L$ are the coefficient factor of 1.5 MeV, the laser intensity in W/cm$^2$, the normalized factor of $10^{18}$ and the scale length in μm, respectively. All $T_{eff}$ data depended on LFEX laser intensity in this experimental series FI01 are shown in Fig. 2.

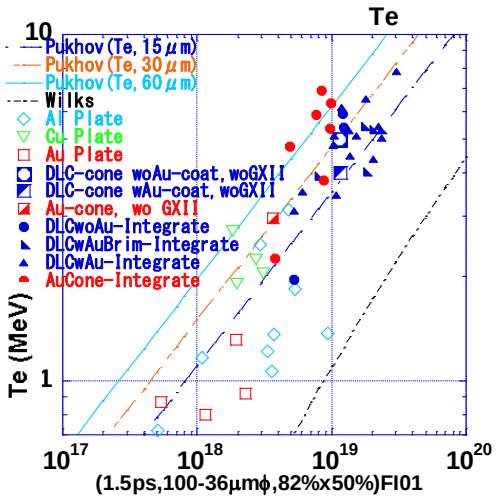


Fig. 2. $T_{eff}$ in FI01

$T_{eff}$ can be obtained from the slope of the hot electron spectrum. Open, half open and closed symbols show the plain, the cone-only and the integrated targets, respectively. Wilks scaling comes from reference [12].

### 3. 1 Plain and cone targets

Generally $T_{eff}$ becomes low when target Z is large. The pre-formed plasma of high-Z does not expand easily because the target mass number A($\propto$Z) is large. However $T_{eff}$ in copper target is much higher than $T_{eff}$ in aluminum one. One possibility is that the pre-formed plasma contains the water on the copper surface.

We compare $T_{eff}$ in cone irradiated by the LFEX laser with $T_{eff}$ in plain. $T_{eff}$ in cone is obviously higher than $T_{eff}$ in plain. Several reasons can be considered. The pre-formed plasma in cone is converged to the cone axis which is the path of the LFEX laser. The effective pass length of the laser in pre-formed plasma becomes long due to the oblique expansion of the pre-formed plasma. According to simulation, oblique injection of the laser makes higher $T_{eff}$.[13)]

### 3.2 Integrated experiments

In the integrated experiments, DLC-cone is used addition to Au-cone in order to prevent a huge X-ray and γn-neutron noise, and to decrease a hot electron loss in cone. However the pre-formed plasma grows quickly because DLC-cone consists of low-Z material. Au-coating on DLC-cone has been performed in order to reduce the expansion of the pre-formed plasma. DLC-cone has also a merit which the interaction between laser and cone can be observed.

In the integrated experiments, four targets of the standard Au-cone shell, DLC-cone shell, open hole-cone shell and open hole-shell have been tested. In previous experimental series FG02[14)], the dependence between $T_{eff}$ and the imploding timing (deviation between the imploding time and the LFEX laser injection time) has been plotted as shown in Fig. 3(a). Maximum $T_{eff}$ could be observed near the implosion time (=imploding timing 0). The residual ω component from imploding 2 ω laser (GXII) may have irradiated the inner wall of the cone. In FI01, $T_{eff}$ can be reduced by elimination of the residual ω component using a mechanical shutter as shown in Fig. 3(b). However $T_{eff}$ seems to be still higher around the implosion time. The reason is that the lower component of the hot electron is dissipated in the imploded core. This phenomenon is remarkable in DLC-cone shell rather than in Au-cone shell because the lower component of the hot electron is already lost in Au-cone itself. Therefore $T_{eff}$ becomes higher.

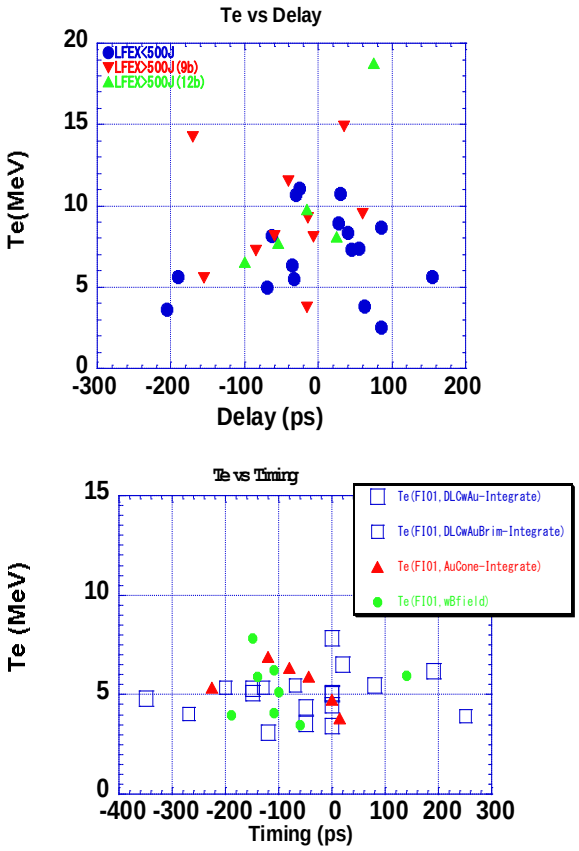


Fig. 3. The implosion timing dependence of $T_{eff}$.
The horizontal axis means the deviation between the maximum compression time of the core and the LFEX injection time.
(a) in FG02, (b) in FI01.

In FI01, we can suppress the pre-formed plasma scale length within 30 μm (Phukov scaling) by elimination of the pre-pulse. $T_{eff}$ can be reduce to be 5 MeV in DLC-cone shell and 6 MeV in Au-cone shell as shown in Fig. 2. $T_{eff}$ in integrated target seems to be determined by

the cone shape because $T_{eff}$ in integrated target is almost same as in the cone only.

In integrated experiments, DD neutron is measured by MANDALA. The neutron yield in Au-cone shell is higher than that in DLC-cone shell. The neutron yield has a strongly positive dependence with the imploding laser power. The large imploding laser power produces the high imploding density core. At the beginning, we expected that lower component of the hot electron can give this energy to the core in DLC-cone. However those facts mean that the imploding core in FI01 well couples with the higher energy electron than that we expected. The neutron source region is localized around the core center.[15] The lower component of the hot electron may heat only the surrounding region of the core but cannot produce the neutron because the electron to ion energy transfer is small due to the low plasma density in the surrounding region.

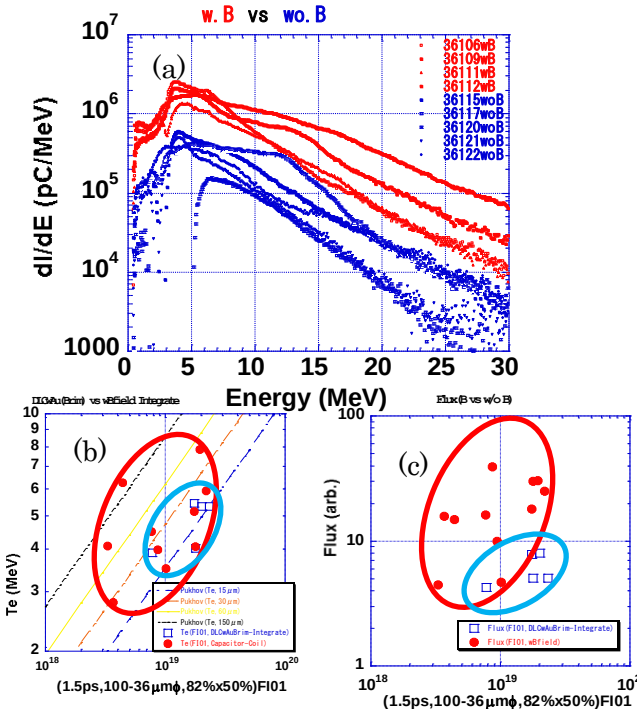


Fig. 4. ESM data with and without $B_{ext}$. $B_{ext}$ is induced by the laser irradiation to the parallel plates.
(a)Hot electron spectra with and without $B_{ext}$,

### 3.3 External magnetic application

In integrated experiments, 9 beams in GXII 12 beams are used for implosion. External magnetic field ($B_{ext}$) can be induced by residual 3 beams of the laser[16]. The laser irradiates the parallel plates with one turn coil in front of the cone. The magnetic field of several hundred Tesla can be easily obtained in the one turn coil. Here the magnetic field line is along to the LFEX laser axis because the space to put all devices is limited. The magnetic field compression by implosion can be expected if the magnetic field is created in shell before implosion. Therefore the hot electron which is trapped on the magnetic line can be expected to be guided toward the imploded core.

In integrated experiments, the hot electron spectra with and without $B_{ext}$ are shown in Fig. 4(a). $T_{eff}$ and the hot electron flux as a function of the LFEX laser intensity are shown in Fig. 4(b) and (c), respectively. The hot electron flux remarkably increases when $B_{ext}$ is applied although $T_{eff}$ slightly becomes low. The increasing of the flux in ESM cannot be explained by hot electron convergence due to the magnetic field. The hot electron convergence due to the magnetic field occurs only around narrow region (<1 mm) around the core. The magnetic field is open at the position far from the core. The hot electron diverges with original divergence angle and is measured at the ESM position (1 m from the core). Therefore almost same flux should be observed by ESM. The increase of flux may be explained by the change of the pre-plasma shape in the magnetic field application.[17] The neutron yield does not change clearly even if $B_{ext}$ is applied. The reason is under consideration.

### 3.4 Open-hole cone shell

Direct heating of the imploded core has been performed by using the open-hole cone shell in order to minimize the energy loss of the hot electron in cone itself.[18,19] At the beginning, we had worried about increase of $T_{eff}$ due to the exploding plasma with long scale length from the open hole. However $T_{eff}$ is not so high as shown in Fig. 5 and high neutron yield can be obtained. This reason may be that the

pre-formed plasma is created in the inner side of the imploding shell, the pre-formed plasma becomes shorten by the shell implosion and the scale length keeps short because the spouting plasma from the open hole is too dense. Actually LFEX laser can reach the imploded core according to the image of MIXS. Although the neutron yield increases, the neutron energy is shifted from 2.45 MeV (thermal DD neutron) because the accelerated deuterium beam is contained. The beam may be accelerated in the spouted plasma from the imploded core by the ponderomotive force of the LFEX. The effective core heating can be expected because the stopping range of the accelerated deuterium ion is too short.

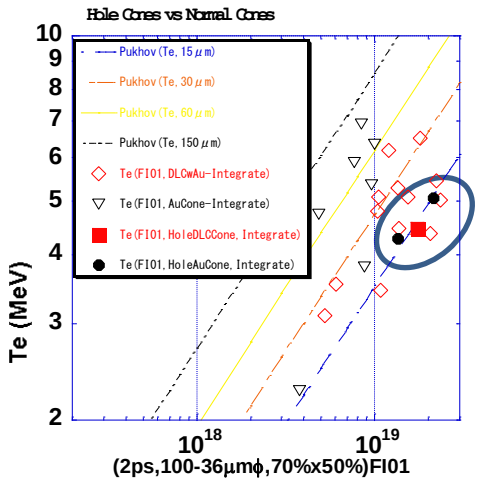


Fig. 5. $T_{eff}$ in open hole cone

$T_{eff}$ in open hole cone is small rather than $T_{eff}$ in standard cone.

## 4. Summary

The most suitable target for FI can be searched by comparison of the spectra between varied targets using ESM. Generally $T_{eff}$ is low when target Z is large. However $T_{eff}$ in copper target may be much higher than $T_{eff}$ in aluminum one due to the contamination of the water contamination on the copper surface.

We compare $T_{eff}$ in cone irradiated by the LFEX laser with $T_{eff}$ in plain. $T_{eff}$ in cone is obviously higher than $T_{eff}$ in plain due to the geometrical effect. In FI01, $T_{eff}$ can be reduced by elimination of the residual ω component in the imploding laser using the mechanical shutter. $T_{eff}$ is high at the implosion time because the lower component of the hot electron is dissipated in the imploded core. In the integrated experiments, DLC-cone is used for lower hot electron loss and merits on the diagnostics although the conversion efficiency in DCL-cone from laser to electron is slightly smaller than that in Au-cone.

The neutron yield in Au-cone shell is higher than that in DLC-cone shell. $T_{eff}$ in Au-cone becomes high. The neutron yield can be obtained in higher density. Those facts mean that the imploding core well couples with the higher energy electron rather than the expected optimum energy. By $B_{ext}$ application, the hot electron is clearly converged. However the neutron yield cannot increase significantly. Direct heating of the imploded core has been performed by using the open-hole cone shell. $T_{eff}$ does not become high and high neutron yield can be obtained. The open-hole cone is another candidate of FI.


### Acknowledgements

This work is supported by budgets of NIFS12UJHH003, NIFS10ULHH025, NIFS12KUGK059 and the Grant-in-Aid for Scientific Research (24561028)


### References


[1] T. Yamanaka, private communication.

[2] M. Tabak, et al., POP, **1** (1994) 1626.

[3] R. Kodama, et al, Nature **418**, 933-934(2002).

[4]T. Jozaki, et al, PP Cont. Fus. **51**, 014002 (2009).

[5] T. Ozaki, et al, JOP:Conf. Ser.2, **244**, 022056(2010).

[6] K. Tanaka, et al, PP Cont. Fus. **46**, B41–B49 (2004).

[7] H. Azechi, et al, J. Physics **112**, 012002 (2008).

[8] T. Johzaki, et al., IFE/P6-01, FEC

(2010).
[9] H. Shiraga, et al., RSI, **66**, 722 (1995).
[10] N. Izumi, N, et al., RSI, **70**, 1221-1224 (1999).
[11] A. Pukhov, et al, POP, 6, 2847(1999).
[12] S. Wilks, et al PRL(1992)69,1383
[13] H. Sakagami, private communication.
[14] T. Ozaki, et al., IFS2011 (to be submitted).
[15] L. Jarrott, et al., FIWS 2012.
[16] S. Fujioka, et al., FIWS 2012.
[17] T. Hosogai, et al., PRL 97 (2006) 075004.
[18] Y. Kitagawa, et al., FIWS 2012.
[19] A. Sunahara, et al., FIWS 2012.

# Interaction between Laser-Produced Plasma and Guiding Magnetic Field

Jun Hasegawa, Kazumasa Takahashi, Shunsuke Ikeda, Mitsuo Nakajima, and Kazuhiko Horioka

*Department of Energy Sciences, Tokyo Institute of Technology, Yokohama 226-8502, Japan*

## ABSTRACT

Transportation properties of laser-produced plasma through a guiding magnetic field were examined. A drifting dense plasma produced by a KrF laser was injected into an axisymmetric magnetic field induced by permanent ring magnets. The plasma ion flux in the guiding magnetic field was measured by a Faraday cup at various distances from the laser target. Numerical analyses based on a collective focusing model were performed to simulate plasma particle trajectories and then compared with the experimental results.

## Keywords

Laser-produced plasma, high-current ion source, guiding magnetic field, plasma transportation, collective effect

## 1. Introduction

Since the invention of laser in early 1960s, dense plasma generated by high-power laser irradiation of solid material has been recognized as a potential source of highly stripped ions, leading to numerous studies on laser ion sources for particle accelerators [1,2]. As one of the pioneering works, Phaneuf reported the generation of $Fe^{16+}$ and $C^{6+}$ by a $CO_2$ laser with a power density of $\sim 10^{10}$ W/cm$^2$ [3]. Luther-Davies *et al*. revealed that when the laser power density reached $\sim 10^{15}$ W/cm$^2$, considerably high charged ions such as $Au^{38+}$ were produced with MeV kinetic energies [4].

Besides the production of highly charged ions, the laser-produced plasma has the potential to supply high-flux, low-emittance ion beams owing to its large drift velocity perpendicular to the laser-irradiated solid surface. Barabash *et al*. recognized this feature of the laser-produce plasma and examined the applicability of the laser ion source to heavy ion fusion (HIF) injectors [5]. They produced low charged ions $Pb^+$ and $Pb^{2+}$ by irradiating a lead target with a $CO_2$ laser. Hasegawa, *et al*. also generated a low temperature, dense plasma composed mainly of $Cu^+$ and $Cu^{2+}$ by using a Nd:YAG laser with a power density slightly above an ablation threshold for copper ($\sim 10^8$ W/cm$^2$) and showed that it meets a demand for the ion flux from HIF driver accelerators.

To achieve high power densities above the ablation thresholds with relatively small laser energies ($\leq$ 1 J), the laser pulse must be shorter than ~1 μs. However, beam pulse lengths longer than 1-10 μs are frequently required to increase the accelerator duty cycle or relax strong space charge repelling forces. To achieve long pulse beam extraction, the laser ion source usually has a long drift space where the plasma freely expands toward the extraction gap [8]. Since ions in the laser-produce plasma have not only large drift velocity but also large momentum spread, a plasma pulse duration larger than ~10 μs is easily achieved by plasma expansion over several meters.

On the other hand, since the laser-produced plasma expands three-dimensionally during the drift, its flux rapidly drops with the drift distance. To suppress the flux decrease, Gray *et al*. applied an axial magnetic field to the drift space and confined the plasma

transversely [9]. They observed the enhancement of highly charged ions as well as the total plasma ion flux. Okamura *et al*. also have recently tested the confinement of a laser-produced plasma using a solenoid magnetic field and succeeded in extending the plasma pulse duration with suppressing the flux decrease [10].

The KEK digital accelerator facility is now planning to replace the present ECR ion source by a laser ion source and adopt a plasma-guiding scheme using a permanent magnet array instead of a solenoid. The use of the permanent magnet is preferable from the engineering viewpoint because it allows us to eliminate the power supply to the high-voltage terminal for the excitation and cooling of the solenoid.

In this study, we investigated both experimentally and numerically the transportation of a laser-produced plasma drifting through a guiding magnetic field induced by coaxially arranged ring magnets. From the viewpoint of ion source engineering, the purpose of this study is to find periodic magnetic field profiles, with which efficient plasma transportation is achieved. In addition, the interaction process between an expanding laser-produced plasma and an axial magnetic field is very complex because the time scale of magnetic field diffusion into the plasma is almost comparable to that of plasma expansion. This fact also motivates us to conduct this study from the viewpoint of plasma physics.

## 2. Experimental Setup

Figure 1 shows a schematic of the experimental setup. A copper target, whose surface was mirror polished by fine alumina particles (~0.3 μm), was set in a vacuum of $10^{-4}$ Pa. A KrF excimer laser irradiated the target with an incidence angle of ~70º and produced a dense plasma plume. The energy and duration of the laser pulse were, respectively, ~120 mJ and ~20 ns. The laser spot on the target surface was a rectangle of 0.5×1.5 mm$^2$, resulting in a power density of ~8×10$^8$ W/cm$^2$.

The laser-produced plasma rapidly expands into vacuum with a large center-of-mass velocity perpendicular to the target surface. Then the plasma plume was guided into a drift tube by an axial magnetic field. The guiding magnetic field was induced by permanent ring magnets, which were coaxially arranged along the tube with equal intervals. Each ring magnet has an inner diameter of 60 mm, an outer diameter of 120 mm, and a thickness of 20 mm. By changing the magnet interval $d$ from 0 to 40 mm, we examined the effect of the field profile on the plasma transportation. The distance from the laser target to the entrance of the magnet array was fixed to be 350 mm throughout this study.

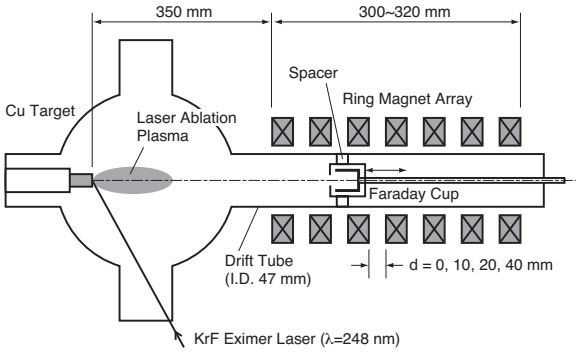


Fig. 1. A schematic of experimental setup.

Figure 2 shows axial magnetic field profiles $B_z(z)$ on the center axis of the drift tube calculated by the Poisson-Superfish code [11]. Note that the magnetic field quickly changes its polarity near the entrance ($L$ ~ 350 mm) and exit ($L$ ~ 650 mm) of the magnet array owing to cusp-like field structures. This reversal of the field is the most remarkable when

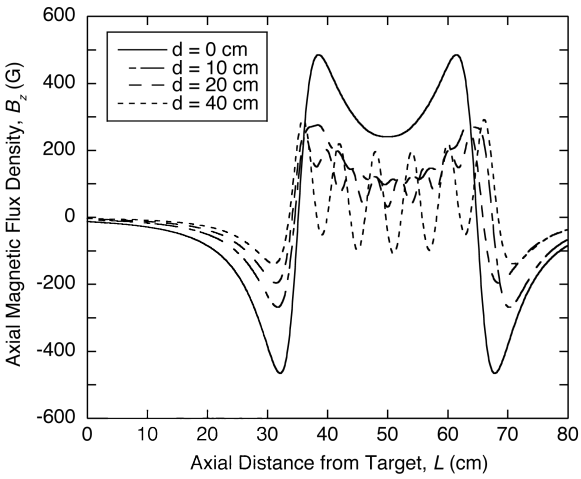


Fig. 2. Magnetic field profiles on drift tube axis.

$d = 0$. Meanwhile, when $d \neq 0$, ripples appear on the field profiles. The amplitude of the ripple becomes larger with magnet interval.

We used a Faraday cup with a secondary electron suppressor to measure the plasma ion flux. The cup was supported by a linear motion feed through having a stroke of 400 mm, enabling us to set the cup at any positions in the drift tube. An insulator spacer was inserted between the cup cage and the drift tube wall so that the entrance aperture of the cup (ø6 mm) could be always located exactly on the center axis of the tube. The cup and the suppressor were biased to –400 V and –300 V, respectively. Before recoding a plasma flux waveform by a digital oscilloscope, we cleaned up the copper target surface by several laser shots in advance to minimize the effect of impurities on the current waveform.

## 3. Numerical Analysis

### 3.1 Fundamental equations

To analyze the behavior of a drifting plasma injected into an axial magnetic field, we adopted the collective focusing model proposed by Robertson [12]. Kraft *et al*. showed that this model well predict the behavior of a neutralized high-current pulsed ion beam in a solenoidal magnetic field [13].

Here we assume that the laser-produced plasma drifts along the center axis of the guiding magnet field and the perturbation of the field induced by the plasma is small enough to be ignored. In addition, the plasma neutrality is assumed to hold always.

The Lagrangian for a charge particle moving a magnetic field is given by:

$$L = \tfrac{1}{2} m\mathbf{v}^2 + q\mathbf{v}\bullet\mathbf{A} - q\phi . \quad (1)$$

Here, $m$, $q$, and $\mathbf{v}$ are, respectively, the mass, charge, and velocity of the particle. $\mathbf{A}$ and $\phi$ are, respectively, the vector and scalar potentials of the field. The canonical momentum of the particle is derived from Eq. (1):

$$\frac{\partial L}{\partial \dot{\theta}} = P_\theta = mr^2 \frac{d\theta}{dt} + qrA_\theta . \quad (2)$$

If we assume that the plasma particle has no momentum in the azimuthal direction when it is produced ($t = 0$), the conservation of the canonical momentum requires that $P_\theta = 0$ hold throughout the particle motion. Then, Eq. (2) gives:

$$\frac{d\theta}{dt} = -qA_\theta / mr . \quad (3)$$

By applying Eq. (3) to the Lagrange equation for radial direction, we obtain the equation of motion for the plasma particle:

$$\frac{d^2 r}{dt^2} = -\frac{q^2}{m^2} A_\theta \frac{\partial A_\theta}{\partial r} + \frac{qE_r}{m} . \quad (4)$$

When we assume $r_i(t) = r_e(t)$ as a plasma quasi-neutrality condition, $dr_i^2(t)/dt^2 = dr_e^2(t)/dt^2$ is satisfied throughout the particle motion, where the subscripts $i$ and $e$ denote ion and electron, respectively. By applying this relationship to Eq. (4) and solving it for the axial electric field $E_r$, we obtain:

$$E_r = \frac{q_i m_e + q_e m_i}{m_e m_i} A_\theta \frac{\partial A_\theta}{\partial r} . \quad (5)$$

By substituting $E_r$ in Eq. (4) by Eq. (5), the equation of motion for the plasma particle finally becomes:

$$\frac{d^2 r}{dt^2} - \frac{q_e q_i}{m_e m_i} A_\theta \frac{\partial A_\theta}{\partial r} = 0 . \quad (6)$$

Eq. (6) means that ions and electrons in the plasma behave as if they were particles having a charge of $(q_e q_i)^{1/2}$ and a mass of $(m_e m_i)^{1/2}$. The electric field and the equation of motion for the axial direction are also derived by the same procedure:

$$E_z = \frac{q_i m_e + q_e m_i}{m_e m_i} A_\theta \frac{\partial A_\theta}{\partial z} , \quad (7)$$

$$\frac{d^2 z}{dt^2} - \frac{q_e q_i}{m_e m_i} A_\theta \frac{\partial A_\theta}{\partial z} = 0 . \quad (8)$$

Eq. (6) and (8) determine the orbit of the plasma particle in an axisymmetric magnetic field.

### 3.2 Numerical simulation

To calculate plasma particle orbits in an axial magnetic field using Eqs. (6) and (8), we used the azimuthal component of the vector potential $A_\theta$ obtained by interpolating the field data output from the Poisson-Superfish code (Fig. 2). The 4th-order

Runge-Kutta method was employed for the time integration of the equations of motion.

In this study, the simulation assumed that all plasma particles are emitted from the center of the copper target ($z = r = 0$) at $t = 0$ because both the laser pulse (~10 ns) and the laser spot (~0.5 mm) are negligibly small compared with the temporal and spatial scales of the plasma expansion (~10 μs, ~100 mm), respectively.

The plasma particles are assumed to have a drift-Maxwellian velocity distribution given by:

$$f(v_r, v_z) = n\left(\frac{m}{2\pi kT}\right)^{3/2} \exp\left(-mv_r^2 / 2kT\right) \times \exp\left(-m(v_z - v_d)^2 / 2kT\right), \quad (9)$$

where $n$ is the plasma number density, $T$ is the plasma temperature, and $v_d$ is the axial drift velocity. The temperature and the drift velocity were determined by fitting a measured plasma-ion-flux waveform by a TOF (time of flight) distribution function derived from Eq. (9):

$$f_{\mathrm{TOF}}(t) = Ct^{-4} \exp\left(-m(L/t - v_d)^2 / 2kT\right). \quad (10)$$

The simulation iteratively calculated the orbits of the plasma particles (typically for 100 test particles) with randomly changing initial velocities based on the above distribution function.

## 3. Results and Discussion

Figure 3 shows a typical plasma ion flux (solid line) observed 350 mm downstream from the copper target when no guiding magnetic field was applied. The reproducibility of the waveform was very high and the shot-to-shot fluctuation of the peak height was less than a few percent.

The dashed line in the figure is the result of a curve fit by Eq. (10), which gives $v_d \approx 7.6\times10^3$ m/s and $T \approx 56$ eV. Note that this $T$ value indicates only that the plasma particles have a large momentum spread because the rapidly expanding laser-produced plasma is considered not in an equilibrium state defined by a single temperature value. We consider that this large momentum spread was induced principally in the hydrodynamic acceleration process in the early stage of the plasma expansion. The experiments in this

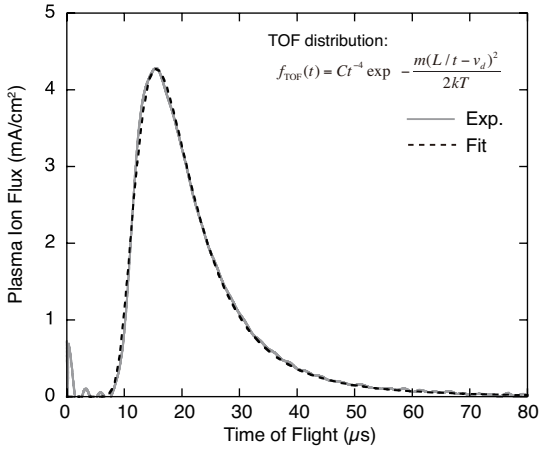


Fig. 3. Typical waveform of plasma ion flux without guiding magnetic field.

study were conducted under a fixed laser irradiation condition, so we used the above values as initial parameters for numerical simulations.

Typical current waveforms of the plasma ion flux measured in a guiding magnetic field ($d = 0$ mm) are shown in Fig. 4. To check the reproducibility, two or three waveforms taken at the same condition are superimposed. One can see that the plasma ion flux is enhanced several times compared with the case without the guiding field. In addition, ripples appear on the waveforms, which degrades the reproducibility. We found that this tendency became more remarkable with increasing magnet interval.

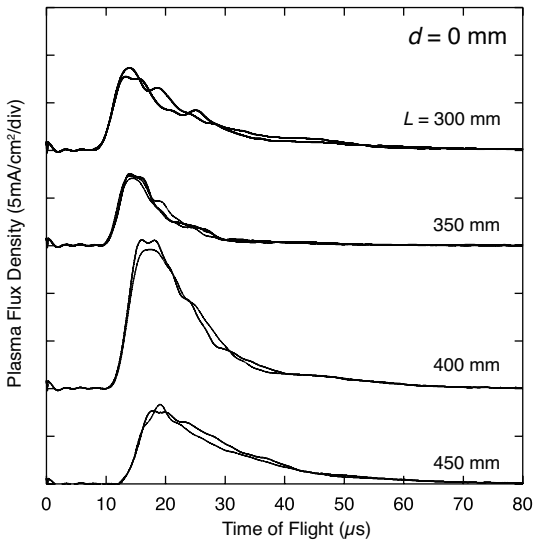


Fig. 4. Typical waveform of plasma ion flux with guiding magnetic field.

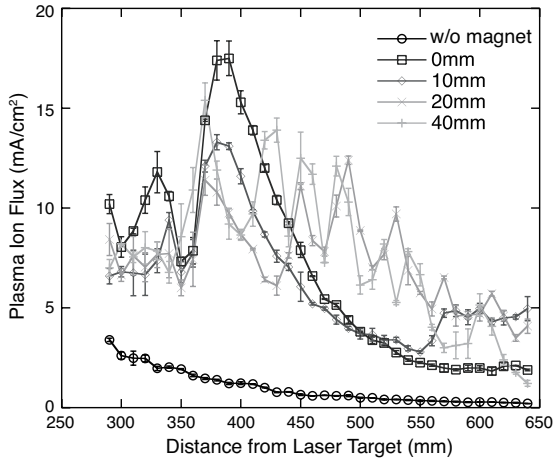


Fig. 5. Dependence of peak ion-current density on plasma drift distance.

The peak value of the plasma ion flux was plotted as a function of drift distance from the target in Fig. 5. The figure compares the cases with a guiding magnetic field ($d$ = 0, 10, 20, and 40 mm) to the case without the field. The plasma ion flux increases by a factor of ~2 even before the plasma enters the magnet array ($L$ < 350 mm). We consider that this enhancement is attributed to the transverse compression of the plasma by the converging magnetic field near the entrance of the magnet array. When $d$ = 0 mm and 10 mm, the plasma ion flux drastically increases immediately after the plasma passes through the cusp-like field region ($L$ ~ 350 mm) and reaches the maximum at $L$ ~ 400 mm. Then the flux decreases gradually with drift distance.

For larger magnet intervals ($d$ = 20 mm and 40 mm), the plasma behavior becomes more complex. Although the overall tendencies are similar to those for smaller interval cases, the plasma ion flux largely fluctuates even at the middle part of the magnet array ($L$ = 400~600 mm). This result implies that the plasma transportation was very sensitive to the perturbation of the guiding magnet field.

Figure 6 plots the calculated trajectories of the plasma particles in the guiding magnetic field. Since the trajectories of 100 test particles are overlaid, the figure shows not an instantaneous spatial plasma distribution but the envelope of the drifting plasma. The maximum initial divergence angle of the plasma

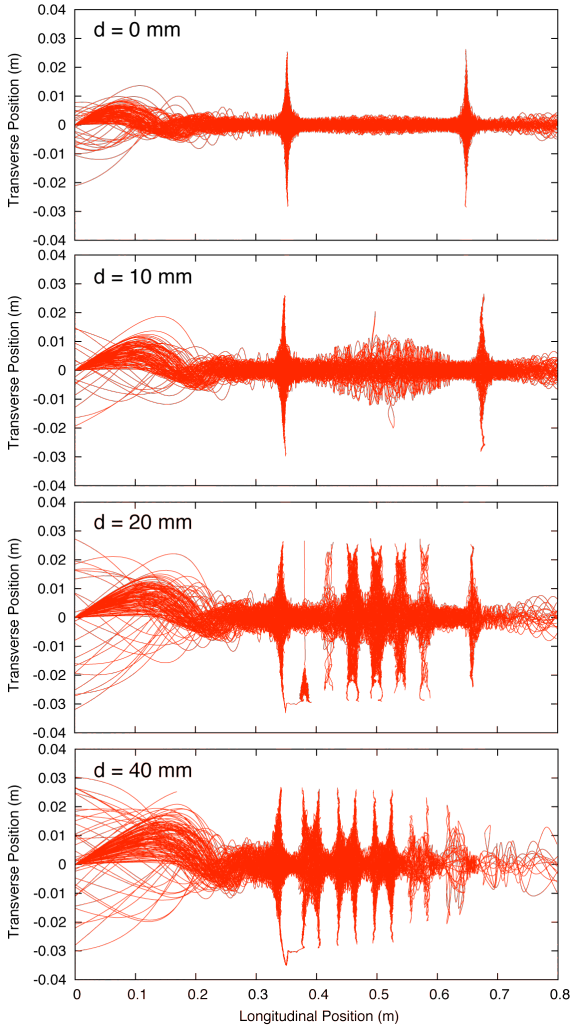


Fig. 6. Trajectories of plasma particles in guiding magnetic fields.

particle was defined to be $\theta_{max}$ = $\tan^{-1}(24/120) \sim 11.3°$ from the drift tube radius (~24 mm) and the distance from the target to the entrance of the drift tube (~120 mm). The initial divergence angle was randomly changed from 0 to $\theta_{max}$ in this calculation by considering the axial symmetry of the magnetic field.

As shown in Fig. 6, the transverse compression of the plasma near the magnet array entrance ($L$ ~ 300 mm) depends slightly on the magnet interval. When $d$ = 0 mm, the plasma compression occurs most strongly, leading to the effective plasma collection. Meanwhile, the compression effect becomes weaker with increasing magnet interval, resulting in relatively larger plasma radius. The

number of reflected plasma particles also increases with magnet interval.

The unwanted effect of the reversal of the field at the array entrance is almost independent of the magnet interval. Since the field strength increases with increasing radial position in the permanent magnet array, plasma particles trapped by the cusp-like field cannot escape from it. Such particles are finally lost at the tube wall. The sudden drop in the observed plasma flux at $L$ = 350 mm is probably due to the rapid plasma expansion by the cusp-like field. After passing through the cusp-like field, the plasma is compressed again and transported to the array exit as shown in Fig. 6. Particularly for $d$ = 0 mm and 10 mm, the plasma transportation is relatively stable in the array. These results well explain experimentally observed plasma behaviors shown in Fig. 5.

On the other hand, when the magnet interval is equal to or larger than each ring magnet width (20 mm), the plasma transportation is largely influenced by the field fluctuations even inside the array. The plasma undergoes expansion and compression repeatedly and the particle loss in the expansion phase largely decreases the transportation efficiency. This result suggests that the magnet interval should be less than the width of the permanent magnet composing the array.

## 4. Concluding remarks

This study proposed to use a permanent magnet array to guide a laser-produced plasma and examined the feasibility of this plasma-guiding scheme by preliminary experiments and simple numerical simulations. In contrast to the solenoidal magnetic field, the magnetic field induced by the permanent magnet array intrinsically has cusp-like structures. We found that such a field structure led to a large plasma loss. However, by setting the magnet intervals to be smaller than the width of each permanent ring magnet, the plasma could be transported effectively. Particularly, the converging field structure near the magnet array entrance may increase the utilization ratio of the laser-produced plasma.

On the other hand, the application of the guiding magnetic field may increase the averaged transverse momentum of the plasma particle, which affects the emittance of the beam extracted from the plasma. This effect must be investigated more precisely. Fortunately, the collective focusing model seems to well reproduce the behavior of the plasma in the axial guiding magnetic field in the parameter regime treated in this study, probably enabling us to examine the emittance problem by using the simulation code employed in this study.

## References


[1] C. De Michelis: “Laser interaction with solids - A bibliographical review”, *IEEE J. Quant. Electronics*, QE-6, p.630 (1970).

[2] G. F. Tonon : “Laser Sources for Multiply-Charged Heavy Ions”, *IEEE Trans. Nucl. Sci.*, NS-19, p.172 (1972).

[3] R. A. Phaneuf: “Production of High-Q Ions by Laser Bombardment Method”, IEEE Trans. Ncul. Sci., NS-28, p.1182 (1981).

[4] B. Luther-Davies and J. L. Hughes, “Observations of MeV ions emitted from a laser produced plasma”, Opt. Commun., vol. 18, pp. 351-353 (1976).

[5] L. Z. Barabash, D. G. Koshkarev, Y. I. Lapitskii, S. V. Latyshev, A. V. Shumshurov, Y. A. Bykovskii, A. A. Golvbev, Y. P. Kosyrev, K. I. Krechet, R. T. Haydarov, and B. Y. Sharkov: “Laser produced plasma as an ion source for heavy ion inertial fusion”, *Laser Part. Beams*, 2, p.49 (1984).

[6] J. Hasegawa, M. Yoshida, Y. Oguri, M. Ogawa, M. Nakajima, and K. Horioka: “High-current laser ion source for induction accelerators”, *Nucl. Instr. and Meth. B* 161-163, pp. 1104-1107 (2000).

[7] M. Yoshida, J. Hasegawa, J. W. Kwan, Y. Oguri, M. Nakajima, K. Horioka, and M. Ogawa: "Grid-Controlled Extraction of Low-Charged Ions from a Laser Ion Source," *Japan. J. Appl. Phys.*, Vol. 42, pp. 5367-5371

(2003).

[8] B. Y. Sharkov, S. Kondrashev, I. Roudskoy, S. Savin, A. Shumshurov, H. Haseroth, et al.: “Laser ion source for heavy ion synchrotrons”, Rev. Sci. Instrum., Vol. 69, pp. 1035-1039 (1998).

[9] L. G. Gray, R. H. Hughes, and R. J. Anderson: “Heavy ion source using a laser generated plasma transported through an axial magnetic field”, J. Appl. Phys., 53, 6628 (1982).

[10] M. Okamura, A. Adeyemi, T. Kanesue, J. Tamura, K. Kondo, and R. Dabrowski: “Magnetic plasma confinement for laser ion source”, Rev Sci Instrum, Vol. 81, p. 02A510 (2010).

[11] http://laacg.lanl.gov/laacg/services/serv_codes.phtml

[12] S. Robertson: “Collective focusing of an intense ion beam”, Phys. Rev. Lett. Vol. 48, No. 3, 149 (1982).

[13] R. Kraft, B. Kusse, and J. Moschella: “Collective focusing of an intense pulsed ion beam”, Phys. Fluids, Vol. 30, 245 (1987).

# Control of laser ablation plasma with longitudinal magnetic field
## - directionality and dependence of charge distribution on magnetic field -

Shunsuke Ikeda, Kazumasa Takahashi, Jun Hasegawa, Tohru Kawamura, Mitsuo Nakajima and Kazuhiko Horioka

Department of Energy Sciences, Tokyo Institute of Technology,
Nagatsuta 4259, Midori-ku, Yokohama, 226-8502, Japan

**ABSTRACT**

To develop high-flux and low-emittance ion source, we discuss controllability of laser ablation plasma with longitudinal magnetic field for making directional plasma. The dependence of flux and charge distribution of the plasma on the magnetic filed was measured with an ion probe and an ion energy analyzer as functions of magnetic field distribution and intensity. Results showed that the magnetic field affects highly charged ions preferentially.

**Keywords**

Laser ablation plasma, Magnetic control, High-flux ion source, Directing plasma, Charge distribution

### 1 Introduction

For high energy density physics, heavy ion inertial fusion [1], ion radiotherapy or neutron source, high-current and low-emittance ion source is needed. However, high-flux and low-emittance are incompatible with typical ion sources. When the sources use static plasma such as electron cyclotron resonance ion source, the ability of current supply into ion beam extractor is described by Bohm current. It is proportional to square root of the electron temperature [2]. Then, the emittance of the ion beam that represents the disorder of beam is intrinsically proportional to square root of the ion temperature. Therefore, usually the emittance increases with the current.

On the other hand, ion source with laser ablation plasma possibly supplies a high-current and low-emittance beam. The dense plasma with laser ablation expands, and then that is accelerated and cooled. Therefore, we can expect to decrease the temperature and to increase the supply current that is proportional to the drift velocity.

We discuss the mechanism of magnetic guiding of laser ablation plasma to increase the current or control the time profile of the extracted ion beam without emittance growth. For the purpose, the flux of the ions into extractor needs to be increased without disturbance. A proper application of longitudinal magnetic field is expected to collects and collimates the plasma without disturbance like a well designed nozzle.

However, the effect of the magnetic field on laser ablation plasma is not clear. The suitable description of the plasma behavior depends on plasma parameter. Meanwhile, the density and temperature of the plasma changes largely and rapidly while the plasma spreading. So, the behavior can not be predicted easily. In addition, the enhancement of the plasma flux with the magnetic field was observed previously [3–5] but the understanding has been rather phenomenological.

Therefore, to investigate the guiding mechanism we measured the plasma ion flux and charge distribution as functions of magnetic field distribution

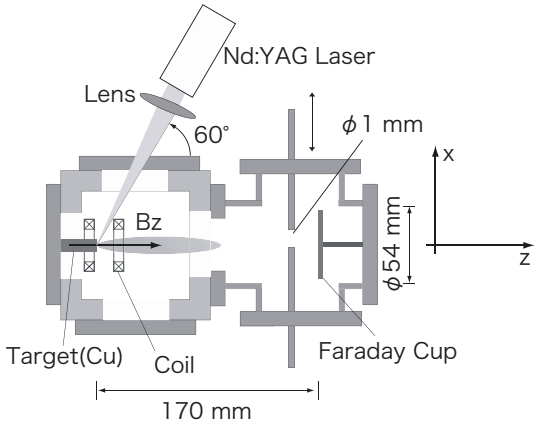


Figure 1: Schematic of experimental arrangement.

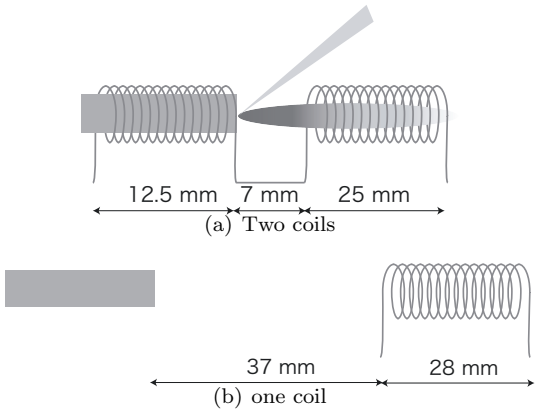


Figure 2: Schematic of coil

and intensity [6].

## 2 Experimental setup

Figure 1 shows a schematic of our experimental setup. A Q-switched Nd:YAG laser (532 nm) with a power density of $\sim 3 \times 10^8$ W/cm$^2$ at the focal spot on the surface of the Cu target, created the ablation plasma. The pulse length of the laser (15 nsec) was sufficiently small compared with the time scale of the plasma motion ($\sim \mu$s) through the magnetic field. The vacuum chamber was evacuated to $\sim$ $10^{-3}$ Pa.

Prior to the measurements, the contaminations on the target surface [7] was removed in-situ (i.e. in the vacuum chamber) by weak laser. It greatly improved the reproducibility of the flux signal. The weak laser was irradiated at 10 Hz between shots for the measurement.

The longitudinal magnetic field was applied by (a) two coils of 10 mm in diameter and 13 mm and 25 mm in length or (b) one coil of 28 mm in length and placed 37 mm from the target as shown in Fig.2. The two coils in Fig.2 (a) applies a stronger magnetic field near the target than the one coil case in Fig.2 (b). The pulse length of the current flowing the coil was a few ms. Then we can regard that the magnetic field was steady while the plasma passing through the coil in a few $\mu$s.

A biased ion probe measured the plasma flux through the longitudinal magnetic field. The bias voltage was 60 V. A 1-mm-diameter aperture was placed in front of the plasma collector. It moved transversely to get the spatial profile of plasma flux as shown in Fig.1.

The energy distribution of ions was analyzed with a cylindrical electrostatic ion energy analyzer (Fig.3). The device is mainly composed of two coaxial cylinders, slits and an electron multiplier (PHOTONIS MUGNUM 31308). Two coaxial cylinders are applied electric potentials.

The kinetic energy of ions that can be detected by the electron multiplier is given by the following equation:

$$\frac{E}{Z} = \frac{eU}{2\ln(R_2/R_1)} \tag{1}$$

where $e$ is the elementary charge, $E$ is the kinetic energy, $Z$ is charge state of the ion, $R_1$ (9.5 cm) and $R_2$ (10.5 cm) are radii of inner and outer cylinders and $U$ is the potential difference between the cylinders. On the other hand, the time of flight of ions from the target to the detector is

$$t = L\sqrt{M/2E} \tag{2}$$

where $M$ is the mass of the ion, $L$ (150 cm) is the path of flight. From equations (1) and (2), the energy distribution of the ion with an $M/z$ can be obtained [8].

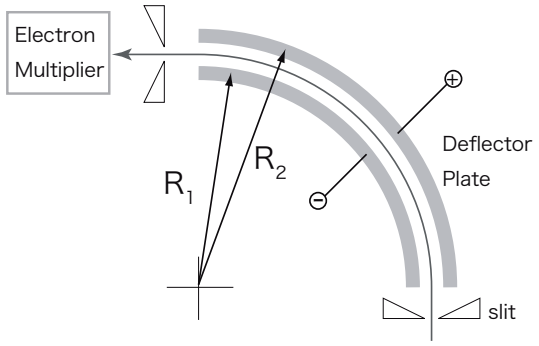


Figure 3: Schematic of electrostatic energy analyzer.

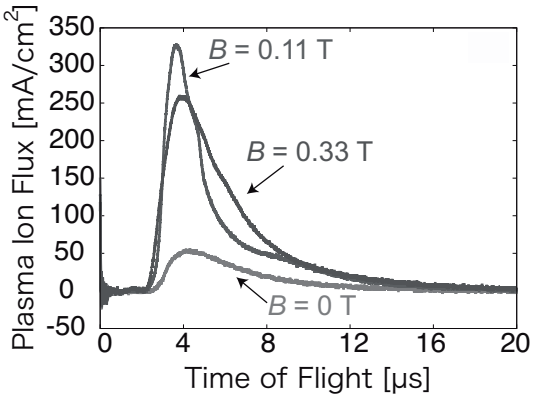


Figure 4: Signals of biased Faraday cup located at $z$ = 170 mm, and $x$ = 0 mm as a function of the magnetic field intensity. (The magnetic field was applied by two solenoids shown in Fig.2 (a)).

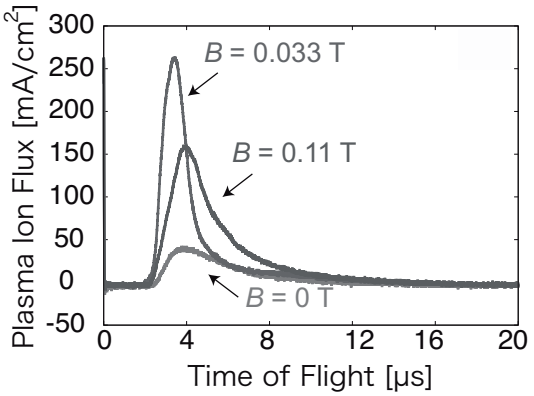


Figure 5: Signals of biased ion probe located at $z$ = 170 mm, and $x$ = 0 mm as a function of magnetic intensity. (The magnetic field was applied by two solenoids shown in Fig.2 (b)).

## 3 Results and discussion

### 3.1 Plasma flux measurements

Figure 4 shows the plasma flux measured as a function of magnetic field intensity applied by two coils shown in Fig.2 (a). The ion probe was placed at $z$ = 170 mm from the target surface and $x$= 0 mm from $z$ axis. The horizontal axis is the time from laser shot and the vertical axis is the plasma ion flux. The applied magnetic field intensity at $z$ = 2 cm (i.e. the middle of the coil) were 0, 0.11 and 0.33 T. The result shows that the peak flux was enhanced at $B$ = 0.11 T. The flux enhancement at $x$ = 0 mm means the increase of the collimated ions. Then the peak declined at $B$ = 0.33 T. In addition, the flux of the low energy particles that arrived at the ion probe after about 6 $\mu$s were enhanced with the field intensity.

Figure 5 shows the plasma flux measured at $z$ = 170 mm with one coil shown in Fig.2 (b). The applied field intensity at $z$ = 5.1 cm (that is the middle of the coil) were 0, 0.033 and 0.11 T. A similar enhancement of the peak flux was observed with the weaker magnetic field $B$ = 0.033 T. Then the decrease of the peak flux with more intense magnetic field was also observed at $B$ = 0.11 T. The similar enhancement mean that the converging magnetic field at the entrance of the coil collected the plasma to the center.

To investigate the collimation of the ions by the magnetic field, we measured the angular distribution of the plasma flux as a function of the field intensity. The result is shown in Fig.6. The horizontal axis is the angle between the direction of the aperture from the target surface and $z$ axis. The vertical axis is the peak value of the plasma ion flux. The distributions with the magnetic field became sharp. In general the angular distribution can be described as $\cos^p \theta$, where the parameter $p$ in the absence of a magnetic field, has been determined in

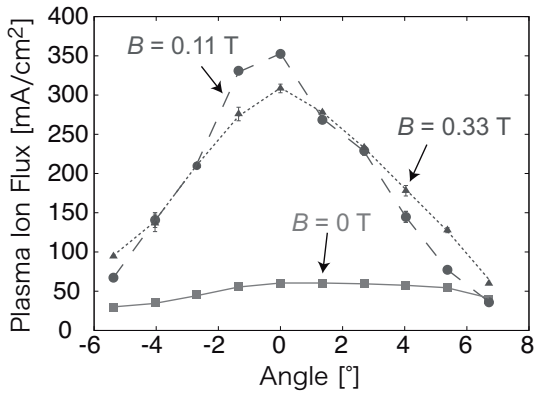


Figure 6: Angular distribution of plasma flux at $z$ = 170 mm as a function of magnetic field intensity applied by two solenoids shown in Fig.2 (a).

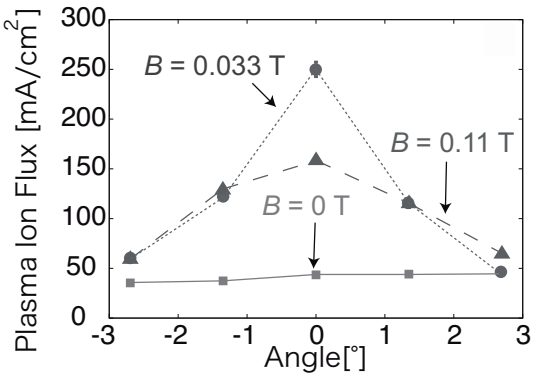


Figure 7: Angular distribution of plasma flux at $z$ = 170 mm as a function of magnetic field intensity applied by two solenoids shown in Fig.2 (b).

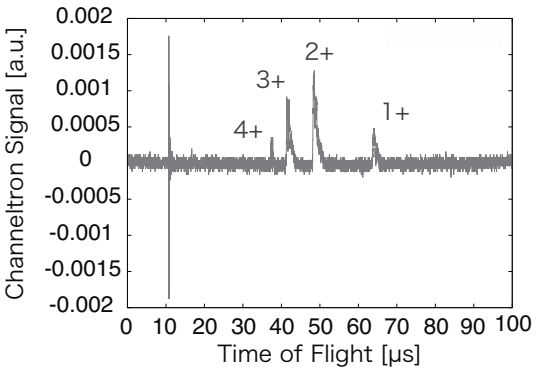


Figure 8: Typical signal of ion energy analyzer.

a previous research to be 10∼30 [9]. On the other hand, in our experiment the angular distribution at B = 0.11 T is well described by $\cos^{250}\theta$. This result indicates that the magnetic field can strongly direct the plasma along the target normal.

On the other hand, the angular distribution at $B$ = 0.33 T was slightly wider than that at $B$ = 0.11 T. This probably means that the ions were less collimated by the more intense magnetic field and hence the flux declined at $x$ = 0 mm.

Figure 7 shows the angular distribution with one coil (Fig.2 (b)). The sharp distribution was also observed at $B$ = 0.033 T. In addition, the distribution was sharper than that with two coils. Then the spread of the distribution with more intense magnetic field ($B$ = 0.11 T) was also observed.

The enhancement of the collimated ions apparently shows that the magnetic field worked like gas-dynamic nozzle. However, the dependency of the height and width of the flux waveform on the field intensity may mean not so. The dependency may be due to different mechanism of the magnetic field on the multiple ions in the plasma.

### 3.2 Charge distribution analysis

Figure 8 shows a typical signal of the ion energy analyzer. The horizontal axis is time of flight from the target to the detector. The vertical axis is a signal of an electron multiplier. The signal at $t$ = 0 is thought to be caused by the stray light from the laser ablation. Each peak corresponds to each ion with a different $M/z$. From the equation (1) and (2), we can identify corresponding $M/z$ as shown. The experimental and calculation results were consistent within $\sim$ 0.1 $\mu$s. (However, because $M/z$ of $Cu^{4+}$ and $O^{1+}$ are equal, we could not separate these ions.) The ion energy analysis was repeated many times by changing the potential $U$ from 30 V to 150 V. From the results, we reconstructed the ion flux of each charge state.

Figure 9 shows the reconstructed ion flux spectrum at $B$ = 0, 0.11 and 0.33 T. The horizontal axis is the time from laser shot. As shown, highly charged ions reached earlier than lowly charged ions. A prior measurement of charge distribution

of laser ablation plasma without magnetic field [10] also showed earlier arrive of highly charged ions. However, the cause has not been clarified.

A comparison of Fig.9 (a) with (b) shows that the highly charged ion flux was preferentially enhanced in the presence of the magnetic field ($B$ = 0.11 T). Therefore, the flux component of highly charged ions caused the sharp flux waveform at $B$ = 0.11 T shown in Fig.4.

The result means that the magnetic field did not work as gasdynamic nozzle. Collimation of a uniform plasma by the pressure gradient cannot explain the dependency on charge state. The possible reasons are the increase of the ionization rate during the laser irradiation, preferential collection or preferential collimation of the highly charged ions.

From comparison of Fig.9 (b) with (c) we know that the peak flux of doubly and triply charged ions decreased by the application of stronger field. The decrease corresponds to the decrease of the peak flux shown in Fig.4.

On the other hand, the enhancement of the flux of the low energy particles that arrived at the ion probe after $\sim 6$ $\mu$s in Fig.4 is not shown after $\sim 50$ $\mu$s in Fig.9. In the ion flux measurement, the ion probe was placed 17 cm from the target while in the ion energy analysis, the electron multiplier was placed 150 cm from the target. Therefore, if the ions did uniform motion, the low energy particles that reached the ion probe after $\sim 6$ $\mu$s should arrive at the electron multiplier after $\sim 50$ $\mu$s. This may mean that the enhancement of the flux of the low energy particles was caused by the increase of the neutral particle. Ion probe can detect the neutral particles due to the generation of secondary electrons on the probe [12]. The magnetic confinement of the plasma may increase the recombination rate during the propagation.

Figure 10 shows the reconstructed ion flux in the case field applied with one coil (Fig.2 (b)). The

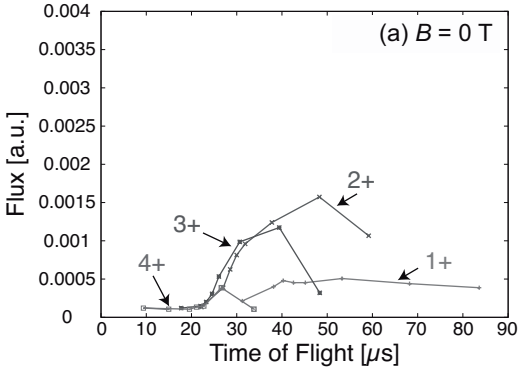


(a) $B$ = 0 [T]

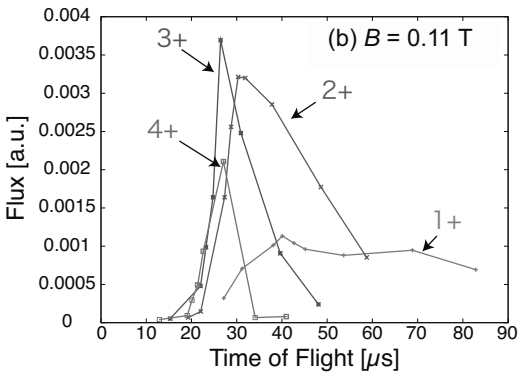


(b) $B$ = 0.11 [T]

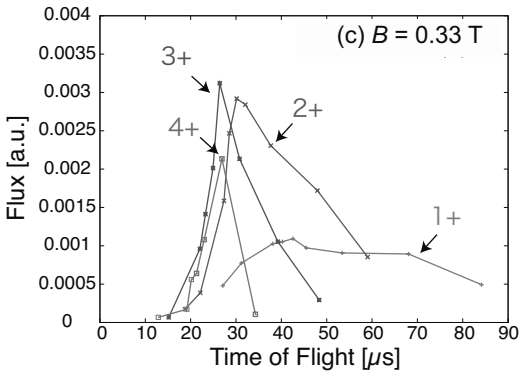


(c) $B$ = 0.33 [T]

Figure 9: Reconstructed plot of ion current spectrum as a function of magnetic intensity applied by two solenoids shown in Fig.2 (a).

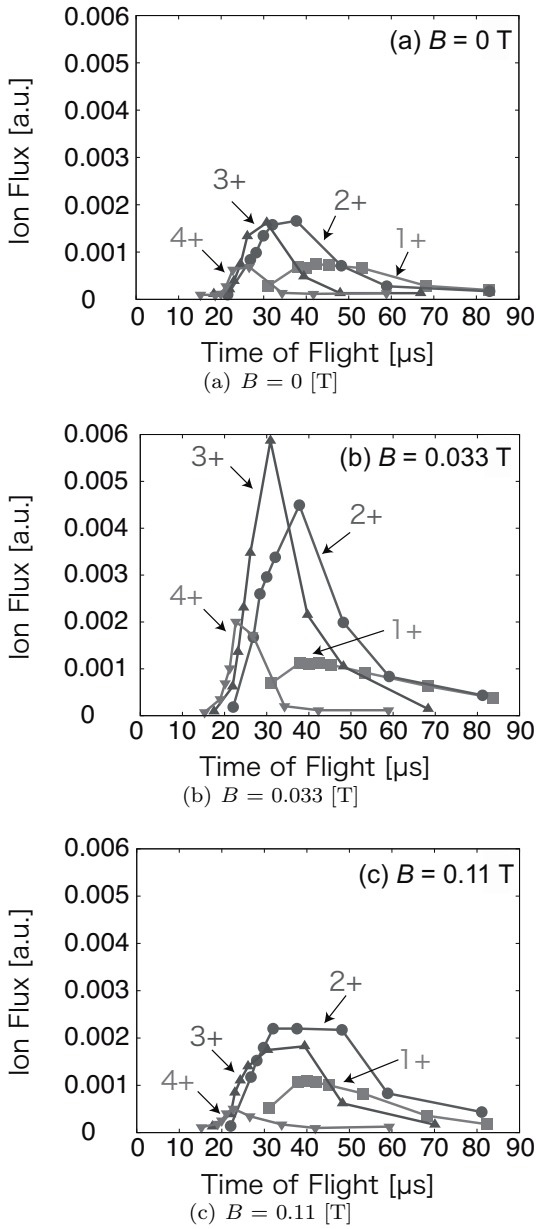


Figure 10: Reconstructed plot of ion current spectrum as a function of magnetic intensity applied by two solenoids shown in Fig.2 (b).

preferential enhancement of the flux of the highly charged ions with a field intensity was also observed. The enhancement indicates that effect on the ionization process is negligibly small because the field intensity was around $10^{-5}$ T near the target surface. Therefore, the enhancement can be attributed to the preferential collection or preferential collimation of the highly charged ions.

On the other hand, results shown in Fig.10 (b) and (c) show that the highly charged ions were preferentially decreased at $B = 0.11$ T. The decrease may be due to the collective effect [11] at the exit of the coil in which the magnetic field diverges. In the collective mode of plasma guiding [11], electrons are expected to move along the magnetic line and preferentially pull the highly charged ions.

## 4 Conclusion

To create highly directional plasma, a better understanding of the plasma dynamics is required. Then we observed behaviors of laser ablation plasma through a longitudinal magnetic field.

The experimental results show that magnetic field increased the ion flux by collecting and collimating. In addition, the preferential enhancement of the flux of the highly charged ions was also observed. The results indicates that with application of longitudinal magnetic field highly directional plasma can be created and degree of ionization can be controlled, which would be advantageous for developing high-flux and low-emittance ion sources.

From comparison of the effects of the magnetic fields applied near and far from the target, the preferential increase of highly charged ions can not be attributed to the increase of the ionization. Results indicates preferential collection or collimation of highly charged ions by the magnetic field. This means that the mechanism of the magnetic guide is not explained by gasdynamic effect.

On the other hand, too intense magnetic field did not increase the flux so much. Besides the wider distribution and the preferential decrease of highly charged ions indicate that ions were pulled by magnetized electrons at the exit of the coil.

## References

[1] J. W. Kwan, IEEE Trans. Plasma Sci., **33**, 6, 1901-1910 (2005)

[2] J. Ishikawa "Iongen Kogaku" Aionikusu Company (1986)

[3] M. Okamura, A. Adeyemi, T. Kanesue, J. Tamura, K. Kondo, et al.,Rev.Sci.Instr., **81**,2, 02A510-1, (2010).

[4] J. Wolowski, J. Badziak, I. Ivanova Stanik, P. Parys, W. Stepniewski and E. Woryna, Rev. Sci. Instr., **75**, 5, 1353-1356, (2004)

[5] V. B. Kutner, Yu. A. Bykovski, V. P. Gusev, Yu. P. Kozyrev and V. D. Peklenkov, Rev. Sci. Instr. **63**, 4, 2835-2837, (1992)

[6] S. Ikeda, M. Nakajima and K. Horioka, J. Plasma and Fusion Res., **7**,1201015,1201015-1-2,(2012).

[7] J. Wolowski, L. Celona, G. Ciavolva, S. Gammino, J. Krasa, L. Laska, P. Parys, K. Rohlena, L. Torrisi and E. Woryna, Laser Part. Beams, **20**, 113, (2002)

[8] E. Woryna, P. Parys, J. Wolowski, and W. Mroz, Laser and Particle Beams **14**, 3, 293-321, (1996).

[9] L. Laska, J. Krasa, M. Pfeifer, K. Rohlena, S. Gammino, L. Torrisi and G. Ciavola, Review of Scientific Instruments **73**, 2, 654-656, (2002).

[10] D. Doria, A. Lorusso, F. Belloni, V. Nassisi, L. Torrisi and S. Gammino, Laser Part. Beams, **22**, 461-467, (2004)

[11] S. Robertson, Phys. Fluids, **29**, 4, (1983)

[12] J.C.S. Kools, S.H. Brongersma, E. van de Riet and J. Dieleman, Appl. Phys. **53**, 3, 125-130, (1991)

# Controlling laser ablation plasma with external electrodes

## - Application to sheath dynamics study and beam physics -

Fumika Isono, Mitsuo Nakajima, Jun Hasegawa, Tohru Kawamura, and Kazuhiko Horioka

Department of Energy Sciences, Tokyo Institute of Technology,
Nagatsuta 4259, Midori-ku, Yokohama, 226-8502, Japan

**ABSTRACT**

The potential of laser ablation plasma was controlled successfully by using external ring electrodes. We found that an electron sheath is formed at the plasma boundary, which plays an important role in the potential formation. When the positively biased plasma reaches a grounded grid, electrons in the plasma are turned away and ions are accelerated, which leads to the formation of a virtual anode between the grid and an ion probe. We think that this device which can raise the plasma potential up to order of kV can be applied to the study of sheath dynamics and to a new type of ion beam extraction.

**Keywords**

laser ablation plasma, sheath, space charge limited current, virtual anode, beam extraction

## 1 Introduction

Since laser ablation plasma expands with extensive velocity and density, and can be produced from almost any kind of solid target, it has been applied to various industrial fields, such as Laser Ion Source, complex thin films made by Pulsed Laser Deposition, plasma etching and surface modification [1] [2].

Laser-produced plasma drifts adiabatically with its pressure gradient under the given boundary conditions. However, its dynamics when electric forces have been applied has not been clarified thoroughly yet. In this study, electric fields are applied to the drifting plasma, detached from the plasma boundary. Therefore, boundary conditions such as electrodes and walls give conditions to the plasma about how to raise self-consistent potential which affect the transportation of ions in plasma. When plasma touches a wall, it keeps quasi-neutrality by forming a sheath which balances the total electron current and the ion current flowing toward the wall, and the plasma potential needs to be determined by the sheath currents.

We have investigated the behavior of plasma by changing the external environment, and succeeded in raising the bulk plasma potential up to 1 kV by using external electrodes. This control was achieved because of the stable formation of an electron sheath in front of the electrode.

This device which can control plasma potential is useful for the research of plasma dynamics. With this device we observe the formation of sheaths, and an virtual anode formed by the extraction of ions from plasma.

In the end, we will show that we can extract a stable ion beam which is not affected by the ion current supply similar to the grid

controlled ion extraction [3].

## 2 Sheath

### 2.1 Interaction between bulk plasma and walls

When plasma touches a wall, a boundary called sheath is formed between the wall and plasma, and the total amount of electron current flowing to walls becomes equal to ion current so that plasma can ensure quasi-neutrality [4].

In general, positive charges remain in bulk plasma, and make the potential higher than the wall potential by forming an ion sheath at the edges because of small inertia of an electron. In this way, the total electron current balances an ion current flowing toward the walls.

For plasma between two walls, the bulk plasma potential approaches to that of the wall where electrons can flow easily, i.e. a positively biased wall, and ion sheaths are usually formed at the both sides of walls.

However, if the electron current is limited in some situations, for example, the positively biased wall is small and/or the wall is distant from the plasma core, the plasma potential becomes lower than that of the wall and forms an electron sheath. When the loss areas of ions and the electrons are different, the existence of an electron sheath is provided around the condition of Eq. (1) [6].

$$\frac{A_\mathrm{i}}{A_\mathrm{e}} \gtrapprox \sqrt{\frac{m_\mathrm{i}}{m_\mathrm{e}}} \tag{1}$$

### 2.2 Space charge limited current

One-dimensional space charge limited current when charged particles are emitted with zero velocity is obtained by solving Poisson's equation

$$\frac{\mathrm{d}^2\phi}{\mathrm{d}x^2} = -\frac{\rho}{\varepsilon_0} \tag{2}$$

with a boundary condition

$$V = 0 \text{ and } \mathrm{d}V/\mathrm{d}x = 0 \text{ at } x = 0,$$
$$V = V_0 \text{ at } x = a. \tag{3}$$

Then, the following Child equation is derived.

$$J = 4\varepsilon_0/9\sqrt{2em}{V_0}^{3/2}/a^2 = \chi {V_0}^{3/2}/a^2 \tag{4}$$

where $\rho$ is charge density and $\chi$ is a constant number.

When the condition $\mathrm{d}V/\mathrm{d}x = 0$ at the emitter is retained, but in which the emitted particles are all given in an initial velocity $v_0$

$$V = V_0 = m{v_0}^2/2e \text{ at } x = 0, \tag{5}$$

we obtain the relation between potential $V$ at distance $x$ and current density $J$ from Eq. (2).

$$(\sqrt{V/V_0} - 1)^{1/2}(\sqrt{V/V_0} + 2){V_0}^{3/4}$$
$$= (3x/2)(m/2e)^{1/4}(J/\varepsilon_0)^{1/2} \tag{6}$$

Figure 1 shows the schematic diagram of a spatial potential profile between a grid and an ion collector. When plasma with a negative potential relative to the grid reaches the grid, electrons are turned away, and an ion sheath is formed in front of the grid.

On the other hand, ions are accelerated, and they pass though the grid. Thus, three types of potential profiles shown in Fig. 1 can be formed between the grid and the ion collector which is placed at $x = a$.

In Case 1, potential gradient is negative at $x = 0$, and all ions with initial velocity are accelerated through the path.

In Case 2, potential has a peak between the two planes, but all the current flows into the ion collector. Potential distributions in both

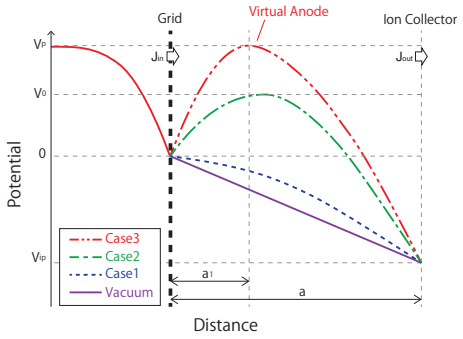


Figure 1: Schematic diagram of a spatial potential profile between a grid and an ion collector.

areas, the left and the right side of the peak, follow Eq. (6). Since the current in these two areas is same, we can obtain the maximal value and the position from a given injected current.

In Case 3, the maximum potential reaches plasma potential $V_{\mathrm{p}}$. The maximum acts as a virtual emission-limited anode emitter, and reflects the portion of the current. Both boundaries of two areas separated at the virtual emitter are equal to the boundary condition (3). Since Poisson's equation is about the distribution of charges, the sum of the absolute value of injected current and reflected current is equal to space charge limited current even though opposing current flows in the left area of the virtual anode. In the result, current in both areas is space charge limited, and can be solved by using two equations given by the Child equation (4), where transmission of a current is $J_{\mathrm{out}} = \alpha J_{\mathrm{in}}$, $0 < \alpha < 1$.

$$\begin{cases} J_{\mathrm{in}} + (1-\alpha)J_{\mathrm{in}} = \chi V_{\mathrm{p}}^{3/2}/{a_1}^2 \\ J_{\mathrm{out}} = \alpha J_{\mathrm{in}} = \chi (V_{\mathrm{p}} - V_{\mathrm{ip}})^{3/2}/(a-a_1)^2 \end{cases} \tag{7}$$

Now we think that ions with an ion current density signal shown in Fig. 2(a) is injected from the left side of the grid as shown by $J_{\mathrm{in}}$ in Fig. 1. The current is assumed to be one-dimensional and static, and transition time is

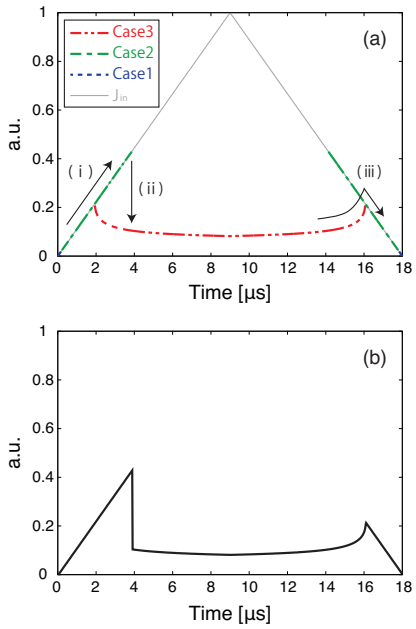


Figure 2: (a) Injected current density $J_{\mathrm{in}}$ and transitions of emission current density $J_{\mathrm{out}}$, (b) Emission current density $J_{\mathrm{out}}$.

neglected for simplicity. The potential between the two planes changes depending on the time change of injected current density $J_{\mathrm{in}}$ as below.

i. While the injected current increases, the potential profile between the grid and the ion collector transits from Case 1 to Case 2. The peak of the potential appears in Case 2, and its value $V_0$ will increase until a maximum value called $V_{\mathrm{m}}$ .

ii. When $V_0$ is near $V_{\mathrm{m}}$, the current is in bistable condition, where the potential profile can take either of Case 2 and Case3. The profile transits from Case 2 to Case 3 when the current reaches the maximum of Case 2. Note that ion current $J_{\mathrm{out}}$ which is collected at the ion collector in Case 3 is less than the maximum of $J_{\mathrm{out}}$ in Case 2. If the injected current $J_{\mathrm{in}}$ then decreased, the distance of virtual anode from the grid $a_1$ shifts toward the

ion collector and the transmitted current $J_{\text{out}}$ will increase.

iii. For the further decrease of $J_{\text{in}}$, the current becomes bistable condition again. The potential profile transits from Case 3 to Case 2 when reflection of the current is ceased, or the operation mode goes back to just before it happens.

As shown above, the potential transforms from Case 1 → Case 2 → Case 3 → Case 2 → Case 1, and the current has a bistable solution when the transition between Case 2 and Case 3 occurs. The signal of current density $J_{\text{out}}$ observed at the ion current is predicted to be like Fig. 2(b).

## 3 Experimental setup

Figure 3 illustrates the schematic drawing of the apparatus. A copper target inside a vacuum chamber was irradiated with a KrF excimer laser ($\lambda = 248$nm) at an incident angle of $70^\circ$. The irradiation power density was $10^8 \sim 10^9$ W/cm$^2$ and the pressure inside the chamber was $10^{-4}$ Pa. Plasma made by the laser ablation drifts toward electrodes while expanding. A tantalum aperture with a diameter of 2 mm was placed in front of the target to limit the angle of plasma so that the plasma doesn't touch electrodes.

The cross-sectional diagram of external electrode is shown in Fig. 4. 4 mm-thick, 32 mm inner diameter ring electrodes and ring insulators were lined up alternately. Electrodes can change external electric field which interacts with the drifting plasma. A voltage in the range of $0 \sim +1$ kV was applied to the electrodes. Langmuir probe was inserted 20 mm before the grid, between 4th and 5th electrodes from the target on a cylindrical axis. The

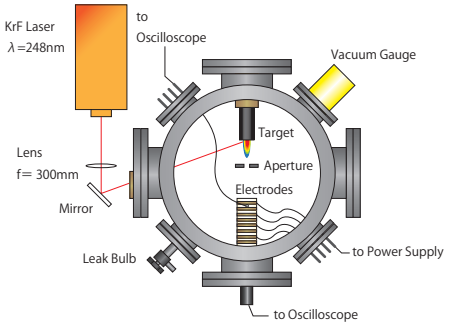


Figure 3: Schematic drawing of the experimental apparatus.

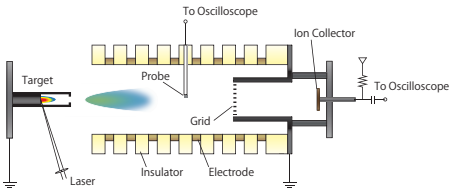


Figure 4: Cross-sectional diagram of electrodes.

probe can measure the plasma potential via a high voltage probe with the input impedance of 100 MΩ.

A 100 mesh grid was placed 81 mm from the target at a side of grounded thimble on the downstream side of the electrodes. An ion collector was biased at -100 V to measure an ion current signal and its distance from the grid $a$ can be changed.

When the plasma potential was measured, the voltage was applied to six electrodes on the left side in Fig. 4. When an ion current was measured, it was applied to the very left side of the electrode which was placed 24 mm from the target. From now, we call the voltage applied electrode "control electrode". The other electrodes were grounded.

## 4 Results and Discussions

### 4.1 controlling the plasma potential

Figure 5 shows the time evolution of plasma potential when a DC voltage was applied to the control electrodes up to +1 kV. We can see that the plasma potential had more than 80 percent of the control electrodes' potential.

The plasma potential becomes close to the potential of the wall where electrons are easy to escape. We consider that the plasma potential rises when the plasma plume is detached from the grounded target and electrons become easier to escape toward the control electrodes.

Once the plasma potential has been raised, electrons can not escape to the grounded grid. When the plume reaches the grid, an ion sheath is formed in front of the grid. At this time, all ions escaping from the plasma core go to the grid and the ion collector, while all electrons escaping from the plasma core go to the control electrodes. We think that the electron sheath and the ion sheath balanced the total electron current and the ion current flowing toward walls, which determined and maintained the plasma potential as shown in Fig. 5.

Note that the plasma potential might not be measured correctly at the beginning of the signal due to dilute plasma at that time.

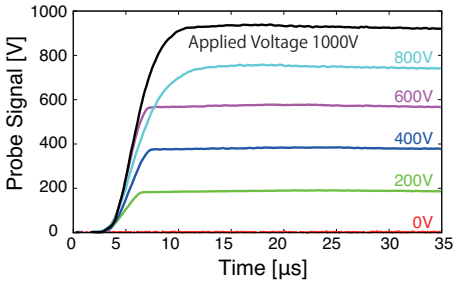


Figure 5: Time evolution of plasma potential when a positive voltage is applied to the control electrodes.

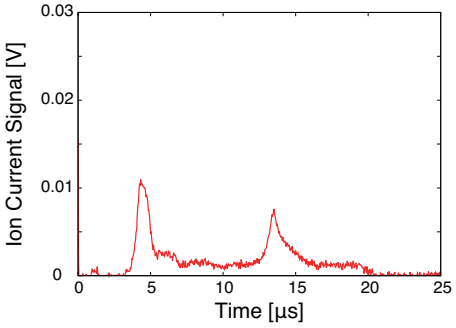


Figure 6: The ion current signal when 80 V is applied to the control electrode ($a$ =29.5 mm).

### 4.2 Extraction of ions from plasma

Figure 6 shows the typical ion current signal measured with the ion collector when a positive voltage was applied to the control electrode. Peaks were formed at the beginning and the end of the signal, and the current was suppressed between these two peaks. The second peak is needed to be examined more as we discuss later.

Next, we changed the distance of the ion collector from the grid $a$, and the voltage applied to the grid under the condition of higher laser irradiation power density. Figure 7 shows the ion current signal when the applied voltage was changed with distance $a$ fixed to 10 mm. In this high plasma flux condition, we can see that Case 3 dominated over Case 2. A flat part appeared in the signal and the value seemed to be gained with the increase of the applied voltage. Here we know that only ions reached the ion collector because the current signal was not changed even though a positive voltage 31.7 V was applied to the ion collector.

Figure 8 shows the ion current signal when the distance $a$ was changed and the applied voltage was fixed to 300 V. We can see that the current was gained with the decrease of distance $a$ from Fig. 8(a). Furthermore,the

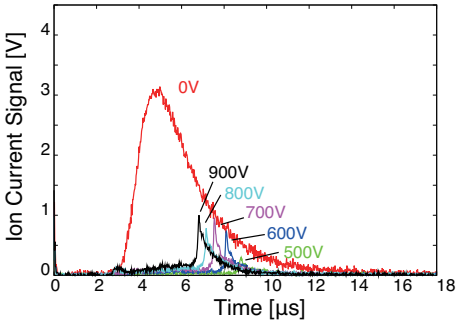


Figure 7: Ion current signals when a positive voltage is applied to the control electrode ($a$ =10 mm).

minima of the flat part of the signal fitted a $a^{-2}$ scaling as shown in Fig. 8(b).

Because the flat part of the signal was gained with the increase of the applied voltage and was inversely proportional to the square of distance $a$, we can say that the formation of a virtual anode is the reason why the flat part was shown. Furthermore, the virtual anode was formed during the increase of injected current and collapsed during the decrease of injected current as seen in Figs. 6 $\sim$ 8. However, the right peak of the the ion current signal has a rapid rise although it has to be Case 3, in which the virtual anode is still to be formed. At this time, almost all current is reflected at the virtual anode because of the large injected current. This dynamics of the injected current might be the cause of this early collapse. Further investigation is needed to clarify the reasons why the virtual anode collapsed early and the current was decreased after the right peak.

From the results above, the potential profile of plasma while ions were extracted in this apparatus is assumed to be like Fig. 9. An electron sheath was formed in front of the electrode where the positive voltage was applied, and plasma with positive potential formed an

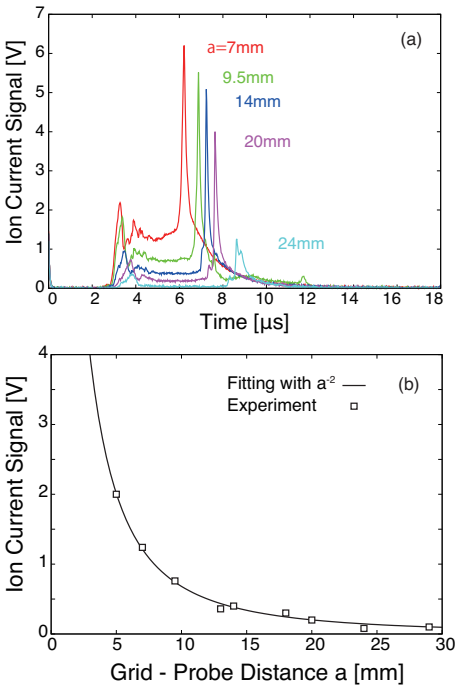


(a) Ion current signals at $a$ = 7 $\sim$ 24mm when 300 V is applied to the control electrode
(b) Ion current signal follows $a^{-2}$ rule

Figure 8: Relation between Ion current and distance $a$.

ion sheath in front of the grid. Then after the extraction of ions at the grid, a virtual anode was formed between the grid and the ion collector.

## 5 Conclusion

We succeeded in controlling the potential of laser ablation plasma up to order of kV. This was obtained by placing ring external electrodes away from plasma plume boundary so that the plasma could form an electron

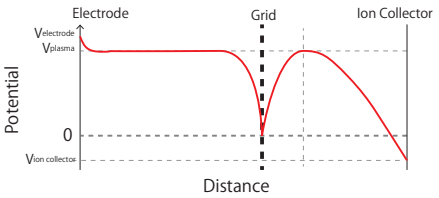


Figure 9: Schematic diagram of the spatial profile of the plasma and ion potential at the whole apparatus.

sheath in front of the electrodes. When the plasma reached a grounded grid, an ion sheath was formed in front of it besides the electron sheath.

One of the advantages this device has is that it can control the plasma potential easily because of the steady formation of an electron sheath. Since the mass of electrons is much smaller than that of ions, we could raise the plasma potential even though there is a distance between plasma and electrodes. This distance makes this device durable for a destructive electric discharge. Another advantage is that this potential controlled plasma is unlikely to be affected by the discharge for the plasma production because the time scale for the laser irradiation is much shorter than the plasma drifting and adiabatic expansion time. We think that this simple and calm device would become useful for the research of sheath dynamics.

Using this device, we observed the formation of a virtual anode. We found that the virtual anode was collapsed during the decrease of injected current, and the timing was dependent on a reflected current growth.

Also, it became clear that we can obtain flat ion current when the virtual anode is formed. By utilizing this potential raising method, we expect that a new type of ion beam extraction will become possible as a replacement of grid controlled ion extraction [3] in which a destructive electric discharge is likely to happen. The challenges for the future would be the further investigation of beam physics using potential controlled plasma source, including the dynamical behavior of unstable virtual anode.

## References


[1] Frederick P. Boody, Reinhard Hpfl, Heinrich Hora and Jak C. Kelly, Laser and Particle Beams, **14**, 443-448 (1995).

[2] P. R. Willmott and J. R. Huber, Reviews of Modern Physics, **72**, 315-328 (2000).

[3] S. Humphries, C. Burkhart, S. Coffey, G. Cooper, K. Len, M. Savage and D. M. Woodall, Journal of Applied Physics, **59**, 1790-1798 (1986).

[4] H. M. Mott-Smith and Irving Langmuir, Physical Review, **28**, 727-763 (1926).

[5] J. Loizu, J. Dominski, P. Ricci and C. Theiler, Physics of Plasmas, **19**, 083507, 1-7 (2012).

[6] Noah Hershkowitz, Physics of Plasmas, **12**, 055502, 1-11 (2005).

[7] A. Theodore Forrester, "Large ion beams: fundamentals of generation and propagation", 5-22, Wiley, California (1988).

# Wobbling-Beam Illumination Nonuniformity in Heavy Ion Inertial Fusion

Kenta Noguchi, Tatsuya Kurosaki, Tomohiro Suzuki, Shunsuke Koseki, Daisuke Barada
Shigeo Kawata, Yan Yun Ma, Alexander Ivanov Ogoyski*

*Utsunomiya University, Japan*

**Verna Technical University, Bulgaria*

## ABSTRACT

In an actual inertial fusion reactor, a fuel target alignment error may happen; the target alignment error induces heavy ion beam illumination non-uniformity on the target. The beam illumination non-uniformity leads a degradation of fusion energy output. On the other hand, heavy ion beam accelerator provides a capability to oscillate beam axis with a high frequency. The wobbling beams may provide a new method to reduce or smooth the beam illumination non-uniformity. In this paper, we focus on the wobbler illumination non-uniformity onto a spherical target. We found that the tolerable displacement of the target illuminated by the wobbling ion beams is about 80~90μm in a fusion reactor.

## Keywords

Inertial fusion, heavy ion beam, illumination non-uniformity

## 1. Introduction

In direct drive method[1], laser or ion beam is used as an energy driver. Laser excels in propagation and focusing, laser energy absorption would be complicated, and laser energy absorption efficiency would be low, because the energy is absorbed at the surface of the fuel target. On the other hand, the ion beam generation and absorption efficiencies are high; heavy ion beam (HIB) deposits its energy inside of the fuel target. HIB has also other preferable characteristics of the stabile and repetitive operation of HIB accelerator and also of a precise beam axis control as well as its high efficiency (~30-40 %) of HIB generation. Therefore, it is considered that HIB would be a promising candidate of an energy driver in inertial fusion[2-5]. In this study, we employ Pb HIBs as the energy driver in order to study the beam illumination non-uniformity onto a spherical target.

In an actual inertial confinement fusion (ICF), a fuel target is irradiated by HIBs, when a fuel target is injected and aligned at the center of the fusion reactor[6]. A fuel target alignment error may happen; the target alignment error induces HIBs illumination non-uniformity on the target. The beam illumination non-uniformity leads a degradation of fusion energy output. The illumination non-uniformity allowed is less than a few percent in inertial fusion target implosion[7-10].

The HIB accelerator also has a unique feature of the HIB axis wobbling capability; The HIB axis can be oscillated or rotated with a high frequency[11]. On the other hand, the wobbling HIBs may smooth or

mitigate the fuel target implosion non-uniformity[12]. In this study, we examine the wobbling-HIBs illumination non-uniformity on a direct drive fuel target, including the fuel target alignment error from the reactor center. As a result, we found that the tolerable displacement of the target illuminated by the wobbling ion beams is about 80~90μm in a fusion reactor.

## 2. Wobbling Beam

The HIBs illumination non-uniformity causes also the growth of Rayleigh-Taylor instability; the non-uniformity of the target implosion may prevent the fuel ignition, and causes a degradation of the fusion energy output. Therefore, it is important to reduce the instability growth and the target implosion non-uniformity.

So far, we have found that the growth of the Rayleigh-Taylor instability is mitigated well by a continuously vibrating non-uniform acceleration field with a small amplitude compared with that of the averaged acceleration[12]. The oscillating non-uniform acceleration field would be obtained by the HIBs axes oscillation[2, 11]. We used the wobbling beam as the irradiation beams. Figure 1 shows a schematic diagram for the wobbling beam. The wobbling HIBs rotate around the illumination axis as shown in Fig. 1. The rotating HIBs may provide the oscillating acceleration field with a small amplitude, and contribute to mitigate the instability growth and consequently the HIBs illumination non-uniformity. In this study, we employs the 32 wobbling HIBs to deposits their energy onto a spherical direct drive target, shown in Fig. 2.

## 3. HIB Illumination Non-uniformity

In this study, we employ lead ($Pb^+$) ion HIBs with the mean energy 8GeV. The HIB temperature is 100MeV and the HIB transverse distribution is the Gaussian profile. The beam radius at the entrance of a fusion reactor is 35mm and radius of a fusion reactor

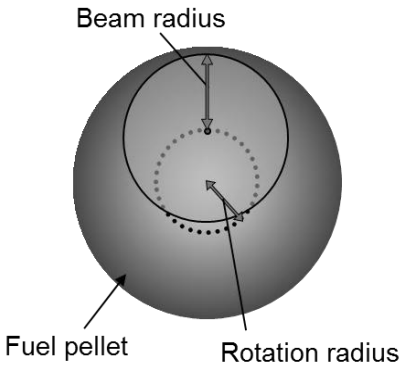


Fig. 1 Schematic diagram for Wobbling beam

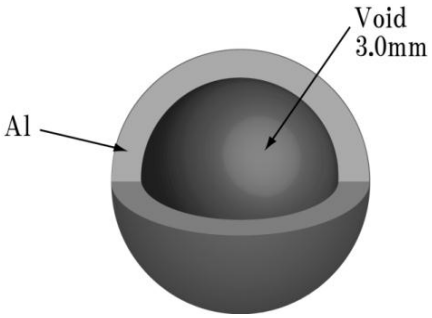


Fig. 2 Target model

is 3m. Figure 2 shows the target model used in this paper. The target has a single layer structure of aluminum (Al) and its outer radius is 4.0mm.

In this study, we employ the 32 HIBs. Table 1 shows the arrangement of the 32 HIBs irradiation.

We used the Root mean square (*RMS*) as an evaluation method of the HIBs illumination non-uniformity. The formula is shown below:

$$\langle \sigma_{rms} \rangle = \sum_i w_i \sigma_i^{rms}, w_i = \frac{E_i^{Total}}{E_{Total}}$$

$$\sigma_i^{rms} = \frac{1}{\langle E \rangle_i} \sqrt{\frac{\sum_j \sum_k \left( \langle E \rangle_i - E_{i,j,k} \right)^2}{J_{mash} K_{mesh}}}$$

Here, $\langle \sigma_{rms} \rangle$ is the global rms non-uniformity, $\sigma_i^{rms}$ is the rms non-uniformity on the $i$-th surface of deposition, $w_i$ is the weight function, $J_{mesh}$ and $K_{mesh}$ are mesh numbers in $\theta$ and $\phi$ directions, $\langle E \rangle_i$ is the averaged energy deposited in each surface layer, $E_i^{Total}$ is the total deposition energy in each surface layer, and $E_{Total}$ is the total deposition

Table 1 Arrangement of the 32 HIBs irradiation

| No. | $\theta$ [deg] | $\phi$ [deg] | No. | $\theta$ [deg] | $\phi$ [deg] |
|---|---|---|---|---|---|
| 1 | 0.00 | 0.000 | 17 | 100.812 | 36.000 |
| 2 | 37.377 | 0.000 | 18 | 100.812 | 108.000 |
| 3 | 37.377 | 72.000 | 19 | 100.812 | 180.000 |
| 4 | 37.377 | 144.000 | 20 | 100.812 | 252.000 |
| 5 | 37.377 | 216.000 | 21 | 100.812 | 324.000 |
| 6 | 37.377 | 288.000 | 22 | 116.565 | 0.000 |
| 7 | 63.435 | 36.000 | 23 | 116.565 | 72.000 |
| 8 | 63.435 | 108.000 | 24 | 116.565 | 144.000 |
| 9 | 63.435 | 180.000 | 25 | 116.565 | 216.000 |
| 10 | 63.435 | 252.000 | 26 | 116.565 | 288.000 |
| 11 | 63.435 | 324.000 | 27 | 142.623 | 36.000 |
| 12 | 79.188 | 0.000 | 28 | 142.623 | 108.000 |
| 13 | 79.188 | 72.000 | 29 | 142.623 | 180.000 |
| 14 | 79.188 | 144.000 | 30 | 142.623 | 252.000 |
| 15 | 79.188 | 216.000 | 31 | 142.623 | 324.000 |
| 16 | 79.188 | 288.000 | 32 | 180.000 | 0.000 |

energy. In this study, one HIB is divided into many beamlets and the precise energy deposition is computed in the three dimensions[7, 14-17].

We also perform a spectral analysis by the spherical harmonics.

$$s_n^m = \frac{1}{4\pi}\int_0^{\pi} d\theta \int_0^{2\pi} d\phi \sin\theta E(\theta,\phi) Y_n^m(\theta,\phi)$$

Here, $s_n^m$ is an amplitude of energy spectrum, $E(\theta,\phi)$ is the HIB deposition energy at each mesh point of a target, $Y_n^m(\theta,\phi)$ is the spherical harmonic function, and $(n,m)$ shows the mode number.

## 4. Robust HIB Illumination

### 4.1 Irradiation of Spiral Wobbling HIBs

First we found that the HIBs illumination non-uniformity at the beginning of the wobbling HIBs irradiation. We then found that the initial imprint is reduced by spiral wobbling beams (see Fig. 3). Figure 4 shows the illumination non-uniformity history during the first few rotations. $\tau_{wb}$ is the time for one rotation of the wobbling beam axis. The non-spiral wobbling beam has the beam radius of 2.0mm and beam rotation radius of 3.0mm. For the spiral wobbling beam the beam radius changes from 3.1mm

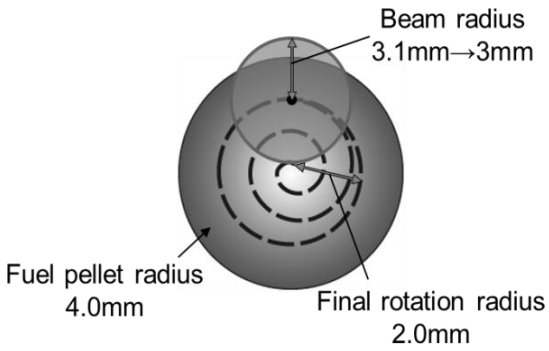


Fig. 3 Schematic diagram for spiral Wobbling beam

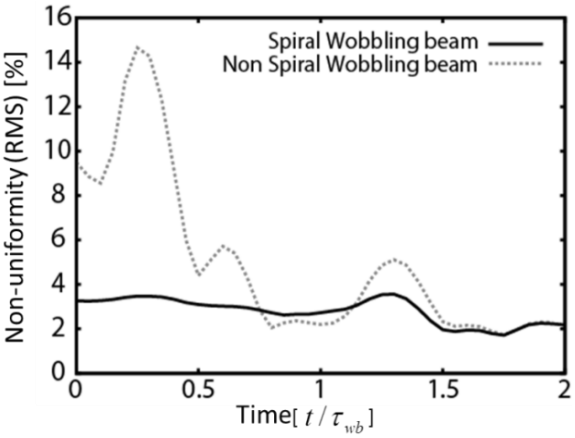


Fig. 4 Histories of the illumination non-uniformity

to 3.0mm at $t = 1.3\tau_{wb}$. As shown in Fig. 4, the initial imprint of the non-uniformity at the beginning of the irradiation is greatly reduced. In this study, we employ the Spiral wobbling beam for the HIBs illumination non-uniformity study.

### 4.2 Spiral wobbling HIBs illumination non-uniformity

As shown in Fig. 5, $dx, dy$ and $dz$ are the fuel target displacements in the $x, y$ and $z$-axis directions from the reactor center. The displacement of $\sqrt{dx^2+dy^2+dz^2}$ is also examined. Figure 6 shows the maximum illumination non-uniformity vs. the fuel target displacement. The illumination non-uniformity increases with the increase in the displacements. When the allowable maximum illumination non-uniformity is set to be less than 4.5%, the allowable $dz$ is about 80~90μm.

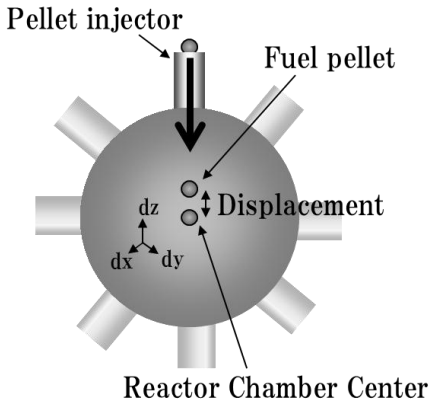


Fig. 5 Target alignment error in a reactor

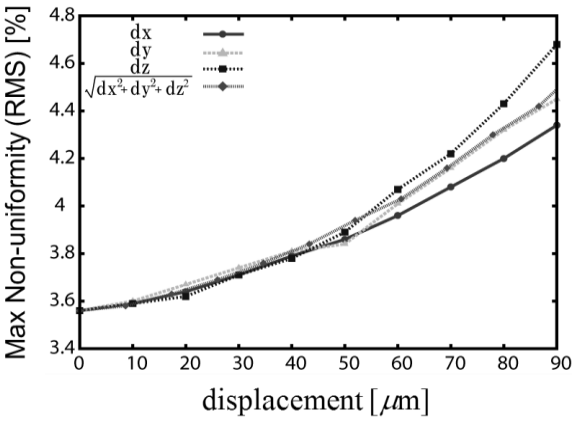


Fig. 6 Maximal non-uniformity vs. pellet displacement

Next, we examine the maximum illumination non-uniformity at the steady state after the 10 beam rotations. The HIB main pulse duration 10~20 nsec and the pre-pulse should also have the similar time duration. So the HIBs would wobble in 10 times or more. Figure 7 shows the maximum non-uniformity vs. pellet the displacement at $t = 10\tau_{wb}$. The non-uniformity becomes less than about 3~4% at the target displacement of 80~90μm.

We also examine the HIBs illumination energy loss. Figure 8 shows the illumination energy loss vs. the pellet displacement. The HIB has a finite beam radius, and some part of HIBs ion particles do not hit the target, when the target misalignment displacement becomes large. The energy loss is about 11% $t = 10\tau_{wb}$, even when the displacement becomes 80~90μm. The energy loss by the beam mishitting

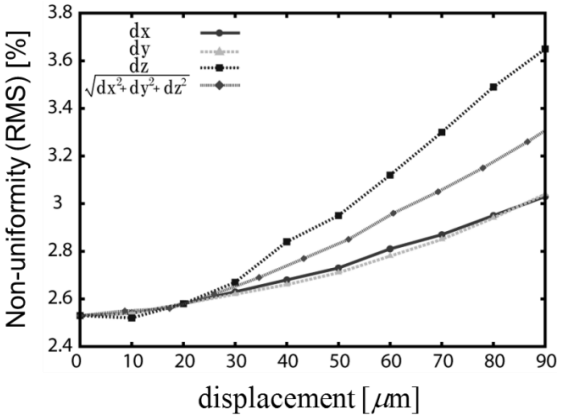


Fig. 7 non-uniformity vs. pellet displacement

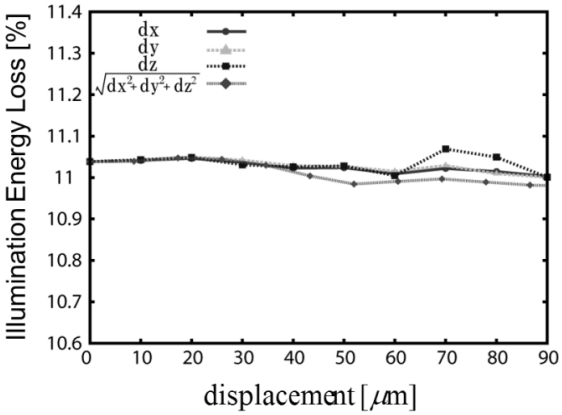


Fig. 8 Illumination energy loss vs. pellet displacement

would be acceptable in ICF.

### 4.3 Optimization of HIBs irradiation scheme

In this sub section, we describe the optimization of the irradiation angles of the beams to the target fuel. Figure 9 shows the schematic diagram of the definition of the angle deviation $\Delta\theta$ from the irradiation arrangement in Table 1. The irradiation arrangement of the HIBs is divided into the upper three layers and lower three layers. We change the angle of $\Delta\theta_1, \Delta\theta_2$ and $\Delta\theta_3$as shown in Fig. 9. We found that the non-uniformity is reduced well, when $\Delta\theta_1 = 0.0$ , $\Delta\theta_2 = 0.2$ , $\Delta\theta_3 = 0.4$ [deg]. Figure 10 shows the maximum non-uniformity for the displacement $dz$ . By optimizing the beam illumination scheme, the HIBs illumination non-uniformity is reduced further.

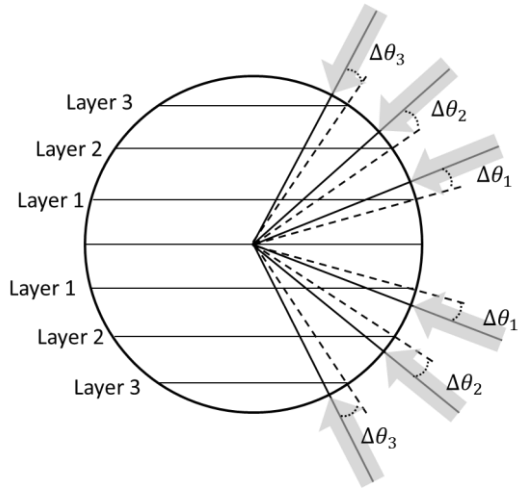


Fig. 9 Schematic diagram for the definition of $\Delta\theta$

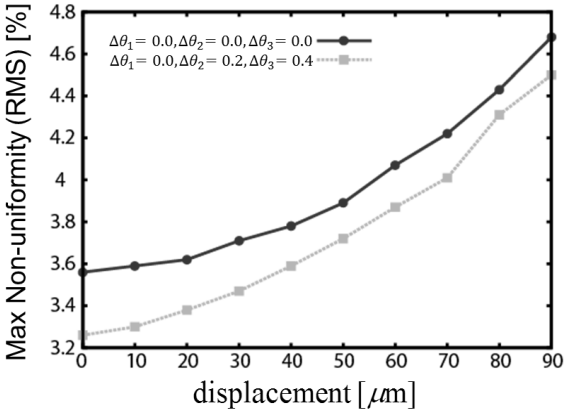


Fig. 10 Maximal non-uniformity vs. pellet displacement

### 4.4 Spectral evaluation

Next, we evaluate the spectrum in order to analyze the vibration of illumination non-uniformity. Figure 11 shows the histories of the illumination non-uniformity at $dz = 90\mu\text{m}$. At this time, we decompose the illumination non-uniformity by the spherical harmonic spectral using the deposition energy distribution. Figure 12 shows the amplitude histories of the spherical harmonic spectrum. Figure 12 shows the spectrum mode $(n, m) = (2, 0)$. From Fig. 12, it is confirmed that the maximum value of the amplitude is reduced by the optimizing the irradiation scheme. Figure 13 presents the spectrum of the mode $(2, 0)$ amplitude in its frequency space. $f_{wb}$ shows the wobbling HIBs rotation frequency. We confirmed the vibration frequency synchronized

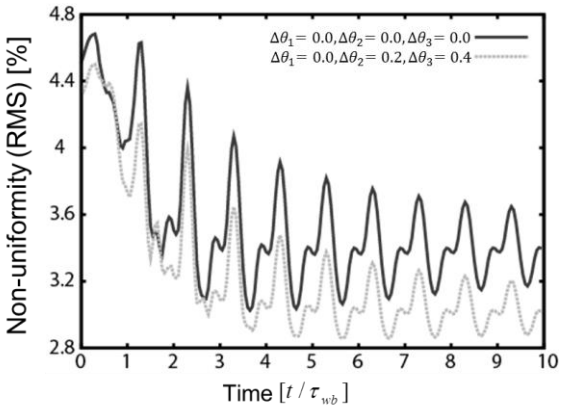


Fig. 11 Histories of the illumination non-uniformity

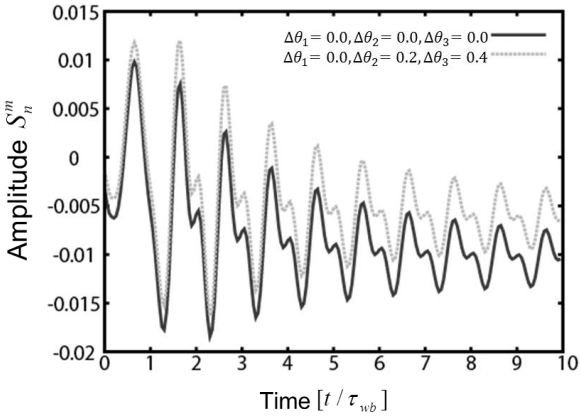


Fig. 12 Histories of the Spherical harmonic spectrum

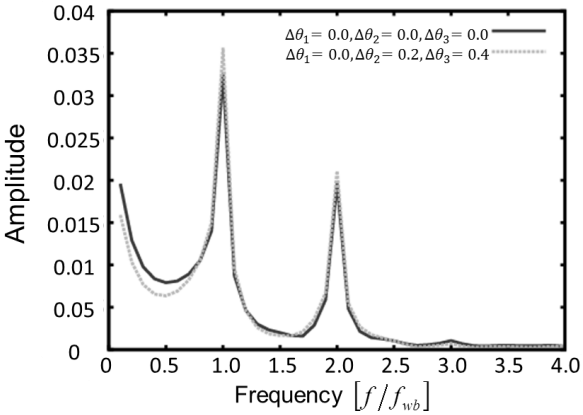


Fig. 13 Frequency spectrum

well with the wobbling frequency of the illumination beam.

## 5. Conclusions

In this study, we examined the wobbling HIBs illumination non-uniformity on the fuel. The target

alignment error leads the increase in the illumination non-uniformity. The tolerable displacement of the target illuminated by the spiral wobbling beams is about 80∼90 μm. The illumination energy loss is not serious in ICF. In addition, by optimizing the beam irradiation scheme, the illumination non-uniformity is reduced further. We confirmed that the frequency spectrum is synchronized with the rotation frequency of the wobbling beams. The results would confirm that the wobbling HIBs illumination induce the oscillating acceleration field continuously, which may reduce the growth of Rayleigh-Taylor instability.

## Acknowledgements

This work is partly supported by Grant-in-Aid for Scientific Research in MEXT and JSPS, CORE (Center for Optical Research and Education, Utsunomiya university), NIFS and ILE/Osaka University.

## References

[1] B. G. LOGAN, et al., "Direct drive heavy-ion-beam inertial fusion at high coupling efficiency", *Phys. Plasmas*, **15**, 072701 (2008).
[2] M. M. BASKO, et al., "On the symmetry of cylindrical implosions driven by a rotating beam of fast ions", *Phys. Plasmas*, **11**, 1577 (2004).
[3] S. MIYAMOTO, et al., "Experimental Technique for Beam-Target Interaction : Heavy Ion Beam-Target Interaction", *J. Plasma Fusion Res.*, **71**, 951 (1995).
[4] R. C. ARNOLD et al., "Inertial confinement fusion driven by heavy-ion beams", *Rep. Prog. Phys.*, **50**, 559 (1987).
[5] J. D. LINDLE, "Development of the indirect-drive approach to inertial confinement fusion and the target physics basis for ignition and gain", *Phys. Plasmas*, **2**, 3933 (1995).
[6] R. W. PETZOLDT, "IFE Target Injection and Tracking Experiment", *Fusion Technol*., **34**, 831 (1998).
[7] S. MIYAZAWA, et al., "Robust heavy-ion-beam illumination against a direct-drive-pellet displacement in inertial confinement fusion", *Phys. Plasmas*, **12**, 122702 (2005).
[8] S. KAWATA, et al., "Effect of nonuniform implosion of target on fusion parameters", *J. Phys. Soc. Jpn.*, **53**, 3416 (1984).
[9] J. SASAKI, et al., "Beam non-uniformity smoothing using density valley formed by heavy ion beam deposition in inertial confinement fusion fuel pellet", *Jpn. J. Apple. Phys.*, **40**, 968 (2001).
[10] S. KAWATA, et al., "Robust fuel target in heavy ion inertial fusion", *Nuccl. Instr. And Meth. A*, **606** (2009).
[11] H. QIN, et al., "Centroid and envelope dynamics of charged particle beams in an oscillating wobbler and external focusing lattice for heavy ion fusion applications", *Laser Part. Beams*, **29**, 365-372 (2011).
[12] S. KAWATA, "Dynamic mitigation of instabilities", Phys. Plasma, **19**, 024503 (2012).
[13] H. QIN, et al., "Centroid and Envelope Dynamics of High-Intensity Chargeed-Particle Beams in an External Focusing Lattice and Oscillating Wobbler", *Phys. Rev. Lett.*, **104**. 254801 (2010).
[14] A. I. OGOYSKI, et al., "Code OK2—A simulation code of ion-beam illumination on an arbitrary shape and structure target", *Compt. Phys. Commun.*, **161**, 143 (2004).
[15] A. I. OGOYSKI, et al., "Code OK3 – An upgraded version of OK2 with beam wobbling function", *Compt, Phys. Commun*., **181**, 1332 (2010).
[16] A. I. OGOYSKI, et al., "Heavy ion beam irradiation non-uniformity in inertial fusion", *Phys. Lett. A*, **315**, 372 (2003).
[17] T. SOMEYA, et al., "Heavy-ion beam illumination on a direct-driven pellet in heavy-ion inertial fusion", *Phys. Rev. ST Accel. Beams*, **7**, 044701 (2004).

# Study on the dynamics during longitudinal compression of intense charged particle beams with a compact simulator

Yasuo Sakai, Mitsuo Nakajima, Jun Hasegawa, Takashi Kikuchi*, Kazuhiko Horioka

*Department of Energy Sciences, Tokyo Institute of Technology*

**Department of Nuclear System Safety Engineering, Nagaoka University of Technology*

## ABSTRACT

Longitudinal bunching is one of the critical techniques to achieve high-power charged particle beams. To investigate the compression process of intense beams, we constructed a compact simulator device composed of an electron gun, an induction modulator, and a solenoidal transport line. We conducted bunching experiment in a parameter region with electron particle density $1.6\times10^6$ /cm$^3$ to $3.1\times10^7$ /cm$^3$ at maximum compression. The results compared by 1D electrostatic Particle-In-Cell simulations. Through experimental results and numerical simulations, we confirmed the device is ready to discuss the bunching dynamics. In addition, we numerically extrapolated the beam bunching to the higher current. The results revealed our device has potential to discuss a dissipation process of charged particle beams during longitudinal compression.

## Keywords

Bunch Compression, Intense Charged Particle Beams, Emittance Growth, Induction Accelerators

## 1. Introduction

For reasons of controllable and uniform target heating, particle beams are expected to be potential drivers for high energy density science [1, 2]. In these researches and applications, for higher specific energy deposition to the target, heavy ion beams with high current, defined particle energy and short pulse length are required. Then, the technology to compress a beam bunch in longitudinal direction is crucially important. Especially, for application in heavy ion fusion, to increase the beam power up to TW level, a process of abrupt longitudinal compression at the final stage of accelerator is essential [3, 4]. However, in this stage, non-adiabatic process induced by space-charge field may degrade the beam quality [5].

In general, space-charge effects induce not only a dissipation of particle energy but a coupling between transverse and longitudinal motions in intense beams also [6]. In such a condition, the space-charge drives beam collective motions [7, 8]. If the beam is manipulated non-linearly and/or rapidly, that induces spatial non-uniformity. Then, a local disturbance propagates into the beam, e.g., as a space-charge wave [9], to relax toward a final uniform state. In this process, conversion of space-charge potential energy into random kinetic energy occurs, with leading a degradation of the beam quality [8, 10, 11].

To understand the mechanism and the emittance growth of intense beams, some groups are investigating the beam dynamics by using a simulator device with electron beams and Paul trap. These researches experimentally confirmed emittance growth during transport of the inhomogeneous beams in periodic focusing line [12], and due both

to rapid non-adiabatic compression in transverse direction [13].

During the final bunching process, the beam is applied modulation voltage to induce the longitudinal velocity tilt. The modulation voltage is up to tenth percent of beam accelerating voltage. If this huge energy is in-coherent, it may dissipate with collective motions, and degrade the beam quality seriously and disturb compression significantly. To achieve a required beam power, it is important to evaluate the degree of degradation of the beam quality during the longitudinal modulation.

To investigate the beam dynamics and dissipation process during the rapid longitudinal compression, we proposed an experiment with compact and flexible bunching simulator device based on electron beams and a stacked induction-adder system. Because of its small inertia, electron can be easy to manipulate by low voltage. In fact, when an electron beam is accelerated by kV levels, it corresponds to heavy ion beams with GeV level in velocity. In addition, because of large specific charge, electrons are easily affected by the space-charge field in its dynamics. From these characteristics, we can expect to conduct a scaled experiment for kA, GeV level heavy ion beam bunching by using mA, keV level electron beams, with a compact device.

Up to now, we constructed a prototype device and have investigated the effects of initial beam spread on the bunching dynamics [14]. In this paper, we show recent results of longitudinal beam compression experiments.

## 2. Experimental Setup

Figure 1 shows a schematic diagram of longitudinal compression experiment. Our device consists of a hot cathode electron gun, an induction voltage adder, a transport line and a Faraday cup (FC). In the experiment, we compress a beam with pulse duration of 100 ns from continuously extracted with an energy of 2.8 keV. First, the extracted beam was injected to an induction cavity. Next, the beam was applied a modulation voltage of peak voltage -2.5 kV and pulse duration of 100 ns for longitudinal compression. The modulation voltage produces a head-to-tail velocity gradient, referred to here as a "velocity tilt". Then, the beam is one-dimensionally compressed in longitudinal direction during a drift in a solenoidal transport line and finally compressed around 2 m downstream of the modulation gap.

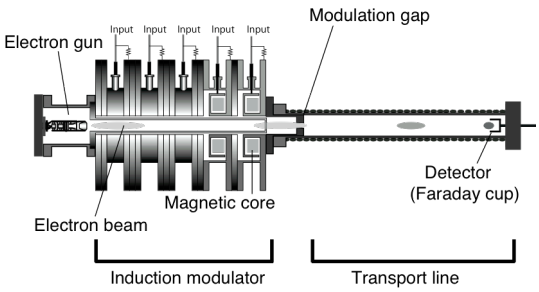


Fig. 1 Schematic diagram of the device for bunching experiment.

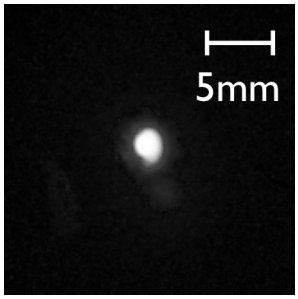


Fig. 2 A fluorescent witness plate image of the beam spot at the entrance of the transport line. The beam spot size is less than 4 mm.

The electron gun can produce continuous beam with the current of about 100 μA at maximum. The beam spot size is estimated to be less than 4 mm by a fluorescent witness plate as shown in Fig. 2. The induction voltage adder is consisting of five driver units (see Fig. 1). Each unit makes a sinusoidal waveform independently and they are synthesized at the modulation gap. By the induction adder configuration, we can apply arbitrarily controlled waveforms for bunch compression. The transport line consists of a stainless tube with

57 mm in diameter and rolled with a solenoidal coil 2 m in length to produce pulsed longitudinal magnetic fields. Maximum magnetic flux density is 42 mT and the pulse duration is a few ms, which is much greater than the time scale of experiment. With this longitudinal fields, the beam transverse motion is limited to be less than 1 mm of Larmor radius at transverse energy of 100 eV. This means we can expect to conduct a one-dimensional compression experiment in longitudinal direction. With this attempts, as will be presented bellow in this paper, our device has a potential to evaluate the dissipation process through the evolution of current waveforms and the behavior of bunched particles on the phase space. The FC consists of cylindrical cup with 20 mm in inner-diameter and 30 mm in depth. As mentioned, the beam spot size was estimated to be less than 4 mm. Since that is smaller than the FC radius and the beam is substantially restricted by the magnetic field, beams are captured with the bottom of the FC. This means there's no time difference of flight times for beam longitudinal slices in the waveform measurements. The FC is connected to a 50 Ω BNC cable with 3 mm length soldering, and the BNC cable is connected to 1GHz oscilloscope. Considering this, the time resolution of the FC measurements can be considered to be ns.

As the modulation voltage for longitudinal compression, we defined the following equation as an ideal voltage waveform to compress the beam bunch into one point at the destination.

$$V(t) = \frac{m_e}{2q_e} \cdot \frac{1}{\left(\sqrt{\frac{m_e}{2q_eV_0}}+\frac{T-t}{L_f}\right)^2} - V_0\,, \qquad (1)$$

where $q_e$ , $m_e$ is charge and mass of the electron respectively. $V_0$ is the extracting voltage of the electron gun, $T$ and $L_f$ are the initial pulse duration of the modulated beam and focus length of bunching from the endpoint of the modulation gap respectively. Eq. (1) was derived by assuming all particles in the beam bunch has no velocity dispersion and no space-charge effects, with in SI unit.

## 3. Results and Discussion

### 3.1 Typical results of the longitudinal compression

Figure 3 shows typical modulation voltage waveforms generated by the induction adder. As shown in Fig. 3, we drove five independent pulsed sinusoidal like voltage (Driver 1 to 5) and synthesized the waveforms into one modulation waveform (black bold line). The designed waveform defined by Eq. (1) (sharp black line) is also shown in the figure. The jitters of the waveform components were estimated to be 0.5% in time and 2% in voltage.

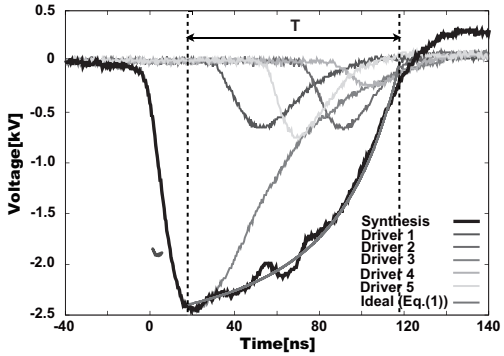


Fig. 3 Typical voltage waveform of induction modulator and modulation voltage for longitudinal compression of e-beam with 2.8 keV by $L_f$ = 2 m

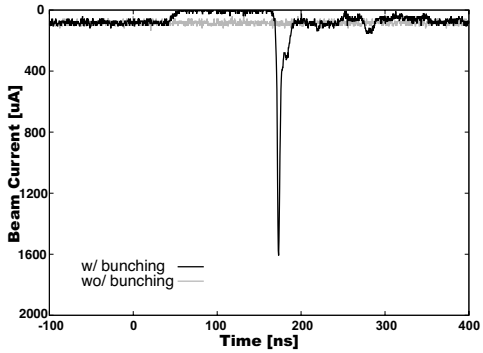


Fig. 4 Typical beam current waveforms with (black) and without (gray) bunching measured at $L$ = 1.94 m. Continuous initial beam of $I_0$ = 84 μA was compressed 19 times of the initial value.

Figure 4 shows typical beam current waveforms with or without bunching. The average current of the continuous beam was estimated to be 84 μA. By applying a modulation voltage of 100 ns to the initial beam (in Fig. 4, referred as wo/ bunching), the beam current was longitudinally compressed as shown by the black line (in Fig. 4, referred as w/bunching). The peak current increased up to $1.6\times10^3$ μA with a peak compression ratio of 19 and a pulse duration (FWHM) of 3.2 ns in this case. Here we defined the compression ratio as a ratio of the bunched beam current to the initial average beam current. This corresponds to a compression process of $1.6\times10^6$ /cm$^3$ to $3.1\times10^7$ /cm$^3$ in number density of the electron.

In a previous paper describing this work [15], the beam parameter was estimated with longitudinal envelope equation [16]. The result indicated that the beam parameter evolves to a space-charge effective region by the longitudinal compression in our experimental condition. So, we conducted detailed analysis with numerical simulations.

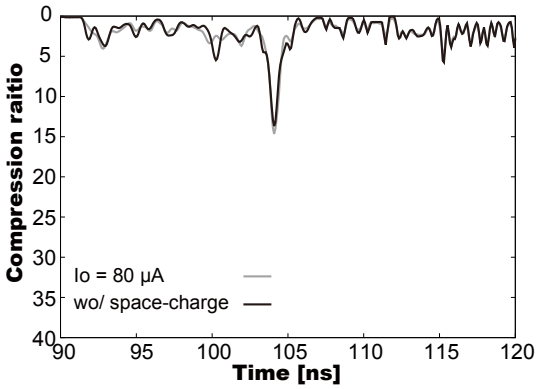


( a ) $L$ = 0.94 m

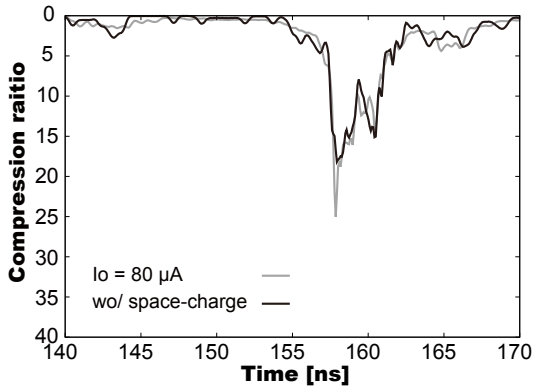


( b ) $L$ = 1.94 m

Fig. 5 Calculation results of beam current waveform (a): at transport distance $L$ = 0.94 m, (b): $L$ = 1.94 m. Black plots: wo/ space-charge. Glay plots: w/ space-charge corresponds to the initial beam current of 80 μA.

### 3.2 Estimation of the beam current waveforms with 1D PIC simulation

To estimate the bunching dynamics, simplified one-dimensional electrostatic Particle-In-Cell (PIC) simulation was carried out. In the simulation, a longitudinal energy dispersion of the initial beam was assumed to be a Maxwell distribution with a temperature of 0.1 eV. To introduce the velocity tilt for compression, the experimental voltage shown in Fig. 3 was adopted. To reflect the transverse geometrical effects on beam longitudinal self-field, we adopted g-factor model [7] for calculation of the longitudinal field. In the g-factor model, the longitudinal field $E_z$ is expressed as the following equation,

$$E_z = -\frac{g}{4\pi\varepsilon_0}\frac{\partial\lambda}{\partial z}, \qquad (2)$$

here $\varepsilon_0$ is electric permittivity in vacuum and $\lambda$ is line charge density of the beam, and $g$ is the geometry factor. Suppose an ellipsoidal envelope with uniform charge distribution of beam profile, the g-factor is defined as following expression [7],

$$g = 2\,ln\left(\frac{R}{r}\right), \qquad (3)$$

where $r$ and $R$ is radii of the beam and the cylindrical conducting pipe respectively. Therefor, under our experimental condition, we estimated to be $g$ = 6.

Figure 5 shows numerically simulated beam current waveforms w/ (with) and wo/ (without) space-charge. A time resolution was set to be 0.5 ns. Figure 5(a) shows the waveforms at transport distance $L$ = 0.94 m, which corresponds to the

early stage of longitudinal bunching. From the calculation results, however we can see the beam head components which corresponds to $t$ = 90 to 100 ns in Fig. 5(a) have slight difference in their waveforms, there's no remarkable difference between calculated waveforms w/ and wo/ self-field. On the other hand, Fig. 4(b) shows simulated waveforms at nominal focus distance $L = L_f$ = 1.94 m. From Fig. 4(b), we can see the waveforms clearly differ in their shapes. The waveform wo/ space-charge has sharp inflections and a peak compression ratio of 18 at $t$ = 157 ns. In contrast, simulated result w/ space-charge has blunt shape and the peak compression ratio of 25. These results indicate that the space-charge affected the bunching dynamics when the bunch compression proceeds. To analyze the result in detail, we calculated the time evolution of the beam particle distribution in longitudinal phase space. Figure 6(a) shows the time evolution of the particle distribution extracted from the initial beam current of 80 μA, where $t$ = 0 ns and 160 ns corresponds to the starting and nominal focusing time of bunching respectively.

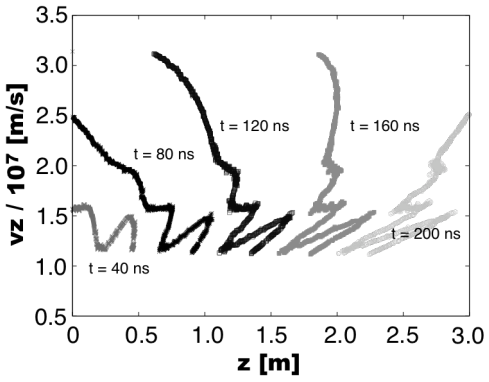


(a)

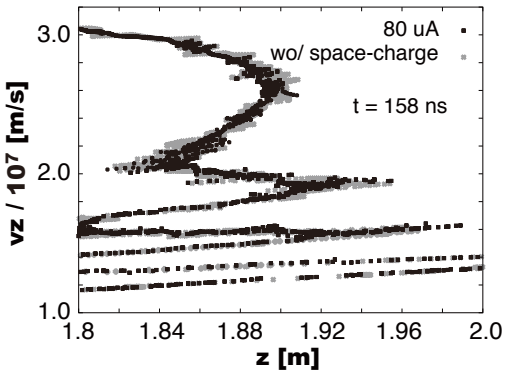


(b)

Fig. 6 Calculation results of particle distribution in longitudinal phase space. (a): Time evolution of beam particle distribution in longitudinal phase space w/ space charge for $I_0$ = 80 μA. (b): The distribution at focus time $t$ = 158 ns, w/ (black) and wo/ (gray) space-charge.

From Fig. 6(a), firstly, we can see the distribution has twisted shape from early stage of the time evolution. These are due to the voltage errors shown by the circle in Fig. 3. As we can see in Fig. 3, the generated modulation voltage waveform in experiment has some reflection points during $t$ = 0 to 60 ns. This fluctuation of the voltage produced the twisted structure in the phase space distribution. Secondly, we can confirm that as the time evolves, the distribution gradually rotates clockwise with almost keeping initial velocity tilt induced by modulation voltage. Figure 6 (b) shows a detail of the distribution w/ and wo/ space-charge at $t$ = 158 ns, focus time. From these plots, however slightly, focused component (e.g., in Fig.5 (b), $z$ = 1.84, $v_z = 2.0\times10^7$) and defocused component (e.g., in Fig.5(b) $z$ = 1.94, $v_z = 1.9\times10^7$ and $z$ = 1.98, $v_z = 1.6\times10^7$) exist in calculation result w/ space-charge.

From these results, we conclude the difference of beam pulse shape and peak compression ratios as shown in Fig.5 (b) are due to a slight dilution of particles induced by space-charge field.

### 3.3 Comparison of simulation and experimental results.

To evaluate the validity of both simulation and experimental results, these results were compared. Figure 7 shows a comparison of simulation and experimental results of current waveform evolutions. As shown in Fig. 7(a), we can see the simulated waveforms have sharp inflection pints and local peaks of compression ratios (which caused

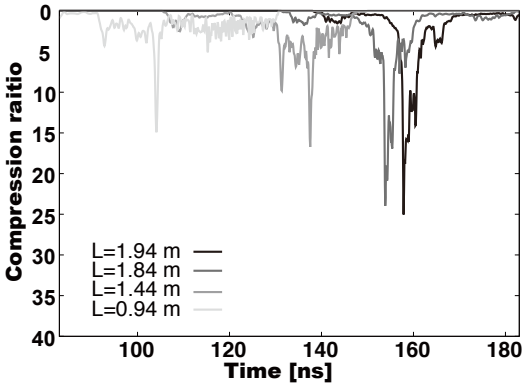


( a ) Simulation ( $I_0$ = 80 μA )

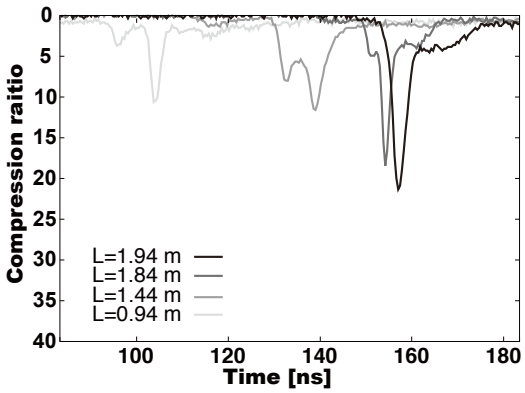


( b ) Experiment ( $I_0$ = 84 μA )

Fig. 7 Simulation (a) and experimental results (b) of evolution of a beam current waveform.

by the twisted distribution of particles discussed in Sec. 3.2). On the other hand, experimentally observed ones have blunt shapes through the transport distance. As mentioned in Sec.2, the time resolution of our device was estimated to be ns. Considering this, these difference between the shapes is considered to be lack of the time resolution of FC.

Comparing these results shown in Fig. 7 (a) and (b), although it seems that the time response of FC needs some improvements, 1D PIC can qualitatively represent experimental results. This indicates one-dimensional experiment was carried out in a well-established experimental condition. This means, we can expect our device has a potential to discuss the beam bunching dynamics. So, our next step is to estimate required initial beam current to discuss the dissipation process with beam collective motions under conditions in which the beam dynamics is strongly affected by space-charge.

### 3.4 Scaling of the bunching process to mA initial beam current.

To survey required beam parameter regions to observe and investigate the space-charge induced dissipation process, we extrapolated the current level of the bunching process with the PIC code.

Figure 8 shows a time evolution of particle distribution in phase space when $I_0$ = 5mA. From Fig. 8, we can see there's a remarkable difference in the particle behavior of higher current beam com-

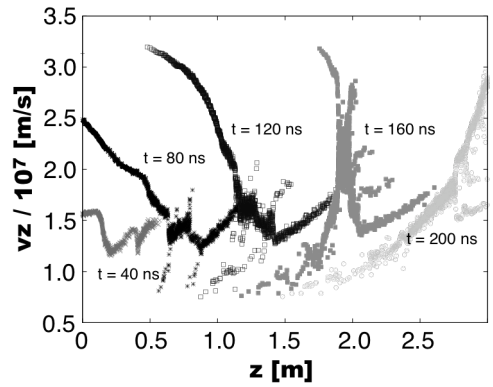


Fig. 8 Calculated time evolution of the particle distributions in longitudinal phase space when $I_0$ = 5 mA.

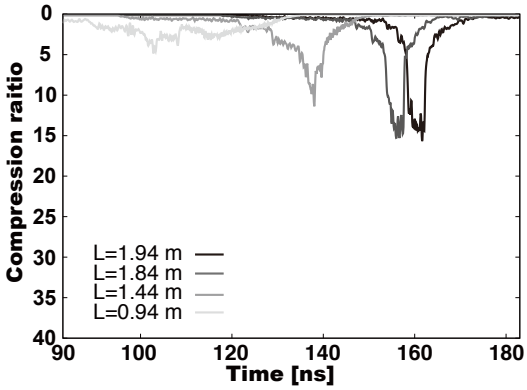


Fig. 9 Evolution of current waveforms when $I_0$ = 5 mA.

pression with the case of $I_0$ = 80 μA, i.e., we can observe diffusion in the phase space can be observed even at the early stage of the time evolution. When the bunching proceeds, the beam particles diffuse faster to form a more diluted particle distribution with diluting the initial velocity tilt for bunching. Figure 9 shows simulation results of the current waveforms when $I_0$ = 5 mA. As shown, the current waveforms take flattened shapes through the transport distance compared to Fig. 7(a).

Finally, when we compare Fig. 8 and 9, we can confirm that the waveforms were modified to flattened shape reflecting the particle behavior in the longitudinal phase space. The peak compression ratio at nominal focus $L = L_f$ = 1.94 m is reduced, where the particles are more thermalized as shown in Fig. 8, $t$ = 160 and 200 ns. This means, we can visualize the dilution of the particle distribution in the phase space by the one-dimensionalized experiment of bunching. This indicates that it's possible to evaluate the dissipation process with higher initial beam current of mA level. through the bunched beam current waveforms and/or compression ratios in one dimensional bunching experiments

## 4. Conclusions

To study the longitudinal compression of intense charged particle beams, we constructed a compact simulator device with electron beams. To analyze the bunching dynamics, 1D PIC simulation was carried out. Simulation results qualitatively agreed with experimental results at 100 μA level. This means one-dimensional compression experiment was conducted in a well-established experimental condition. We numerically extrapolated the beam bunching to a higher current level. From the results, particle dilution in phase space was clearly observed at initial beam current larger than mA level. Our device has a potential to visualize the dilution of the particle distribution in phase space, through the bunched beam current waveforms. Now, we are planning to increase the initial beam current and investigate the dissipation process in a wider parameter region.

## References


[1] K. Horioka et al., Nucl. Instr. Meth., A-606 (2009) 1-5

[2] P. A. Seidl, A. Aneders, F. M. Bieniosek et al., Nucl. Instr. Meth, A-606 (2009) 75-82

[3] Bangerter, R.O, Fusion Eng. Des. 44 (1998) 71

[4] Edward. P. Lee and J. Hovingh, AIP Conference Proceedings, No249, PT.2 (1992) 1713-1724

[5] T. Kikuchi, K. Horioka, Nucl. Instr. Meth., A606 (2009) 31-36

[6] P. S. Babu, A. Goswami, V. S. Pandit, Nucl. Instr. Meth., A642 (2011) 1-9

[7] M.Reiser, Theory and Design of Charged Particle Beams (Wiley, NewYork, 1994)

[8] R. A. Kishek, S. Bernal, C. L. Bohn, et.al,. Phys. plasmas, 10 (2003) 2016

[9] H. Rudd, Phys.Rev.Lett, 61, (1988) 26

[10] M. Reiser, J. Apple. Phys. 70, (1991) 1919

[11] B. Beaudoin, I. Harber, R. A. Kishek, et al., Phys. Plasmas, 18, (2011) 013104

[12] I. Haber, et al., Phys. Rev. A, 44, 8 (1991) 5194

[13] M.Chang, E. P. Gilson et al., Phys. Rev. ST Accel. Beams 10 (2009) 064202

[14] A. Nakayama, Y. Miyazaki, T. Kikuchi, M. Nakajima and K. Horioka, 7th International Conference on Inertial Fusion Science and Applications, Book of Abstract (2011)

[15] Y. Sakai, M. Nakajima, J. Hasegawa, T. Kikuchi, and K. Horioka, 18th International Symposium in Heavy Ion Fusion, Book of Proceeding (2012)

[16] D. Neuffer, IEEE, Trans Nucl Sci, vol. NS-26, No.3 (1979)

# Characteristic of Intense Pulsed Heavy Ion Beam by Bipolar Pulse Accelerator

K. Kitajima, Takashi Kanda, K. Masugata, and H. Ito

*Dep. of Electrical and Electronic Engineering, University of Toyama, 3190 Gofuku, Toyama 930-8555, Japan*

**ABSTRACT**

To improve the purity of the intense pulsed ion beam a new type of a pulsed ion beam accelerator named "bipolar pulse accelerator"has been proposed. In order to confirm the principle of the accelerator, a double coaxial type bipolar pulse generator and a prototype of the experimental system were developed. The system utilizes a magnetically insulated acceleration gap and was operated with the bipolar pulse. A coaxial gas puff plasma gun was used as an ion source, which was placed inside of the grounded anode. Source plasma (nitrogen) of current density of $\approx$ 30 A/cm$^2$ and pulse duration of $\approx$ 1.0 $\mu$s was injected into the acceleration gap. When the bipolar pulse with voltage of about $\pm$ 110 kV and pulse duration of about 70 ns was applied to the drift tube, the ions were successfully accelerated from the grounded anode to the drift tube in the 1st gap by the negative pulse of the bipolar pulse. The pulsed ion beam with current density of 70 A/cm$^2$ and pulse duration of $\approx$ 50 ns was obtained at 50 mm downstream from the anode surface. The energy spectrum of the ion beam was evaluated by a magnetic energy spectrometer. The ion energy was in reasonable good agreement with the acceleration voltage, i.e., 1st pulse (negative pulse) voltage of the bipolar pulse.

**Keywords**

Intense pulsed ion beam, Bipolar pulse accelerator, Pulse power technology,

## 1 Introduction

Pulsed ion beam (PIB) technology has been developed primarily for nuclear fusion and high energy density physics research [1,2]. Recently, however, these PIBs with an ion energy of several 100 keV, a high ion current density of several 100 A/cm$^2$, and a short pulse duration of $< 1\mu$s, has been widely used for materials surface properties modification by the methods of ion implantation, ion plasma coatings deposition, and high energy ion beam energetic impact [3-5]. Compared with the traditional ion implantation method, the PIB irradiation into materials enables the accumulation of energy in very short time into the near surface region while it maintains a low substrate temperature. The annealing by PIB is expected to be novel annealing techniques for the next generation semiconductor materials such as silicon carbide (SiC). In the case of SiC, a high temperature annealing is normally done by using a traditional thermal method, which requires temperatures as high as 1500-1700 °C to recover the crystal damage and activate the dopants after the implantation. The conventional method at such a high temperature causes several disadvantages such as the redistribution of implanted dopants and increasing of surface roughness. Therefore, PIB has received extensive attention as a tool for a new ion implantation technology named "pulsed ion beam implantation "to semiconductor materials, since the ion implantation and the annealing can be completed simultaneously.

To meet the requirements of research and industrial application, a number of PIB sources have been developed so far for different applications of PIBs [6-8]. The producible ion species, how-

ever, is limited to the material of electrode (anode), since the anode plasma is produced by a high-voltage flashover and an electron bombardment to the anode surface. In addition, the purity of the PIB is usually deteriorated by absorbed matter on the anode surface and residual gas molecules in the diode chamber. Therefore, the conventional pulsed ion diode is not suitable for the application to the ion implantation.

We have developed a new type of the magnetically insulated ion diode (MID) with an ion source of a gas puff plasma gun and were successful in generating the high-purity pulsed nitrogen ion beam with an ion current density of 54 A/cm$^2$, a pulse duration of 90 ns and purity of the nitrogen beam of 94 % [9]. In order to improve the purity of the intense pulsed ion beam, we have proposed a new type of pulsed ion beam accelerator named "bipolar pulse accelerator (BPA)"and developed a prototype of the accelerator and a bipolar pulse generator as the power supply of the BPA [10,11]. The bipolar pulse generator consists of a Marx generator and a pulse forming line (PFL) with a rail gap switch on its end. The BPA utilizes a magnetically insulated ion diode with an ion source of a coaxial gas puff plasma gun. In this paper, the experimental results of the evaluation of the pulsed ion beam accelerated by the bipolar pulse are presented.

## 2 Principle of bipolar pulse accelerator

Figure 1 shows the concept diagram of the bipolar pulse accelerator. A conventional PIB diode is also shown for comparison. As shown in Fig. 1 (a), proposed ion accelerator consists of a grounded ion source, a drift tube and a grounded cathode and is an electrostatic two-stage accelerator. In the system, a bipolar pulse of voltage $\pm V_0$, duration $\tau_{\rm p}$ each is applied to the drift tube. At first the negative voltage pulse of duration $\tau_{\rm p}$ is applied to the drift tube and ions on the grounded ion source are accelerated toward the drift tube. If $\tau_{\rm p}$ is adjusted to the time of flight delay of the ions to pass the drift tube, the pulse is reversed and the positive voltage of duration $\tau_{\rm p}$ is applied to the drift tube when top of the ion beam reaches the 2nd gap. As a result, the ions are again accelerated in the 2nd gap toward the grounded cathode. As seen in Fig. 1 (b), in the conventional PIB diode, the ion source is placed on the anode where high voltage pulse is applied, while in the proposed ion diode, the ion source is on the grounded anode, which extremely enhances the accessibility to the anode.

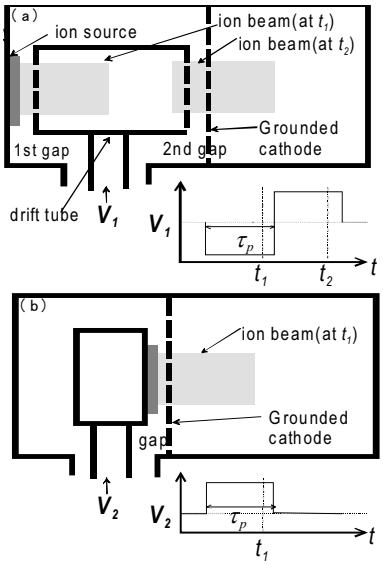


Fig.1 Conceptual drawing of (a) bipolar pulse accelerator and (b) conventional pulsed ion beam accelerator.

Figure 2 illustrates the principle of the improvement of the purity of the ion beam. Let us now consider the acceleration of ions in the case that the ion beam produced in the ion source consists of $N^+$ ion and impurity of $H^+$ ion. Each ion of $N^+$ and $H^+$ is accelerated in the 1st gap toward the drift tube when the negative voltage is applied, where $N^+$ and $H^+$ ion beams are schematically described in Fig. 2. As seen in Fig. 2, the length of $H^+$ beam is much longer than that of $N^+$ beam due to the difference of the velocity. We assume that the length of the drift tube is designed to be same as the beam length of $N^+$ beam with a beam pulse duration $\tau_{\rm p}$ at an acceleration voltage $V_0$. It is, for example, calculated to be 11.6 cm when $V_0 = 200$ kV and $\tau_{\rm p} = 70$ ns. On the other hand, the length of $H^+$ beam at $V_0 = 200$ kV and $\tau_{\rm p} = 70$ ns is 43.3 cm. When the voltage is reversed and the positive voltage is applied to the drift tube ($t = t_1$), $N^+$ beam with the length of

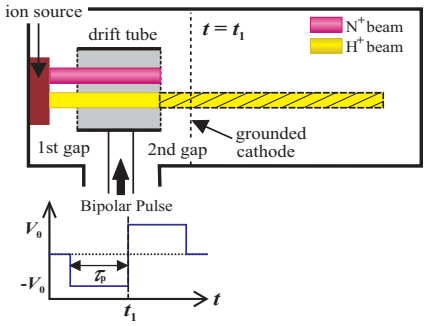


Fig.2 Principle of the improvement of the purity of the ion beam.

11.6 cm in the drift tube is accelerated in the 2nd gap. In contrast, 73 % of the beam is out of the drift tube and decelerated in the 2nd gap by the first pulse (negative voltage pulse). Hence 73 % of $H^+$ beam is not accelerated in the 2nd gap by the positive voltage pulse of the bipolar pulse and is removed in the bipolar pulse accelerator. As a result, the purity of the ion beam is improved.

## 3 Experimental Setup

Figure 6 shows the schematic configuration of the bipolar pulse accelerator in the present experiment. The system consists of a bipolar pulse generator and an accelerator. The bipolar pulse generator consists of a Marx generator and a pulse forming line (PFL). The designed output of the bipolar pulse generator is the negative and positive pulses of voltage ± 200 kV with pulse duration of 70 ns each. In the present system, the double coaxial type is employed as the PFL for the formation of the bipolar pulse. The line consists of three coaxial cylinders with a rail gap switch on the end of the line, which is connected between the intermediate and outer conductors. The characteristic impedance of the line between the inner and intermediate conductors and one between the intermediate adn outer conductors are 6.7 Ω and 7.6 Ω, respectively. The PFL is filled with the deionized water as a dielectric and charged positively by the low inductance Marx generator with maximum output voltage of 300 kV through the intermediate conductor. The rail gap switch is filled with pure $SF_6$ gas and the pressure can be adjusted to control the optimum trigger timing for each experimental condition.

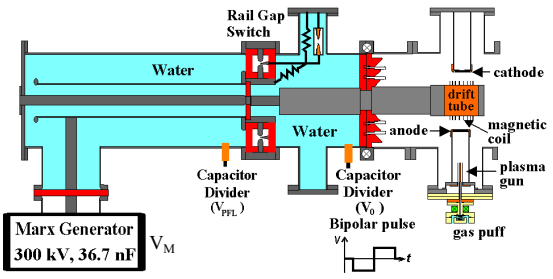


Fig.3 Schematic configuration of bipolar pulse accelerator.

The bipolar pulse voltage ($V_0$) and charging voltage of the PFL ($V_{PFL}$) are measured by the resistive voltage divider and capacitive voltage divider placed near the rail gap switch, respectively. The values of $V_{PFL}$ and $V_0$ are calculated by the ratio factor of the two voltage dividers (K=48500 and 1840, respectively). The Rogowski coil with the coefficient of 7 kA/V is used for the measurement of the bipolar pulse current.

Figure 4 shows in detail the acceleration gap design of the BPA, which consists of a grounded anode, a drift tube, a grounded cathode and a magnetically insulated acceleration gap (MIG). The drift tube is connected to a high voltage terminal of a high voltage pulsed power generator. A double coaxial type bipolar pulse generator was used [11], which generate an output pulse of the negative and positive pulses of voltage ± 200 kV with pulse duration of 70 ns each. The anode and the cathode are the copper electrodes of diameter 78 mm, thickness 5 mm. The electrodes are uniformly drilled with apertures of diameter 4 mm, giving beam transmission efficiency of 58 %. In order to produce insulating magnetic fields in

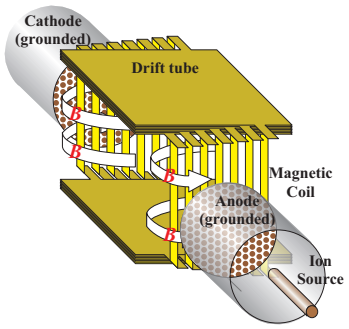


Fig.4 Conceptual drawing of magnetically insulated gap of bipolar pulse accelerator.

both acceleration gaps for suppression of the electron flow, a magnetic field coil of grating structure is used, which produces a uniform magnetic field in direction transverse to the acceleration gap. The magnetic coil of the MIG is installed on the rectangular drift tube. The uniform magnetic field with strength of $0.3-0.4$ T is produced in the acceleration gap of gap length $d_{\mathrm{A-K}} = 10$ mm by a capacitor bank with capacitance of 500 $\mu$F and charging voltage of 5 kV. At peak of the magnetic field, the bipolar pulse voltage supplied from bipolar pulse generator is applied to the drift tube. To obtain higher transmission efficiency of the ion beam, right and left sides of the coil consist of 8 blades each and have a grating structure. Each of the blades (10 $\mathrm{mm}^W$ $\times$ 118 $\mathrm{mm}^L$ $\times$ 1 $\mathrm{mm}^T$) is connected in series and works as an 8-turn coil. Since high voltage pulse is applied to the drift tube, the pulsed current produced by the capacitor bank is applied to the coil through an inductively isolated current feeder (IC). The IC is a helically winded coaxial cable and the outer conductor of the IC is connecting the grounded vacuum chamber and the drift tube with inductance of 12.4 $\mu$H.

A gas puff plasma gun was used as the ion source and installed inside the anode. Figure 5 shows the detail of the gas puff plasma gun used in the experiment. The plasma gun is composed of a coaxial plasma gun and a high-speed gas puff valve. The plasma gun has a pair of coaxial electrodes, i.e. an inner electrode of 80 mm length by 6 mm outer diameter and an outer electrode of 18 mm inner diameter. The inner electrode has six gas nozzles of 1 mm diameter. The gas puff valve

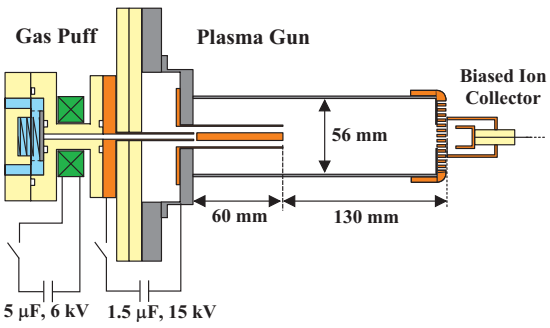


Fig.5 Cross-sectional view of the gas puff plasma gun.

consists of a nylon vessel, an aluminum valve and a drive coil and the vessel is pre-filled with $N_2$ gas. By applying a pulse current to the driver coil, a pulsed strong magnetic field is produced and the magnetic pressure pushes the aluminum valve to open the valve. As a result, the gas expands with a supersonic velocity and is injected into the plasma gun via the nozzles on the inner electrode of the plasma gun. The ion source plasma is produced by discharging the capacitor bank of the plasma gun with a delay time of $\tau_{\mathrm{PG}}$ around 260-320 $\mu$s, since it takes about a hundred $\mu$s to open the valve and several tens $\mu$s for $N_2$ gas to reach the gas nozzle on the inner electrode of the plasma gun. To apply pulsed current to the gas puff coil and the plasma gun, capacitor banks of 5 $\mu$F and 1.5 $\mu$F were used, respectively. Each capacitor bank is usually charged up to 6 kV and 15 kV, respectively.

The ion current density of the source plasma produced by the plasma gun was evaluated by a biased ion collector (BIC) placed at 130 mm downstream from the top of the plasma gun where the anode is placed in the acceleration experiment. The collector of BIC was biased at a voltage of -200 V to remove accompanying electrons. Figure 6 shows the waveforms of the discharge current of the plasma gun ($I_{\mathrm{PG}}$) and the ion current density ($J_{\mathrm{i}}$) of the plasma gun at the condition of $\tau_{\mathrm{PG}}$=270 $\mu$s. Here the filling gas pressure of the vessel is 2.0 atm. As seen in Fig. 6, the discharge current $I_{\mathrm{PG}}$ has a sinusoidal waveform of peak current 4 kA and quarter cycle 2.4 $\mu$s. The ion beam with a peak current density of $J_{\mathrm{i}}$=34 A/cm$^2$ and a pulse duration of 1 $\mu$s is observed at about $\tau_{\mathrm{d}} = 4.2$ $\mu$s after the rise of $I_{\mathrm{PG}}$. The

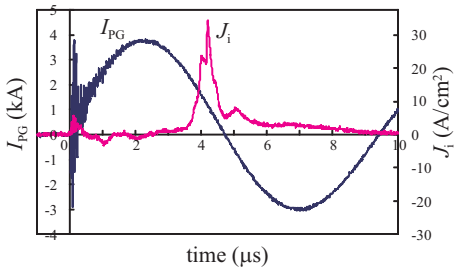


Fig.6 Typical waveforms of discharge current of plasma gun ($I_{\mathrm{PG}}$) and ion current density ($J_{\mathrm{i}}$).

result suggests that it takes 4 $\mu$s after the rise of the discharge current of the plasma gun ($I_{\rm PG}$) for the ion beam produced in the plasma gun to reach the acceleration gap. Figure 7 shows the dependence of $J_{\rm i}$ on the delay time of the discharge current rise from the rise of the gas puff current ($\tau_{\rm PG}$) and the filling $N_2$ gas pressure. As seen in Fig. 7, $J_{\rm i}$ rises at $\tau_{\rm PG} \approx 250$ $\mu$s and has a peak around 290 $\mu$s, and after that decreased. The result suggests that it takes 250 $\mu$s after the rise of the gas puff coil for the gas to reach the nozzles.

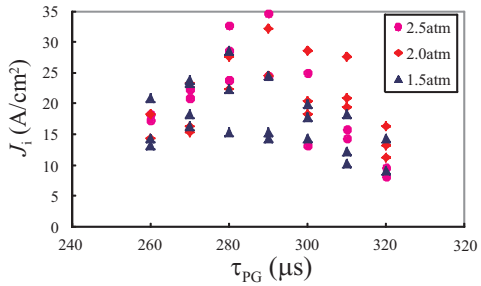


Fig.7 Dependence of ion current density ($J_{\rm i}$) on delay time of discharge current rise from rise of gas puff current ($\tau_{\rm PG}$).

## 4 Experimental Results

In order to confirm the acceleration of ions in the 1st gap, the bipolar pulse was applied to the drift tube. Figure 8 shows the set-up of beam acceleration experiment to measure the ion beam accelerated in the 1st gap by the first pulse of the bipolar pulse. BIC was installed inside the drift tube to observe the ion current density ($J_{\rm i}$). Since high voltage pulse is applied to the drift tube, the inductively isolated coaxial cable of same structure as IC was used to transport the BIC signal.

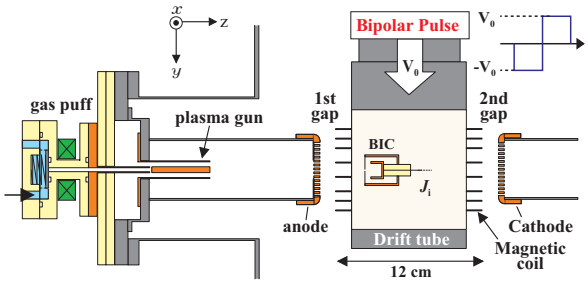


Fig.8 Experimental setup of bipolar pulse accelerator.

The bipolar pulse generator was operated at 70 % of the full charge condition of the PFL. Insulating magnetic field with strength of 0.3-0.4 T was applied to the acceleration gap of gap length $d_{\rm A-K}$ = 10 mm. The plasma gun was operated at the condition of $\tau_{\rm PG} \approx 290$ $\mu$s and the Marx generator was fired at $\tau_{\rm PM}$ =8-20 $\mu$s after the rise of the $I_{\rm PG}$.

Figure 9 shows the typical waveforms of the charging voltage of the PFL ($V_{\rm PFL}$), the output voltage ($V_0$) and the ion current density ($J_{\rm i}$) accelerated in the 1st gap. They were obtained at the condition of $\tau_{\rm PM}$ =15 $\mu$s. $J_{\rm i}$ was measured at 40 mm downstream from the anode surface. As seen in the Fig. 9, the first pulse of $V_0$ rises at $t$ = 240 ns and has a peak voltage of -110 kV and a pulse duration of 70 ns. The ion beam with a current density of $J_{\rm i}$ = 70 A/cm$^2$ and a pulse duration of 50 ns(FWHM) was obtained at around 50 ns after the peak of the first voltage pulse. Considering the time of flight delay, the peak current density corresponds to nitrogen ions ($N^+$, $N^{2+}$) and the ion beam corresponding the peak of $J_{\rm i}$ seems to be accelerated around the peak of the first pulse. Assuming that the accelerated ion beam consists of nitrogen ions, we can estimate from the time of flight delay that the ion energy is about 108 keV/Z, where Z is the charge state of the ions. The estimated ion energy seems to be in reasonable good agreement with the accelerating voltage. Figure 11 shows the dependence of the peak value of $J_{\rm i}$ on the delay time ($\tau_{\rm PM}$) for the fixed condition of $\tau_{\rm PG}$, the insulating magnetic field and the charging voltage of the PFL.

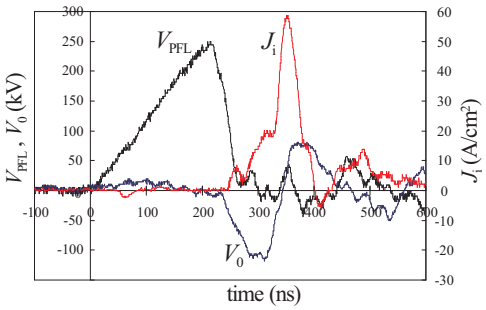


Fig.9 Typical waveforms of charging voltage of PFL ($V_{\rm PFL}$), output voltage ($V_0$) and ion current density ($J_{\rm i}$).

As seen in the Fig. 11, $J_i$ increases monotonically with increasing $\tau_{PM}$ and reaches a peak at around $\tau_{PM}$ =15 $\mu$s and after that decreased. This seems to be due to that quantity of the plasma on the anode or in the 1st gap increases with increasing $\tau_{PM}$.

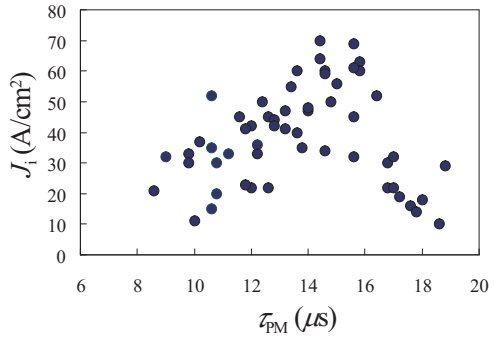


Fig.10 Dependence of the peak values of ion current density ($J_i$) on the delay time ($\tau_{PM}$).

In order to evaluate the energy spectrum of the ion beam, we used a magnetic energy spectrometer. The energy spectrometer consists of a 1st pinhole, a 2nd pinhole, a magnetic deflector and an ion detecting plate of CR-39. A small portion of the ion beam is collimated by a pair of pinholes with diameters of 0.3 mm. The collimated beam is passed through deflection plates having a parallel magnetic field of 0.8 T to the beam direction. Figure **??** illustrates an example of the track recorded on a CR-39 ion track detecting plate. Assuming that the accelerated ion beam consists of nitrogen ions, the tracks correspond to singly- and doubly-ionized nitrogen. From the deflecting distance, the energy of the nitrogen ion beam was estimated to be about 120 keV/Z. The ion energy was in reasonable good agreement with the 1st pulse voltage of the bipolar pulse ($V_0 \approx 110$ kV).

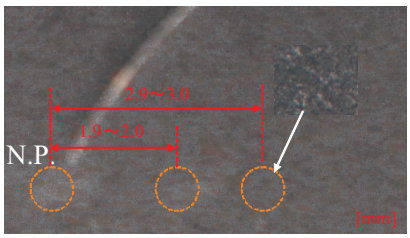


Fig.11 Ion track obtained by magnetic energy spectrometer.

## 5 Summary

We have developed a prototype of the accelerator to perform proof of principle experiments on the BPA. When the bipolar pulse was applied to the drift tube, the ions were successfully accelerated in 1st acceleration gap by the bipolar pulse. To confirm the principle of the BPA, we are planning to evaluate the ion species and the energy spectrum of the ion beam in detail.


### Acknowledgement

This work was supported in part by the Grant-in-Aid for Scientific Research from the Ministry of Education, Science, Sports and Culture, Japan.


### References


[1] S. Humphries, Jr, Nucl. Fusion, **20**, pp.1549-1612, (1980).

[2] J. P. VanDevender and D.L. Cook, Science, **232**, pp.831-836, (1986).

[3] K. Yatsui *et al.*, Phys. Plasma, **1**, pp.1730-1737, (1994).

[4] D. J. Rej *et al.*, J. Vac. Sci. Technol. **15**, pp.1089-1097, (1997).

[5] H. Akamatsu, T. Ikeda, K. Azuma, E. Fujiwara and M. Yatsuzuka, Suf. Coat. Technol. **136**, p.269 (2001).

[6] Y. Hashimoto, M. Sato, M. Yatsuzuka, and S. Nobuhara, Jpn. J. Appl. Phys. **31**, 1922 (1992).

[7] D. J. Rej, R. R. Bartsch, H. A. Davis, R. J. Faehl, J. B. Greenly, and W. J. Waganaar, Rev. Sci. Instrum. **64**, 2753 (1993).

[8] X. P. Zhu, M. K. Lei, and T. C. Ma, Rev. Sci. Instrum. **73**, 1728 (2002).

[9] H. Ito, H. Miyake and K. Masugata, Rev. Sci. Instrum. **79**, 103502 (2008).

[10] K. Masugata, Y. Shimizu, Y. Fujioka, I. Kitamura, H. Tanoue and K. Arai, Nucl. Instrum. & Methods in Phys. Res. A **535**, 614 (2004).

[11] H. Ito, K. Igawa, I. Kitamura and K. Masugata, Rev. Sci. Instrum. **78**, 013502 (2007).

# Radial and Axial Compression of Pure Electron

Y. Park, Y. Soga, Y. Mihara, M. Takeda and K. Kamada

*Graduate School of Natural Science, Kanazawa University*

*Kakuma-machi, Kanazawa-shi, Ishikawa 920-1192,Japan*

## ABSTRACT

Experimental studies are carried out on compression of the density distribution of a pure electron plasma confined in a Malmberg-Penning Trap in Kanazawa University. More than six times increase of the on-axis density is observed under application of an external rotating electric field that couples to low-order Trivelpiece-Gould modes. Axial compression of the density distribution with the axial length of a factor of two is achieved by controlling the confining potential at both ends of the plasma. Substantial increase of the axial kinetic energy is observed during the axial compression.

## Keywords

Nonneutral plasma, Rotating Wall, Space-charge-dominated beams

## 1. Introduction

A pure electron plasma has been expected to use for the investigation of the fundamental properties of space-charge-dominated beam. In principle, the system of a pure electron plasma can reproduce actual situations in high-intensity beam transport channels [1]. Consequently, it is important to understand the accessible density of the electron plasma to simulate the space charge effect of electron beam. In order to control the density of the trapped electron plasma, two methods are usually adopted. One is the rotating wall (RW) technique developed by UCSD group, in which the rotating electric field couples to low-order Trivelpiece-Gould mode [2] or a strong radio-frequency field drives a torque for plasma without tuning to plasma mode [3], as a result plasma density distribution contracts radially. The other is axial compression of the density distribution by controlling the shape of a trap potential.

In this paper we report a preliminary experimental study of the density control of a pure electron plasma by the RW technique and the axial compression in a Malmberg-Penning trap in Kanazawa University. The axial parallel energy distribution of the electron column was estimated as a first step in order to study various features of bunched electron beam.

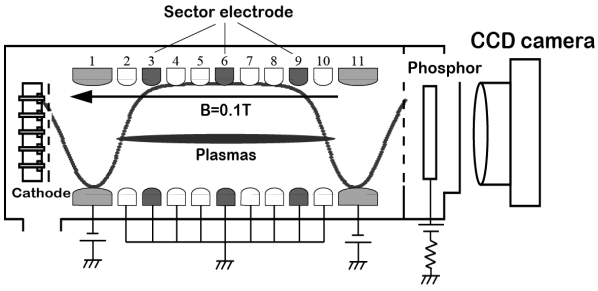


FIG. 1 Schematic configuration of the electron trap.

## 2. Experimental methods

The schematic configuration of the compression experiments is shown in Fig. 1. The basic scheme of the electron confinement consists of the homogeneous magnetic field B = 0.1 T along the z-axis and the saddle shaped axisymmetric potential with negative barriers at both ends [4]. The electrons are provided from an array of small electron emitters placed in the weaker field zone through the left

barrier, while the confining potential at the plug cylinder is raised to ground in a variable short time. The electrons are disconnected from the sources on the recovery of the potential barrier, the trapped in the cylindrical volume at the center to form a bundle of straight strings with equal length of 170 mm and diameter 1 mm. A radially extended column of electrons is produced by mixing and relaxation of about 500 strings of electrons which accumulate in the trap through multiple injection-hold-mixing cycles. This distribution serves as the initial profile of an electron plasma for the present experimental studies.

Rotating waves are excited in the electron column by applying radio-frequency voltages at variable frequency to the four wall segments azimuthally separated at the axial locations labeled with No. 9 with a phase shift of 90 degrees so as to create a forward-rotating m = 1 mode.

Axial compression is achieved by applying negative voltage to ring electrodes labeled with No.2, 3, 4, 5 and 6 after the confinement, so that a factor of 2 decrease in axial confinement region leads to decrease in the axial length of the eletron plasma.

The measurements of the density profile are made by dumping the whole electrons through the end cylinder on the other side of the cathodes onto a phosphor screen that is biased up to 5 kV from the machine ground. The luminosity distribution on the screen is detected with a charge-coupled-device camera with 512 times 512 pixels and recorded on a computer for numerical analyses. A linear relationship has been confirmed between the total electron number and the luminosity integrated over the screen [5].

## 3. Experimental Results

### 3.1 Radial compression analysis

Figure 2 shows time evolution of the two-dimensional density distributions of electrons confined for a period varied up to t = 5 s. The initial density distribution shown in FIG. 2 (a) is axisymmetric and broad. In FIG. 2 (b), with the addition of a rotating voltage of the amplitude 2.0 V at the frequency linearly ramped up from 0.1 to 5 MHz for 5 s, the particle distribution contracts radially and the on-axis density is maximized. Figure 2 (c) quantitatively displays the time evolution of the radial density profiles of the images in FIG. 2 (a) and (b). The addition of a rotating field leads to more than 6 times increase of the on-axis density during the period from 0 to 5 sec.

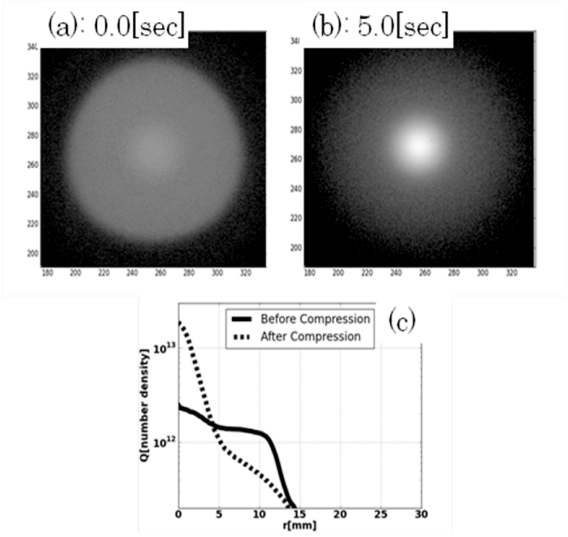


FIG. 2 CCD image describing the density profile of the pure electron plasma in the initial state (a) and after compression (b). (c) Radial distribution of the density profile under the rotating wave. The wall is located at r = 30 mm.

The compression rate (on-axis density normalized by the initial value) under the RW drive depends on various parameters, such as RW amplitude, RW frequency range, and sweep rate of the frequency etc. Time evolutions of the compression rate are compared in FIG.3 (a). Here, the RW drive is carried out during the period from 0 to 0.5 sec under the different frequency range. With the RW drive in broad frequency range from 0.1 to 4 MHz the compression rate reaches 2.8 while the drive with low frequency range from 0.1 to 1 MHz shows no compression. The effective compression occurs in the frequency range from 1 to 2.5 MHz for the initial density distribution. When the RW drive is turned off, the density gradually decays. The maximum compression rate is plotted as a function of the RW

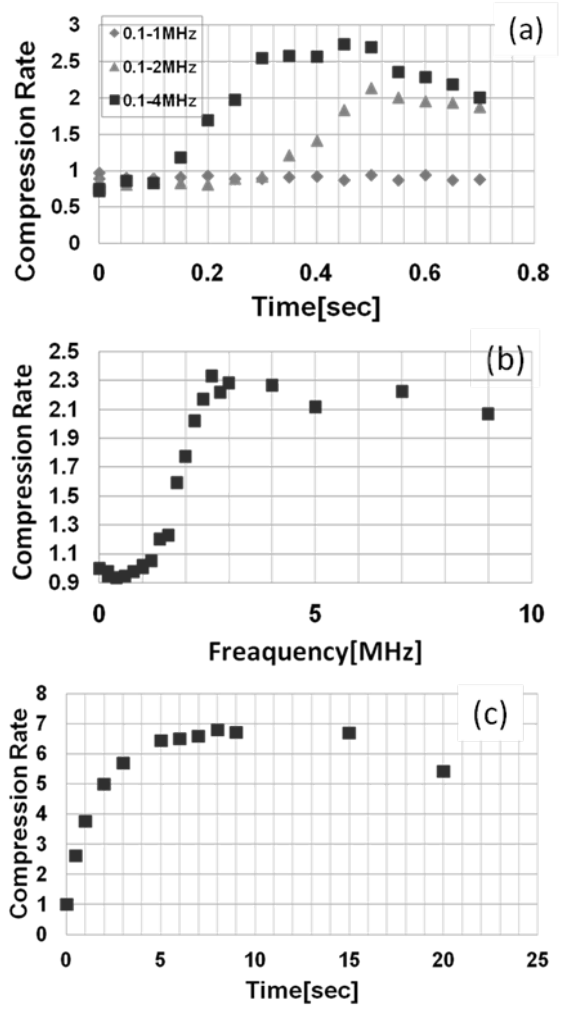


FIG. 3 (a) Time evolution of the compression rate. RW is applied during the period from 0 to 0.5 sec. (b) Compression rate is plotted as a function of stop frequency of RW. (c) Compression rate is plotted as a function of time during RW drive at fixed frequency at 2.8 - 3.0 MHz

stop frequency in FIG. 3 (b). The maximum compression rate rapidly increases in the stop frequency from 1 to 2.5 MHz. Figure 3 (c) shows the maximum compression rate vs. time for RW drive at fixed frequency of 2.8 - 3.0 MHz. For more than 8 s of RW drive the compression rate is nearly constant. The decrease of compression rate for 20 s is due to the outward transport of the particles.

### 3.2 Axial compression and energy analysis

Next we axially compress the electron plasma right

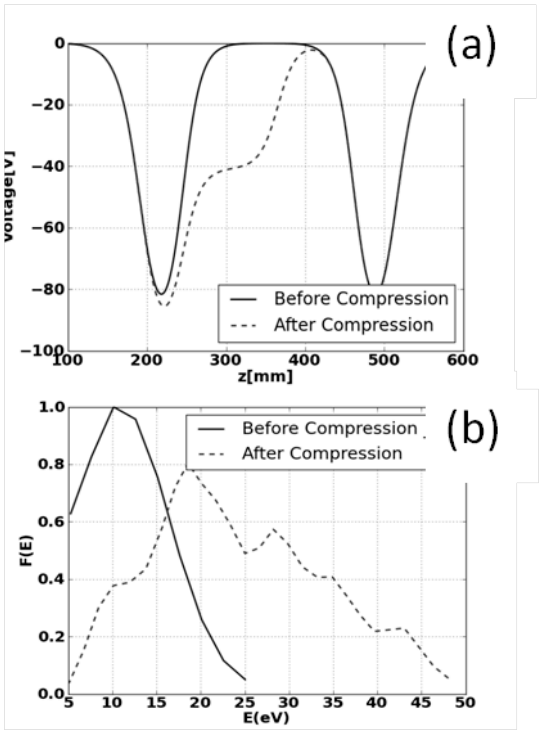


FIG. 4 (a) Axial profile of confining potential on axis for axial compression. (b) Energy distribution function in the initial state (solid line) and after axial compression (dashed line).

after the radial compression with RW drive and measure the parallel energy distribution of the electron plasma. The confinement potential on axis is shown in Fig. 4 (a). Additional negative voltage -42.8 V is applied to the axial region from z = 260 to 330 mm. The method of analyzing the axial kinetic energy of electrons is as follows [6,7]. After the electron plasma is confined for an arbitrary time, the electrons are dumped by a lowered, but non-zero, confinement potential. Electrons with sufficient energy escape from the potential barrier along the magnetic field lines and are collected at a phosphor screen. We measured both the total electron number and the luminosity distribution of phosphor. By repeating the procedure with various barrier potentials, we measured a number of electrons $Q_{esc}$ as a function of the energy E. By differentiating the data, we obtained the parallel energy distribution of the electrons

$$F(E) = \frac{d}{dE}\frac{Q_{esc}}{Q_{all}}.$$

Here $Q_{all}$ is the total electron number. Figure 4 (b) represents the parallel energy distribution function of the plasma. Before compression the distribution has a peak at 10 eV and no particles with the energy more than 30 eV exist. The energy distribution after compression shows a widely expanded distribution from low energy to a high energy of 50 eV. The increase of parallel energy with axial compression may be attributed to an axial acceleration of the particles by rapid change of the confinement potential. Based on the observed axially integrated density and the energy distribution function, we solve the Poisson equation to determine the plasma length. In the result the plasma is compressed with the length from 170 to 80 mm, the density $4.3 \times 10^{13}$ /m$^3$.

## 4. Discussion and Conclusion

In our electron trap system plasma waves can be detected at axial locations of 9 positions during the compression of electrons. In addition to the energy analysis the observation of plasma waves with a spatial resolution may be the advantage in the investigation on space-charge effects of electron beam. However, it is necessary to identify the relationship of parameters between the electron plasma and electron-beam system [1].

In conclusion, we studied on compression of the density distribution of a pure electron plasma confined in a Malmberg-Penning Trap in Kanazawa University. On-axis density increases for 6.8 times higher than that of initial state under application of an external rotating electric field that couples to Trivelpiece-Gould modes. Axial compression of the density distribution for a factor of two is achieved by controlling the confined potential at both ends of the plasma. Substantial increase of the axial kinetic energy was observed during the axial compression.

## References


[1] H. Okamoto, H. Tanaka, ”Proposed experiments for the study of beam halo formation”, *Phys. Res.* A **437** pp178-187 (1999).

[2] E. M. Hollmann, F. Anderegg, and C.F. Driscoll, ”Confinement and manipulation of non-neutral plasmas”, *Phys. Plasmas*. **7** pp.2776 (2000).

[3] J. R. Danielson and C.M. Surko, ”Torque –Balanced High-Density Steady States of Single –Component Plasmas”, *Phys. Rev. Lett.* **94** 035001 (2005).

[4] J. H. Malmberg and J. S. deGrassie, "Properties of a Nonneutral Plasma", *Phys. Rev. Lett.* **35**, 577 (1975).

[5] Y. Kiwamoto, K. Ito, et al, “Dynamics of Electron –Plasma Vortex in Background Vorticity Distribution”, *Phys. Rev. Lett.* **85** pp3173 - 3176 (2000).

[6] D. L. Eggleston, C. F. Driscoll, et al. “Parallel energy analyzer for pure electron plasma devices” *Phys. Fluids. B* **4** pp.3432-3439 (1992).

[7] Y. Soga, T. Mimura, et al, “Mechanisms of E × B Drift Rotation of a Vortex String in a Pure Electron Plasma”, *Plasmas. Fusion. Res.* **8** 2401034 (2013).

# Frequency measurement of High Power Microwave by Virtual Cathode Oscillator

Rie Matsuda, Weihua Jiang

*Extreme Energy-Density Research Institute, Nagaoka University of Technology*

## ABSTRACT

Main frequency of a high power microwave which was generated by a Virtual Cathode Oscillator, was measured. It was confirmed that the microwave have two main frequency, 3-4 GHz and 5-6 GHz which result from reciprocating motion of the particle and vibration of the virtual cathode, respectively. The main frequency was affected to an Anode-Cathode Gap and a charge voltage of a pulsed power generator "ETIGO-IV".

## Keywords

Virtual Cathode Oscillator (Vircator), High Power Microwave

## 1. Introduction

A high power microwave is an electromagnetic wave whose wave length is 1–30 cm. It has been applied to some fields, e.g. an accelerator, a nuclear fusion reactor, and space development.

Radiation sources of the high power microwave are a Virtual Cathode Oscillator (vircator), a Magnetron, a Gyrotron, a Klystron and so on. We have studied the vircator [1][2].

As advantages of the vircator, it is simple structure, don't require an external magnetic field, and enable the higher power microwave. Disadvantages are low conversion efficiency and poor frequency stability.

Eventually, we attempt to improve the conversion efficiency by using a resonator. For the resonator design, a main frequency of the microwave was measured.

## 2. Principle of a Vircator

Figure 1 shows the principle of the vircator. When a high pulsed voltage is applied to a cathode electrode, the electrons are emitted from the surface of the cathode. The emitted electrons accelerate and pass through an anode mesh electrode. When the

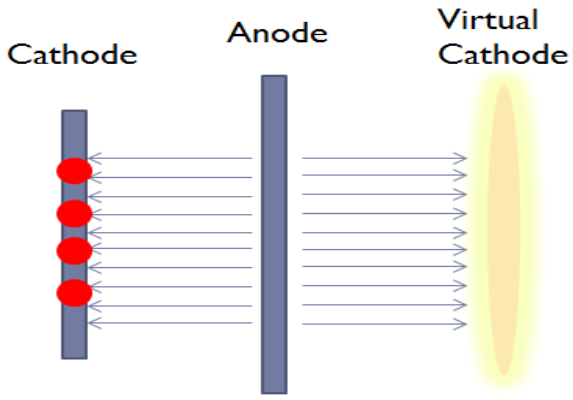


Fig. 1. Principle of the vircator

electrons exceed space charge limited current, high potential barrier occurs. The potential barrier is called "virtual cathode". The electrons cannot go over the virtual cathode. Therefore, the electrons come back to the cathode electrode through the anode. Because the virtual cathode and the cathode electrode are same voltage, the distance between the virtual cathode and the anode becomes same as the distance between the cathode electrode and the anode. The electrons which approach the cathode electrode accelerate to the anode again owing to the high negative electric field. The electrons repeat reciprocation by continuity of

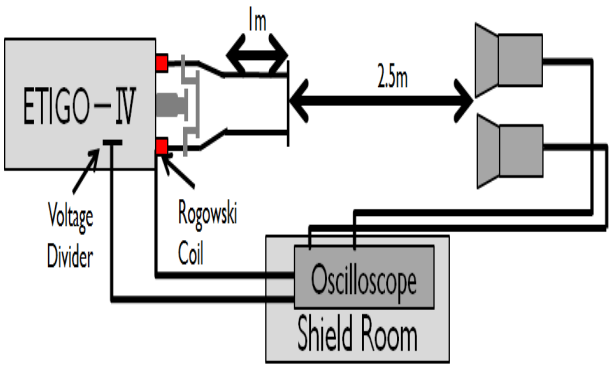


Fig. 2. Schematic diagram for frequency measurement of the microwave by the virtual cathode oscillator


Fig. 3. Outside appearance of ETIGO-IV.

abovementioned motion. The microwave is oscillated by the reciprocation and the vibration of the virtual cathode.

When microwave is oscillated by the reciprocation of electrons, the frequency is defined by

$$\omega_{ref} = \frac{\pi}{2\tau}. \quad \text{..... (1)}$$

$$\tau = \left(\frac{m\gamma_0}{2\pi n_0 e^2}\right)^{\frac{1}{2}}. \quad \text{..... (2)}$$

where $\omega_{ref}$ is the angular frequency of electrons of the reciprocation, τ is transit time between the cathode and the anode, $m$ is mass of the electron, $\gamma_0$ is the relativity factor, $n_0$ is the electron number density, and $e$ is the electric charge[3][4]. Another microwave oscillation is caused by the vibration of the virtual cathode. It is defined by following equation;[3],[4]

$$\omega_{osc} = \frac{4\pi}{3\tau}. \quad \text{..... (3)}$$

## 3. Experimental Setup

Figure 2 and 3 show a schematic diagram for frequency measurement of the microwave and outside appearance of a pulsed power generator "ETIGO-IV", respectively. In this experiment, diode voltage divided by the voltage divider, diode current, and the microwave are observed, using oscilloscope via a voltage prove, a Rogowsky coil, and two horn antennas, respectively.

## 4. Results and Discussion

### 4.1 Typical experimental data

Figure 4 shows the diode voltage, diode current, and microwave. In this experiment, the charge voltage was 22 kV, and the anode-cathode gap was 22 mm. Figure 5 also shows the Fourier Translate data of the microwave. Two large groups can be seen at range of 3-4 GHz and 5-6 GHz in the Fourier translate data. It is thought that the spectrum group of 3-4 GHz and 5-6 GHz is oscillated by reciprocating motion of the particle and by vibration of the virtual cathode, respectively. Figure 6 shows a result of time-frequency analysis. The darker color is, the stronger spectrum is. That shows that spectrum of 5-6 GHz at 50-150 ns and that of 3-4 GHz at 100-200 ns

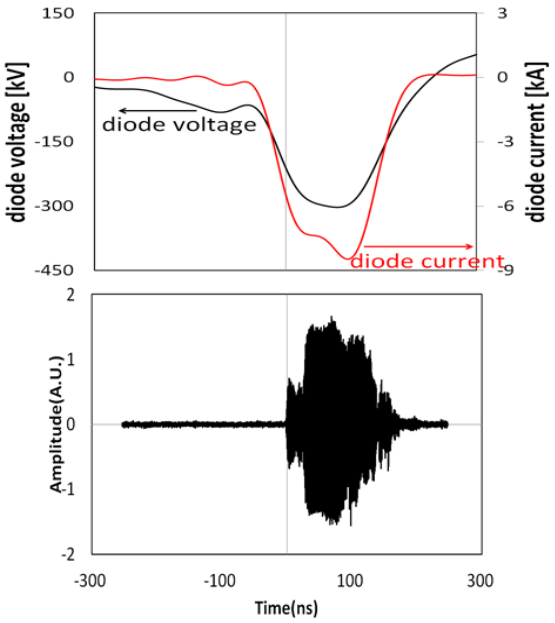


Fig. 4. Upper figure is the diode voltage and diode current wave forms, Bottom figure is the measured typical microwave

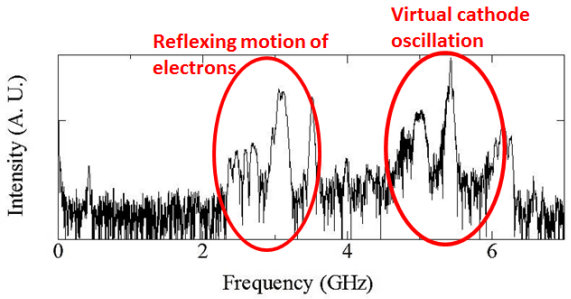


Fig. 5. Fourier transform of the microwave

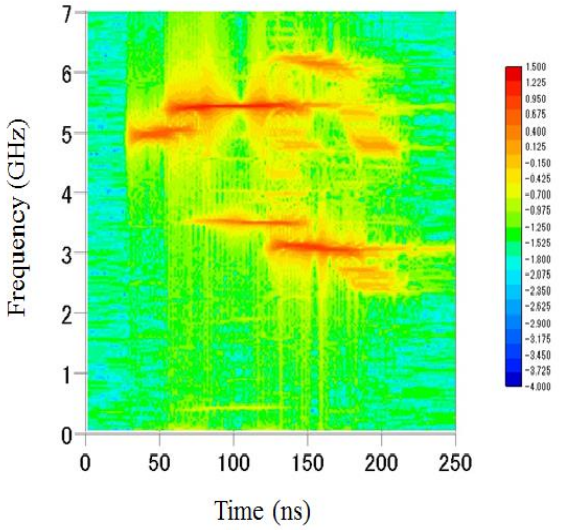


Fig. 6. Time - frequency analysis for the microwave

are stronger. Further, 3GHz oscillation is caused after 5 GHz oscillation. It means that the microwave by the reciprocating motion of the electrons is generated after that by the oscillation of virtual cathode.

### 4.2 Comparison of theoretical values and experimental data

Figure 7 shows the Fourier transforms of the microwaves generated by different charge voltage of the ETIGO-IV. The dot line is theoretical value of main frequency by reciprocating motion of the electrons. The solid line is theoretical value of main frequency by the vibration of the virtual cathode. Main frequencies (two groups of spectrum) of experimental data tend to increase with an increase of the charge voltage. Theoretical data also increases. Figure 8 shows the Fourier transforms of the microwaves for different anode - cathode gap. The theoretical values are also shown. Main

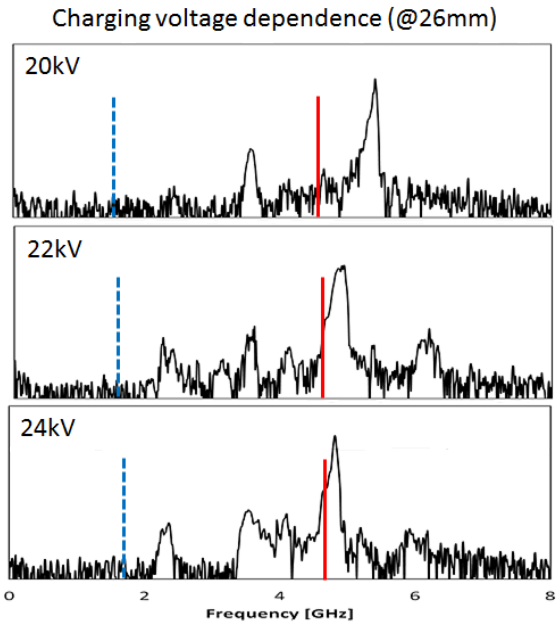


Fig. 7. Fourie transforms of the microwaves generated by different charging voltage of the ETIGO-IV. Charged voltage was 20, 22, and 24 kV. The dot line and solid line are theoretical values which show reciprocating motion of the particle and vibration of the virtual cathode respectively.

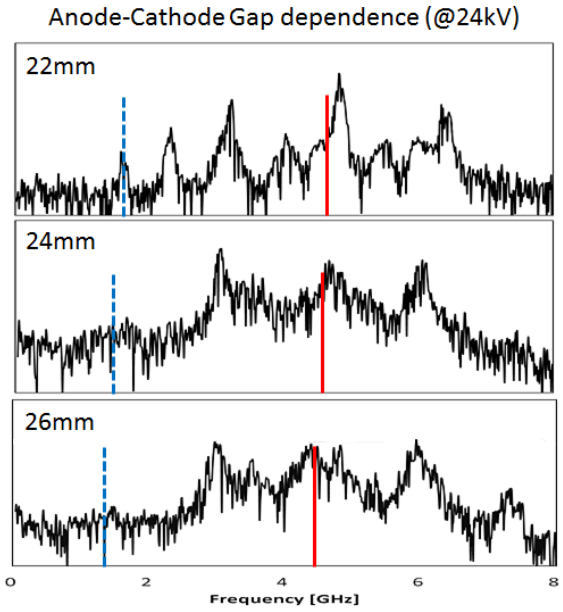


Fig. 8. Fourie transforms of the microwaves for different anode-cathode gap. A-K gap was 22, 24, and 26 mm. the dot line and solid line is theoretical values which show reciprocating motion of the particle and vibration of the virtual cathode respectively.

Frequencies (two groups of spectrum) of the experimental data tend to decrease with an increase of the gap. Theoretical data also decreases.

Figure 9 shows comparison of the experimental data and a simulation data. In this case, the charge voltage is 20 kV and Anode – Cathode gap is 22 mm. The simulation data was simulated by a MAGIC. Both of the experimental data and the simulation data have two groups of spectrum. However, the simulation data's spectrums are lower than the experimental data.

## 5. Conclusions

We measured frequency of the microwave by the Virtual Cathode Oscillator. It was confirmed that the frequency spectrum of the output microwave has two groups mainly 3-4 GHz and 5-6 GHz. Each spectrum group is due to the reciprocating motion of the particle and vibration of the virtual cathode. Each frequency depends on the charged voltage and the gap distance between the electrodes of the diode. Further, the numerical simulation result also has two spectrum groups. However, they are lower than the experimental data. This reason is considered in future.

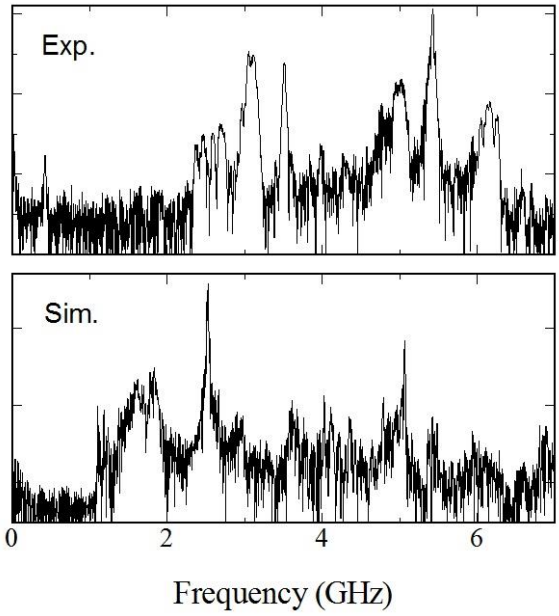


Figure 9 Comparison of Experimental data and Simulation data

## References

[1] D.J.Sullivan, J.E.Walsh, , and E.A..Coutsias : "Virtual cathode oscillator (vircator) theory," in *High Power Microwave Sources*, V.Granatstein and I.Alexeff,Eds. Norwood, MA:Artech House, pp.441-505 (1987)

[2] L.E.Thode,"Virtual-cathode microwave device research: Experiment and simuation,"in High Power Sources, V.Granatstein and I.Alexeff,Eds. Norwood, MA:Artech House, pp.507-562(1987).

[3] W.Jiang et al., "Mechanism of microwave generation by virtual cathode oscillation", American Institute of Physics,*Phys.Plasmas*,**2** pp.982–986 (1995).

[4] W.Jiang et al., "New configuration of a virtual cathode oscillator for microwave generation", American Institute of Physics,*Phys.Plasmas*,**2** pp.4635–4640 (1995).

# Considerations of Improvement of Energy Efficiency for Pulsed Power Generator with Semiconductor Opening Switch

Kodo Ogasawara, Tran Nam Son, Nobuhiro Aoyagi,
Taichi Sugai, Tokuchi Akira, Weihua Jiang

*Extreme Energy-Density Research Institute, Nagaoka University of Technology*

## ABSTRACT

As high efficiency high voltage pulsed power generator for industrial application we had developed an inductive energy storage circuit using a semiconductor opening switch. Initially, the energy is transferred from input capacitor $C_0$ to capacitor $C_1$ via a pulse transformer. Then, the energy of $C_1$ is transferred to capacitor $C_2$ via a magnetic switch. The energy transfer efficiency between capacitor $C_0$ and $C_2$ was 55 %. The main cause of the loss was the energy return from $C_0$ to $C_1$ and the loss of the magnetic switch. To improve it, inductance to primary side was added. Thereby a core of the magnetic switch was saturated before the energy return to the primary circuit and the energy transfer efficiency became 7 % higher.

## Keywords

Pulsed power, Semiconductor opening switch

## 1. Introduction

Pulsed power technology has been studied for industrial applications such as medical science, chemistry, civil engineering, biology, and environmentology [1].

As a pulsed power generator for industrial applications, we have studied an inductive energy storage (IES) system. It stores energy in an inductor by a current flow initially, and rapidly releases the energy to the load by opening the switch connected in parallel to the load. The pulse duration becomes short with an increase of the load impedance. Furthermore, its output voltage is determined by the current decreasing rate *dI/dt* which can be very high if the switch opens fast. To output a short high voltage pulse, an opening switch should interrupt a large current quickly and withstand high voltage. [2]

A semiconductor opening switch (SOS) has incredible properties, such as high current capacity, high pulse repetition rate, high withstand voltage, a current cutoff time on the order of nanosecond, and stable and long life-time operation [2][3].

We had developed an inductive energy storage circuit using a semiconductor opening switch as shown in Figure 1 [4]. However, energy efficiency of this structure is too low at present. Therefore, improvement of the energy transfer from an input to capacitor $C_2$ was attempted initially.

## 2. Operating principle of circuit

The operation process of the circuit shown in Fig.1 is described as follows. When the initial switch (IGBT) is turned on, capacitor $C_0$ which is initially charged by the high-voltage dc power supply, discharges through the loop of $C_0$–PT–$C_1$, resulting in charging of $C_1$ by PT voltage. A magnetic switch $MS_1$ saturates at the time of maximum $C_1$ voltage allowing $C_1$ discharge

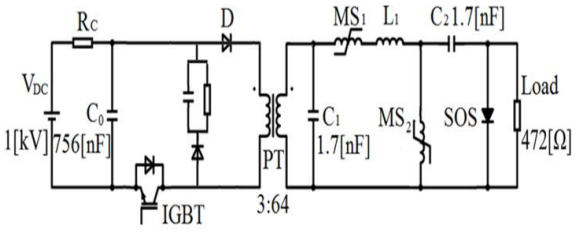


Fig. 1 Circuit diagram of the IES generator

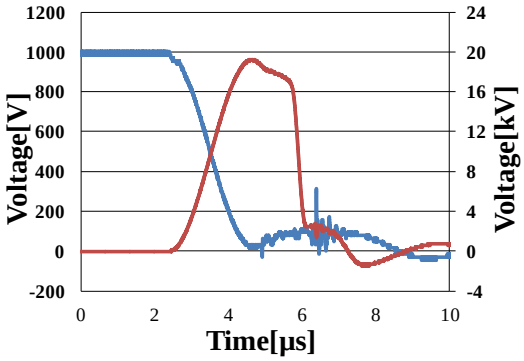


Fig. 2 Voltage waveforms of $C_0$ and $C_1$

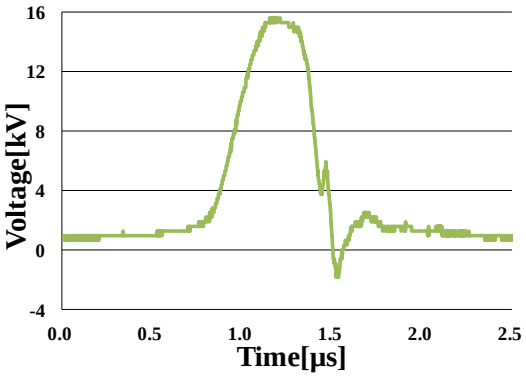


Fig. 3 Voltage waveform of $C_2$

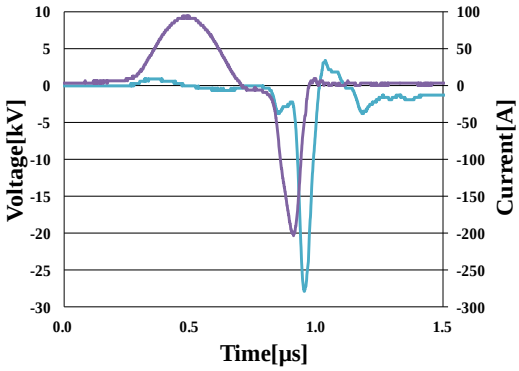


Fig.4 Output voltage and SOS current waveforms

through the loop of C1–MS1–L1–C2–SOS,resulting in charging of C2 and SOS forward current. A magnetic switch MS2 saturates at the time of maximum C2 voltage allowing C2 discharge through the loop of C2–MS2–SOS, resulting in SOS reverse current. At the time of peak reverse current, SOS diodes suddenly recover, and the inductively stored energy in MS2 is released to the load.

## 3. Result and Discussion

When the charge voltage of $C_0$ was 1 kV corresponding to the energy of 378 mJ, the peak voltage at $C_1$ was 19.2 kV, as shown in Figure 2, which corresponds to the stored energy of 313 mJ.

By the transfer from $C_1$, $C_2$ was charged to 15.6 kV, as shown in Figure 3, which corresponds to 208 mJ.

By the saturation of $MS_2$ core, the reverse current flows through SOS, and after reaching 203 A, it was interrupted at the cutoff time of 40 ns, as shown in Figure 4. By the current interruption, the pulsed voltage whose peak and FWHM are 27.8 kV and 32 ns, respectively, was outputted.

Table 1 shows the energy stored and consumed at each element and the energy transfer efficiency. The energy transfer efficiency from $C_0$ to $C_2$ was 55 %.

Figure 5 gives a detailed description of the $C_1$ voltage and the current flowing secondary side of the pulse transformer. The residual energy after the energy transfer from $C_1$ to $C_2$ was 7.49 mJ, corresponding to

Table 1 Peak voltage and the energy at each element and the energy transfer efficiency

| | $C_0$ 756[nF] | $C_1$ 1.7[nF] | $C_2$ 1.7[nF] | $L_{C2\text{-}L2\text{-}MS2\text{-}SOS}$ 5.95[μH] | Load 472[Ω] |
|---|---|---|---|---|---|
| Peak | 1.00 | 19.2 | 15.6 | | 27.8 |
| Peak Current[A] | | | | 203 | |
| Energy[mJ] | 378 | 313 | 208 | 123 | 65.5 |
| Efficiency[%] | 82.8 | | | | |
| | | 66.2 | | | |
| | | | 93.0 | | |
| | | | | 33.9 | |
| | 17.3 | | | | |

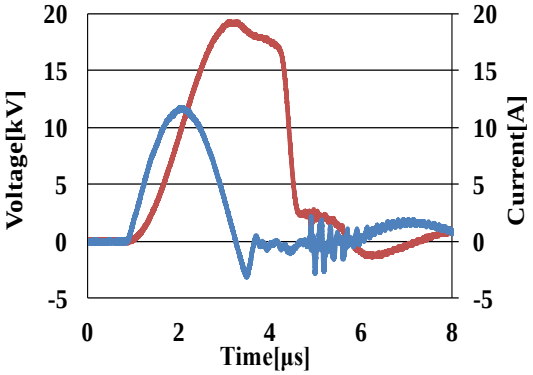


Fig. 5 Voltage and current waveforms at $C_1$

1.98 % of the total. It is a little bit influence. A fatal impact is that $C_1$ voltage decreased from 19.2 kV to 17.3 kV before the saturation of the $MS_1$ core. This energy loss was 60 mJ. The main cause of this voltage depression is energy return to the primary circuit owing to the inverse current of diodes in the primary circuit.

To prevent it, the $MS_1$ core should be saturated before the energy return. Two solutions were attempted for that. One is to decrease the turns of $MS_1$ to decrease the integral value of the $C_1$ voltage over time. The other is to increase inductance L in primary circuit to increase the rise time of the $C_1$ voltage.

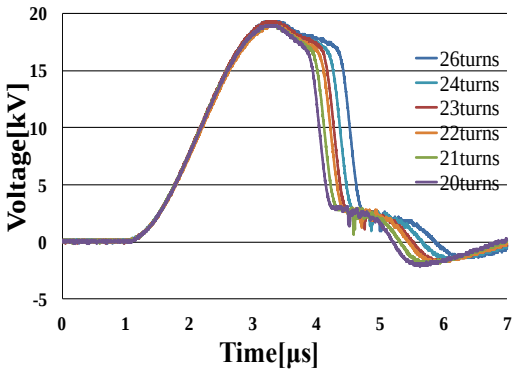


Fig. 6 Waveforms of $C_1$ voltage for each turns of $MS_1$

Table 2 Peak voltage at $C_1$ and $C_2$ for each turns of $MS_1$

| Number of turns | 26 | 24 | 23 | 22 | 21 | 20 |
|---|---|---|---|---|---|---|
| Voltage_C1[kV] | 19.2 | 19.2 | 19.2 | 19.0 | 19.0 | 19.0 |
| Voltage_C2[kV] | 15.6 | 15.6 | 15.6 | 15.3 | 15.3 | 15.3 |

### 3.1 Effect of $MS_1$ turns

Figure 6 show voltage waveforms of $C_1$ for each $MS_1$ turns. The pulse width of $V_{C1}$ decreased with a decrease in $MS_1$ turns, but the peak voltage also decreased when the $MS_1$ was less than 22 turn. The main cause of this voltage decrease is the increase of the core loss at the $MS_1$. Table 2 shows the peak voltage of $C_1$ and $C_2$. The decrease of the $C_1$ voltage led to the decrease of $C_2$ voltage. Therefore, the efficiency of the generator was improved by the variation of $MS_1$.

### 3.2 Effect by increasing inductance

As indicated in Figure 7, when the inductance L in the primary circuit increased, the rise time of $V_{C1}$ swelled. Thereby the $MS_1$ core was saturated before the energy return to the primary circuit. Although the peak of $V_{C1}$ decreased with an increase of inductance L

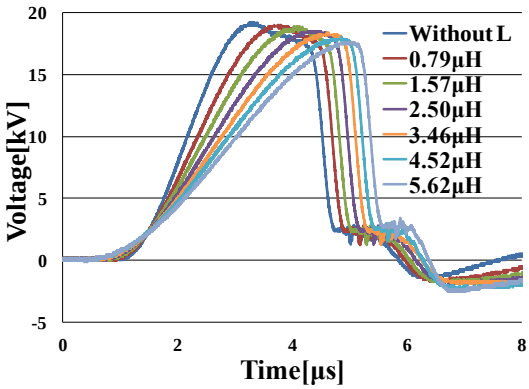


Fig. 7 Waveforms of $C_1$ voltage
for each inductance in primary circuit

Table 3 Variation of each parameter of $C_1$ and $C_2$
for each inductance in primary circuit

| | Without L | 0.79[μH] | 1.57[μH] | 2.50[μH] | 3.46[μH] | 4.52[μH] | 5.62[μH] |
|---|---|---|---|---|---|---|---|
| Voltage $C_1$[kV] | 19.2 | 19.0 | 18.9 | 18.5 | 18.4 | 18.1 | 17.6 |
| Voltage $C_2$[kV] | 15.6 | 15.9 | 15.9 | 16.2 | 16.6 | 16.5 | 16.2 |
| Energy $C_1$[mJ] | 313 | 307 | 304 | 291 | 288 | 278 | 263 |
| Energy $C_2$[mJ] | 208 | 216 | 216 | 224 | 234 | 232 | 223 |
| Efficiency $C_0$-$C_2$[%] | 55.0 | 57.0 | 57.0 | 59.2 | 62.0 | 61.4 | 59.1 |

because the MS1 core was saturated while $V_{C1}$ rose, $V_{C2}$ was the highest at 16.6 kV when L = 3.46 $\mu$H. Table 3 represents that the energy transfer efficiency from $C_0$ to $C_2$ is varied by inductance. The energy efficiency from $C_0$ to $C_2$ for L = 3.46 $\mu$H was 62.0 % which is 7 % higher than that without L.

**4. Conclusion**

In the IES generator using the SOS, the energy efficiency from $C_1$ to $C_2$ was small because of the energy return to the primary circuit. Two solutions were attempted to solve it.

As one solution, the pulsed width was decreased by decreasing turns of $MS_1$. However, the peak voltage of $V_{C1}$ and $V_{C2}$ decreased.

As the other solution, the inductance in the primary circuit was increased for the increase of the rise time of $V_{C1}$. Thereby, the $MS_1$ core was saturated before the energy return to the primary circuit, and the energy transfer efficiency from $C_0$ to $C_2$ became 7 % higher.

## References

[1]Taichi Sugai, Wei Liu, Akira Tokuchi, Weihua Jiang, "Influence of a Circuit Parameter for Plasma Water Treatment by an Inductive Energy Storage Circuit Using Semiconductor Opening Switch" IEEE TRANSACTIONS ON PLASMA SCIENCE, VOL. 41, NO. 4 (2013)

[2] J. Mankowski and M. Kristiansen, "A review of short pulse generator technology" IEEE TRANS. PLASMA SCI., VOL. 28, NO. 1, (2000)

[3] Igor V. Grekhov, Gennady A. Mesyats, "Physical Basis for High-Power Semiconductor Nanosecond Opening Switches" IEEE TRANSACTIONS ON PLASMA SCIENCE, VOL. 28, NO. 5, (2000)

[4]Tomoyuki Yokoo, Weihua Jiang et al., "Repetitive Pulsed High-Voltage Generator Using Semiconductor Opening Switch for Atmospheric Discharge" IEEE TRANSACTIONS ON PLASMA SCIENCE, VOL. 36, NO. 5, (2008)

# Evaluation of Plasma Water Treatment by Pulsed Power Generator Using Semiconductor Opening Switch

Taichi Sugai, Nobuhiro Aoyagi, Tran Nam Son, Kodo Ogasawara,
Weihua Jiang, Akira Tokuchi*, Yasushi Minamitani**

*Nagaoka University of Technology*

**Pulsed Power Japan Laboratory, Nagaoka University of Technology*

***Yamagata University*

## ABSTRACT

We investigated a water treatment using plasma generated by Inductive Energy Storage (IES) circuit using semiconductor Opening Switch (SOS). For improvement of energy efficiency of this method, the water treatment was carried out, varying turn ratio of pulse transformer (PT). The result showed that the ratio of thermal loss to the discharge energy approached a constant value with an increase of the pulse width of the output voltage. The energy consumed at the entire water treatment system to decompose indigo carmine, decreased with an increase of the turn ratio of the PT because of a decrease of the circuit loss.

## Keywords

Inductive energy storage, Semiconductor opening switch, Streamer discharge, Water treatment

## 1. Introduction

Recently, water treatment using a pulsed streamer discharge in water has been studied [1, 2]. As pulsed streamer discharge in water is generated, many active species, including ozone and OH radicals, are generated. Ultraviolet rays and shock waves are also generated in water in this process. All of these products can be utilized for the decomposition of organic compounds.

We have studied a water treatment method that sprays waste water droplets from the top of a pulsed discharge area [3]. This method has higher energy efficiency than other methods [4].

However, it is difficult to implement this method in a practical application because it consumes a significant amount of power. To solve this problem, we attempt to develop a power source for the water treatment that has high efficiency, low losses, and low cost.

A past study has shown that the optimum pulse waveform that is applied between electrodes for plasma generation should have a short pulse width and a fast rise time [5]. This pulse increases the treatment efficiency because the plasma is stopped at the phase of the primary streamer, which wastes less energy. The secondary streamer consumes more energy [5-7]. Therefore, a required pulsed power generator for the water treatment should output the abovementioned pulse with a low circuit loss and a high repetition rate. Additionally, an entire circuit should be the solid state because the life-time of a generator must be semi-permanence.

An inductive energy storage (IES) method using a semiconductor opening switch (SOS) and a capacitive energy storage (CES) method by a magnetic pulse compression circuit are suitable to the abovementioned requirement. However, they have the large circuit loss because a process of the amplification and the compression is required. Hence, we have attempted to decrease the circuit loss of the

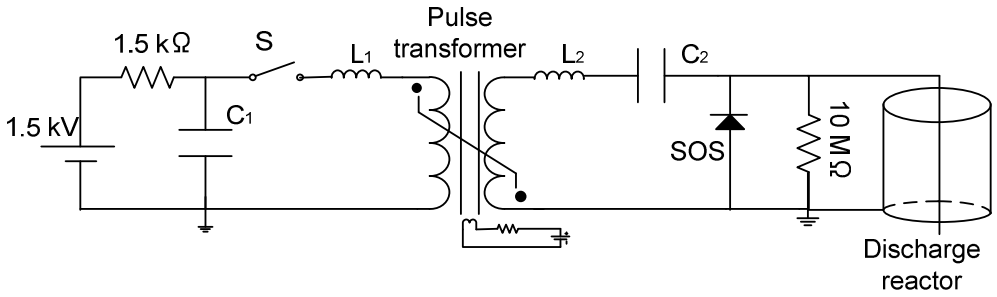


Fig. 1. Pulsed power generator using SOS.

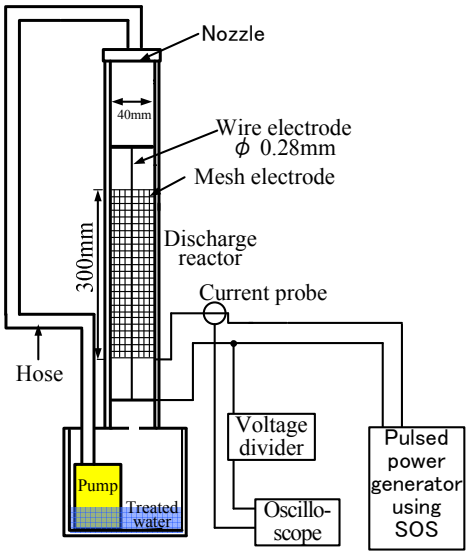


Fig. 2. Reactor for the water treatment using pulsed discharge generated in air by spraying water droplets.

IES method using the SOS, which is shown in Figure 1. The energy stored to the inductor is transferred to the load by the SOS. The current flowing the load is attenuated according to the time constant $L_2/R$, where $L_2$ and $R$ are the inductance in the secondary circuit in Figure 1 and the impedance of the load, respectively. Because the impedance $R$ of the streamer discharge is high, the pulse width of the output voltage is short.

A past study has shown that the energy transfer efficiency is improved by the decrease of the capacitance of capacitor and the increase of parasitic inductance, in the secondary circuit because it decreases the SOS loss. On the other hand, the pulse width of the output becomes long owing to the increase of parasitic inductance in the secondary circuit. We report how the energy transfer efficiency and the pulse width that are varied by the variation of the capacitance and the inductance affect the water treatment efficiency.

## 2. Experimental Setup

### 2.1 IES circuit using SOS

The detailed circuit is shown in Figure 1. It consists of the primary and secondary circuits via a pulse transformer (PT). The primary circuit consists of a capacitor with capacitance $C_1$, a switch (SI thyristor), and the inductance in the primary circuit $L_1$; the secondary circuit consists of a capacitor with capacitance $C_2$, the inductance in the secondary circuit $L_2$, and the SOS. The SOS used is the SOS-60-4 made by the Institute of Electrophysics.

The circuit operation is described as follows. When the initial switch (SI thyristor) is turned on, capacitor $C_1$ (initially charged by a high-voltage dc power supply) discharges through the loop of $C_1$-$L_1$-PT-SOS-$C_2$, resulting in a SOS forward current and charging of capacitor $C_2$ by the PT voltage. When the PT saturates at the time of maximum capacitor $C_2$ voltage, capacitor $C_2$ discharges through the loop $C_2$-SOS-PT-$L_2$, resulting in a SOS reverse current. Then, energy does not return to the primary circuit because of the PT saturation. During the reverse current, the SOS diodes suddenly recover, and the inductively stored energy in inductor $L_2$ is discharged to the load.

### 2.2 Water treatment reactor

The water treatment reactor is shown in Figure 2. The system is composed of a reactor module and a water tank module. In the reactor module,

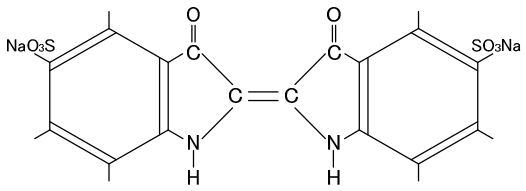


Fig. 3. Structural formula of indigo carmine.

wire-to-cylinder coaxial electrodes are installed in the reactor cylinder, with an inner diameter of 40 mm. The wire electrode is made of stainless steel wire (diameter = 0.28 mm), and the cylindrical electrode is made of stainless steel wire mesh (diameter = 38 mm, length = 300 mm, and mesh size = 1.2 mm × 1.2 mm).

The water tank is provided with a pump for circulation of the treated water. The treated water is transformed to droplets by the nozzle and sprayed into the reactor from the top of the lid. The diameter of the droplets is 0.5~1.5 mm.

## 3. Influence of PT Turn Ratio on Water Treatment

### 3.1 Experimental method

The water treatment was performed by the IES generator whose PT turn ratio was 2:14, 2:22, 2:32, or 2:48. The PT turn ratio was varied to vary the capacitance and the inductance in the secondary circuit. $C_1$ was 250 nF, and $C_2$ was equal to $a^2$ times of $C_1$ to transfer almost all energy from capacitor $C_1$ to capacitor $C_2$, where $a$ is the turn ratio of the PT, i.e., $C_2$ was 5, 2, 1, and 0.4 nF when the PT turn ratio was 2:14, 2:22, 2:32, and 2:48, respectively. When the secondary turns are varied from 14 to 48, the inductance in the secondary circuit after the PT saturation increased from 3 to 6.5 μH. The charge voltage of capacitor $C_1$ was 1.50kV for the turn ratio of 2:14, 2:22, and 2:32, or was 1.25 kV for 2:48. The repetition rate was 100 pps.

For the sample water, an indigo carmine ($C_{18}H_8N_2Na_2O_8S_2$) solution was used. It was a blue-colored dye, and its decomposition ratio can be easily determined on the basis of its absorption of light. Its structure formula is shown in Figure 3. Indigo carmine was dissolved in purified water. The concentration of the water solution was 20 mg/L. One liter of this indigo carmine solution was sprayed at the rate of 3L/min. The absorbance of the indigo carmine solution in the 250-nm-wavelength light was measured for each treatment time to investigate the rate of decomposition of the benzene ring of the indigo carmine. The benzene ring of the indigo carmine corresponds to the absorbance in the 250 nm. To measure the absorbance, the indigo carmine solution was placed in a cuvette with a thickness of 10 mm and set to a UV and visible-light spectrometer (SHIMADZU, UV-1800).

The voltage and current waveforms between the electrodes were observed using an oscilloscope (LeCroy, WaveRunner6030) via probes. A 1/1000 high-voltage probe (LeCroy, PEE20kV) and a 0.5-V/A current probe (Pearson, Model6595) were used to measure the electrode voltage and current, respectively.

### 3.2 Characteristics of output voltage and current

The voltage and current waveforms shown in Figure 4(a) and 4(b) appeared in the electrode during the water treatment when the PT turn ratio is 2:14 and 2:48, respectively. The voltage and current in the case of 2:48 was greater than that of 2:14. Table 1 express the characteristics of the IES circuit for each turn ratio. The energy transfer efficiency and the pulse width of the pulsed voltage increased with an increase in the turn ratio. The increase of the energy transfer efficiency is owing to the increase of the induced voltage $L_2dI/dt$, where $I$ is the reverse current in secondary circuit [8]. The increase of the turn ratio leads to the increase of $L_2$; however, the variation of $dI/dt$ was small because $C_2$ was decreased with an increase of the turn ratio. The discharge energy in the case of 2:48 was similar to that of 2:32 because of the difference of charge voltage of capacitor $C_1$. The increase of the pulse width is because the attenuation time of the output current increased owing to an increase of the time constant $L_2/R$ [8].

### 3.3 Water treatment result

Figure 5 shows the result of the treatment of the indigo carmine with different turn ratios. The

Table 1. Characteristics of IES circuit using SOS.

| Turn ratio of PT | $C_1$ (nF) | $C_2$ (nF) | Energy stored to $C_1$ (mJ) | Voltage applied to the electrode | | Discharge energy (mJ) | Energy transfer efficiency (%) ($C_1$→Load) |
|---|---|---|---|---|---|---|---|
| | | | | Maximum (kV) | FWHM (ns) | | |
| 2:14 | 250 | 5 | 281 | 27.7 | 31 | 14 | 4.9 |
| 2:22 | 250 | 2 | 281 | 29.2 | 36 | 34 | 12.2 |
| 2:32 | 250 | 1 | 281 | 31.4 | 41 | 51 | 18.1 |
| 2:48 | 250 | 0.4 | 195 | 29.4 | 48 | 49 | 25.1 |

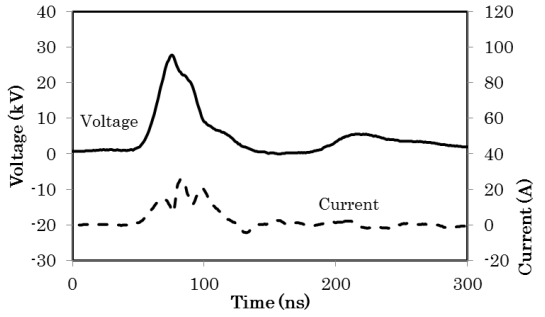


(a) Turn ratio 2:14, $C_2$=5 nF, $L_2$=3 μH

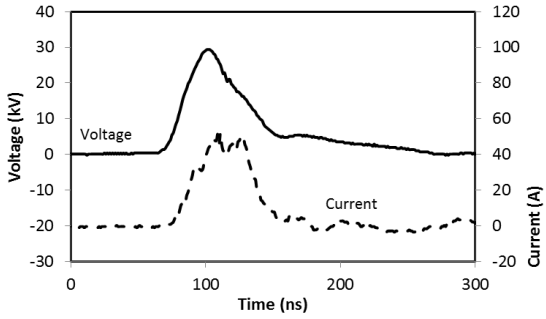


(b) Turn ratio 2:48, $C_2$=0.4 nF, $L_2$=6.5 μH

Fig. 4. Voltage and current waveforms applied to the electrode for each turn ratio of PT.

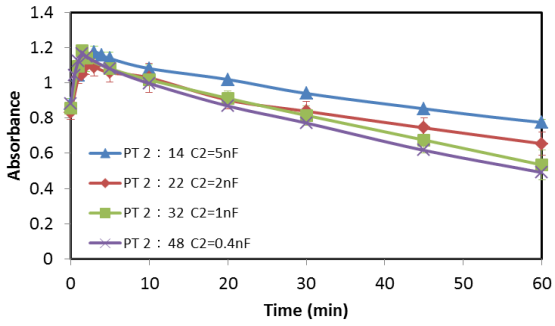


Fig. 5. Time variation of absorbance of wavelength 250 nm for each turn ratio.

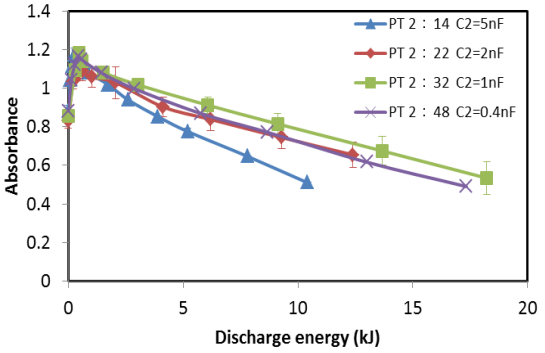


Fig. 6. Absorbance of wavelength 250 nm as a function of discharge energy. The parameter is the turn ratio of the PT and the capacitance $C_2$.

horizontal axis represents the treatment time, and the vertical axis represents the absorbance of the indigo carmine in the 250-nm-wavelength light. The decrease of the absorbance means the decomposition of the benzene ring of the indigo carmine. Initial absorbance was 0.85. The absorbance first increased at the beginning of the treatment, then decreased continuously. The increase in absorbance can be attributed to the by-product generated by the discharge, e.g., $H_2O_2$ and $NO_3^-$, which absorb the 250-nm-light. In the case of 2:14, 2:22, and 2:32, the absorbance decreased more rapidly with larger turn ratio. This is because active species increased with an increase of the discharge energy owing to an increase of the turn ratio.

The absorbance of the indigo carmine as a function of the energy consumed at the discharge load is shown in Figure 6. The discharge energy was calculated from the waveform of the discharge load, as shown in Figure 4. In the case of 2:14, the discharge energy needed to decrease the absorbance from 0.85 to 0.5 was about 10 kJ which was smaller energy than that of other turn ratio. On the other hand, in the other turn ratio, the discharge energy needed to decrease the absorbance from 0.85 to 0.5 was the

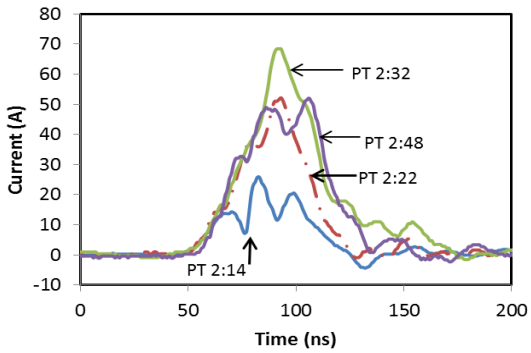


Fig. 7. Current waveforms at discharge load

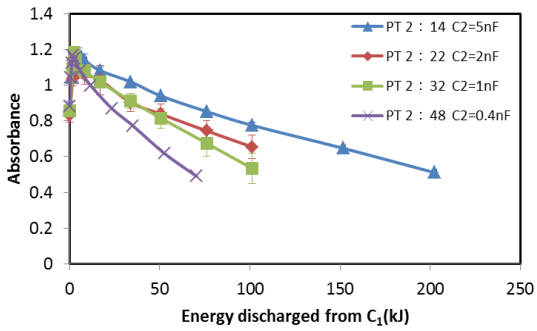


Fig. 8. Absorbance of wavelength 250 nm as a function of energy discharged from $C_1$. The parameter is the turn ratio of the PT and the capacitance $C_2$.

same at 17-18 kJ. Hence, the energy efficiency became higher in the case of 2:14, but was not varied in the case of turn ratios which are higher than 2:22. This result can be explained from the difference of the thermal loss of a primary streamer and a secondary streamer as following. A past study has shown that thermal loss occurs at the secondary streamer phase, owing to the large current through the plasma channels generated by the primary streamers [5]-[7]. Now, the load current waveforms for each turn ratio are shown in Figure 7. The duration time of the current increased with an increase of the turn ratio. The propagation rate of the primary streamer is 1.8-3.3 mm/ns, and the radius of the electrode is 18 mm; thus, the propagation time of the primary streamer is less than 10 ns. The secondary streamer appears after the propagation of the primary streamer. Therefore, almost all current indicated in Figure 7 is the phase of the secondary streamer which causes the thermal loss. When the duration time of the discharge is short, the ratio of the thermal loss to the discharge energy is lesser because the influence of the primary streamer is strong. This is the reason why the discharge energy needed to decrease the absorbance in the case of 2:14 was smaller. With an increase of the duration time, the ratio of the thermal loss to the discharge energy increases but approaches a constant value because the influence of the secondary streamer is strong and the ratio of the thermal loss at the secondary streamer phase is constant. This is the reason why the discharge energy needed to decrease the absorbance in the case of turn ratios which are higher than that of 2:22, was the same.

The absorbance of the indigo carmine as a function of the input energy, i.e., the energy discharged from the capacitor $C_1$ is shown in Figure 8. It is the most important that the decrease ratio of the absorbance shown in Figure 8 is high because it corresponds to the energy efficiency of the entire water treatment system. In the case of 2:14, the energy needed to decrease the absorbance from 0.85 to 0.5 was about 200 kJ which was larger than that of other turn ratio. In the case of 2:14, the ratio of the thermal loss to the discharge energy was lowest, but the energy transfer efficiency was lowest at 4.9%. This means that the circuit loss increased the input energy needed to decrease the absorbance. The input energy needed to decrease the absorbance decreased with an increase in the turn ratio. In the case of 2:48, the input energy needed to decrease from 0.85 to 0.5 was about 70 kJ which was 35% smaller than that of 2:14. In the turn ratio which is higher than 2:22, the ratio of the thermal loss to the discharge energy was the same. Therefore, the reason why the input energy needed for the decrease of the absorbance in the case of the turn ratio which is higher than that of 2:22 decreased with an increase in the turn ratio is the decrease of the circuit loss.

## 4. Conclusion

The turn ratio of the PT, and the parasitic

inductance and the capacitance in the secondary circuit affects the energy transfer efficiency and the pulse width of the output voltage. It was investigated how that variation affects to the water treatment.

For the influence of the pulse width, when the FWHM is until 48 ns, the ratio of the thermal loss to the discharge energy approached a constant value with an increase of the pulse width. From that result, we considered that the ratio of the thermal loss to the discharge energy at the secondary streamer phase is constant.

For the influence of the energy transfer efficiency, the input energy needed for decomposition of the indigo carmine decreased with an increase of the energy transfer efficiency because of the decrease of the circuit loss. When the ratio of the circuit loss was low, the ratio of the thermal loss by the discharge was high; however the influence of the circuit loss on the water treatment system was greater than that of the thermal loss.

At the IES generator using the SOS, the output of the short pulsed voltage and the high energy transfer efficiency are related to the trade-off. Hence, the above-mentioned proves that high energy transfer efficiency is required for high water treatment efficiency than the output of a short pulsed width.

## References


[1] B. Sun M. Sato, and J. S. Clements, "Optical study of active species produced by a pulsed streamer corona discharge in water", *J. Electrostatics*, **39**, 3, pp.189–202 (1997).

[2] P. Bruggeman and C. Leys, "Non-thermal plasmas in and in contact with liquids", *J. Phys. D: Appl. Phys.*, **42**, pp.1–28 (2009).

[3] Y. Minamitani, S. Shoji, Y. Ohba, and Y. Higashiyama, "Decomposition of dye in water solution by pulsed power discharge in water droplets spray", *IEEE Trans. Plasma Sci.*, **36**, 5, pp.2586–28 (2008).

[4] M. A. Malik, "Water purification by plasmas: Which reactors are most energy efficient?", *Plasma Chem. Plasma Process*, **30**, pp.21–31 (2010).

[5] T. Sugai, T. Suzuki, Y. Minamitani, and T. Nose, "Investigation of optimum applied voltage for water treatment by pulsed streamer discharge in air-sprayed droplets", *Electrical Engineering in Japan*, **180**, 2, pp.1–8 (2012).

[6] T. Namihira, S. Tsukamoto, D. Wang, S. Katsuki, R. Hackam, H. Akiyama, Y. Uchida, and M. Koike, "Improvement of $NO_X$ removal efficiency using short-width pulsed power", *IEEE Trans. Plasma Sci.*, **28**, 2, pp.434–442 (2000).

[7] T. Namihira, D. Wang, S. Katsuki, R. Hackam, and H. Akiyama, "Propagation velocity of pulsed streamer discharge in atmospheric air", *IEEE Trans. Plasma Sci.*, **31**, 5, pp.1091–1094 (2003).

[8] T. Sugai, W. Jiang, A. Tokuchi, and Y. Minamitani, "Improvement way of energy efficiency for plasma water treatment by pulsed high-voltage generator using semiconductor opening switch", *The Paper of Joint Technical Meeting on "Plasma Science and Technology" and "Pulsed Power Technology", IEEJ*, PST-12-110, PPT-12-133 (2012.12).

# Spectroscopic Measurement of Discharge Plasma on Treatment of Volatile Organic Compound by High-Pressure, Pulsed Glow Discharge

Masayuki Onda, Keishi Fujisawa, Shinya Yamada, and Go Imada

*Niigata Institute of Technology*

## ABSTRACT

High-pressure, pulsed glow discharge is applied to treatment of volatile organic compound (VOC) in gaseous atmosphere. Formaldehyde is diffused into a treatment chamber filled up with dry air around atmospheric pressure. The peak power of the discharge reaches 189 MW with the pulse duration of 50 ns. The spectrum of light emission form the discharge is measured to estimate the treatment process. The strong lines of N and O are confirmed, while the line of OH radical are weak. It indicates that electron impact with the formaldehyde is considerable path for the VOC treatment.

## Keywords

Pulsed power, Glow discharge, Volatile organic compound, Spectroscopic measurement, Gas treatment

## 1. Introduction

Air pollution caused by a volatile organic compounds (VOC) tends to induce a problem of human health [1]. A few apparatuses are developed to treat the VOC in flue gas, where chemicals adsorb the VOC. Since no chemicals are used in the treatment system, on the other hand, some treatment methods using a discharge are developed [2]-[4].

In this paper, a high-pressure, pulsed glow discharge is applied to treat a formaldehyde in an atmospheric pressure air. To estimate chemical reactions in the treatment process, a spectrum of light emission form the discharge is measured.

## 2. Experimental Setup

### 2.1 Gas treatment apparatus

Figure 1 shows the schematic diagram of gas treatment apparatus by the high-pressure, pulsed glow discharge. The apparatus is modified from an excimer laser device. The electrical circuit to excite the discharge is conventional charge-transfer type circuit, where the capacitance of capacitor is as follows; $C_1$ = 56 nF and $C_2$ = 32 nF. The storage capacitor $C_1$ is charged up to 28 kV with a direct-current high-voltage power supply. The charge is transferred from $C_1$ to $C_2$ just after the gap switch is closed with the signal from the pulse generator, and then the UV light emitted from discharge at the pre-ionization pins ionizes the gas before the discharge occurs and the voltage of $C_2$ rises gradually. When the voltage of $C_2$ reaches a breakdown voltage

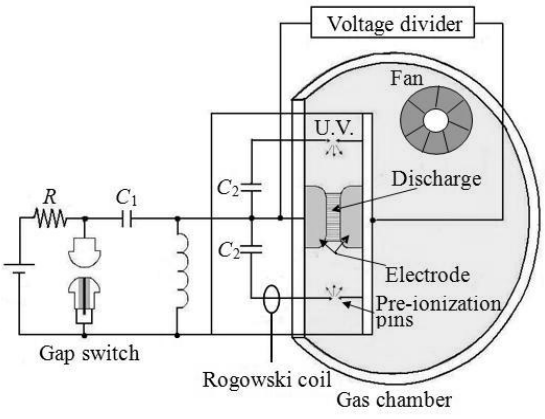


Fig. 1 Schematic diagram of gas treatment apparatus by high-pressure, pulsed glow discharge.

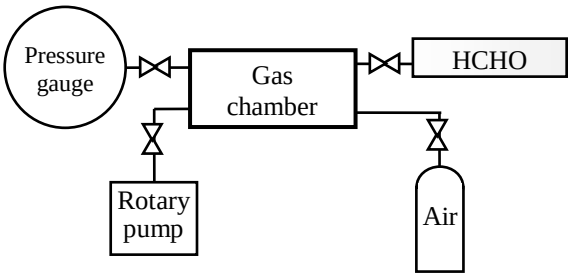


Fig. 2 Block diagram of gas and volatile organic supply system.

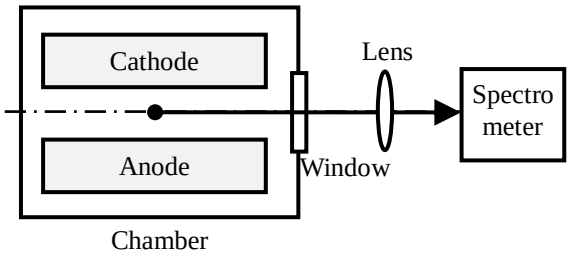


Fig. 3 Arrangement of spectroscopic measurement.

of the gap at the electrode, the discharge occurs between the anode and cathode. The discharge voltage (*V*) and the current (*I*) are measured with a resistive voltage divider and a current transformer, respectively, and recorded on a digital storage scope. The electrodes, made of nickel-plated aluminum, consist of semi-cylindrical anode and cathode where the width, length, gap distance, and radius of curvature are 35, 690, 20, and 100 mm, respectively. The discharge volume is estimated to be 0.48 L. The capacity of the gas chamber is 50 L.

Figure 2 shows the block diagram of gas and volatile organic supply system. The gas chamber is vacuumed to 30 Pa to purge it, and then it is filled with dry air at 20 kPa. The formaldehyde (HCHO) solvent, as a VOC, is evaporated into the gas. The initial concentration of HCHO is around 500 ppm. The concentration of HCHO in the gas is measured with a gas detector tube (GASTEC Co., #91M) before and after the discharge applied.

### 2.2 Spectroscopic measurement system

Figure 3 shows the arrangement of spectroscopic measurement. The light emission from the center of discharge is focused onto the inlet slit of the spectrometer (KLV Inc., SPM-002) with the fused silica lens through the fused silica window. The measured wavelength is in the range of 200 to 600 nm.

## 3. Results and Discussion

### 3.1 Discharge characteristics

(a) Discharge in air

Figure 4 typically shows the time evolution of voltage and current of the discharge in the air. The breakdown voltage and peak current are estimated to be 17 kV and 23 kA, respectively. During the first half-cycle of discharge current, the pulse width is approximately 50 ns (FWHM).

Figure 5 shows the discharge power *P*. The power

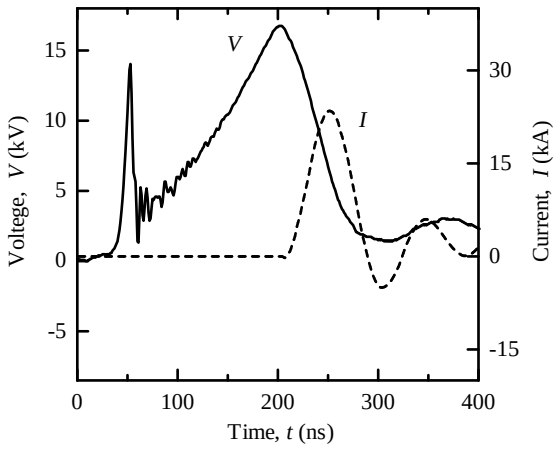


Fig. 4 Discharge voltage and current in air.

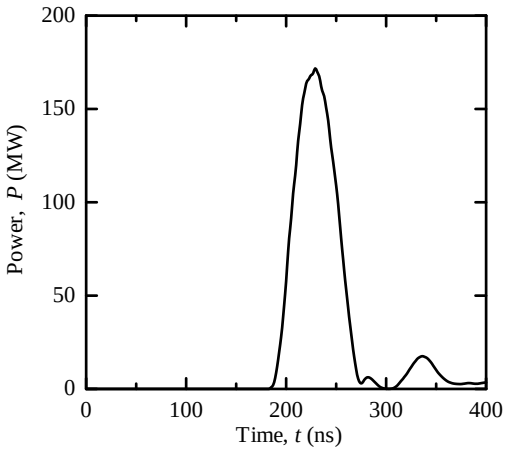


Fig. 5 Discharge power in air.

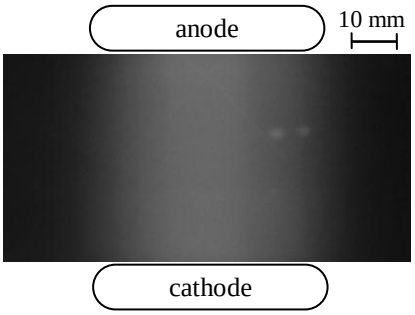


Fig. 6 Light emission from discharge in air.

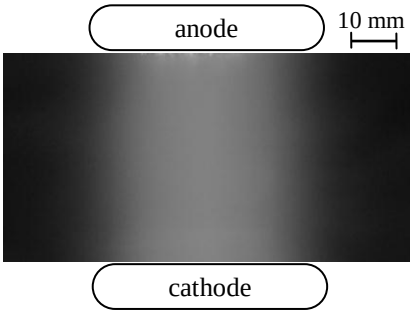


Fig. 9 Light emission from discharge in air containing HCHO.

is calculated as the product of $V$ and $I$. The peak power reaches 171 MW.

Figure 6 shows the bulb-exposure direct image of light emitted from the discharge in the air. The homogeneous and wide glow discharge is obtained in the air.

(b) Discharge in air containing HCHO

Figure 7 typically shows the time evolution of voltage and current of the discharge in the air containing 500 ppm of HCHO. The breakdown voltage and peak current are estimated to be 16 kV and 26 kA, respectively. The current slightly increases compared with that in the air. The sustained voltage of the discharge is estimated to be 5 kV.

Figure 8 shows the discharge power $P$. The peak power reaches 189 MW. Since the pulse width is approximately 50 ns, the injected energy into the discharge is calculated to be 2 mWh/pulse.

Figure 9 shows the bulb-exposure direct image of light emitted from the discharge. The homogeneous and wide glow discharge is also obtained.

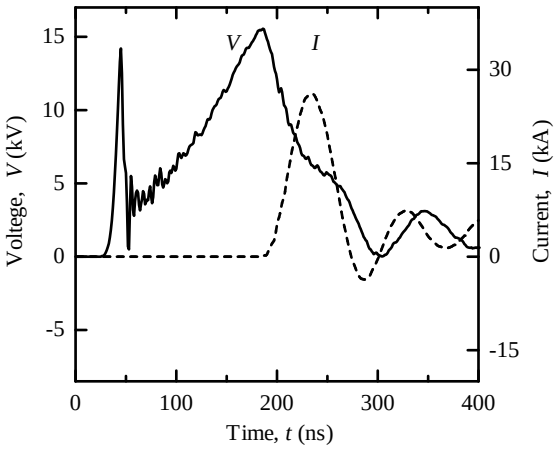


Fig. 7 Discharge voltage and current in air containing HCHO.

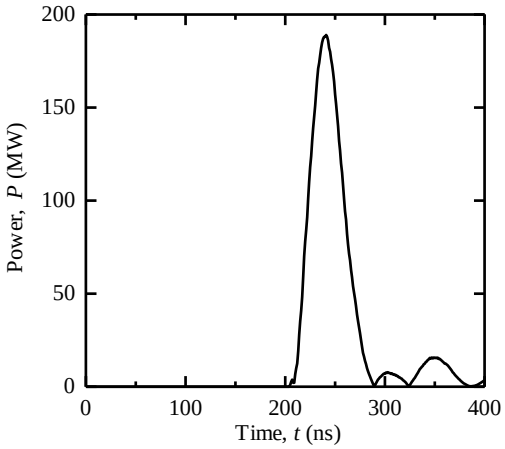


Fig. 8 Discharge power in air containing HCHO.

### 3.2 Treatment of HCHO

Table 1 summarize the concentration of HCHO and ozone (O) before and after the pulsed discharge. The concentration of HCHO decreases from 500 ppm to 300 ppm. It is found that the high-pressure, pulsed glow discharge has ability to treat the VOC in the air. Since the ozone has not been detected, it may be consumed to treat the HCHO.

Table 1 Concentration of HCHO and O.

| Initial HCHO | After 10 shots of discharge | |
|---|---|---|
| | HCHO | O |
| 500 ppm | 300 ppm | 0 ppm |

### 3.3 Spectroscopic measurement of discharge plasma

Figure 10 shows the emission spectrum of the discharge in the air. The line emissions from nitrogen and oxygen are confirmed. Since the weak line emission is confirmed at 434 nm, the hydrogen is present in minor amounts in the discharge plasma.

Figure 11 shows the emission spectrum of the discharge on HCHO treatment in air. Here, the initial concentration of HCHO is 500 ppm. The line emissions from nitrogen and oxygen are also confirmed. We find that the line emission of hydrogen at 434 nm increases in intensity compared with the discharge in the air. It indicates that the electrons *e* in the discharge direct collide with HCHO, and then the following reaction occurs in the discharge plasma..

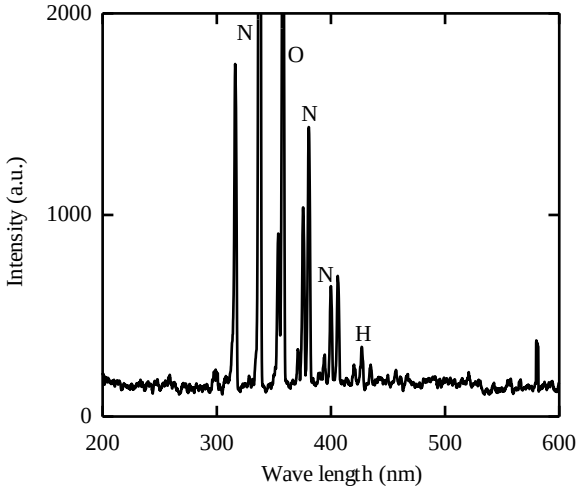


Fig. 10 Emission spectrum of discharge in air.

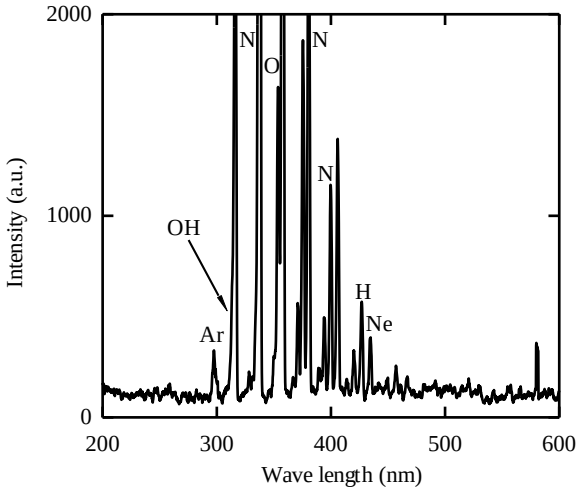


Fig. 11 Emission spectrum of discharge on HCHO treatment in air.

$$e\ (\text{fast}) + \text{HCHO} \rightarrow \text{H} + \text{HCO} + e\ (\text{slow}), \qquad (1)$$

Since the strong line emission is seen at 357 nm, the OH radical might be generated as the following reaction.

$$\text{O} + \text{HCHO} \rightarrow \text{OH} + \text{HCO}, \qquad (2)$$

Unfortunately, it is difficult to determine the line emission from the OH radical because the strong line emissions from argon and oxygen appear around 310 nm which is the wavelength of the emission from the OH radical. When we observe the spectrum carefully, a shoulder is recognized on left side of strong line at 310 nm. It indicates that the OH radical is present in the discharge plasma. Therefore, the following reaction contributes to the treatment of HCHO.

$$\text{OH} + \text{HCHO} \rightarrow \text{H}_2\text{O} + \text{HCO}, \qquad (3)$$

In this reaction, the HCO radical is produced as by-products.

When rearranging the results,

(1) the bond in the HCHO molecule is broken with the direct impact of discharge electron,

(2) the HCHO is treated with the O and OH radicals which are generated in the discharge plasma.

## 4. Conclusions

In the treatment of formaldehyde in an atmospheric pressure air by the high-pressure, pulsed glow discharge, the electron impact and the radical reaction act on the decomposition of HCHO. The investigation of the handling of by-products is the subject for a future study.

## Acknowledgement

This work was supported in part by the Ministry of Education, Culture, Sports, Science, and Technology in Japan under a Grant-in-Aid for the Scientific Research (KAKENHI #2354058).

## References


[1] http://www.env.go.jp/air/osen/voc/voc.html

[2] J. S. Chang: "Recent Development of Gaseous Pollution Control Technologies Based on Non-Thermal Plasmas", *Oyo buturi*, **69**(3), 268-277 (2000).

[3] C. Jiang, A. H. Mohamed, R. H. Stark, J. H. Yuan, and K. H. Schoenbach: "Removal of Volatile Organic Compounds in Atmospheric Pressure Air by Means of Direct Current Glow Discharges", *IEEE Trans. Plasma Sci.*, **33**(4), 1416-1425 (2005).

[4] N. B. Simiand, S. Pasquiers, F. Jorand, C. Postel, and J. R. Vacher: "Removal of Formaldehyde in Nitrogen and in Dry Air by a DBD", *J. Phys. D*, **42**(12), 1-5 (2009).

# Fundamental study on metal plating removal using pulsed power technology

Kiminobu Imasaka, Sebastian Gnapowski*, Hidenori Akiyama*

*Department of Electrical Engineering and Information Technology, Kyushu Sangyo University*

**Graduate School of Science and Technology, Kumamoto University*

## ABSTRACT

A novel method for the metal removal from metal-plated substrate using pulsed power technology is proposed. A metal-plated substrate with three metal-layers structure (Cu, Ni and Au) is used as the sample substrate. Repetitive pulsed arc discharge plasma is generated between a rod electrode and the surface of substrate. Effect of the type of electrode system on metal plating removal was investigated. The removal region is produced by the moving phenomena of the pulsed arc discharge. A part of Au layer, which is the topmost metal surface of the substrate is vaporized and removed by the repetitive pulsed arc discharges. The proposed method can be used for recycle of metal-plated substrate.

## Keywords

Key Words : metal plating removal, pulsed arc discharge, recycle

## 1. Introduction

Environmental destruction and depletion of resources has become a problem due to the economic growth of recent years on a global scale. Therefore, there is a need for conversion to a sustainable, recycling-oriented society from traditional mass disposal type society by 3R (Reduce, Reuse, Recycle). There is a recycle of printed circuit board for mounting electronic circuit parts with respect to recycle in the 3R. In order to recycle the printed circuit board, it is necessary to recover the metal plating material from the insulator substrate such as metal-plated plastics.

The purpose of this study is to develop recycle technology to separate and recover the metal plating material from the insulator substrate used as printed circuit board.

## 2. Experimental Setup

Schematic diagram of printed circuit board used in this experiment was shown in Figure 1. The printed circuit board has a structure in which three metal-plated layers are formed on an insulator substrate made of FRP. Materials of the three metal-layers are composed of cupper (Cu), nickel (Ni) and gold (Au).

On the other hand, it is reported that as an electrode system for the removal of metal plating by the pulsed arc discharge, a thin wire or rod-shaped metal electrode covered with an insulator such as a ceramic tube is effective electrode system [1-3]. Therefore, the similar electrode system was also used in this

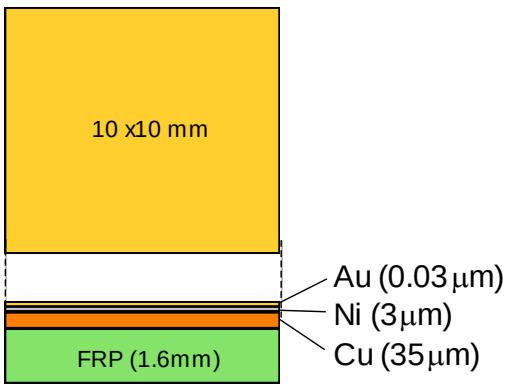


Fig. 1 Metal plating substrate

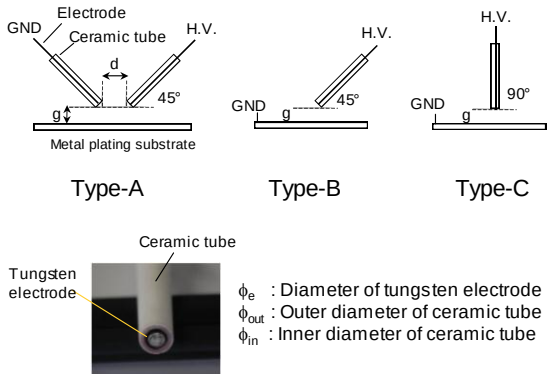


Fig. 2 Electrode system

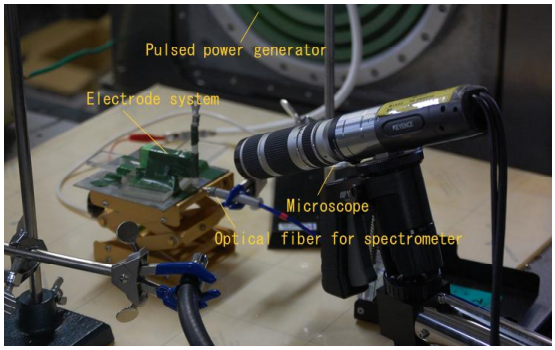


Fig. 3 Experimental setup.

study. Three types of electrode system (Type-A, Type-B and Type-C) were used to investigate the effects of the relative positional relationship between the electrode and metal-plated substrate on the removal of metal plating. The electrode systems were shown in Figure 2.

<Type-A> Rod electrodes made of tungsten inserted into the ceramic tubes were used as the high voltage and ground electrode. Both electrodes were set up above the metal plated substrate at the angle of 45 degrees. In this case, we defined the separation between two electrodes and the distance from the substrate as *d* and *g*, respectively.

<Type-B> The tungsten rod electrode inserted into the ceramic tube and the metal plated substrate were used as the high voltage and ground electrode, respectively. The rod electrode was set up at the distance of *g* from the metal plated substrate, which was used as the ground electrode. Angle of the rod and substrate was 45 degrees.

Table 1 Experimental condition.

| | |
|---|---|
| Pulsed power generator | Output voltage(%)---Max. 120kV |
| | Repetition rate(pps)---Max. 40pps |
| | Number of shots |
| Electrode system | Diameter of tungsten electrode, $\phi_e$ (mm) |
| | Inner diameter of ceramic tube, $\phi_{in}$ (mm) |
| | Gap length,g(mm) |

<Type-C> Type-C electrode system was similar that of Type-B, however, Angle of the rod and substrate in Type-C was 90 degrees.

Experimental apparatus was shown in Figure 3. A pulsed power generator was used to generate the pulsed arc discharge on the metal-plated substrate. The specification of the generator has the maximum output voltage of 120kV, discharge repetition rate of 40pps and the energy of 40J/shot. Output voltage and current were measured with a high voltage probe (Pulse electronics co. ltd, EP-100K) and Rogowski coil (Pearson electronics, Inc, Model101). A high-speed microscope (Keyence co., VW-6000) was used to observe the surface condition of metal-plated substrate and the behavior of repetitive pulsed arc discharges. Optical emission spectra from the discharge were measured with a spectrometer (Ocean optics co, HR4000CG-UV-NIR). An electron probe microanalyser (Shimazu co, EPMA-1720) was employed in order to investigate the metal elemental analysis on the surface of the metal-plated substrate.

Experiments were performed concerned with effects of the electrode systems on removal of metal plating from the substrate, relationship between the removal region of metal plating and the discharge phenomena, and surface analysis of the metal-plated substrate after the repetitive pulsed arc discharge.

## 3. Results and Discussion

### 3.1 Effects of electrode systems on the removal of metal plating

Figure 4 shows the surface condition of metal plating substrate after the pulsed arc discharge

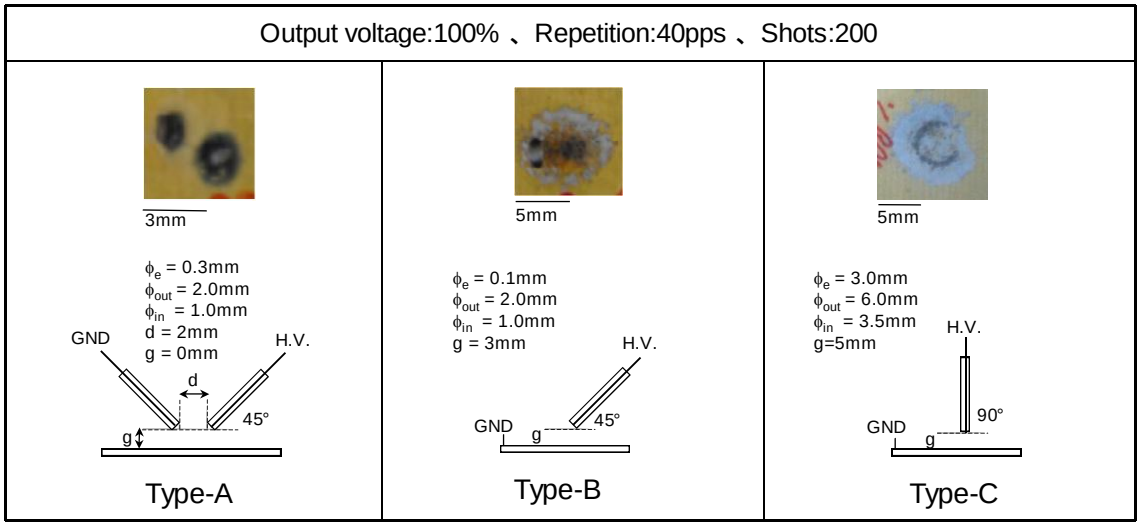


Fig. 4 Metal removal using pulsed arc discharge on different type of electrode systems.

generated in the three types of electrode system. Settings of the output voltage, repetition rate and number of shots were 100%, 40pps and 200shots, respectively. Details of the results for each electrode system are follows.

<Type-A> Pulsed arc discharge was generated between electrodes through the metal plating surface by applying the pulsed high voltage between electrodes. After the discharge of 200 shots, removal region of the metal plating were formed on the substrate just below the high voltage and ground electrode. Size of the removal region was several mm in diameter. The removal region tended to become larger as increasing the number of shots and output voltage setting value. However, the removal regions were formed at only two positions corresponding to each electrode below and it was difficult to remove the metal plating from the substrate efficiently between electrodes as a whole.

<Type-B> When the pulsed high voltage was applied between electrodes, pulsed arc discharge was generated between electrodes and the metal plating was removed. Size of the removal region of the metal plating was increased to approximately 10 mm in diameter compared to that in case of the Type-A electrode system.

<Type-C> The metal plating was removed by the pulsed arc discharge and the size of removal region

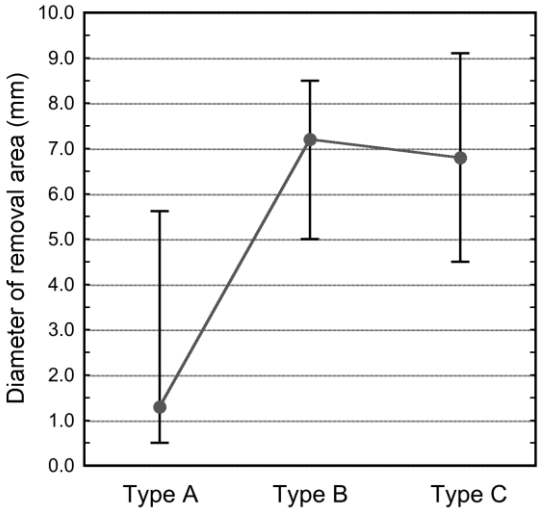


Fig. 5 Dependency of diameter of removal area on 3-type of electrode systems.

was approximately 10 mm in diameter, which was almost same size in case of the Type-B electrode system. However, ring-shaped arc discharge spots were formed in the removal region. It was different from the result of the Type-B electrode system.

Figure 5 shows relationship between the removal region and type of electrode system. The removal region was evaluated by its diameter. Diameter of the removal region formed in the Type-A electrode system was about 5 mm and it was varied widely. Meanwhile, Diameter of the removal region formed

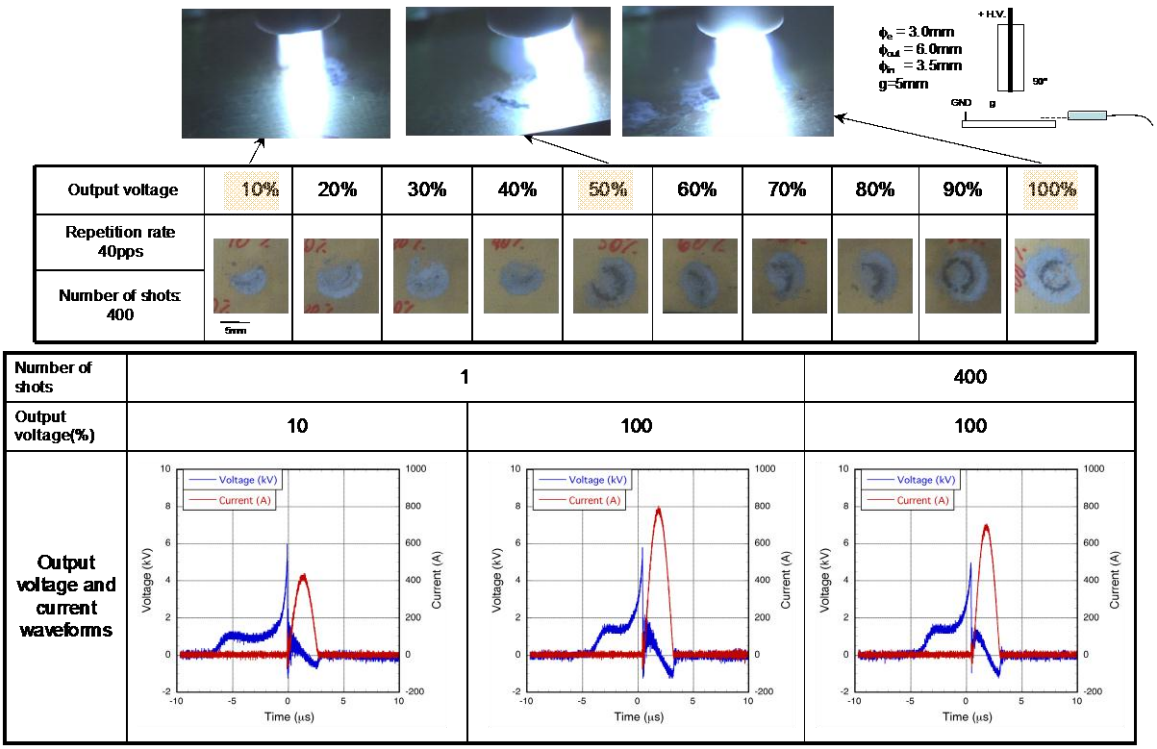


Fig. 6 Effects of pulsed arc discharge on metal removable. Top: photos of pulsed arc discharge, middle: surface condition after discharge, bottom: output voltage and current waveforms.

in the Type-B and Type-C electrode system was increased to about 2 times. From Figure 5, it was found that the Type-B or Type-C electrode system was more effective on the removal of metal plating in this experiment. In particular, the characteristic ring-shaped discharge region is formed in the Type-C electrode system as shown in Figure 4. Therefore, then we investigated relationship between the removal region and the discharge phenomena using the electrode system Type-C.

### 3.2 Relationship between removal area of metal plating and discharge phenomena

Figure 6 shows the metal removal region and the pulsed arc discharge phenomena by changing the output voltage setting value from 10% to 100% in case of the Type-C electrode system. Repetition rate of the discharge and number of shots were 40 pps and 400 shots, respectively. It was found that the ring-shaped discharge region was formed at the output voltage setting value of 50% and the removal region became larger as increasing the voltage setting value. The high-speed microscope observation revealed that the formation of ring-shaped discharge region was due to the behavior of pulsed arc discharge. The discharge plasma channels were produced between electrodes shot to shot and these plasma channels were moved in the shape of the ring between the tungsten rod and ceramic tube. This result suggested that the metal plating was gradually removed from the substrate by the repetitive pulsed arc discharge.

Output voltage and current waveforms were also shown in Figure 6. The peak output voltage and current value at the voltage setting value of 10% was 6kV and 400A, respectively for 1 shot discharge. When the voltage setting value was increased to 100%, the peak output voltage was almost same but the current was increased to 800A. As increasing number of shots up to 400 the current value was decreased to 700A. The decrease of current was thought to be due the increase of impedance between electrodes because of the removal of metal plating

from the substrate.

### 3.3 Surface analysis of the metal-plated substrate after the discharge

Figure 7 shows the metal elemental analysis of metal plating substrate after pulsed arc discharge. The metal plating materials were composed of Cu, Ni and Au. The material of topmost surface of the metal plating three layers was Au and the middle layer material was Ni. It was clear from Figure 7 that the Au layer was removed by the pulsed arc discharge. However, the Ni layer could not be removed by the repetitive pulsed arc discharge.

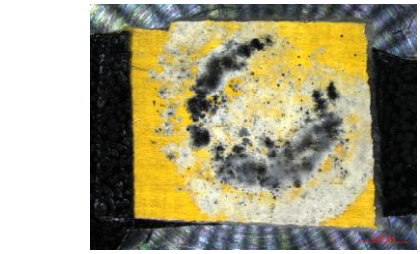

(a) Metal plating substrate after pulsed arc discharge for surface analysis.
(Output voltage:100% Repetition :40pps 200shots)

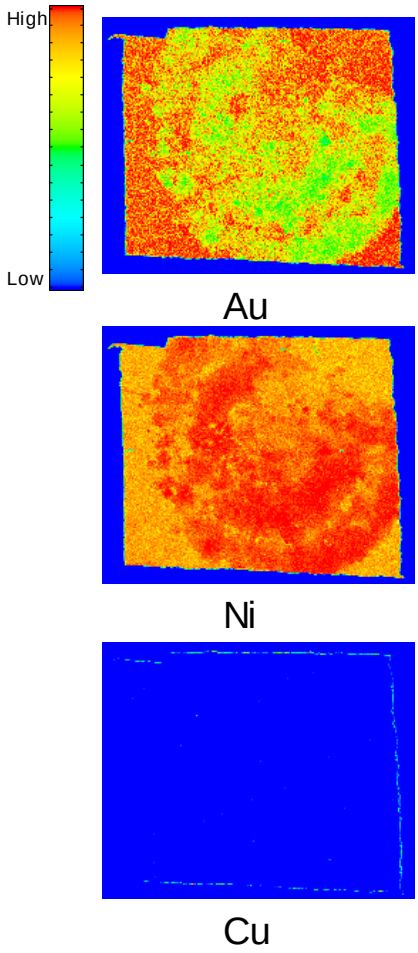


(b) Mapping images of metal elements

Fig. 7 Metal elemental analysis of metal plating substrate after pulsed arc discharge.

## 4. Conclusions

The removal method of metal plating by the pulsed arc discharge was proposed. Obtained results were summarized below.

(1) The rod electrode inserted into ceramic tube to plane electrode system (Type-C) was most effective to the removal of metal plating.

(2) The metal plating was removed from the substrate by the repetitive pulsed arc discharge, which formed the ring-shaped discharge region.

(3) Au layer, which was the topmost material of the metal plating layer was removed by the pulsed arc discharge.

These results suggest that the metal plating layers can be removed selectively by controlling the parameters of the electrode system and the pulsed power generator.

## References

[1] T. Nagashima et al., "Recycle of Metal-Plating on Plastics by Pulse Arc Discharge", *Digest of Technical Papers-IEEE Int.Pulsed Power Conf.*, pp.1437-1440 (2007).

[2] H.Akiyama et al., "Separation of Metal from Metal-Plated Plastics by Pulsed Power", *IEEJ Trans. on Fundamentals and Materials*, **125**, 12, pp.1006-1010 (2005).

[3] T. Nagashima et al., "Recycle of Metal-Plating Plastics by Pulse Arc Discharge", *J. Plasma Fusion Res. SERIES*, **8**, pp.1471-1476 (2009).

# Unresolved transition array based water window soft x-ray source by laser-produced high-*Z* plasma

Takeshi Higashiguchi[1], Padraig Dunne[2], and Gerry O'Sullivan[2]

[1]*Department of Advanced Interdisciplinary Sciences, Center for Optical Research ¥& Education (CORE), and Optical Technology Innovation Center (OpTIC), Utsunomiya University, Yoto 7-1-2, Utsunomiya, Tochigi 321-8585 Japan*

[2]*School of Physics, University College Dublin, Belfield, Dublin 4, Ireland*

## ABSTRACT

We demonstrate a table-top broadband emission water window source based on laser-produced high-$Z$ plasmas. Resonance emission from multiply charged ions merges to produce intense unresolved transition arrays (UTAs) in the 2 to 4 nm region, extending below the carbon K edge (4.37 nm). Arrays resulting from $n = 4–n = 4$ transitions are overlaid with $n = 4–n = 5$ emission and shift to shorter wavelength with increasing atomic number. An outline of a microscope design for single-shot live cell imaging is proposed based on a bismuth plasma UTA source, coupled to multilayer mirror optics. At power densities available from "table-top" solid-state lasers, comparison of emission from a number of targets has shown that 3*d*–4*f* UTA in zirconium plasmas have highest overall brightness and in an imaging system based on reflective multilayer mirrors, may, depending on bandwidth, have superior performance than either line or broader-band sources.

## Keywords

Unresolved transition array (UTA), water window, soft x-ray, laser-produced plasma, high-*Z*

## 1. Introduction

Development of shorter wavelength sources in the extreme ultraviolet (EUV) and soft x-ray spectral regions has been motivated by their application in a number of high profile areas of science and technology. One such topic is the challenge of three-dimensional imaging and single-shot flash photography of microscopic biological structures, such as cells and macromolecules, *in vivo* [1]. For x-ray microscopy, the x-ray source should emit a sufficient photon flux to expose the image of the biological sample on the detector. To date the most practical light source of high-power, high-brightness x-rays has been radiation from synchrotrons and more recently from free electron lasers (FEL) [2]. Table-top sources using ethanol sprays and liquid nitrogen droplets are being developed for use with zone plates for transmission microscopy. Recently $\lambda$ = 2.48 nm narrowband emission from a liquid-nitrogen-jet laser-plasma [3] was successfully combined with state-of-the-art normal-incidence multilayer condenser optics and 20-nm zone-plate imaging optics to demonstrate laboratory water-window x-ray microscopy [4] with resolution less than 25 nm and synchrotron-like image quality on biological and soil science samples. In addition, the development of a high-brightness source based on a focused electron-beam impacting a liquid water jet resulting in $\lambda$ = 2.36 nm emission has also been reported [5]. However, the total collected energy is low, when one combines the narrow line emission with the low reflectivity of the collector mirror. As a result long exposures are needed to record an image and there is not yet published evidence of single-shot

exposures using a laboratory-scale source. To overcome the low efficiency imposed by line sources, we propose using high power water-window emission from laser-produced high-$Z$ plasmas, analogous to the scheme used for efficient, high-volume manufacturing EUV sources.

Efficient, high-power extreme-ultraviolet (EUV) sources for semiconductor lithography at 13.5 [6] and 6.7 nm [7-9] based on laser-produced plasmas have been demonstrated in high-volume manufacturing of integrated circuits (IC) having node sizes of 22 nm or less [10]. Plasmas of the high-$Z$ elements Sn and Gd produce strong resonant emission due to $4d$–$4f$ and $4p$–$4d$ transitions at 13.5 nm and 6.7 nm, respectively, which overlap in adjacent ion stages to yield an intense unresolved transition array (UTA) in their spectra. The in-band high-energy emission is thus attributable to hundreds of thousands of near-degenerate resonance lines lying within a narrow wavelength range.

Before discussing the high-power water window source, it is important to summarize the characteristics of efficient UTA light sources used in the 5 to 15 nm region. All are based on $n = 4$–$n = 4$ ($4d$–$4f$ and $4p$–$4d$) transitions that overlap to generate an intense UTA. For efficient 13.5-nm operation, which corresponds to a photon energy $h\nu \approx 92$ eV, it is important to produce an optimum plasma electron temperature of 30–50 eV. The rare-earth elements of gadolinium (Gd, $Z = 64$) and terbium (Tb, $Z = 65$) produce strong emission near $\lambda = 6.7$ nm ($h\nu \approx 183$ eV) which is maximized at electron temperatures in the 100–120 eV range depending on initial focusing conditions [7-9]. The spectral behavior of Gd and Tb plasmas is expected to be largely similar to that of Sn plasmas, because in the temperature range of interest, both are dominated by $4d$ open-shell ions. Although the conversion efficiency (CE) from the input laser energy to the output in-band EUV emission energy depends on the bandwidth (BW) of the reflection coefficient of the multilayer mirror (MLM), the maximum CEs have been observed to be higher than 1%. Because it moves to shorter wavelength with increasing atomic number, $Z$, the $n = 4$–$n = 4$ UTA is expected to lie in the water window if higher $Z$ elements from $Z = 79$ (Au) to $Z = 83$ (Bi) are used [11-13]. Higher $Z$ elements such as uranium also emit in the water window but their radioactivity prohibits their use. Much of the previous work on high-$Z$ plasmas has concentrated on the production of quasicontinuum spectra at moderate laser intensities, employing electron temperatures below 100 eV [14-16].

In this paper, we report the efficient water window source by strong UTA band emission in laser-produced high-$Z$ plasmas. Our proposed procedure for producing the water window emission is expected to be efficient and scalable in output yield. We have initiated a number of experiments to explore how this emission may be optimized in practice.

## 2. Experimental setup

To evaluate the spectral behavior, two Nd:YAG lasers operating at 1064 nm produced maximum pulse energies of 200 mJ for a pulse duration of 150 ps (FWHM) and 400 mJ at a pulse duration of 10 ns (FWHM), respectively. The laser was focused perpendicularly onto a target with a 10-cm focal length lens. The maximum focused intensity was approximately $1 \times 10^{14}$ W/cm$^2$ at a constant focal spot diameter of 30–40 μm (FWHM). Under these conditions the maximum electron temperature attainable is predicted within the collisional radiative (CR) plasma regime to be greater than 3 keV and the corresponding maximum ion stage close to fifty times ionized [17]. In practice however, the ion stages responsible for the observed emission will be lower as the bulk of the emission is produced during the recombining expanding phase and because of the finite time required to attain the maximum stage consistent with the CR model predictions. The laser was operated in single shot mode. A flat-field grazing incidence spectrometer with 2400 grooves/mm variable line space grating was positioned at 45° with respect to the incident laser axis. Time-integrated spectra were measured by a thermoelectrically cooled back-illuminated x-ray CCD camera. The typical spectral resolution was better than 0.005 nm [18,19].

## 3. Au, Pb, and Bi plasmas

Figures 1(a)–1(c) show time-integrated spectra from Au, Pb, and Bi plasmas at a laser intensity of 1 × $10^{14}$ W/cm$^2$ with a 150-ps pulse duration. Time-integrated EUV spectra between 1 and 6 nm from each element display strong broadband emission near 4 nm, which is mainly due to $n = 4–n = 4$ transitions from ions with an open 4*f* or 4*d* outermost subshell, together with broadband emission around 2–4 nm due to $n = 4–n = 5$ transitions from multi-charged state ions with an outermost 4*f* subshell. The latter merge to form a structured feature from which the contributing ion stages may be readily inferred. The intensity of the $n = 4–n = 4$ UTA emission is higher than that of the $n = 4–n = 5$$ emission. The atomic number spectral dependence is summarized in Fig. 1(d). The predicted photon energy of each experimental peak wavelength was shifted to higher photon energy with increasing atomic number. Neither the emission spectra nor the plasma electron temperatures, however, have been optimized, as shown below. The emission intensity of the $n = 4–n = 5$ transitions, however, was compared with that of the $n = 4–n = 4$ UTAs.

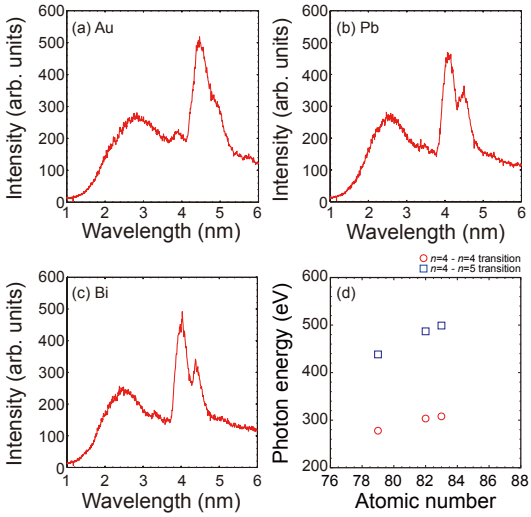


Fig. 1. Time-integrated spectra from the picosecond-laser-produced high-*Z* plasmas by use of Au (a), Pb (b), and Bi (c), and the atomic number dependence on the photon energies of peak emission of the $n = 4–4$ transition (circles) and the $n = 4– 5$ transition (rectangles).

The strong emission at 3.15 nm due to the $n = 4–n = 4$ UTA in Bi plasmas may be coupled with a Sc/Cr MLM with a reflection coefficient of 15% [20]. The variation of this emission with electron temperature was calculated with Cowan's suite of atomic structure codes in order to predict its evolution with increasing laser flux [21]. The predicted spectral evolution as a function of electron temperature is summarized in Fig. 2. In this figure the spectra generated for each ion stage are based on excited state populations that allow for electron temperature assuming a Boltzmann distribution. These spectra are then weighted by an ion fraction appropriate to that temperature, calculated assuming CR equilibrium to yield the distributions shown.

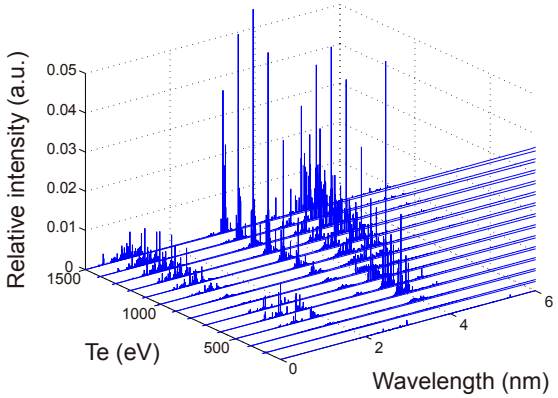


Fig. 2. Calculated spectral variation as a function of electron temperature.

To explain the Bi spectra, we compare the results of calculation for some experimental temperatures with the experimental spectrum, as shown in Fig. 3(a). Four regions corresponding to emission peaks are identified. Note that this spectrum is integrated both spatially and temporally over the duration of the laser pulse. The emission in region "1" results primarily from 4*f*–5*g* transitions in ions with an open 4*f* subshell, i.e., stages lower than $Bi^{35+}$. The emission in regions "2" and "3" comes from 4*p*–4*d* and 4*d*–4*f* transitions in ions with an open 4*d* subshell ($Bi^{36+}$–$Bi^{45+}$), and calculations show that the higher energy feature results from the more highly ionized species (> $Bi^{42+}$). The emission in region "4" is again associated mainly with 4*d*–4*f* emission from lower stages with an open 4*f* outmost subshell. Thus the

bulk of the emission, especially from regions "1" and "4", is associated with the recombining phase of the expanding plasma plume. In this figure we show for comparison spectra calculated for steady state electron temperatures of 180 and 700 eV, while the higher temperatures are required to generate the emission in region "2", the calculations verify that both the longer and shorter wavelength features are consistent with much lower plasma temperatures.

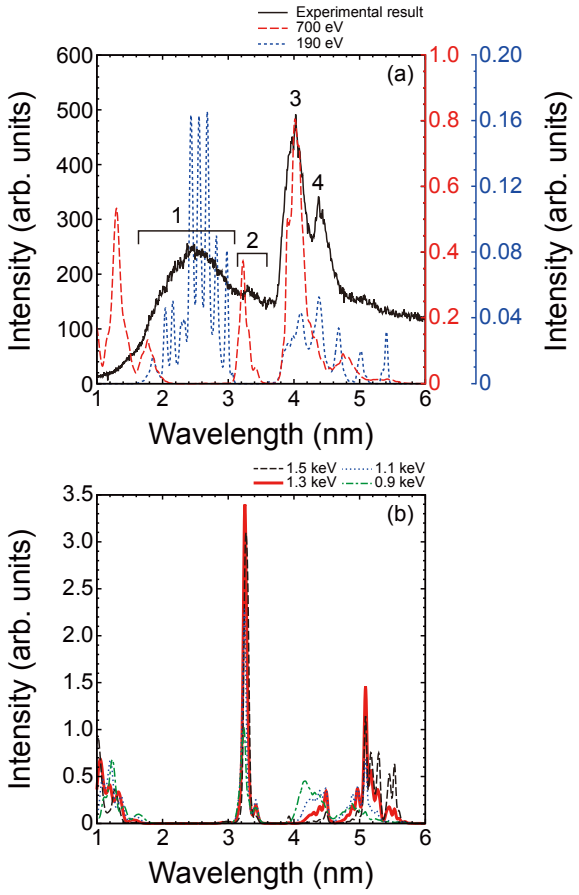


Fig. 3. Spectral behaviors of the Bi plasmas in the laser intensity dependence on the observed emission spectra (a), the peak wavelength of the $n$ = 4–4 transition (circles) and the $n$ = 4–5 transition (rectangles) (b).

In Fig. 3(b) calculated spectra at different electron temperatures higher than 900 eV are presented. Our calculations show that high-$Z$ plasmas, at an electron temperature lower than 700 eV, as shown in Fig. 3(a), radiate strongly near 3.9 nm. However, in the case of higher electron temperatures, from 800 to 1500 eV, the strongest emission is expected at around 3.2 nm, suitable for coupling to Sc/Cr MLMs [20]. Thus for an optimized source, we should produce a plasma at a higher electron temperature plasma of around 1 keV. The intensity of the Bi plasma emission in our experiment was compared with 2.48-nm nitrogen line emission from a $Si_3N_4$ planar target, in the same experimental setup, and was observed to be 1.2 times higher within a bandwidth of 0.008 nm (FWHM) [20,22] even though the plasma electron temperature was much lower than the optimum value.

## 4. Proposal by Bi plasma source

Taking the experimental and numerical results into account, we now propose a high brightness, high power water window source for single shot imaging at the laboratory scale. Our proposed method has the advantage that the EUV energy efficiency and atomic number dependence can be scaled based on the fundamental properties of the plasma source. The electron temperature, $T_e$, in a high-$Z$ plasma rises with increasing laser intensity as $T_e \propto (I_L\lambda_L^2)^{0.4}$, where $I_L$ and $\lambda_L$ are the laser intensity and wavelength, respectively [17]. To produce not only a Bi plasma with a high electron temperature of the order of 1 keV but also one that has low density and is optically thin, we should switch to a $CO_2$ laser operating at a wavelength of 10.6 μm due to the low critical density of $1 \times 10^{19}$ $cm^{-3}$ attainable [23], with a pulse duration to permit ionization to the appropriate ion stages ($Bi^{36+}$–$Bi^{45+}$ i.e., > 150 ps), while at the same time maintaining a laser intensity of the order of $10^{13}$ $W/cm^2$ [24]. In addition, for this proof of principle, we propose a dot Bi target with a diameter less than 20 μm with a thickness less than 1 μm to generate a microplasma (to fulfill the requirements for high brightness and a point source) as the expected focal spot size will be the order of 100 μm in the case of the $CO_2$ laser wavelength of 10.6 μm. Because of the broadband nature of the emission, zone plate components cannot be used, so one possible solution would be to use a transmission planar x-ray nano-waveguide to image the sample [25]. To achieve high resolution in the recorded image, we should also switch the recording device from x-ray

CCD cameras to sensitive EUV resists to overcome the resolution limitation of the CCD pixel size, coupled with Schwarzschild optics, consisting of Sc/Cr MLMs with a reflection coefficient of the order of 15% around 3.2 nm [20]. Although our proposal is based on a simple microscope construction, the key component is the UTA emitted at 3.2 nm from a hot dense Bi plasma point source, combined with Sc/Cr MLMs and sensitive EUV resists based on photochemical reaction [26,27].

## 5. Zr plasmas

Two key aspects emerged from experimental studies on Bi. The first was that the high plasma temperatures required to produce the ion stages involved ($Bi^{36+}$–$Bi^{45+}$) necessitated the use of a very high laser flux higher than $10^{13}$ W/cm$^2$ at $\lambda$ = 10.6 μm. Such fluxes are not currently available in ns pulses from "table-top" laser systems and the realization of a Bi plasma source is predicated on the future development of new high pulse energy $CO_2$ lasers with pulse durations of around one nanosecond [18]. The second was that spectra obtained at lower laser power densities with plasmas produced by a 10-ns duration Nd:YAG laser pulse contained a large contribution from $\Delta n$ = 1, 4*f*–5*g* transitions from significantly lower ion stages in the 2–3.5 nm region that was actually comparable in intensity to the UTA emission from $\Delta n$ = 0, $n$ = 4–$n$ = 4 transitions centered near 4.0 nm. This observation suggested the feasibility of using the emission of $\Delta n$ = 1 transitions in other elements as possible candidates for water window sources. Indeed, such transitions in laser produced plasmas formed on Ar and Kr gas jets are in widespread use for nanopatterning of photoresists [26-28].

As well as requiring lower laser fluxes as they originate from lower ion stages, plasma emission based on these transitions has the advantage of being less optically thick since it is well known that the emission from $\Delta n$ = 1 transitions shifts almost monotonically to higher energy with increasing ion stage so that radiation trapping amongst overlapping transitions is not a problem. In addition, the emission from satellites, which are favored in emission from solid targets, can to some extent fill in the regions between the resonance arrays in adjacent stages giving an almost continuous distribution of intensity [19].

Figure 4 shows the time-integrated spectra from C, $Si_3N_4$, Mo, Zr and Bi plasmas recorded at a laser intensity of 5 × $10^{11}$ W/cm$^2$ with a 10-ns pulse duration in the 2–9 nm region. For the lighter two elements, as is well known, spectra are dominated by H and He like ion emission, while for Mo and Zr the spectra are dominated in the water window region by $\Delta n$ = 1, 3*d*–4*f* transitions. Indeed, from the available literature it was possible to identify all of the strong peaks in the 2.3–4.2 nm region of the Mo spectrum and assign them to ion stages from $Mo^{14+}$ to $Mo^{21+}$. From Fig. 4 it is obvious that the main contribution from Mo plasmas to the water window region begins at a wavelength lower than 3.5 nm. In order to have greater wavelength coverage, a lower $Z$ target where the corresponding isoelectronic emission is displaced to longer wavelength is a more suitable choice. This consideration allied to the fact that each in these spectra emission from adjacent ion stages is displaced by 0.3–0.5 nm in successive ion stages suggested that Zr plasmas should provide the optimum water widow coverage.

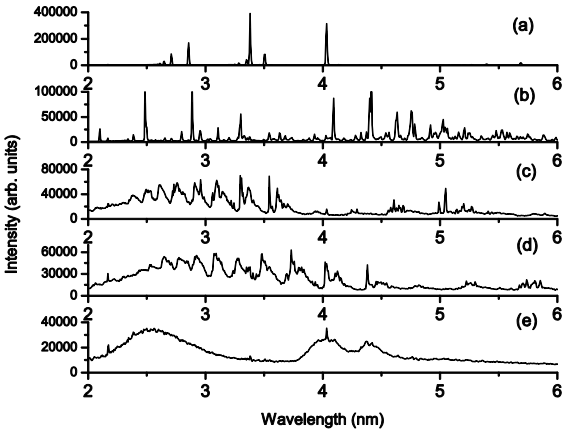


Fig. 4. Spectral behaviors of the Bi plasmas in the laser intensity dependence on the observed emission spectra (a), the peak wavelength of the $n$ = 4–4 transition (circles) and the $n$ = 4–5 transition (rectangles) (b).

The spectrum of Bi is also shown in this figure for comparison and while the $n = 4–n = 4$ UTA emission is quite intense near 4 nm and the $4f–5g$ transitions contribute to a broad Gaussian shaped feature centered near 2.5 nm, the overall emission does not "fill" the water window region as completely as that from Zr targets.

In Fig. 5 we present the variation of spectral emission for a range of power densities. While the intensity increases with the laser intensity, the appearance of the spectrum changes only slightly, with short wavelength features being more distinct higher than $10^{13}$ W/cm$^2$. The corresponding electron temperatures are evaluated to range from 100–200 eV while calculations within the collisional-radiative (CR) framework indicate that plasmas with peak temperatures of at least 230 eV are required to optimize the water window emission [17].

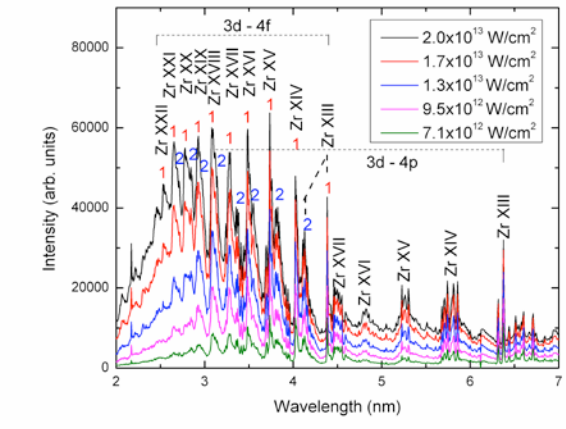


Fig. 5. Spectral behavior of Zr plasmas showing the laser intensity dependence of the observed emission spectra. Resonant $3d–4f$ (1) and $3d–4p$ transitions as well as satellite lines from $3d^{n-1}4s4f–3d^{n-2}4s4f$ (2) are clearly seen for $Zr^{12+}–Zr^{21+}$ in this figure.

In order to make a relative comparison of the total emission, the total number of counts was integrated between 2.3 and 4.2 nm for each of the targets shown in Fig. 4 for the range of power densities covered in the experiments. The results are shown for both ns and ps pulse irradiation in Fig. 6 and show that the total emission in the 10 ns plasmas is some 50% greater in the case of Mo and Zr while it is almost 50% less in the case of Bi. This results from the need to have significantly higher ion stages and therefore a hotter plasma for efficient Bi emission which is favored at the higher laser flux. In order to obtain $4f–5g$ emission the ion stages must lie in the range from $Bi^{22+}$ to $Bi^{35+}$, while for strong $4p–4d$ and $4d–4f$ transitions ions must possess an open $4d$ subshell ($Bi^{36+}–Bi^{45+}$). It is interesting also to compare the total flux available from C and N containing plasmas; while the intensity of the individual lines is certainly greater, the total in-band emission is significantly less than for any of the higher $Z$ targets. In addition, it is interesting to note that while the C emission is consistently stronger than that from the $Si_3N_4$ in the ps laser-produced plasmas, for ns plasmas the behavior is more complex and the emission of $Si_3N_4$ exceeds that of C plasmas at both lowest and highest laser fluxes used for 10-ns irradiation.

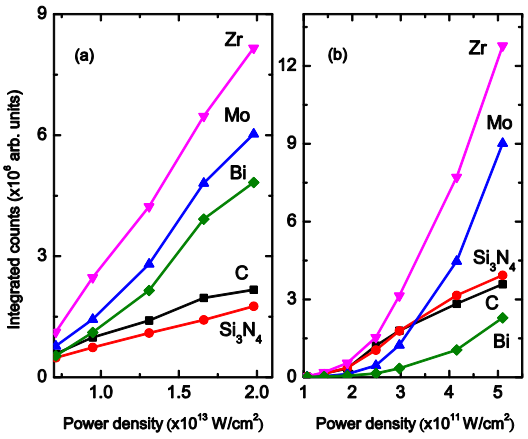


Fig. 6. Water window emission (total counts) as a function of power density for 150 ps (a) and 10 ns (b) laser pulses showing the variation of total count rate for plasmas of the elements presented in Fig. 4.

Since the intensity depends on both photon energy and count rate, in order to get a measure of the total flux, the quantity $N(E)EdE$, where $N(E)$ is the number of counts occurring at energy $E$, was integrated over the water window and the results yielded curves very similar to those of Fig. 6 and again showed that of the elements considered here, Zr

is the brightest emitter in the water window for laser fluxes in the $10^{12}$–$10^{13}$ W/cm$^2$ range.

## 6. Summary

We have demonstrated high-efficiency emission in the water window spectral region based on laser-produced Zr and Bi plasmas, and have proposed methods to increase it still further. Resonance emission from multiply charged ions merges to produce intense UTA, extending to wavelengths below the carbon K edge. The overall spectral behavior is well described by simulations. The experimental results also provide an outline for the design concept for single-shot cell imaging with a novel microscope optical system. The method presented here opens the way for applications in next-generation biological science.

## Acknowledgements

The authors are deeply indebted to Prof. Weihua Jiang (Nagaoka University of Technology), Prof. Akira Endo (HiLASE Project, Institute of Physics AS), for useful discussion. The authors are grateful to Takamitsu Otsuka, Bowen Li, Yusuke Suzuki, and Ryoichi Hirose for their unparalleled technical support. A part of this work was performed under the auspices of MEXT (Ministry of Education, Culture, Science and Technology, Japan) and was also supported by the high education donation program funded by Intel K.K., which is a subsidiary of Intel Corp. One of the authors (T.H) also acknowledges support from The Canon Foundation and Research Grant (Basic Research) on TEPCO Memorial Foundation. The UCD group is supported by Science Foundation Ireland under Principal Investigator Research Grant No. 07/IN.1/I1771. We are also grateful to Gigaphoton Inc. for providing the picosecond laser system.

## References

[1] J. C. Solem and G. C. Baldwin, *Science,* **218**, 229 (1982).

[2] T. Gorniak et al., *Opt. Exp.* **19**, 11059 (2011).

[3] P. A. C. Jansson et al., *Rev. Sci. Instrum.,* **76**, 043503 (2005).

[4] P. A. C. Takman et al., *J. Microsc.,* **226**, 175 (2007).

[5] P. Skoglund et al., *Appl. Phys. Lett*., **96**, 084103 (2010).

[6] "EUV Sources for Lithography", edited by V. Bakshi (SPIE, Bellingham, WA, 2005).

[7] T. Otsuka et al., *Appl. Phys. Lett*., **97**, 111503 (2010).

[8] T. Otsuka et al., *Appl. Phys. Lett*., **97**, 231503 (2010).

[9] T. Higashiguchi et al., *Appl. Phys. Lett*., **99**, 191502 (2011).

[10] C. Wagner and N. Harned, *Nat. Photonics*, **4**, 24 (2010).

[11] D. Kilbane, *J. Phys. B: At. Mol. Opt. Phys.*, **44**, 165006 (2011).

[12] B. Li et al., *Proc. SPIE*, **8139**, 81390P (2011).

[13] T. Higashiguchi et al., *SPIE Newsroom* (DOI: 10.1117/2.1201109.003765, 2011).

[14] P. K. Carroll and G. O'Sullivan, *Phys. Rev. A*, **25**, 275 (1982).

[15] G.-M. Zeng et al., *J. Appl. Phys.*, **67**, 3597 (1990).

[16] G.-M. Zeng et al., *J. Appl. Phys.*, **69**, 7460 (1991).

[17] D. Colombant and G. F. Tonon, *J. Appl. Phys.*, **44**, 3524 (1973).

[18] T. Higashiguchi et al., *Appl. Phys. Lett*., **100**, 014103 (2012).

[19] B. Li et al., *Appl. Phys. Lett*., **102**, 041117 (2013).

[20] K. Sakano and M. Yamamoto, *Proc. SPIE*, **3767**, 238 (1999).

[21] R. D. Cowan, "The Theory of Atomic Structure and Spectra" (University of California Press, Berkeley, 1981).

[22] M. Bertilson et al., *Opt. Exp*., **17**, 11057 (2009).

[23] H. Tanaka et al., *Appl. Phys. Lett*., **87**, 041503 (2005).

[24] Y. Ueno et al., *Appl. Phys. Lett*., **90**, 191503 (2007).

[25] S. P. Kruger et al., *Opt. Exp*., **18**, 13492 (2010).

[26] T. Gowa et al., *J. Photopolym. Sci. Technol.*, **22**, 273 (2009).
[27] T. Gowa et al., *Radiat. Phys. Chem.*, **80**, 248 (2011).
[28] T. G. Oyama et al., *AIP Advances*, **1**, 042153 (2011).